3-2005

Mixing Effects of Pylon-aided Fuel Injection Located Upstream of a Flameholding Cavity in Supersonic Flow

Daniel R. Montes

MIXING EFFECTS OF PYLON-AIDED FUEL INJECTION LOCATED UPSTREAM OF A FLAMEHOLDING CAVITY IN SUPERSONIC FLOW

THESIS

Daniel R. Montes, Second Lieutenant, USAF

AFIT/GAE/ENY/05-M12

DEPARTMENT OF THE AIR FORCE
AIR UNIVERSITY

AIR FORCE INSTITUTE OF TECHNOLOGY

Wright-Patterson Air Force Base, Ohio

The views expressed in this thesis are those of the author and do not reflect the official policy or position of the United States Air Force, Department of Defense, or the U.S. Government.

AFIT/GAE/ENY/05-M12

MIXING EFFECTS OF PYLON-AIDED FUEL INJECTION LOCATED UPSTREAM OF A FLAMEHOLDING CAVITY IN SUPERSONIC FLOW

THESIS

Presented to the Faculty

Department of Aeronautics and Astronautics

Graduate School of Engineering and Management

Air Force Institute of Technology

Air University

Air Education and Training Command

In Partial Fulfillment of the Requirements for the

Degree of Master of Science in Aeronautical Engineering

Daniel R. Montes, B.S. Astronautical Engineering
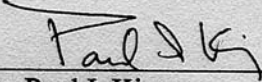
Second Lieutenant, USAF

March 2005
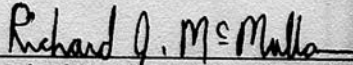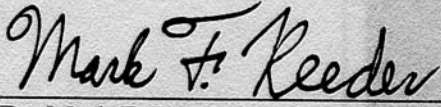
AFIT/GAE/ENY/05-M12

MIXING EFFECTS OF PYLON-AIDED FUEL INJECTION LOCATED UPSTREAM OF A FLAMEHOLDING CAVITY IN SUPERSONIC FLOW

Daniel R. Montes, B.S. Astronautical Engineering

Second Lieutenant, USAF

Approved:

_____   _____
Dr. Paul I. King   9 Mar 05
(Chairman)   Date

_____   _____
Maj Richard J. McMullan, PhD, USAF   9 Mar 05
(Member)   Date

_____   _____
Dr. Mark F. Reeder   9 Mar 05
(Member)   Date

AFIT/GAE/ENY/05-M12

Abstract

The Air Force Research Lab (AFRL), Propulsion Directorate, Wright-Patterson Air Force Base, Ohio is conducting ongoing research into propulsive efficiency in supersonic ramjet (scramjet) technology. One current focus of this research is the usefulness of flameholding cavities implemented in the supersonic hydrocarbon-fueled combustion chamber. Because good mixing and proper cavity-core interaction lead to more efficient combustion, methods of optimizing fuel/air mixing both within and upstream of the cavity are investigated. In a cooperative effort with the Air Force Institute of Technology (AFIT), AFRL provided a supersonic (Mach 2) wind tunnel outfitted with an existing cavity design. A circular injection port was placed upstream of the cavity, and a series of three pylons (medium, tall, wide geometries) were in turn fitted just upstream of the port to improve mixing and penetration of the fuel into the core airflow. The main goals of this experiment were to characterize the mixing ability of injected fuel with the core flow as it propagated downstream of the pylon and to analyze the effects, if any, of this mixing strategy on cavity flow and overall efficiency compared to a no pylon case. The experiment was a non-reacting mixing study. Measurements were obtained from pressure transducers, Planar Laser-Induced Fluorescence (PLIF), and Mie scattering visualization. Of the three pylon geometries tested, the wide pylon (1.6 jet diameters wide, 4 diameters high) provided a 135% increase in penetration. The taller pylon improved penetration as well (190% increase) but incurred a large loss penalty. All pylons lifted the fuel from the injector to prevent flashback, and all pylons demonstrated equivalent or better mixing potential than the flat reference.

<u>Acknowledgments</u>

Table of Contents

List of Figures

List of Tables

List of Symbols

X_f	Fueling Distance from Cavity
X_p	Pylon Proximity to Injector
d	Injection Port Diameter
A	Injection Port Area
L	Cavity Length
D	Cavity Depth
h	Pylon Height
ℓ	Pylon Length
W	Pylon Width
θ	Pylon Wedge Angle
M_∞	Flight Freestream Mach Number
C_D	Discharge Coefficient
$\dot{m}$	Mass Flow Rate
γ	Ratio of Specific Heats
R	Specific Gas Constant
P_j	Fuel Jet Pressure
ρ_j	Fuel Jet Density
T_j	Fuel Jet Temperature
M_j	Fuel Jet Mach Number
P_c	Core Pressure
ρ_c	Core Density
T_c	Core Temperature
M_c	Core Mach Number
P_{0c}	Tunnel Stagnation Pressure
T_{0c}	Tunnel Stagnation Temperature
P_{0j}	Fuel Jet Total Pressure
ρ_{std}	Standard Atmospheric Density
q	Dynamic Pressure Ratio
F1	Flat Insert, First Injection Pressure
F2	Flat Insert, Second Injection Pressure
F3	Flat Insert, Third Injection Pressure
M1	Medium Pylon, First Injection Pressure
M2	Medium Pylon, Second Injection Pressure
M3	Medium Pylon, Third Injection Pressure
T1	Tall Pylon, First Injection Pressure
T2	Tall Pylon, Second Injection Pressure
T3	Tall Pylon, Third Injection Pressure
W1	Wide Pylon, First Injection Pressure
W2	Wide Pylon, Second Injection Pressure
W3	Wide Pylon, Third Injection Pressure

BP	Back Pressure Condition
M0	No Injection Pylon Characterization
x	Streamwise Axis
y	Transverse Axis
z	Spanwise Axis
y_j	Jet Penetration Height
Δy	Vertical Fuel Spread
g	Floor Gap
Δz	Max Spanwise Fuel Spread
A_j	End View Jet Spread Area
A_s	End View Mixing Potential Area

MIXING EFFECTS OF PYLON-AIDED FUEL INJECTION LOCATED UPSTREAM OF A FLAMEHOLDING CAVITY IN SUPERSONIC FLOW

I. Introduction

Background

A key area of study to advance supersonic combustor development is the characterization of cavity-based fuel injection and flameholding. Cavity-based flameholders are commonly found in hydrocarbon-fueled scramjet combustors, but low residence time and interactions with disturbances in the main air flow (i.e., shock trains or shock-boundary layer interactions) raise issues on which detailed information is largely unavailable in the existing literature.[1]

One area of interest to the Air Force concerns the creation of disturbances in the main flow by the use of small pylon devices. Provided that aerodynamic drag and shock losses are minimized, injection behind a pylon has many advantages. Combined with injection, the shock-jet interactions created by these devices cause vorticity via baroclinic torque and cross-stream shear and may improve mixing.[2] This concept may be applied to an upstream pre-injection mechanism that aims to provide a well mixed flow over a downstream cavity. Injection behind pylons also causes an increase in the penetration height of the fuel for a given dynamic pressure ratio, defined later.

The penetration effect serves to conceivably enhance mixing, shorten the isolator and combustor (the two components of a dual mode scramjet combustion system), and possibly simplify the fuel control system. The effect also lifts fuel out of the boundary

layer, a technique that prevents flashback (ignition of fuel that has been seeded into the subsonic boundary layer) as has been shown in the case of liquid injection.[3]

A pylon was aligned streamwise with an ordinary circular injector so that focus on the fuel jet as it propagates downstream could be easily emphasized and understood. Straightforwardness and reusability of the hardware was another consideration in the design. Reproducibility of this experiment and follow-on trials should be simple by the use of the visualization techniques and non-dimensional standards established in this investigation. In fact, AFRL/PR follow-on studies have begun to take results and existing hardware from this research and apply them to dedicated cavity-core interaction and combustion experiments.

Three pylon sizes with several injection pressures as well as a no pylon baseline were employed in this experiment. The hardware was installed with injection immediately behind the pylon and at a distance of 0.9L (cavity lengths) upstream of the cavity employed by Gruber et al.[1] Each pylon is a thin triangular wedge with a 30° inclination angle. Optimal pylon heights, widths, and pylon distances from injection were determined from previous computational research[4] and correlate with sizes used in prior experimentation.[2-3] The investigation included measuring the effects of penetration height and width, shock effects, mixing effectiveness and pressure profiles.

The downstream flameholding cavity was an existing design utilized by the Air Force Research Laboratory, Propulsion Directorate (AFRL/PRAS). The cavity is recessed from the surface with a 90-degree rearward-facing step and a trailing edge is configured with a 22.5-degree ramp.

Aim of Experimental Investigation

The purpose of this research is to aid the ongoing effort to improve combustion efficiency in hydrocarbon fueled scramjet engines. By employing a flameholding cavity in the supersonic flow, this issue may be divided into three parts, namely: mixing fuel into the core airflow (freestream), mixing and igniting fuel in the cavity flameholder, and coupling these two processes to provide complete combustion. This experiment focused mainly on the first task. A look at the coupling effect is also briefly covered in the investigation.

The method chosen in this research for injecting and mixing was to use a pylon device affixed to the injection surface just upstream of the injection port, acting as a barrier to the high velocity air flow. This creates a tiny low pressure area in the region of the fuel jet, which aids in jet penetration. Vorticity and other effects created by the pylon perturbing the airflow influence the mixing of the jet with the freestream. Thus, one of these small pylons could be used to improve the mixing and penetration of a single fuel jet into a supersonic core flow. By placing the configuration upstream of the cavity, the mixed flow can subsequently be observed in front of the flameholder. The ultimate intent of this experiment was to gauge the effectiveness of using this injection method for supersonic mixing and to obtain information that leads to the design of practical combustor configurations containing complex combinations of pylons and cavities.

Research Objectives

Four hardware inserts (three containing pylons, one containing no pylon as a reference) were tested at three injection pressures. The object of this research was to determine the following:

    1) The effect of pylons on basic jet geometries, such as penetration height, plume width (as seen from an end, or spanwise, view), floor separation, and cross-sectional area, as compared to the no pylon case, and the preventability of flashback.

    2) Affected mixing potential, in the form of visible structures and measured standard deviation intensity and turbulent mixing area.

    3) The effect of pylons on the supersonic airflow (such as bow shocks and pressure distribution) as compared amongst each other and against the pure jet with no pylon.

    4) Changes in freestream behavior upstream of and above the flameholder, suggesting cavity shear layer interaction

    5) Behavior in dual mode (high back pressure) conditions.

Hardware from this experiment may be used in various configurations to support follow-on investigations (including combustion studies).

II. Literature Review

Scramjet Combustion: Overview

> "Man's search for higher speeds, as for flight itself, is limited by the propulsion system required for the task." (McClinton et al.)[5]

Supersonic combustion research for use in supersonic and hypersonic airbreathing propulsion has been actively underway in the United States for over forty years. The effort to successfully employ high speed propulsion systems is slowly becoming a reality, as organizations such as NASA have publicly demonstrated.[6] However, the design and optimization of these systems are still experiencing stages of component concept testing. Mission requirements must be balanced with an integrated engine system consisting of the inlet and isolator, combustor, nozzle, airframe, fuel type, and cooling mechanism.[7] Each of these components has a body of dedicated research attached to it.

The ramjet concept is valid for flight speeds in the range $2 < M_\infty < 6$. The inlet section of this engine type compresses and slows the air to subsonic velocities during internal flow (including into the combustor). However, at higher speed flight regimes ($M_\infty > 4$), compression of the working fluid to subsonic flow can result in static properties rising to the point where disassociation losses would take place and the fluid temperature would be too high for effective hydrocarbon combustion. Figure 1 and Figure 2, obtained from www.aviation-history.com, demonstrate the basic design of a

ramjet engine, and its supersonic equivalent, the scramjet, which encompasses the same flow and propulsion concepts as a ramjet but retains supersonic flow throughout the core of the engine.[7]

INLET   DIFFUSER   BURNER   NOZZLE
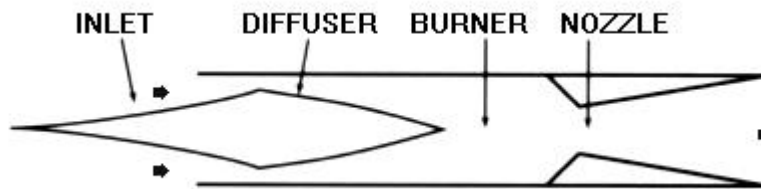
Figure 1. Ramjet layout

INLET   BURNER   NOZZLE
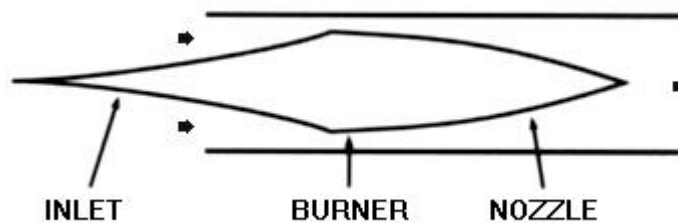
Figure 2. Scramjet layout

Problems arise when the flow is kept supersonic through the core. The low residence time of flow in the combustor section (~1 ms) is not conducive to achieving full, efficient combustion at the relatively slow hydrocarbon kinematic rates. The short time span also does not leave enough opportunity for full mixing of injected fuel and core airflow, which is the necessary precursor to effective ignition and flameholding.[8] Applying complex core geometry adjustments to solve these issues results in drag

penalties incurred from the nature of introducing radical disturbances into supersonic flow and from allowing too much surface area inside the engine. Thus, sometimes at the expense of not attaining complete mixing, the combustor length must be kept as short as possible.[7]

Recent mission requirements (for both manned flights and high speed missiles) have led to the call for a dual mode scramjet. This engine type operates in the full flight regime of both a ramjet and scramjet, and utilizes the combination of a complex inlet geometry and a dual mode combustor. The engine core consists of a constant area isolator section followed by a diverging combustion section. The isolator section is designed to manage the complex shock train structures that form to slow down the core flow when the engine is operating at lower flight velocities, as discussed at length by Billig.[9] In this flight regime, injection and combustion occur downstream of the isolator (as combustion farther upstream would cause a high enough pressure rise to possibly unstart the inlet). The thermally choked flow propagates through the diverging portion and exhaust, once again supersonic.[10-11] In the high velocity mode this engine injects in the isolator section that is completely supersonic, taking advantage of the extended residence time for mixing. Figure 3 highlights this concept.
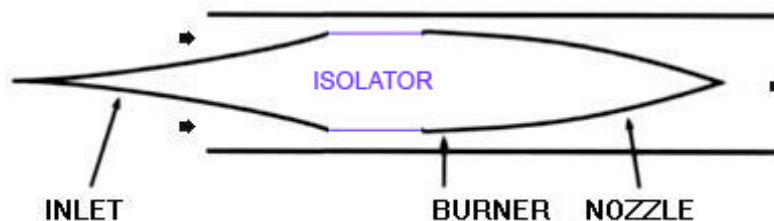
Figure 3. Dual mode scramjet layout

Issues arise with creating an injection and combustion scheme that is robust during both flight conditions. Hydrocarbon fuels are generally preferred for military applications due their higher densities and thus lower fuel tank size. The combustion characteristics of this fuel require fast and efficient mixing, as discussed above. When particularly in the faster flight regime, the dual mode engine suffers greatly when the core contains complicated injection obstructions that aim to improve the mixing and/or combustion.[12] The complexities of three-dimensional combustion and its effect on pressure, shock trains, and mixing is the subject of past and current studies.[13-16] Research has since progressed toward the development of recessed cavity geometries that impose tolerable disturbances to the main flow. Prolonged residence time of airflow through one of these cavities coupled with proper injection can establish a stable flameholder adjacent to the core, supersonic flow.

Cavity Flameholders

Supersonic cavity flameholders were developed in the early 1990's, although cavities have existed in subsonic engines for some time and continue to be investigated.[17] Scramjets with cavity flameholders have been developed and demonstrated in operational flight tests.[18] The current optimal design for flameholding consists of a recessed rearward-facing step, the cavity floor, and a ramp that angles back into the main combustor floor. A shear layer forms between the main flow and the cavity. The angled nature of the rear wall prevents acoustic oscillations that result when the shear layer

8

reattaches and impinges the surface. Figure 4 demonstrates this geometry and shows the

shear layer effects when injection or disturbances occur upstream of the cavity.
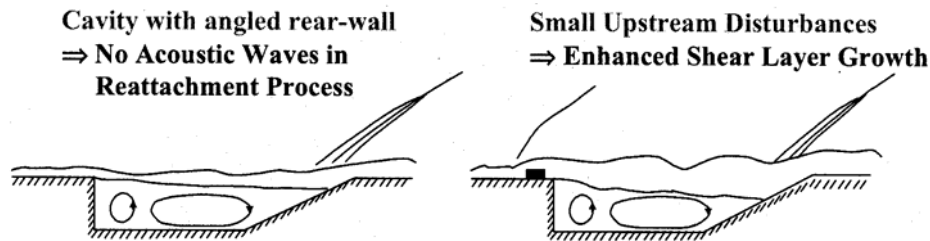
Figure 4. Flameholding cavity example with shear layer emphasized (from Ref. 18)
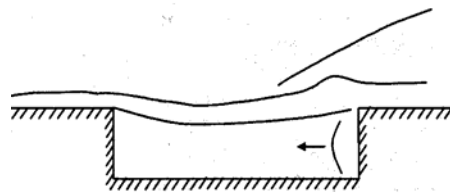
Figure 5. Rectangular cavity design experiencing shear layer impingement (from Ref. 18)

Cavities can be designed to be various shapes and sizes, and thus are not used

only for flameholding purposes. Another form of open cavity does not employ a rear

ramp but simply takes a rectangular shape, as seen in Figure 5. This form of cavity

contains large pockets of subsonic flow, generally at the cost of unstable resonance. The

oscillations from this type of cavity may be useful for mixing purposes, a long as a design

balance is achieved between thrust and additional drag.[19-21] While this is not always the

case as cavity size, geometry, and flight conditions govern this complex behavior, past

studies have aimed to understand and predict how these cavities behave and how to take

advantage of the resonant behavior.[22] More modern research has investigated how to reduce unwanted oscillations in a cavity designed for flameholding.[23-24]

Another variation of cavity geometry is the closed cavity. This is one in which the shear layer has ample distance with which to reattach on the cavity floor, negating the need for a back wall found in open cavities. The simplest example is a single rearward facing step. Although this method provides a recirculation zone, the combustion advantage gained is not as high as the open cavity design; both incur the same drag penalty due to the presence of the step.[18]

Designing open cavities with geometric advantages for stable recirculation is the preferred direction for current research in supersonic flameholding. Gruber and Hsu show results based on differing cavity length to depth (L/D) ratios, ramp angles, and total cavity size.[25] Ignition, fueling, and sustained combustion in a stable flameholding cavity continue to be the focus of current research. While fuel injection into the core flow does not alone provide efficient flameholding, it is still considered for its mixing potential, and various methods exists for achieving this, as discussed in the following section. The future of effective scramjet combustion lies in combining a robust cavity flameholder with an upstream mixing system that employs cavities, innovative injection schemes, or both.[26-27]

Fuel Injection and Mixing

There exist volumes of research and theory on subsonic and supersonic fluid injection and interactions. The value of sensible fuel injection strategies employed upstream of a flameholding cavity is that adequate mixing and dispersion on the fuel into

the freestream can be achieved before it is ignited over the cavity. The challenge lies in attaining suitable penetration and mixing potential with as minimal a drag penalty as possible.

Above $M_\infty \approx 10$, fuel momentum becomes increasingly important in contributing to the thrust of a scramjet, and drag penalties from obtrusive injection cannot be ignored. Injection of fuel in this regime must be in the streamwise or near-streamwise direction.[9] At slower flight velocities (such as the one in the current investigation), fuel injection may occur at an off-axial angle or even in the transverse direction in order to enhance penetration.

Scramjet combustor effectiveness is measured by thrust potential. In a qualitative non-combustive study, this can be narrowed down to mixing potential and fuel penetration.[28] Mixing is difficult to predict, as current visualization systems provide insight into the large scale turbulent structures that encourage macromixing. Because chemical reactions take place at the molecular levels, mixing (and hence combustion) potential must be determined by inferring the presence (or opportunity for) micromixing. Devices that introduce strong vorticity into the freestream for the purpose of stretching fuel/air interaction area may actually diminish the ability for the intended small scale interactions to take place because of strong centrifugal action.[8]

The simplest injection scheme is transverse injection from a flush injector. An underexpanded jet enters the main flow and experiences an expansion contained by a barrel shock, followed by a normal shock (Mach disc). The spread of the jet creates a separation region within which fuel and air interact via turbulent structures. A relatively

strong detached bow shock appears upstream of the injection port. An illustration is seen in Figure 6.
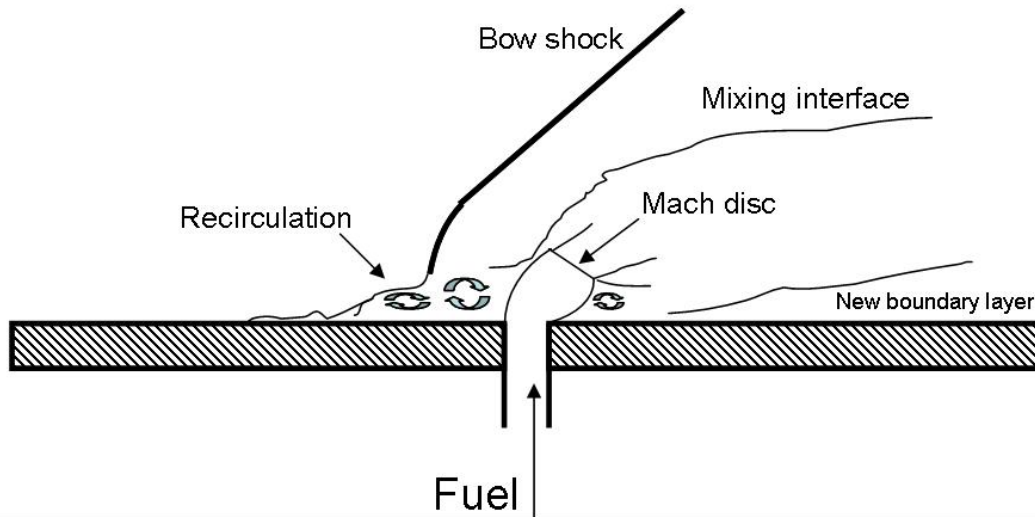
Figure 6. Profile view of a transverse jet injected into a supersonic cross-stream

Several studies have characterized the development of the jet and described the strong counter-rotating vortices that form when the jet is observed from the end (spanwise) view.[29-32] Papamoschou determined that penetration height is almost solely affected by the jet to freestream dynamic pressure ratio (q – also referred to as the momentum flux ratio) as opposed to jet Mach number (M_j) or pressure and density ratios.[33] Gruber and Nejad showed that for a given injection fluid (e.g., helium or air), compressible shear layer mixing is consistent and depends on the convective properties of that fluid.[34] This allows researchers to vary injection to more complicated schemes and compare output to a simple transverse jet, as long as the same jet fluid is used. Figure 7 illustrates the vortices that contribute to possible mixing and lifting of the fuel jet.
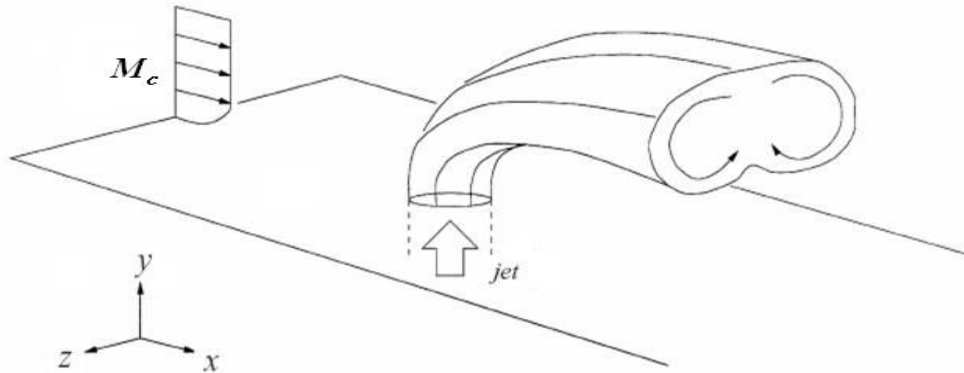
Figure 7. Counter-rotating vortices observed downstream of transverse injection (from Ref. 32)

Penetration and turbulent mixing potential can be directly affected in a transverse jet by varying q. This method also increases drag and total pressure loss. Orth et al. investigated varying injection angles, pressures, and injector shapes, and they confirmed this.[35] Others have varied jet fluid types and densities.[36] Parallel injection enhances thrust and diminishes the strong shock losses, at the cost of low penetration.[37] This leads to the design of innovative injection schemes that aim to provide the same penetration capability and adequate mixing opportunity, but with lower losses. Some of these are examined at length by Gutmark et al.[38] and Drummond and Carpenter.[39]

Murugappan and Gutmark recently conducted studies using a new transverse swirl injector to achieve higher penetration than a simple circular injector.[40-41] Their results were successful; good mixing potential and penetration are achievable at the cost of more complicated injection control schemes and similar shock losses to transverse injection.

Vorticity may be initiated by introducing passive geometric disturbances into the freestream that cause shock interactions. These devices must not cause large disruption of the flow that produce unwanted drag and also require complex cooling schemes at higher Mach numbers.[12] Numerous studies, both theoretical and experimental, have investigated varieties of swept-ramp injectors, first proposed by Marble, which generate axial vorticity-enhancing shocks through series of ramps and troughs.[42-51] Studies show that a strong local shock causes vorticity via baroclinic torque, a phenomenon attributed to differing density and pressure gradients.[52-53] Cross-stream shear created by the presence of obtrusions also contributes to vorticity, in the form of a lifting force on the local fluid. Figure 8 shows an example of two swept ramp configurations. Although the compression ramp creates good large scale mixing interactions via vorticity, the expansion ramp is found to produce more efficient combustion because small scale mixing is not as hampered by centrifugal effects, as mentioned earlier.
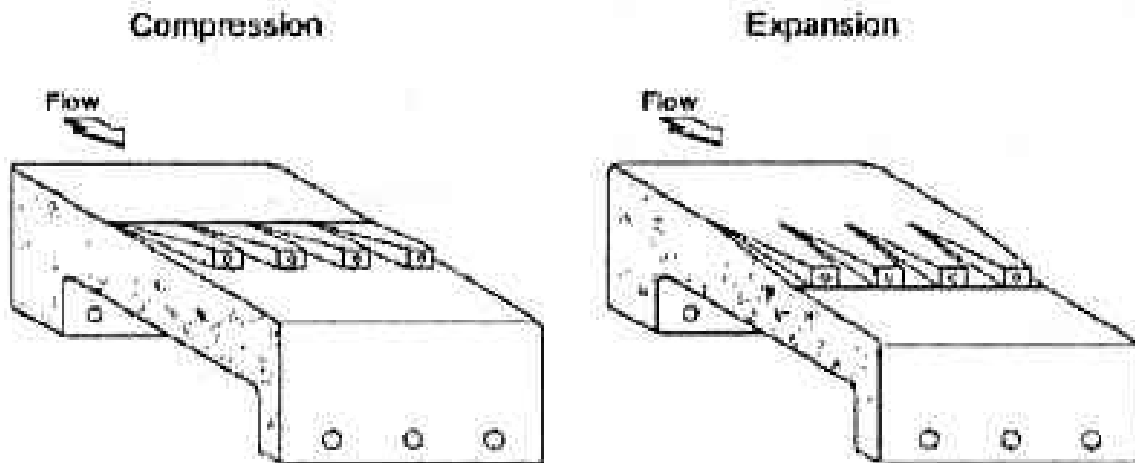
Figure 8. Scramjet fuel injector compression and expansion ramps (from Ref. 8)

Because ramp configurations inherently contain a large surface area that adds to engine drag, the insertion of thin pylons upstream of a transverse injector has been suggested and examined.[2-3] Results show that penetration is greatly improved without significant pressure losses as compared to transverse injection alone. Further numerical studies have begun to propose optimal geometries for these pylons.[4] The current research aims to investigate the use of these optimal pylon geometries and introduce imaging techniques that have not been applied to this configuration as of yet.

Summary

Mixing studies aim to find the functional balance between effective mixing and high penetration of fuel into the core flow of a combustor. Combustion studies validate these ideas, although combustion itself changes mixing characteristics. Although flameholding is possible directly behind a transverse jet due to shock boundary interactions, a cavity is more efficient. Thus, injection alone is more useful for pre-ignition mixing ahead of a cavity flameholder, which also serves to lift the shear layer. The more complex injection becomes, generally the more losses associated with it. Schemes that protrude injection ports into the freestream via struts or grids require too much cooling ability. Swept ramps enhance mixing and penetration at the cost of surface area penalty.

The use of small pylons in conjunction with transverse injection is aimed at enhancing penetration of fuel without diminishing mixing capabilities to a great extent. Transverse injection has been shown to produce combustible mixtures. Fluid stretching vortices are thus desired (perhaps through baroclinic torque or cross-stream shear coupled

15

with the preexisting transverse jet structures), but not to such a great extent that micro mixing is not possible. Using the same working fluid as simulated fuel injectant, it is possible to compare the effect of pylon-aided injection against ordinary transverse injection.

III. Methodology

Overview

Four hardware inserts were designed for the purposes of this experiment. After initial design these pieces were contracted out by AFIT for manufacturing and then shipped to AFRL for fit testing with existing hardware. Seamless integration was required due to the nature of high pressure, high velocity flow and the need for accurate flow development and visualization in the wind tunnel. The design of the inserts provides for maximum ease of installation and number of configuration possibilities with the existing hardware.

The supersonic wind tunnel is located in Test Cell 19 of the Propulsion Directorate Building 18, AFRL, Wright Patterson AFB, Ohio. AFRL permanent party and contracted personnel operate the facility, coordinate the scheduling of the various experiments that utilize the facility, and assist with hardware installation. While technicians controlled the tunnel, the author worked with visualization experts to acquire the proper data once the appropriate condition was running.

There were three pylons and one flat (no pylon reference) piece available for use in this experiment. The pylons are of varying sizes. Each insert contains an injection port and the respectively sized pylon at a set distance from the port; that distance depends on the size of the pylon (to be discussed later). The flat insert contains only the injection port, and all four pieces contain the injection port in the same location. The base plate, which contains the flameholding cavity, has two fixtures that may hold any of the four inserts. One location is just upstream of the cavity, while the other is much farther

upstream. The farther location was employed for the entire investigation. This allowed ample distance for the mixing flow to develop before reaching the cavity. Future studies may utilize combinations of these two locations. A simple illustration of the setup is shown in Figure 9, with the arrow indicating direction of core flow, and the unused fixture location highlighted in white.
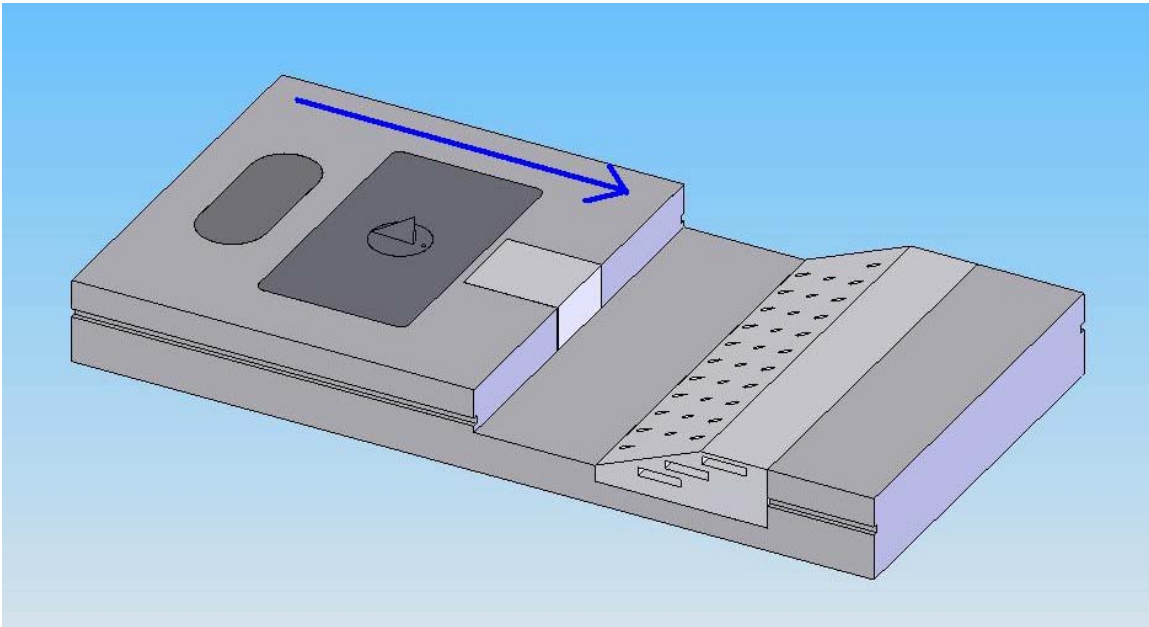
Figure 9. Basic hardware configuration showing pylon and flameholding cavity

Pressure readings were obtained from taps on the top and bottom walls of the wind tunnel. Simulated fuel injection was provided by a mixture of compressed air and flowmeter controlled nitrogen gas. Windows on the side walls and top wall provided optical access for Mie scattering and PLIF visualization. All data were stored on the respective measuring instrument's hard drive and backed up on a common server, all

housed in Test Cell 19. Visual software was used to further reduce data and present

results.

Test Facility

Testing in this experiment was done in a Mach 2 flow environment supplied by a

supersonic combustion research facility (Test Cell 19) located in the AFRL/PR Building

18 complex. The facility has been in operation since 1993. All the general information

in this section is summarized by Gruber et al.[1] and further details may be found in the

facility paper.[54]

Wind Tunnel

The wind tunnel employed by AFRL is capable of variable Mach number

continuous flow and can produce a variety of test conditions. It is able to deliver

stagnation conditions (P_{0c} and T_{0c}) as high as 400 psia and 1660°R, and it produces

nominal properties through the test section (P_c and T_c) of 7.35 psia and 525°R at $M_c =$

1.98 (simulated flight velocity of $M_\infty = 4 - 5$; much higher enthalpies are not attainable

with this continuous flow facility). Optical access of the test section is available through

three fused silica windows: one on each side wall and another on the top wall. The

original design of the tunnel called for an additional end view window located

downstream of the test section before the flow is diverted into the diffuser section. Poor

visualization through this window has resulted in all end view images now being

collected through one of the side wall windows. Figure 10 shows the component layout

for the tunnel, noting that the end viewing window no longer exists.

19
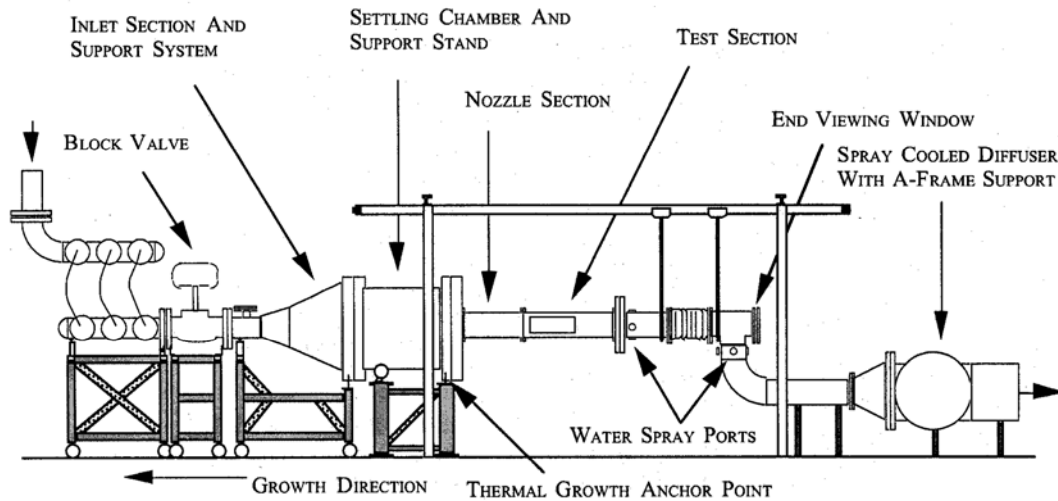
Figure 10. Windtunnel schematic (from Ref. 53)

Source air is provided by a gas-fired heat exchanger and a series of reciprocating compressors and turbines. Hot and cold inputs flow through a mixing section then a supply manifold that contains a pressure relief line. When the tunnel is not in operation the constantly supplied air vents out through an exhaust valve and out a muffled vent line. This valve is closed and a main block valve opened to begin flow into the tunnel assembly.

An expanding inlet in the form of a perforated cone distributes flow from the block valve to the settling chamber. Within the chamber, mesh screens and sections of honeycomb condition the air prior to its acceleration through a converging-diverging supersonic nozzle. Pressure and temperature readings are available from the chamber and provide approximate stagnation conditions. Before the nozzle, flow is geometrically transitioned from the three dimensional circular settling chamber to a two dimensional rectangular section. A two dimensional nozzle designed via method of characteristics

accelerates the flow to nominal conditions. There exist five nozzles that can be alternated through the facility in order to accommodate various experiments. The tunnel is capable of Mach 2 or Mach 3 flow at full or half test section height. Mach 4.5 is attainable for the full test section height only. Figure 11 shows the nozzle and test section configuration. Flow is from right to left.
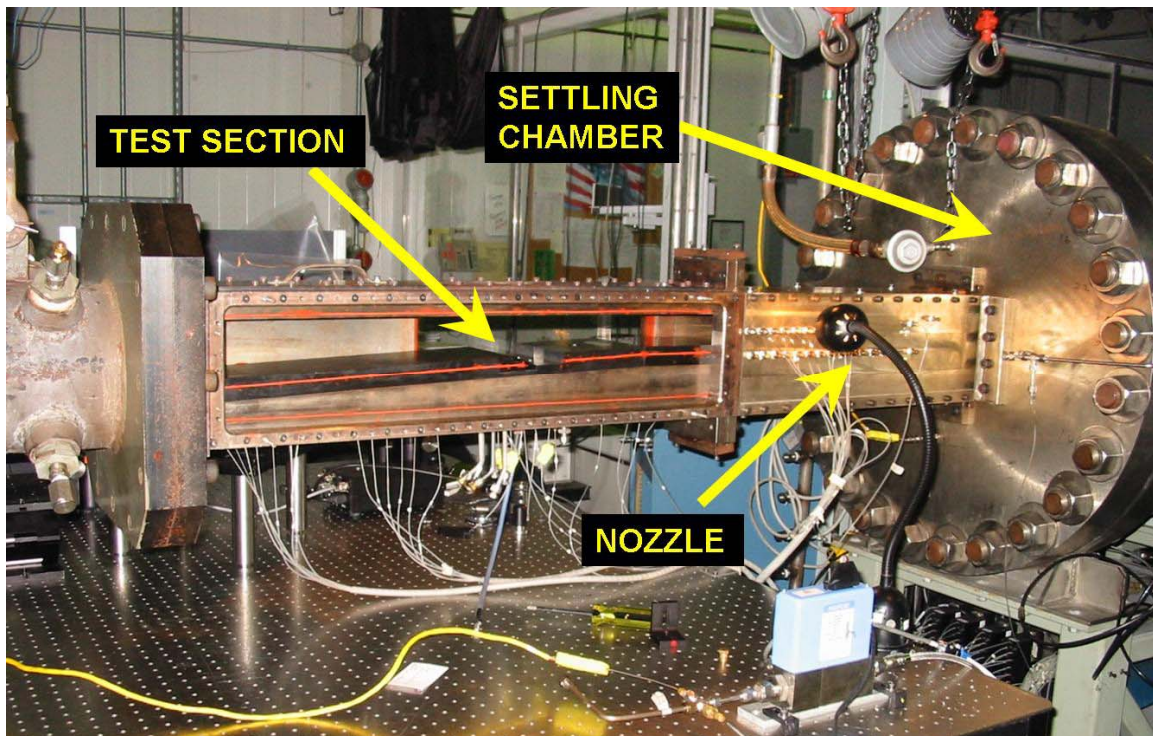
Figure 11. Tunnel midsection

The nozzle exit (Mach 2 flow, half test section configuration) is 2 inches high by 6 inches wide, located where viewing becomes available through the side wall windows. Seen there is a constant area isolator 7 inches in length, followed by a divergent floor ramp almost 30 inches long; this ramp has a 2.5 degree slope. The fused silica windows provide excellent optical opportunities and transmissive properties for the visualization

equipment. Each side window provides access to the entire transverse dimension, while the top window allows viewing of half the spanwise dimension (window is 3 inches wide).

The diffuser section utilizes water sprayed cooling to reduce exhaust temperatures to acceptable levels before air reaches the facility cooling system. Pressures and temperatures are monitored and recorded in the control room through an assortment of static pressure taps and Type K thermocouples located along the sidewalls of the nozzle, the top and bottom walls of the test section including the cavity (pressure only), and throughout the diffuser section. Pressure is read from the taps through a Pressure Systems Incorporated (PSI)® transducer board. A detailed schematic of test section pressure tap placement is found in Appendix A.

Cavity and Injection Setup

The cavity section was installed along the first 12 inches of the bottom wall on the diverging ramp using a configurable base plate. This plate and the other floor segments of the test section were installed into its frame with standard bolt fittings and sealed with silicon o-ring cord. The cavity is designed to accommodate various injection schemes by the use of fuel ports both within and upstream of the cavity. The cavity has a length (L) of 2.6 inches, and a depth (D) of 0.65 inches. The measurement convention is illustrated in Figure 12. The cavity is recessed in the floor with a 90 degree rearward facing step, and the trailing edge contains a 22.5 degree ramp. $L/D = 4$.
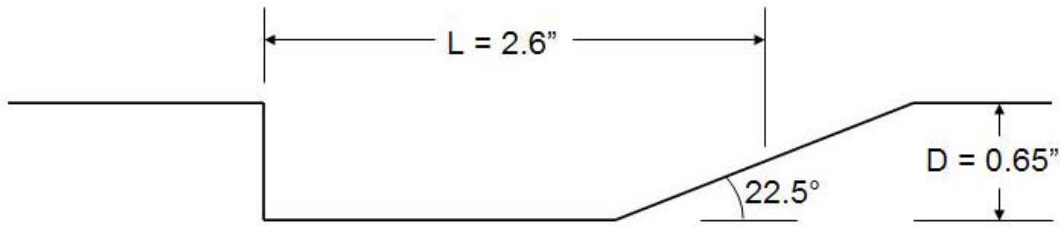
Figure 12. Cavity dimensions used by AFRL/PR

The 12 inch base plate has four fixtures. One houses the cavity floor and has the capability for interchangeable cavity ramps. The other three fixtures are located in a 6 inch section upstream of the cavity. They are devoted to housing various hardware schemes, including the pylons used in this project. A detailed diagram of the entire base plate, showing the cavity and the upstream fixtures (two of which were configured to hold pylons), is included in Appendix A. A close up photograph of the cavity is shown in Figure 13. The injection ports observed on the cavity ramp and the spark plugs in the cavity floor are used for combustion studies that were not covered by this specific research.[1] The fixture used for housing the pylons is visible upstream of the cavity; it contains a circular slot, where any of the four pylon inserts may be installed (more detail in the following section).
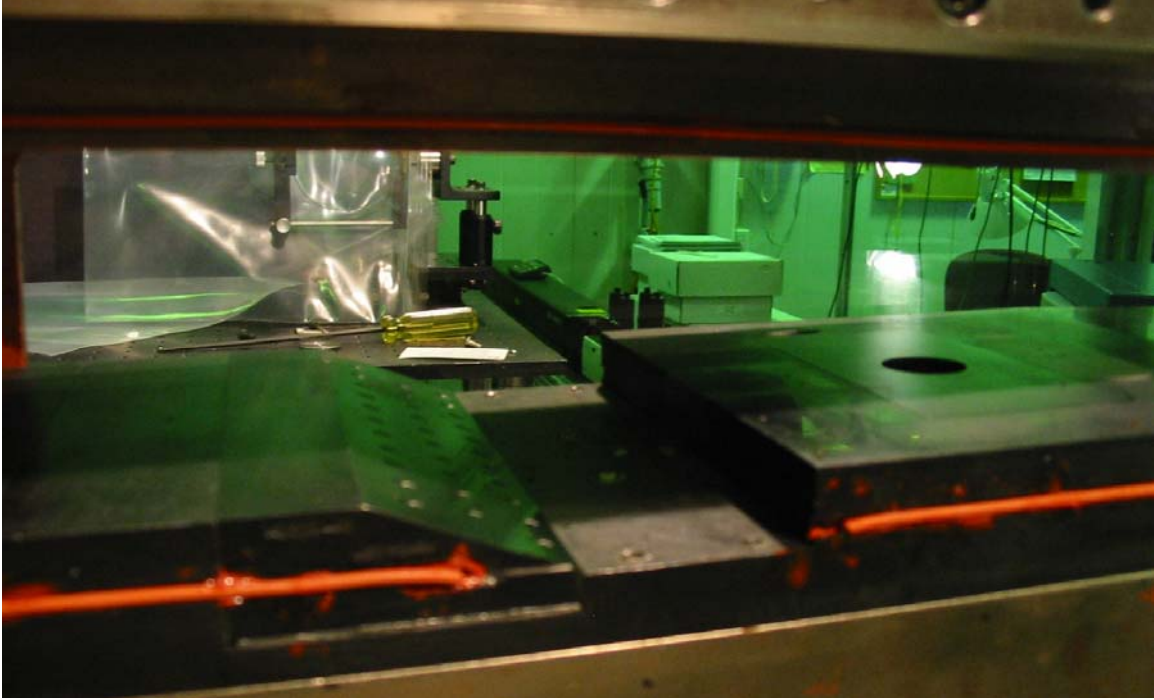
Figure 13. Cavity and hardware fixture (which houses the pylon inserts)

The pylon inserts were pressure sealed into the fixture with a 7/8 inch o-ring. The bottom of each insert was drilled with a 1/8 inch NPT (National Pipe Thread) fitting that enabled a fuel line to be attached for injection through the port behind the pylon. Other injection and measurement ports capable of supporting numerous fueling schemes exist beneath the plate. These can be seen in Figure 14, which also demonstrates the viewing range of the top window.

Simulated fuel injection was achieved by a combination of analog valves and digital flow controllers. Dry compressed air was provided by a facility high pressure system, while the nitrogen required for the PLIF measurements was provided from a pressurized bottle and was seeded into the dry air with a Tylan® 2925 series mass flowmeter and monitored by a Tylan® RO-28 controller.
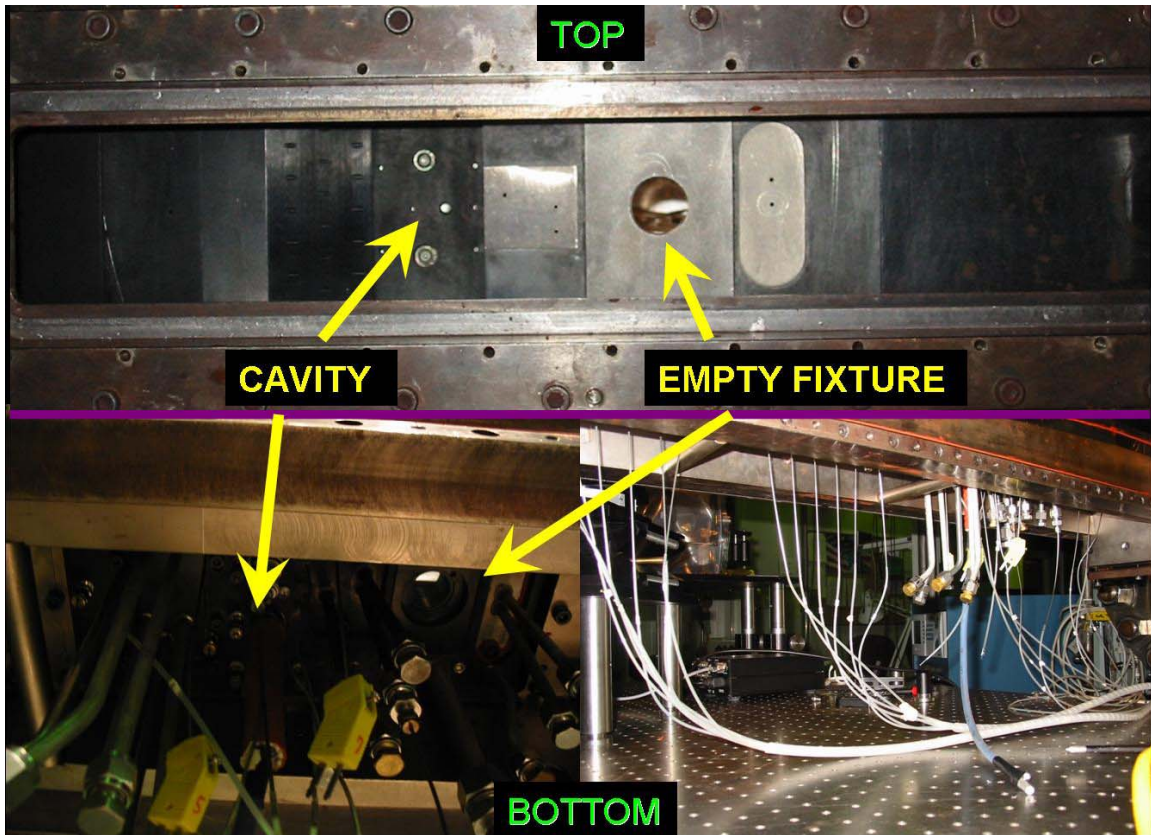
Figure 14. Top and bottom view of installed base plate

The facility is capable of closing a pre-diffuser valve that enables the buildup of a high back pressure. This provided simulation of dual mode conditions upstream of and over the cavity, in the form of a shock train inside the combustor and isolator. Ignition capability and effective mixing are desired in this regime.[16] Figure 15 shows a Schlieren image which demonstrates the back pressure condition over the cavity in comparison to fully supersonic flow. Flow direction is designated by the arrows.
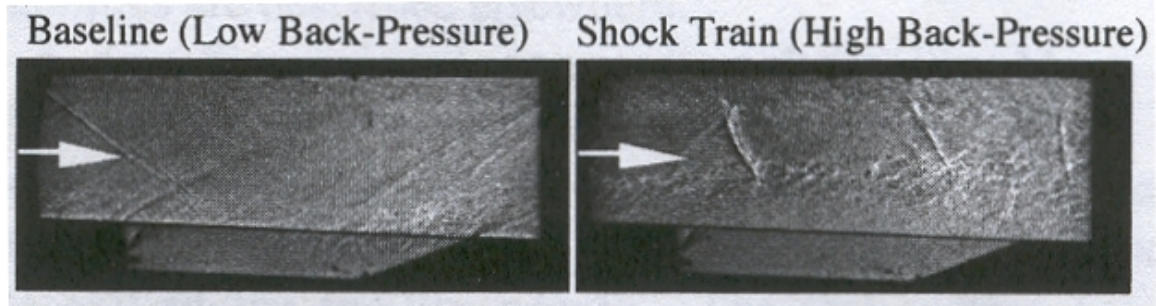
Figure 15. Shock train condition (from Ref. 1)

Hardware Design

The pylon inserts used for this experiment were designed with simplicity and compatibility in mind. Two of the fixtures located on the base plate upstream of the cavity were modified in order to allow pylon testing either far upstream or directly upstream of the flameholder. While only the farther upstream fixture was used in the investigation, having the capability to place a pylon close to the flameholder is useful for follow-on experiments aimed at investigating the coupled effects of pylon injection and cavity combustion. More detail on these experiments can be found in the recommendations section of this report.

Inserts

Of the three fixtures located upstream of the cavity, two were compatible with the pylon hardware inserts. A rendering of the empty base plate and the two fixtures is shown in Figure 16, along with the dimensions of the fixture faces. The larger is termed Fixture A, while the smaller is Fixture B. The goal of designing pylon inserts was to be able to successfully deploy both a pylon and an appropriately distanced fuel port into

26

either Fixture A or B. Manufacturing expense and simplicity dictated that an insert be

compatible with both fixtures.
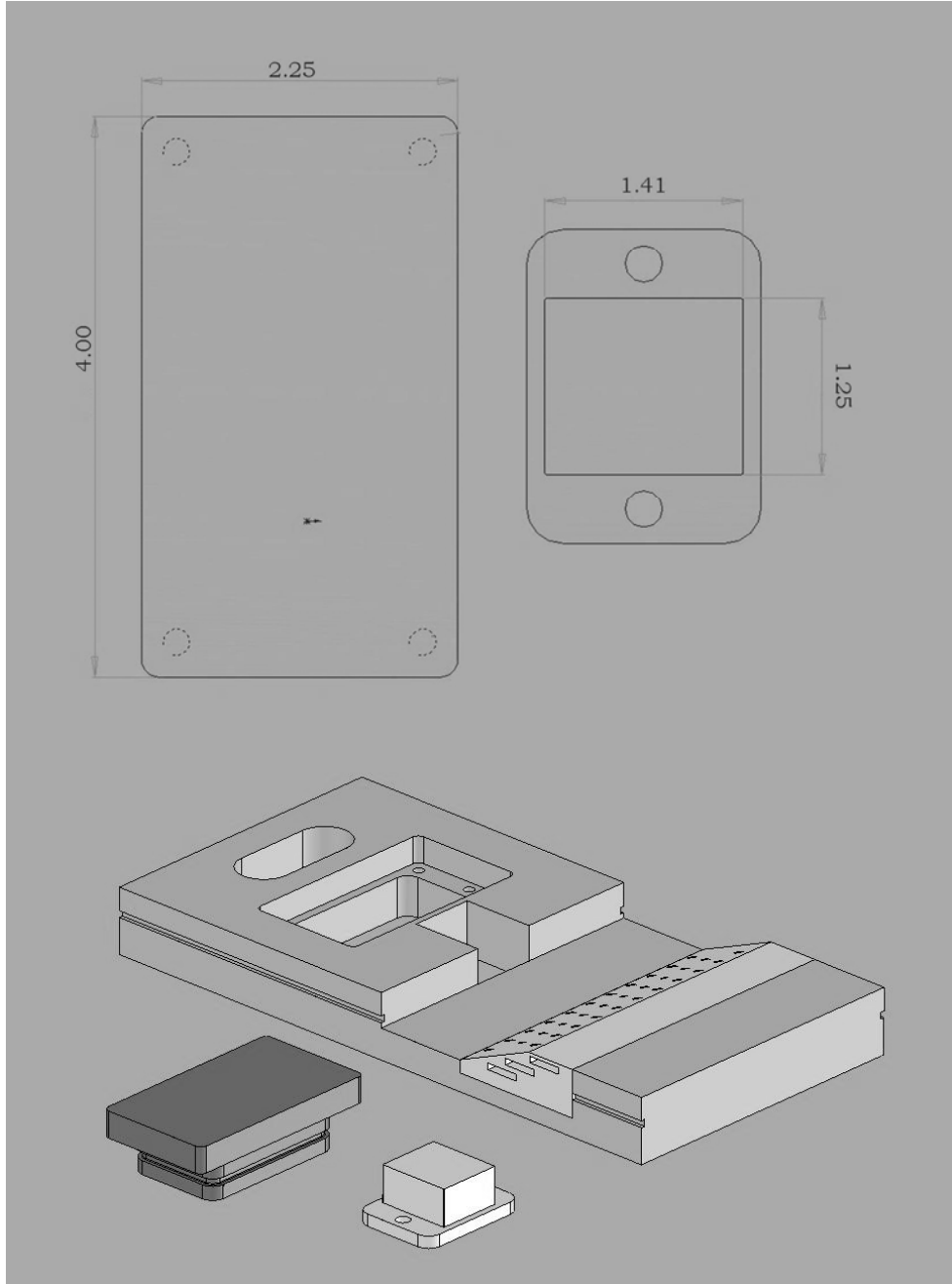
Figure 16. Cavity baseplate and the original fixtures that were modified to accept pylons

Several early designs were brainstormed and drawn using Rhinoceros® software. One of the more popular original ideas was to make Fixture B an insert in itself; this would call for different pylon pieces to be attached on top of the insert. While no modifications would need to be made to Fixture B (since the insert *was* Fixture B), that only left the task of boring out a crevice in Fixture A which could receive the Fixture B piece as an insert. Concerns with the difficulty in machining such a crevice and with the securing and sealing methods for the pylon attachments led to that idea being rejected. Rhinoceros® renderings of this concept are shown in Figure 17.
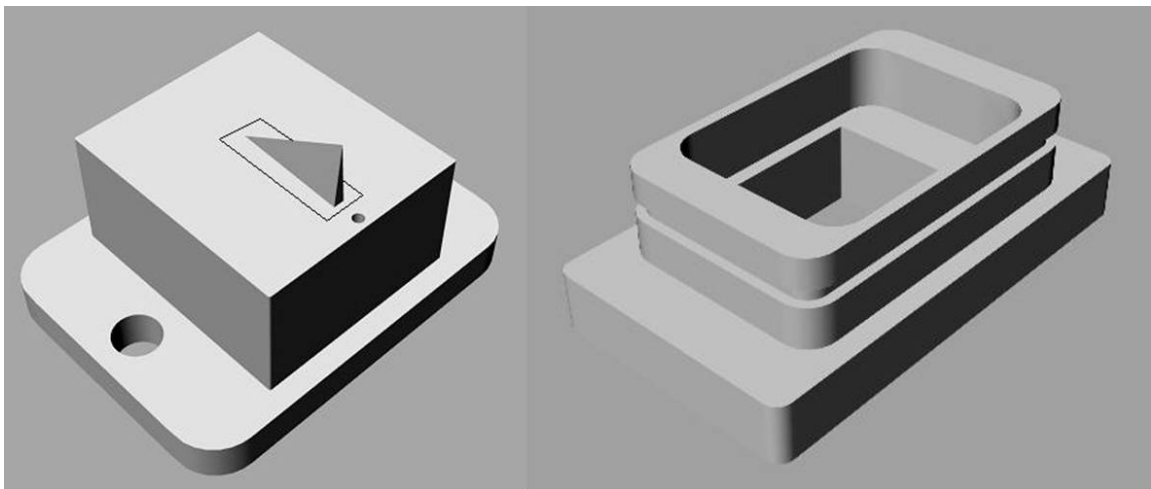
Figure 17. Early concept for pylon inserts showing Fixture B (left) and Fixture A (right) with crevice

It was finally decided to design a small insert that contained both a pylon and an injection port (for sealing considerations) and which could be inserted into modified versions of Fixtures A and B. Coincidentally, a change was made in design software to SolidWorks® for its availability in AFIT labs and use in the mainstream community. The new inserts are circular and all contain a fuel port in the same location; the only thing that

differs with each insert is the pylon size and location relative to the injection port.

Figures 18 and 19 show the inserts and the bored out fixtures, respectively.
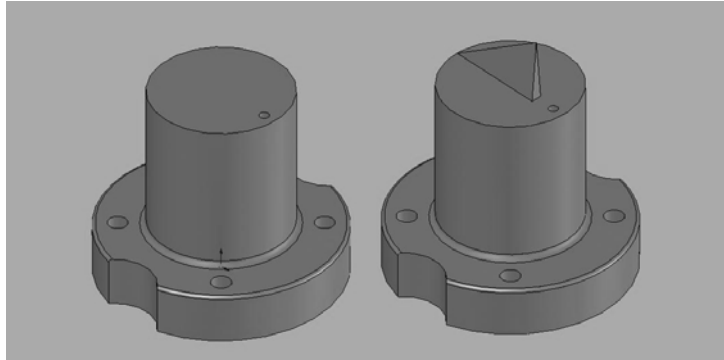
Figure 18. Inserts containing no pylon and arbitrary pylon
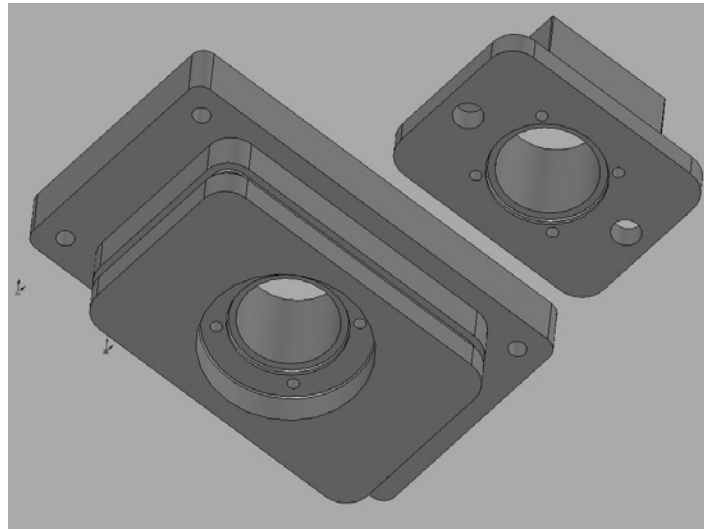
Figure 19. Fixtures A and B modified to receive inserts

The exact dimensions of the inserts are contained in Appendix A. Figure 20 shows a cross-sectional view of an insert with an arbitrarily sized pylon. Injection diameter (d) in these experiments is 1/16 inch. This port becomes a 1/8 inch hole before reaching the bottom of the insert, where an NPT is fitted for fueling. The insert fits

snugly into either modified Fixture A or B and sealed with an o-ring. This versatility

allows two inserts to be used simultaneously if it is required in future experiments.
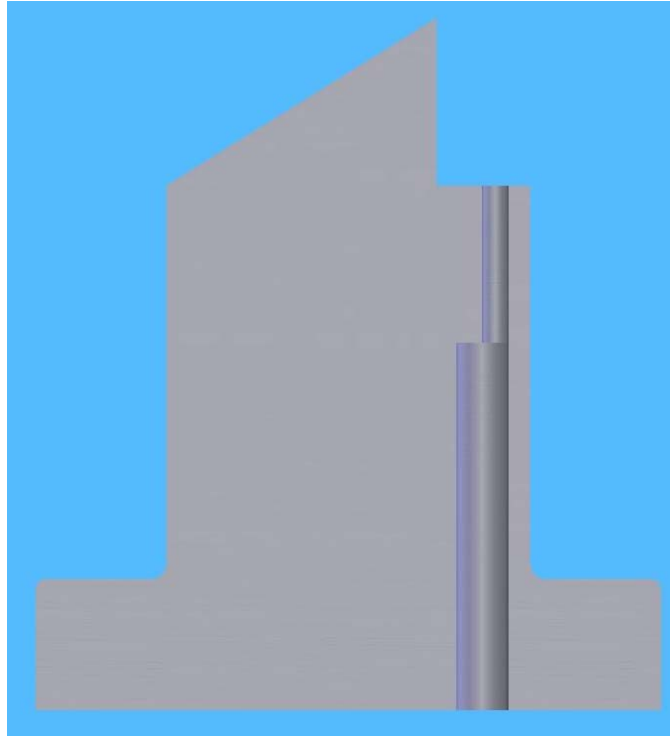
Figure 20. Cross-section of a pylon insert

Fixture A alone was used in the investigation. With the insert installed, the

injection port center is located at a distance (X_f) of 2.3 inches upstream of the cavity step,

resulting in $X_f/d = 37$ and $X_f/L = 0.9$. If Fixture B were to be employed, X_f/d would

equal 5.6 and X_f/L would be 0.1 ($X_f = 0.35$"). These values will be summarized in the

testing strategy section of this report.

<u>Pylons</u>

Separate studies by Livingston and Segal and by Owens et al. established pylon geometries that were used for liquid injection experimentation.[2-3] Gouskov et. al performed a numerical analysis of gaseous jet injection behind pylons, and the results from various geometries and injection distances were tabulated.[4] All three of these studies estimated penetration height to equal about 1.5 times the pylon height. Based on the top two configurations found to enhance fuel penetration height and using a wedge angle established by the liquid injection studies, three pylons were designed for this experiment. Figure 21 shows a diagram of the pylon, injection port, and their geometric properties. The streamwise (x), transverse (y), and spanwise (z) axes are labeled. The origin of this coordinate system lies on the center of the injection port at the surface.
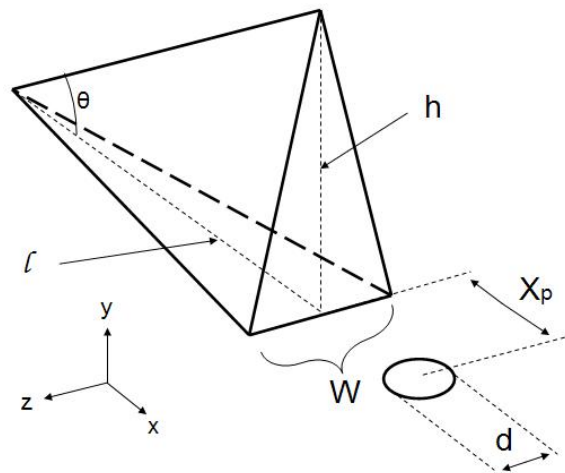
Figure 21. Pylon geometry shown with injection port and defined axis system

Injection diameter (d) is 1/16 inch for all the cases that were tested. X_p is the injection proximity to the pylon, measured from the pylon base to the centerline of

injection. The three independent geometric parameters on the pylon were chosen as length, width, and height (ℓ, W, and h, respectively). The wedge angle (θ) is derived from ℓ and h.

The two parameters that were emphasized in the numerical study were X_p and W. Two pylons in this experiment were designed using the optimal case ($X_p/d \approx 2$, $W/d \approx 1$). One is termed the Medium (M) pylon and is 1/8 the height of the test section (0.25"). The larger pylon is termed Tall (T) and is 3/16 the height of the test section (0.375"); it is designed to differ from Pylon M only in length and height but preserve width and angle. The third pylon uses the second best case ($X_p/d \approx 3$, $W/d \approx 1.5$), and is termed the Wide (W) pylon. It has the same length and height as Pylon M and has a higher X_p. In all three pylons, $X_p/W \approx 2$ and $\theta \approx 30°$ as previous liquid fueling studies used the same approximate wedge angle in their geometries. Pylon dimensions are presented in Table 1.

Table 1. Pylon dimensions for Medium, Tall, and Wide geometries

d = 0.0625 in	Medium (M)	Tall (T)	Wide (W)
Height: h (in)	0.25	0.375	0.25
Length: ℓ (in)	0.43	0.65	0.43
Width: W (in)	0.07	0.07	0.1
Proximity: X_p (in)	0.14	0.14	0.2
Wedge Angle: θ (deg)	30.2	30	30.2
h/d	4	6	4
W/d	1.12	1.12	1.6
Xp/d	2.24	2.24	3.2

One hardware insert contained no pylon and is termed the Flat (F) insert. This piece was used as a reference condition. It was useful for obtaining baseline tunnel conditions (no injection) as well as simple transverse injection without pylon aid. The piece may also be used as a plug should both modified Fixtures A and B be installed in the base plate. Figure 22 shows a photograph of the F insert installed in Fixture B, as well as the three pylon inserts (M, T, and W). A picture of the base plate configured with the Wide insert is shown in Figure 23.
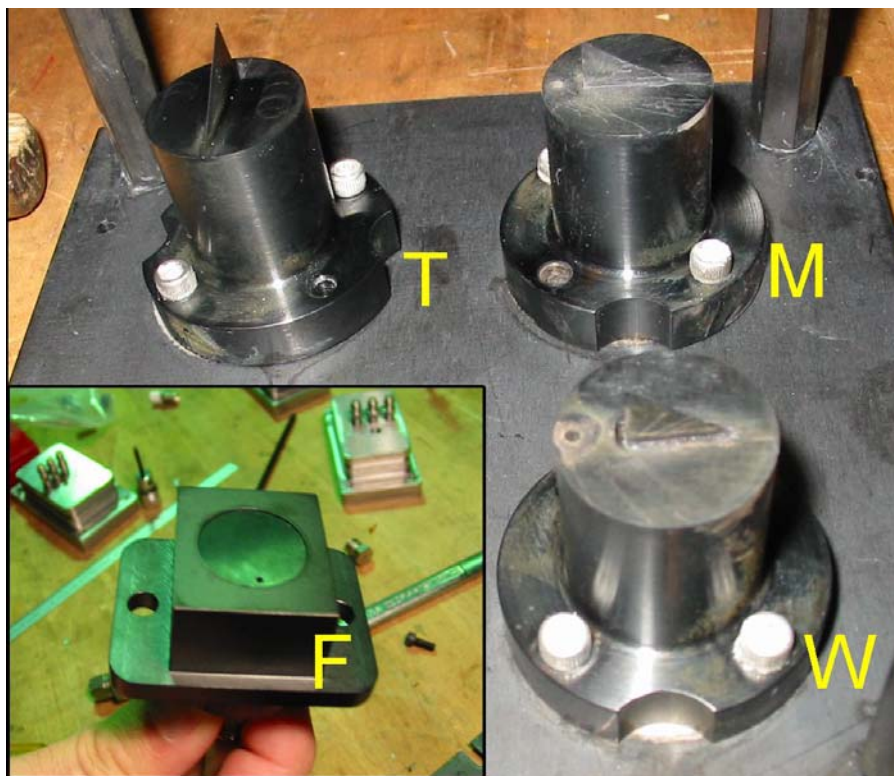
Figure 22. The four hardware inserts (three pylons and one flat)
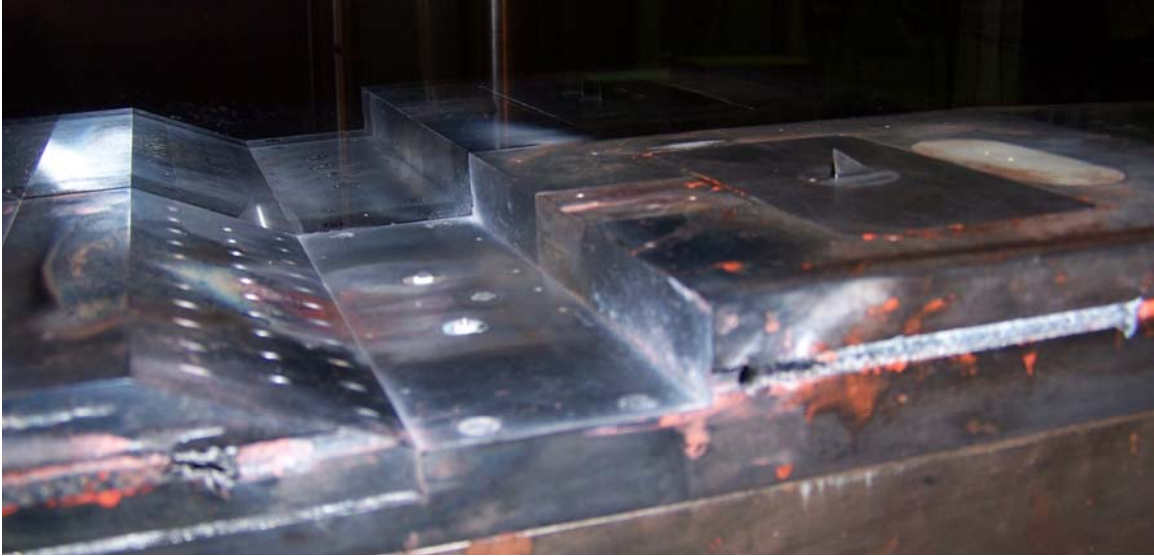
Figure 23. Installed pylon (flow from right to left)

Injection Characterization

Three different fuel injection pressures (200, 100, and 50 psia total pressure) were tested with each hardware insert through the choked, circular nozzle located at $X_f/L = 0.9$. Depending on the type of visualization employed for a particular run, the simulated fuel was either dry air or a mixture of air seeded with nitric oxide (NO) laden nitrogen (N_2). Because it is important to characterize and monitor injection pressures, a discharge coefficient (C_D) analysis was performed on each of the four inserts. Once measurement error was corrected with the C_D value for each port, a value for the dynamic pressure ratio (q) was obtained for every condition.

Discharge Coefficient

The assumption of fully isentropic processes through an injection port leads to some slight error when measuring properties of the injected jet, particularly pressure.

Friction losses and non adiabatic flow precede the choked jet. Thus any jet

characterization based on pressure (such as dynamic pressure ratio) may be slightly

inaccurate due to experimental error if based on a direct pressure reading upstream of the

port exit (in the tube). If characterization is allowed to be based on another parameter

that can be accounted for, such as mass flow rate ($\dot{m}$), more accurate interpretations may

be made from the results.

Measurements of pressure and temperature in the injection tube were obtained

from trial injections and used to calculate a mass flow rate. These calculated values of $\dot{m}$

were compared to the real mass flow rate using a controlled Tylan® 2900 series mass

flowmeter. The ratio of these two results is the discharge coefficient (C_D), which was

used to calculate the dynamic pressure ratios for each injection pressure. Appendix B

goes through this process.

Dynamic Pressure Ratio

The dynamic pressure ratio is literally defined as

$$q = \frac{(\rho \cdot v^2)_{jet}}{(\rho \cdot v^2)_{core}} \tag{1}$$

or

$$q = \frac{(\gamma \cdot P \cdot M^2)_{jet}}{(\gamma \cdot P \cdot M^2)_{core}} \tag{2}$$

where γ is the ratio of specific heats of the fluid in question (taken in all cases to be approximately equal to 1.4 for core and jet flow), and jet properties are at the port exit.

Core conditions ($M_c \approx 1.98$ and $P_c \approx 6.77$ psia) were gathered from experimentation. Although M_j is known to be unity, a true value of P_j at the port exit cannot be measured; only tube readings are available. An equivalent relation for q using mass flow rate as an alternative is

$$ q = \frac{\left(\dfrac{\dot{m}_{true}^{2}}{\rho \cdot A^{2}} \right)_{jet}}{(\gamma \cdot P \cdot M^{2})_{core}} \tag{3} $$

where A is the jet area ($d^2 \pi/4$) and ρ_j may be calculated. This relation allows the true mass flow rate, if known, to be used.

The fuel jets were monitored using total pressure (P_{0j}). For each insert, total pressures of 200, 100, and 50 psia were injected behind the pylon. In subsequent discussions, these will be identified as Pressures 1, 2, and 3 respectively. These readings are not accurate as they are in the tube. In an analysis similar to the method discussed in the preceding section (and Appendix B), the true mass flow rate was found and q was calculated for each insert and each injection pressure. Table 2 summarizes those values. The "uncorrected" values refer to the q that would be obtained if the tube pressure (using Equation 2) or uncorrected mass flow rate (using Equation 3) were to be used. Either equation yields the same uncorrected value.

Table 2. Discharge coefficients and dynamic pressure ratios for the four inserts

P_c = 6.77 psia	Corrected q				Uncorrected q
P_{oj} (psia)	Flat	Medium	Tall	Wide	
50	0.75	0.76	0.77	0.83	0.98
100	1.51	1.51	1.54	1.67	1.95
200	3.01	3.02	3.08	3.34	3.90
C_D	0.879	0.880	0.888	0.925	

Visualization Techniques

Instantaneous measurements of the fuel jet at various locations were obtained by both Mie scattering and Planar Laser-Induced Fluorescence of nitric oxide (NO-PLIF). Mie scattering is an imaging method that detects scattering signals from ice crystals naturally present in a flow field. Past studies have taken great advantage of this technique for its clear and qualitative data.[30] NO-PLIF is a method that detects laser-excited NO molecules that are seeded into the simulated fuel jet. Detailed information on this imaging method and a variety of sample results are presented by Lee et al.[29] Murugappan and Gutmark conducted experiments in the same facility as the present research using the same visualization equipment.[40-41]

Mie Scattering

Mie scattering is simple in principle, because the source of scattering is already present in the flowfield; water vapor in the cold main flow naturally forms into small ice crystals. Radiation in the form of a laser sheet produces strong scattering signals from

these particles which are captured by a camera; the pure simulated fuel jet emits a low signal because it is 100% dry compressed air. Any perturbations to the core flow that increase temperature will also reduce the scattering proportionally to the reduction in ice crystal concentration. Other studies performed the imaging with ice crystals in the injection instead of the core flow.[30] In this experiment, Mie scattering produced images that qualitatively characterized the jet fluid, associated shocks, and boundary layer heating.

NO-PLIF

NO-PLIF relies on fluorescence to produce images that capture the presence of NO in the fuel jet (and thus capture the fuel jet). Although this method is qualitative in nature, the species-specific images capture mixing developments that conventional visual methods and Mie scattering cannot reveal.[29] The basic premise is that NO bombarded at a certain radiation wavelength (226.298 nm) by a laser sheet will cause electronic excitation. A fraction (less than 1%) of the excited electrons is not quenched by unexcited molecules but instead radiatively decays to the ground state and emits photons of equivalent energy. The resultant fluorescence is captured from the direction normal to the laser sheet by a camera imaging system described in the next section. Dry compressed air seeded with a 1% NO in N_2 mixture was used as the simulated fuel. Ideally the amount of nitrogen in the air was tuned to achieve a value of roughly 1,000 ppm of NO in the total mixture. A good value was confirmed by checking diagnostic and image readouts on the laser equipment, explained next. The reason for varying this amount is to retain a relatively constant electronic quenching rate and mole fraction of

NO and produce a clear fluorescence signal for every hardware/injection configuration. The images themselves were not corrected for discrepancies in electronic quenching, collisional line broadening, laser coupling effects, or ground state population. Although signal strength varies slightly with the above phenomena (which depend on core pressure and temperature), a decrease in signal intensity can be taken to represent a decrease in NO concentration and therefore mixing and dilution of the jet fluid with the freestream. Appendix C contains a calculation worksheet produced by Dr. Campbell Carter of AFRL that plots the negligible pressure and temperature effects on fluorescence. As it is a self-contained document, its symbol convention will not be defined or referred to in this report.

Laser and Camera Equipment

The same laser equipment and laser sheet radiation wavelength of 226 nm was used in the test facility to support both imaging methods. The difference between Mie scattering and NO-PLIF, from an imaging standpoint, was the camera needed to be reconfigured to capture the differing signals.

In order to access the NO A-X state transitions, the laser system consisted of a Lumonics Hyperdye dye laser and an injection-seeded Spectra Physics® Nd: YAG laser (GCR-170). The second harmonic of the Nd: YAG was pumped into the dye laser. The dye output was frequency doubled and then frequency mixed with residual IR output from the Nd: YAG using Inrad® Autotraker III's to produce frequency mixed radiation at 226 nm. A sample signal was monitored on an oscilloscope to ensure good overlap of the laser and transition. Using this, small adjustments were made to the dye laser grating

position to account for temperature variance on the signal. The signal was also used to tune the amount of nitrogen mixed in air for the PLIF readings. A picture of the two lasers is shown in Figure 24.
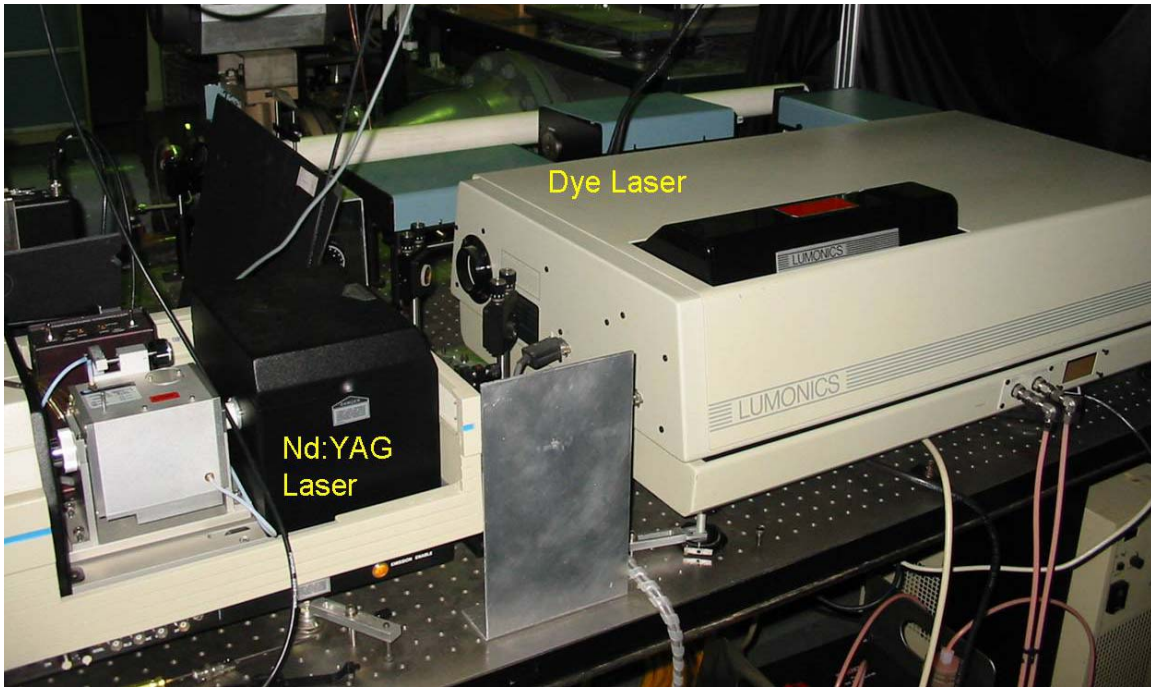
Figure 24. Laser equipment

The laser sheet was created using a plano-concave cylindrical lens (negative 50 mm focal length) and a plano-convex spherical lens (1000 mm focal length). The resulting sheet height was roughly 75 mm, and thickness is estimated at 250 – 300 μm. Scattering and fluorescence were both captured normal to the laser sheet using a Princeton Instruments® PIMAX intensified CCD (Charged Couple Device) Camera at a 512 x 512 pixel resolution. The camera was fitted with a 45 mm focal length f/1.8 Cerco® UV lens. For NO-PLIF measurements, a UG-5 filter was used to block scattering

at 226 nm and collect fluorescence from the (0,1), (0,2), and (0,3) bands. This filter was not required for Mie scattering measurement. For streamwise view (profile) images, the laser sheet was directed down through the top wall window and centered on the injection centerline; imaging occurred normal to the sheet through a side wall window. For end views, the sheet was transmitted over the test section span through the side wall windows, and imaging took place from a side window as well. The camera was positioned at an off-normal angle to the sheet, so the image needed to be corrected for blur. This was achieved with a Scheimpflug mount, a device that allows adjustment of the CCD camera lens to allow focus correctly over the entire range of the off normal plane. Figure 25 shows the end view camera configuration as well as a comparison of the sheet orientations.
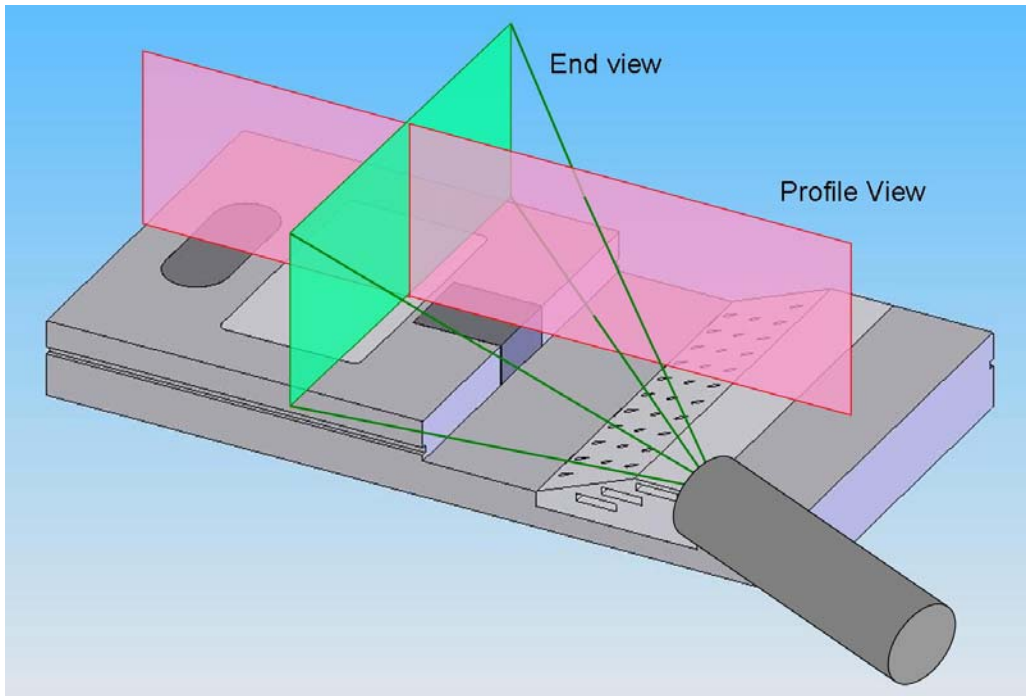
Figure 25. Laser sheet orientations with end view camera shown

Testing Strategy

Table 3 contains a summary of the relevant parameters used in the experiment. Each insert (F, M, T, W) was combined with the different injection pressures (1, 2, 3). The twelve hardware/pressure combinations are named F1, F2, F3, M1, M2, etc. Additionally, the wind tunnel was able to simulate a back pressure condition. For the F2, M2, T2, and W2 configurations, the tunnel diffuser valve was partly closed to provide additional readings with the shock train condition over the cavity. These conditions are labeled F2BP, M2BP, T2BP, and W2BP, respectively. This brings the total number of unique conditions to sixteen. The tunnel back pressure in the Tall case was higher in order to observe the effects of a shock train located farther upstream. Visualization was obtained using Mie scattering and NO-PLIF on two orthogonal planes (profile and end view), and pressure information was collected and stored on the lab server. Data were reduced using a combination of several imaging software programs (described later) for the pictures and Microsoft Excel® for the pressure information plots. The full test matrix for the sixteen main cases is presented as Appendix D. Two auxiliary runs were also made. One was performed with zero injection behind the Medium pylon to compare shock heights against the injection cases using Mie imaging (further details are explained in the results section). Another run was made with the Flat insert at zero injection to obtain baseline bottom wall pressure readings in the tunnel.

Table 3. Summary of important testing parameters and nomenclature

F	Flat insert
M	Medium insert
T	Tall insert
W	Wide insert
Injection 1	P_{0j} = 200 psia
Injection 2	P_{0j} = 100 psia
Injection 3	P_{0j} = 50 psia
BP	Shock train
X_f/d	37
X_f/L	0.9
q	~ 0.7 — 3.3 injection dependant
X_p/d	~ 1 or 1.5 pylon insert
W/d	~ 2 or 3 dependant

Laboratory Procedure

Each of the four inserts was tested in Mach 2 cross-stream at three injection

pressures. The only hardware adjustment required between pylon changes was removal

of one insert and installation of the next. The average configuration swap time was

fifteen minutes. Tunnel properties were measured for each hardware configuration and

injection pressure, and acquisition occurred on an AFRL internally developed system that

uses standard computer components. Later, these data were averaged and appropriate

parameters plotted using a spreadsheet (Excel®) for use in analyzing flow efficiency.

After an insert was installed and the facility was run up to nominal conditions, an

injection pressure was applied and at least 20 readings were taken of the tunnel properties

and recorded onto the main server. Images were then acquired. Figure 26 shows the equipment configured for profile viewing. For the end views, 8 locations were chosen, with 0 corresponding to fuel jet center as defined previously in the pylon section. Marching the laser sheet downstream (x direction), the distances are 0 (jet center), 0.25, 0.5, 0.75, 1.0, 1.25, 1.5, and 2.0 inches downstream of injection (x/d = 0, 4, 8, 12, 16, 20, 24, 32). A remotely controlled traversing table ensured both laser sheet and camera remained precisely coordinated. After all readings were taken the injection pressure was changed and the process was repeated.
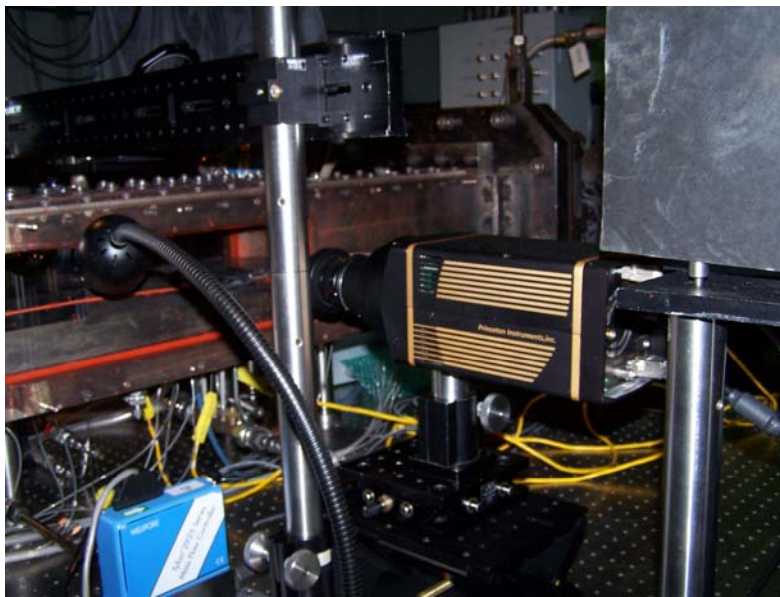
Figure 26. Streamwise (profile) view imaging setup

When NO-PLIF was the imaging method being used, it was necessary to meter the mixture of NO laden N_2 to obtain a clear and detailed fluorescence signal for a given injection pressure. The percentage of nitrogen gas mixed into the injection air was monitored and varied between 5 and 20 percent (yielding the required 500 to 2,000 ppm

44

of NO in the total mixture). Figure 27 shows the facility nitrogen metering system, which is controlled by a Tylan controller from the main control room. Total mixture pressure for NO-PLIF and Mie scattering was adjusted by analog valves in the control room and digitally monitored.

Figure 27. Nitrogen mixing system

Image Data Reduction

Raw images acquired from the diagnostic equipment were stored as Princeton Instruments® (.spe) files. They were saved as "unsigned 16-bit" at a size of 256 x 256 super-pixels (reduced from the 512 x 512 capture resolution). 200 images were stored

per capture. These files contain numerical values of fluorescence/scattering intensity per pixel. Reducing these images to a presentable format involved 1) taking the means and standard deviations for each image set, 2) correcting for residual signals from the test section and laser sheet, 3) scaling the pertinent pixel values to a visible gray scale, 4) skew correcting and cropping each image to account for camera angle (in the end view cases), and 5) adding real dimensions.

The software used for initial image reduction was developed internally by Innovative Scientific Solutions, Inc. (ISSI) and is called PDView$^{©}$ (version 4.21). It is capable of basic image handling of many raw data types. Each .spe file contains a set of 200 readings from one hardware configuration at one injection pressure and one camera position. Each reading produces an instantaneous image, which is useful for showing large scale turbulent structures. All of the readings in one set may be sum averaged into mean images to trace fluid spread, or a standard deviation may be obtained to qualitatively observe turbulence and mixing potential. Figure 28 demonstrates these functions. Differences in brightness of the Mie images exist and are explained in further detail later.
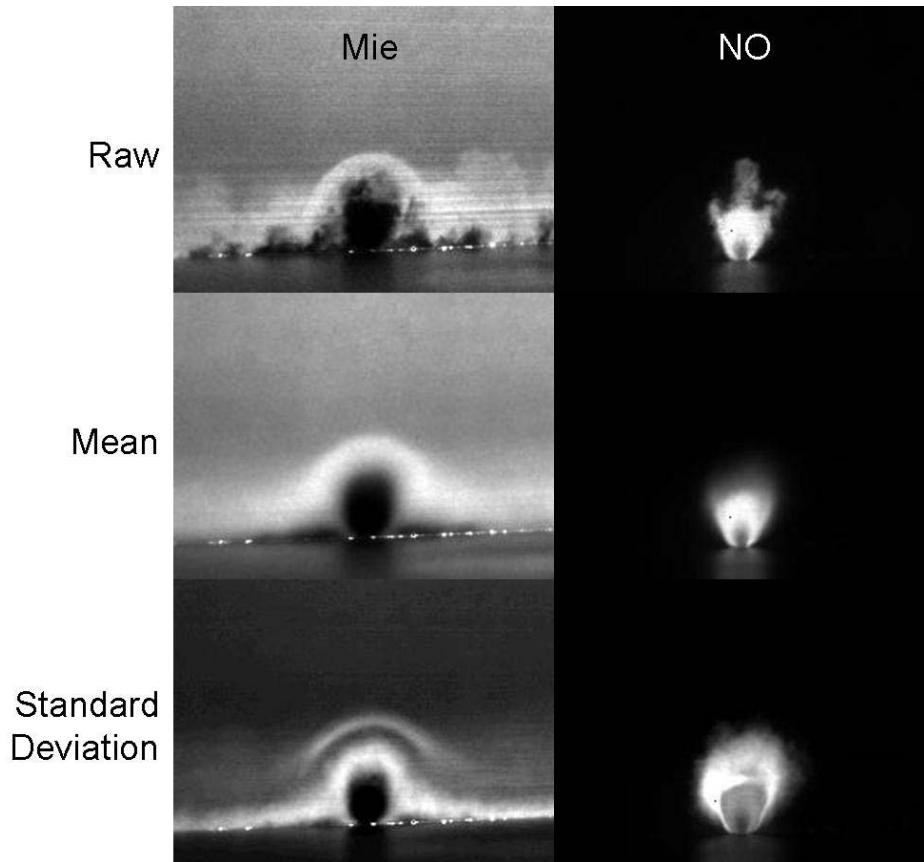
Figure 28. Example of conversion processes in PDView[©]

Averaged Mie scattering measurements produce thermally dependent images; the darker regions, which represent a lack of ice crystals, highlight the fuel jet, as well as viscous effects around shocks and boundary layers. NO-PLIF averaged images display just the fuel jet; the lighter regions represent the presence of NO-PLIF and point to the fuel jet location. The standard deviations for both Mie and NO-PLIF show the highest turbulence as lighter shades (stronger signal). Reflections on the floor of the test section are visible in both types of imaging.

Unwanted information existed in the form of residual signals from reflections off the hardware in the tunnel. This background information was acquired separately while

the experiment was not running. Additionally, a subset of information on the laser sheet intensities and inconsistencies was acquired and saved as a reference image. Both background and reference information was gathered at each camera location. Once the raw data from the fuel jet was averaged, the background image was subtracted from both the injection image and the reference reading. Unfortunately this process did not always remove all hardware reflections, and the results section will show pylon edges clearly visible in some of the pictures. After the background was subtracted, the mean jet image was then divided by the reference image, yielding a normalized image with unitless pixel values. Zero represents no fluorescence, and maximum fluorescence occurred anywhere from 0.01 – 2.50. Standard deviation images did not go through the subtraction or division process because they measure dynamic changes in the jet that do not simultaneously occur in the hardware or the laser sheet. Although the standard deviation pixel values were not normalized, 0 still represents no value while the maximum output can vary from 1000 – 3000.

Applying the proper grayscale to each image was a tedious process that differed in Mie mean images, NO-PLIF mean images, and standard deviation images. NO-PLIF means were the most straightforward. PDView[©] contains an autoscale feature that automatically ranges the grayscale depending on the maximum and minimum pixel values found in the entire image. Because the mean NO-PLIF signals were comprised solely from the fuel jet and there were few extraneous signals, the autoscale chose proper values almost every time. Figure 29 below shows an example output of an image PDView[©] autoscaled.

48
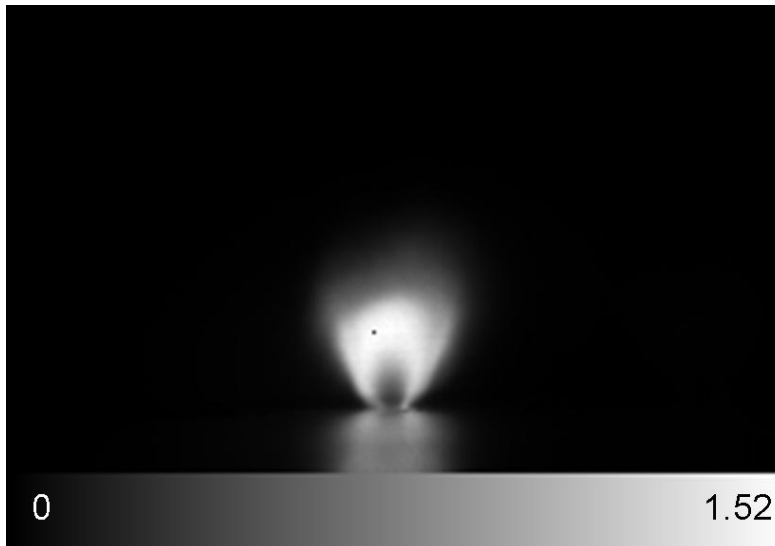
Figure 29. PDView© scaled mean NO-PLIF output (1.52 represents the maximum intensity for this image)

Standard deviation images for NO-PLIF and Mie scattering contained

respectively increasing outlying signals (created by uncorrectable hardware or laser sheet

reflections) which diminished the autoscale capability in PDView©. Often the scale had

to be manually set to 0 on the lower bound and the necessary value on the upper bound

that presented a clear image. If the upper value was too low, the information "wrapped"

around the scale, causing black blotches to appear where the highest signal intensity

exists. If the upper value was too high, a darkened or faded image was the result.

Sometimes to produce clear Mie standard deviation images that highlighted the jet over

other turbulent signals, the chosen upper bound value produced wrap around blotches in

the boundary layer where intensity was highest. This result was acceptable because the

boundary layer presence was still visible.

Mean Mie images were difficult to scale manually even within PDView©, as

unpredictable ice crystal scattering caused irregular pixel values, some of them negative.

The solution to this issue was to leave the autoscale turned on (to capture all the data, even the outliers) and export the images as bitmaps. Using a freeware program called ImageJ (version 1.32j), these bitmaps were imported and histograms created. The histogram shows every brightness value present and a pixel frequency for that value. The brightness scale was then adjusted to surround the frequent middle values and exclude the outliers. Figure 30 shows one such histogram.
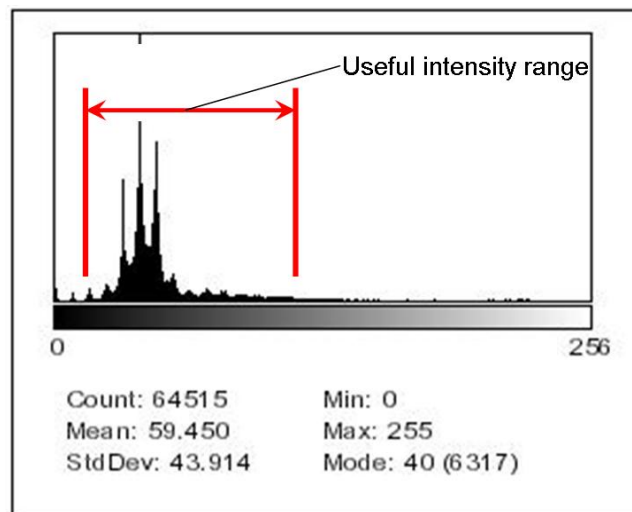
Figure 30. Image histogram

In the end view images (both Mie and PLIF) the camera angle required the use of the Scheimpflug mount to mitigate image blur (and intensity) due to off-normal imaging. This adaptation did not correct for perspective skewing. Because the images acquired from this configuration were not truly end views, they needed to be skew corrected using a first order interpolation. This adjustment preserved pixel intensity values (which were already corrected with the mount) and allowed accurate geometric measurements to be performed on the images. The interpolation process had a mean squared error of 0.997

pixels for the Mie images and 1.300 pixels for the NO-PLIF images. An example of the skew correction using the calibration dot cards can be seen in Figure 31. Once the image was unskewed, a simple crop procedure was used to remove the floor and standardize the size of the images.
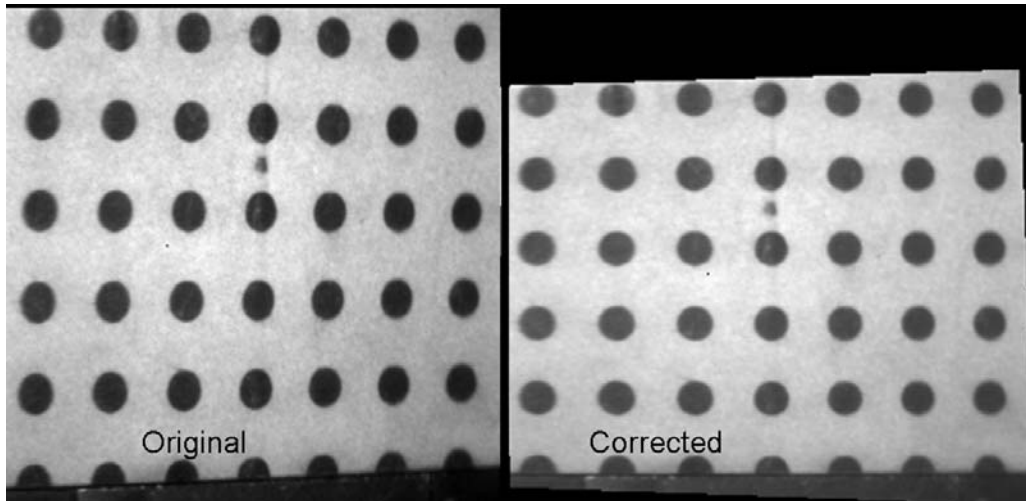
Figure 31. Skew correction example

Determining real dimensions once all the above had been accomplished was simply a matter of measuring distances in pixels, then converting to any desired unit. The dots on the dot cards were ¼ inches in diameter, providing the necessary information for true distance measurement. The Mie and the NO-PLIF images (as well as end view versus streamwise views) had different conversion factors due to differing camera zooms. Adobe Photoshop® (7.0) was used for dimensioning and final presentation of the images.

IV. Analysis and Results

Overview of Data Measurement

There were twelve hardware/injection configurations tested in a Mach 2 cross-stream that produced sixteen total runs. Each of these conditions was captured by the full suite of imagery described previously, with the exception that back pressure conditions were not imaged with Mie scattering (thermal shock effects melt the ice crystals). In some end view cases, the last few distances ($x/d = 20, 24, 32$) were omitted due to complete mixing and a non-informative signal. The profile view looked only at the Medium pylon and the Flat insert. For this measurement the Medium pylon was also tested at a no injection condition (labeled M0) to characterize the effect of the pylon alone on the supersonic freestream. In general, raw (instantaneous) images help to capture large scale turbulent structures that form at the interaction between the jet and the core flow, as well as development and unsteadiness of the bow shock and jet penetration through the boundary layer (Mie scattering only). Mean images show average location, spread and penetration of the jet. Standard deviations offer an estimate on mixing potential.

Mie Scattering Data

Mie scattering images offer interesting first-look data. Visible in the profile view is the pylon (if installed), the jet fluid (when injected), and the shockwave developments (bow shocks) that occur from combinations of pylon and jet disturbances. Standard deviations highlight these phenomena as well. The end views were all acquired with

injection present. Bow shocks are visible in these views as well, although their expanding boundaries were not captured by the range of the camera in the last few distances. Measurements on shockwave heights were performed with the end view images.

NO-PLIF Data

This technique is useful as it displays information only where jet fluid exists. Although Mie scattering provides an outline of the jet, it is not nearly as detailed and concentration-correlated as NO readings. Using the mean NO images, measurements were made on the maximum penetration height (y_j) and maximum vertical and horizontal spreads (Δy and Δz, respectively). The separation distance of the jet fluid from the test section floor is termed the floor gap (g) and was calculated as $g = y_j - \Delta y$. Jet area (A_j) was measured as the area in the mean images encompassed by at least 10% max intensity, in a manner similar to previous experiments.[40] Mixing area (A_s) was gathered from the standard deviation images as the area encompassed by an intensity value of 70% or greater. These two areas were determined by analyzing the histograms of each image and counting the appropriate number of pixels at a given brightness level percentage.

For each individual image, the grayscale was adjusted so that pure white represents the maximum intensity at that laser sheet location. This allows the jet structure to be accurately measured and observed. Because NO-PLIF image intensity is directly correlated to concentration, plots are presented that show the decreasing maximum intensities as the laser sheet traverses downstream, normalized by the $x/d = 0$ initial max intensity in each case. This way image brightness and clarity, although not

predictors of fluid dilution, present a consistent illustration of jet geometry. The two methods (image geometry mapping and intensity measurements) paint the full picture.

Pressure Data

Tunnel top and bottom wall static pressure readings are presented and comparisons are discussed for the sixteen main cases. These readings tend to show slight pressure disturbances by the pylons, fuel jets, and shock impingements created by the cavity farther downstream. In the back pressure conditions the shock train location was evident.

NO-PLIF Intensity Reduction

Tabulated values of the maximum intensity for each individual image for both mean and standard deviation cases are shown in Appendix E. Starting at the jet center (x/d = 0), mean readings show a steady powered regression curve along the downstream direction. The standard deviation images show a decrease, but with inconsistencies (namely at x/d = 4). It is possible that maximum standard deviation does not occur immediately at x/d = 0. Localized turbulence and mixing which affect the maximum standard deviation intensity of each image are going to cause the series of images not to exhibit steady decay behavior. These trends are observed in all the inserts. Figures 32 through 35 show the mean readings (and trends), while Figures 36 through 39 show the standard deviation readings.
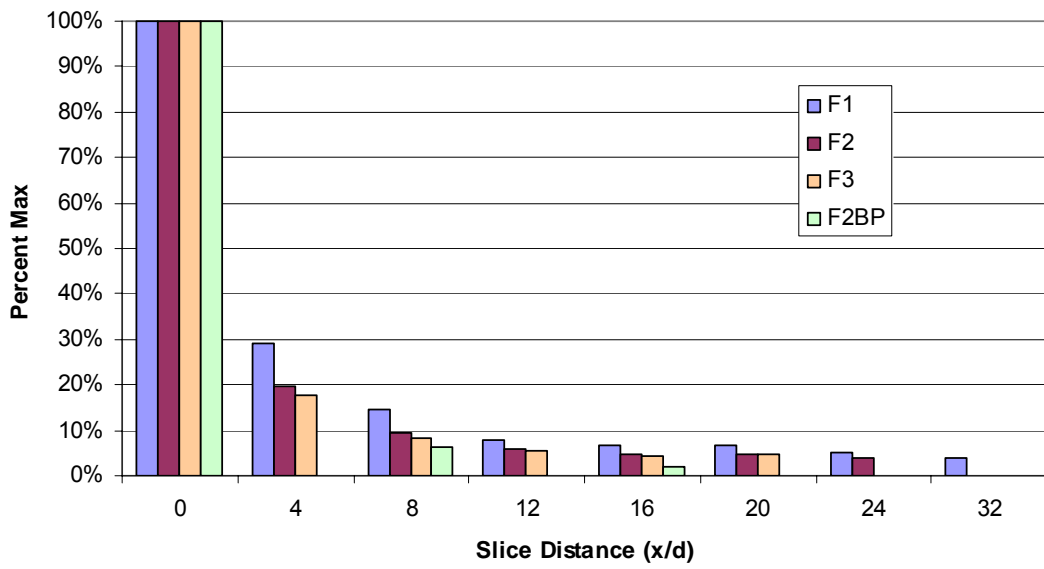
(a)
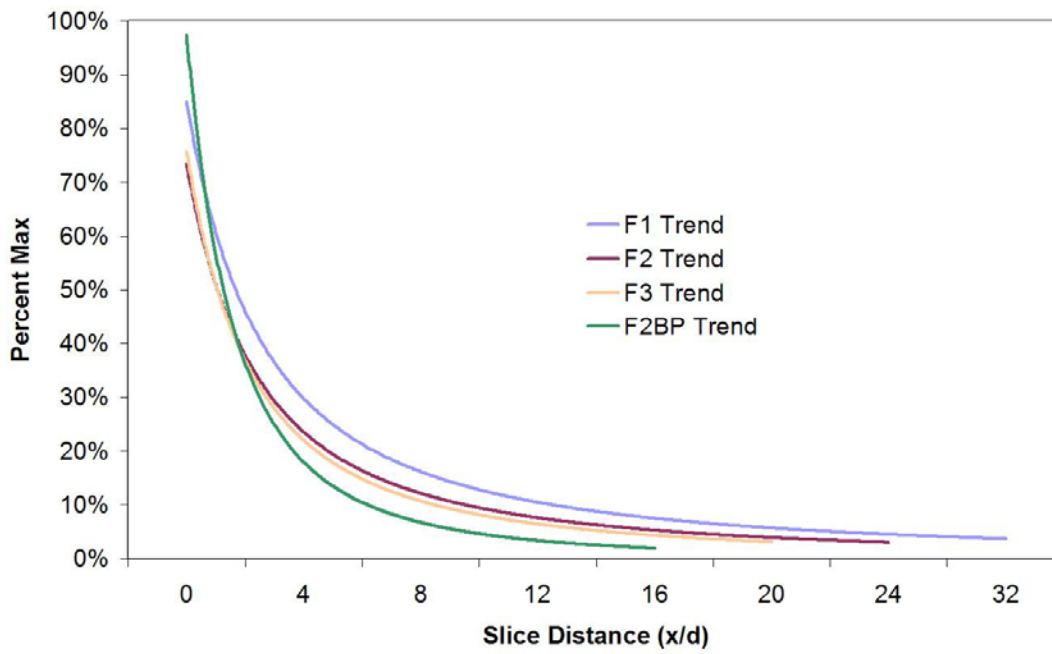
(b)

Figure 32. Flat mean maximum intensity reduction
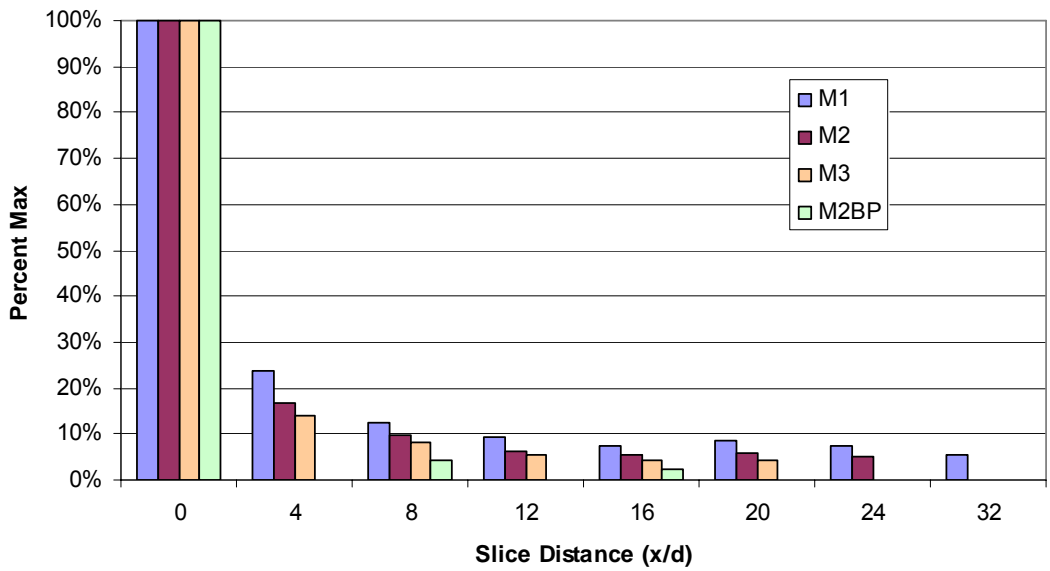
(a)
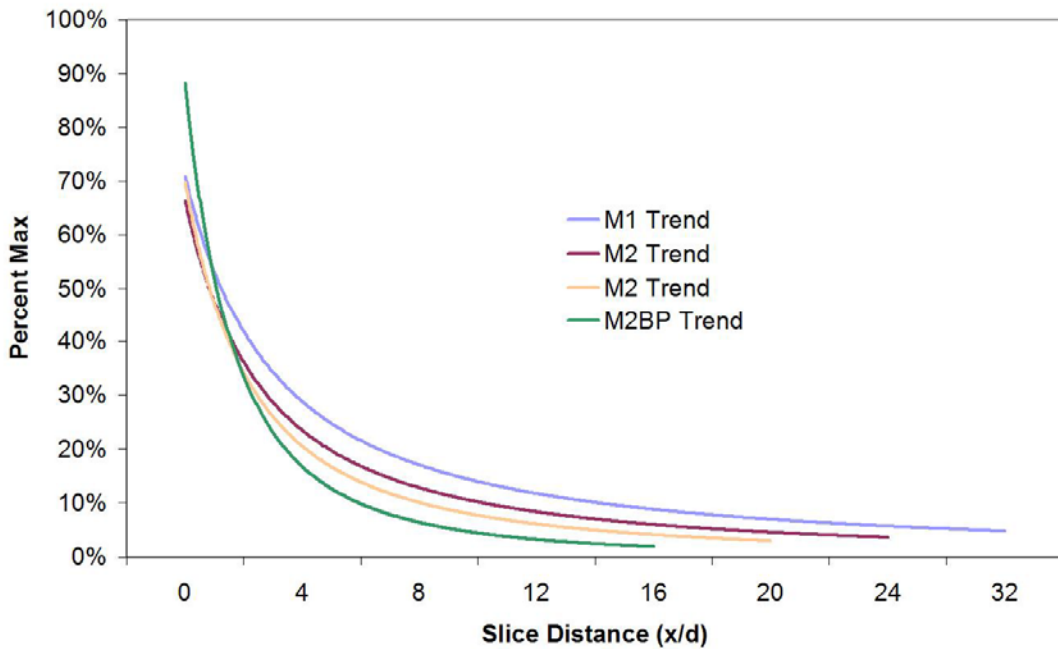
(b)

Figure 33. Medium mean maximum intensity reduction
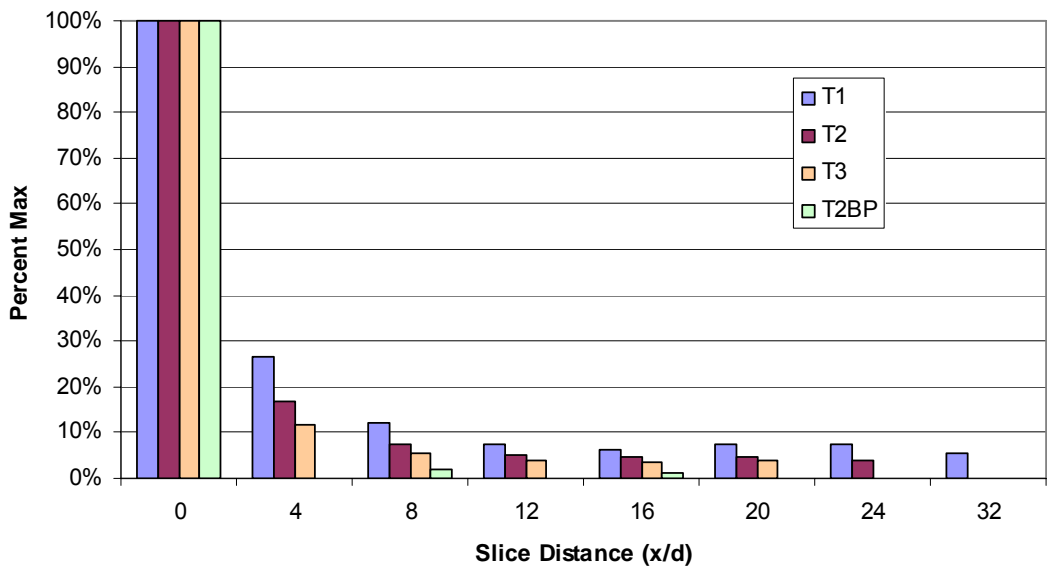
(a)
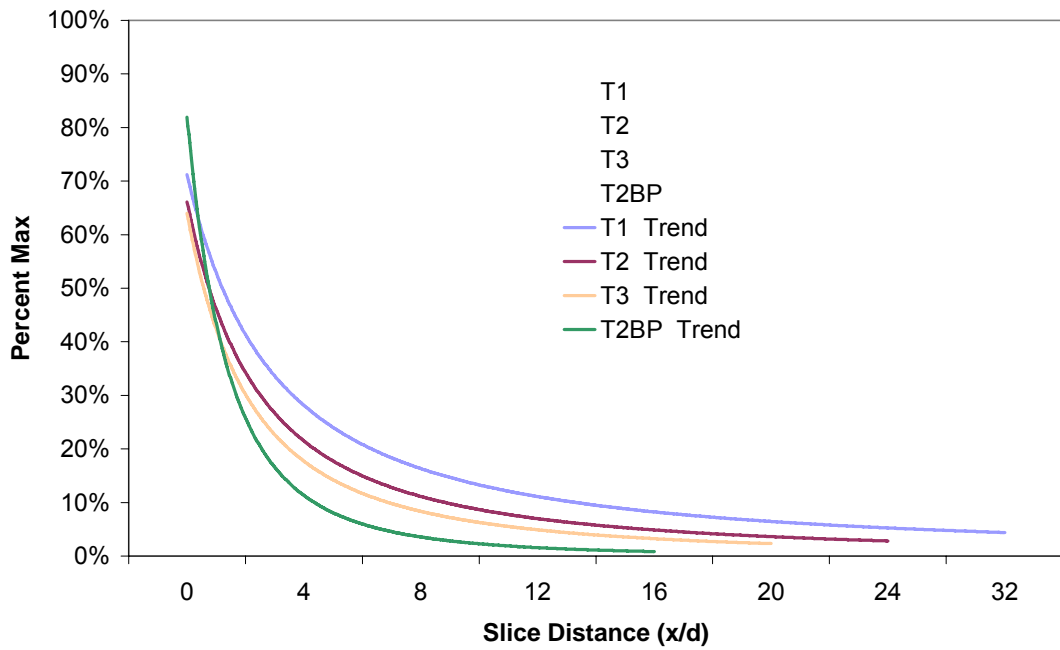
(b)

Figure 34. Tall mean maximum intensity reduction
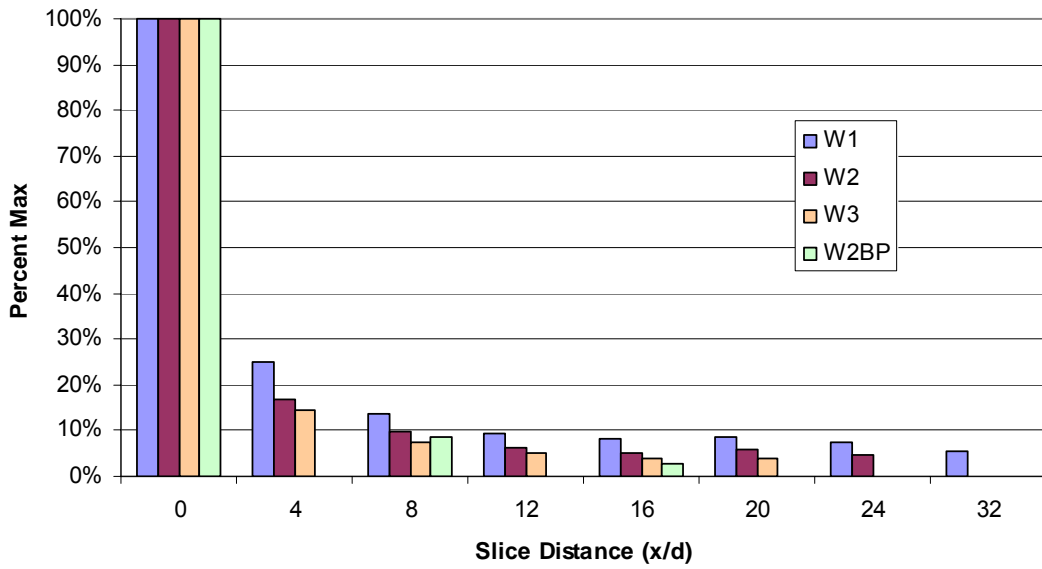
(a)
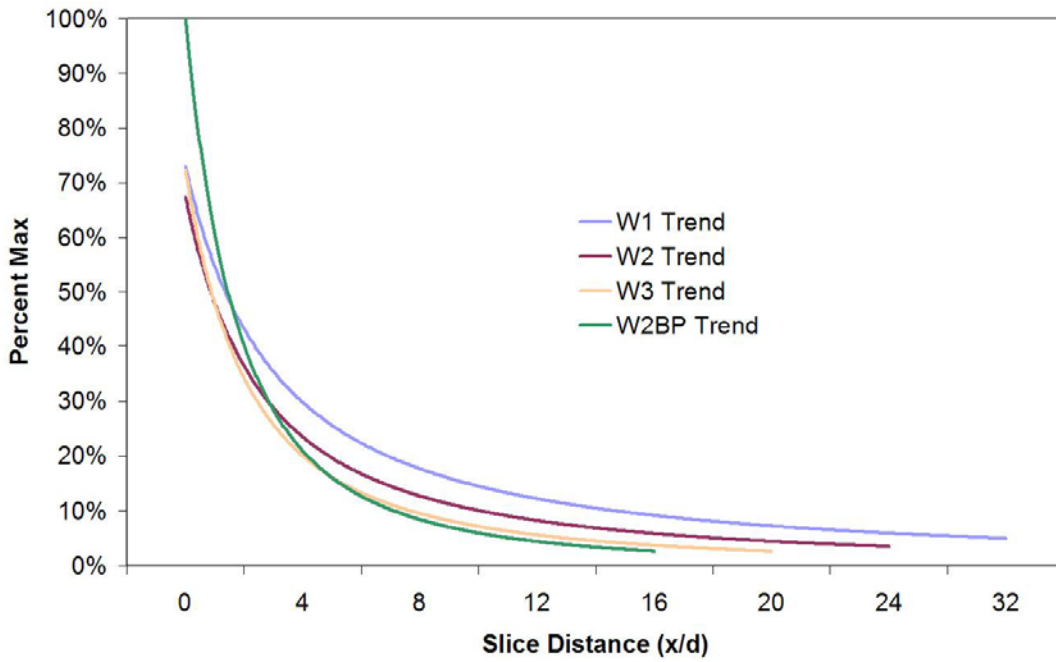
(b)

Figure 35. Wide mean maximum intensity reduction
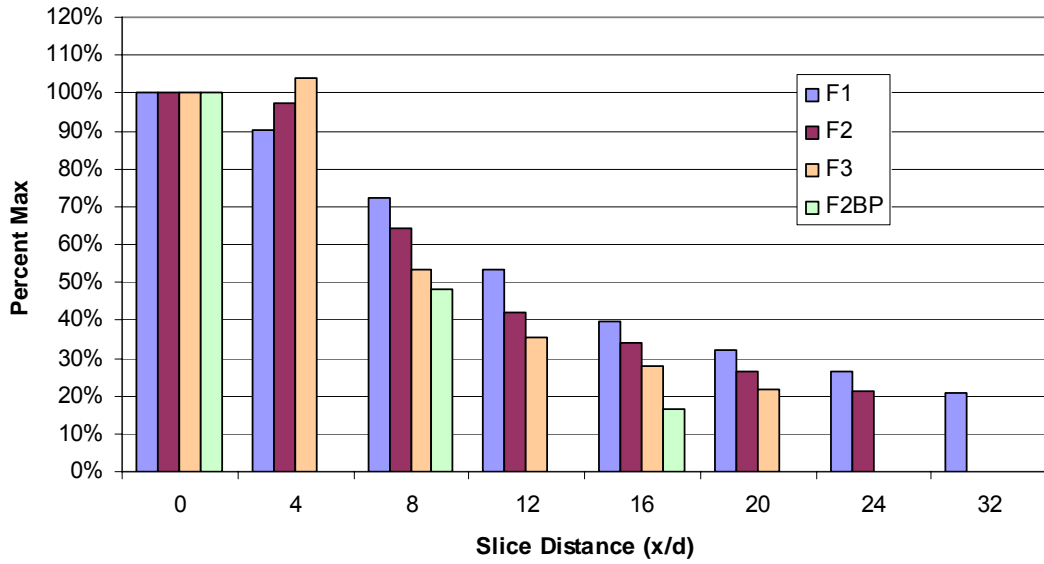
Figure 36. Flat standard deviation maximum intensity reduction
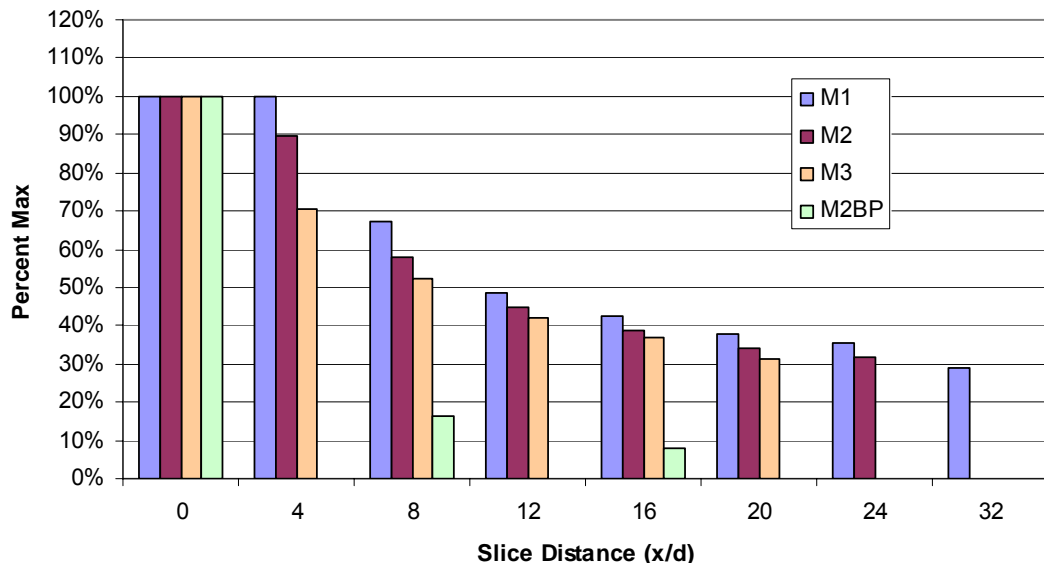
Figure 37. Medium standard deviation maximum intensity reduction
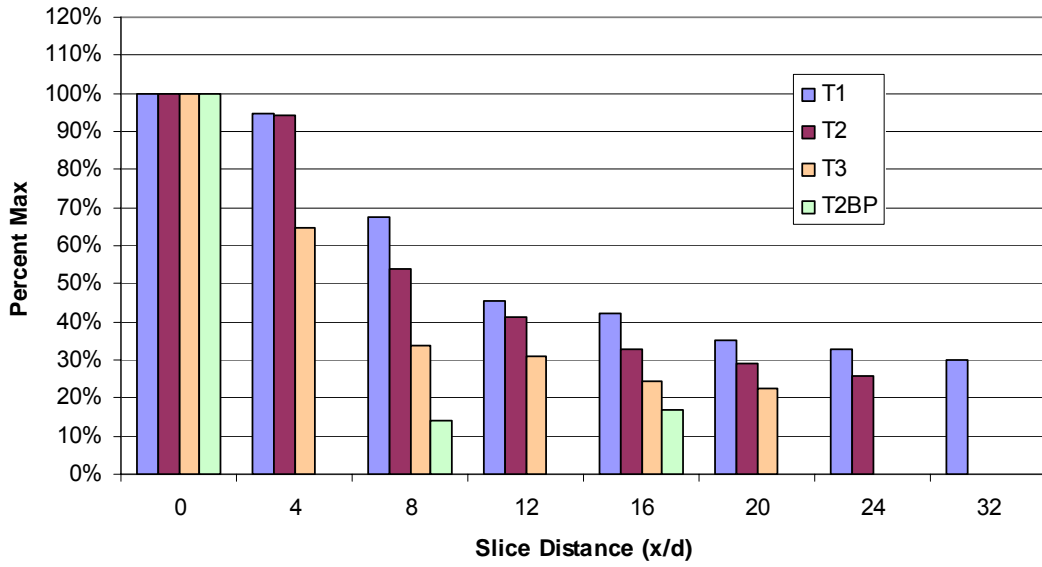
Figure 38. Tall standard deviation maximum intensity reduction
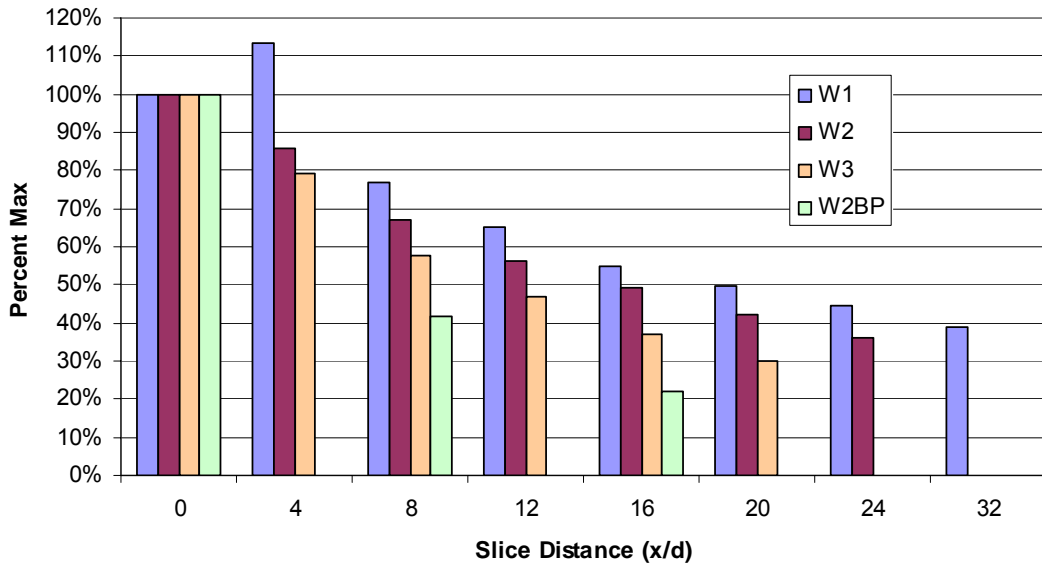
Figure 39. Wide standard deviation maximum intensity reduction

When x/d = 32, the jet is about 95 percent diluted into the freestream for pylon injection as well as the no pylon (Flat) reference. The standard deviation graphs show that all three pylon sizes show a higher intensity than the Flat reference at the farther downstream locations (x/d > 16). At x/d = 32, the Wide pylon shows the most normalized intensity with 38%, indicating more global interaction compared to the other inserts. At x/d = 4, injection pressure 1 shows a high standard deviation, sometimes of an equal or higher magnitude than at x/d = 0 (Medium and Wide cases). The tall pylon, which extends higher into the freestream, does not show this trend because its large presence overcomes injection pressure effects. When there is no pylon, injection pressure 3 experiences the higher standard deviation. This demonstrates that the shorter pylons have some effect on fluid interactions shortly downstream of injection when enough injection pressure is present. The Tall back pressure condition standard deviation intensity increases from x/d = 8 to x/d = 16 while the other back pressure intensities do not because the shock train structures in the Tall case occur much farther upstream than in the other cases, as the pressure plots will demonstrate. In summary, these charts show that in the flat case, large scale interactions diminish sooner, providing a fluid which only continues turbulent behavior within its local spread, as the images will show. The pylons continue to interact with the core flow farther downstream, and the images will highlight the extent of local interactions.

The extent of penetration and mixing potential will be determined from the visual images. The images do not depict dilution, but they highlight the local geometry of the present jet fluid intensity.

NO-PLIF End View Results

NO-PLIF end view images are presented in the following manner: Mean and standard deviation images are shown for the low back pressure cases. Each image is grayscale adjusted to show white at its maximum intensity. Discussion follows after each insert (F, M, T, W), then high back pressure images are shown followed by a separate discussion. Subsequently, a comparative analysis using plots created from the geometric information is presented. Refer again to Table 3 for nomenclature.

Sample instantaneous images and tabulated geometrical data are presented in Appendix F. The raw images may be referenced in order to grasp the nature of the complicated flow, especially at the interface between jet fluid and freestream flow. Those structures suggest a large mixing interface (seen with all cases) which is not evident from the averaged images. These interfaces exist in the shock boundary layer, which previous research confirms.[31] Large formations are a good indicator of mixing potential. Further conclusions are drawn from standard deviation results.

The Flat insert images are shown in Figures 40 through 42. The Medium insert images are found in Figures 43 through 45. The Tall case is presented in Figures 46 through 48, the Wide case in Figures 49 through 51. Finally, the shock train images are found in Figures 52 through 55.

Injection pressure 1 refers to the 200 psia case, while injection pressures 2 and 3 are 100 and 50 psia, respectively.

NO-PLIF

END VIEW

FLAT INSERT

IMAGES

Mean   a) x = 0 d   **Standard Deviation**

b) x = 4 d

c) x = 8 d
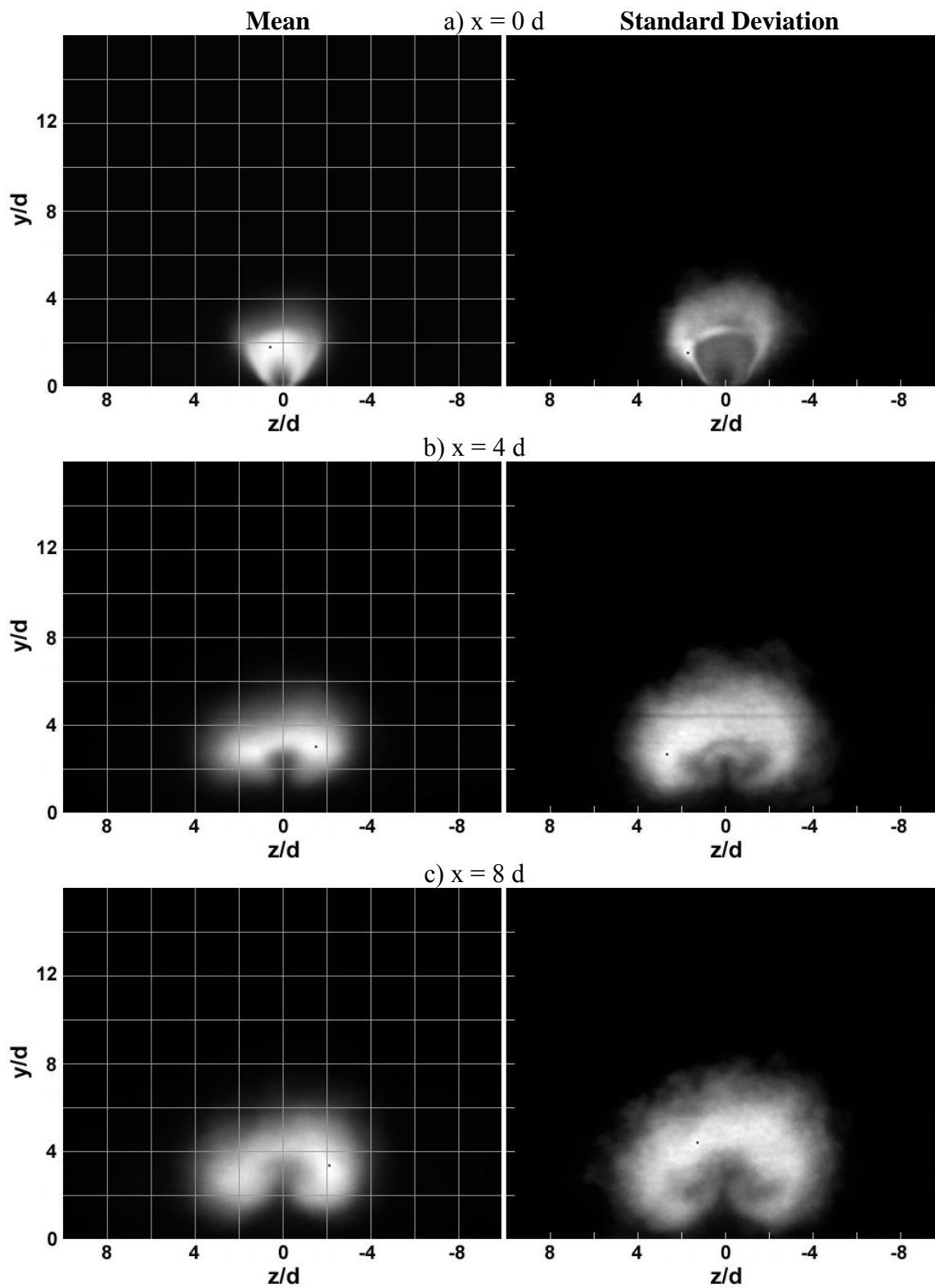
Figure 40. (F1) NO-PLIF, Flat insert, injection pressure 1, x/d = 0, 4, 8
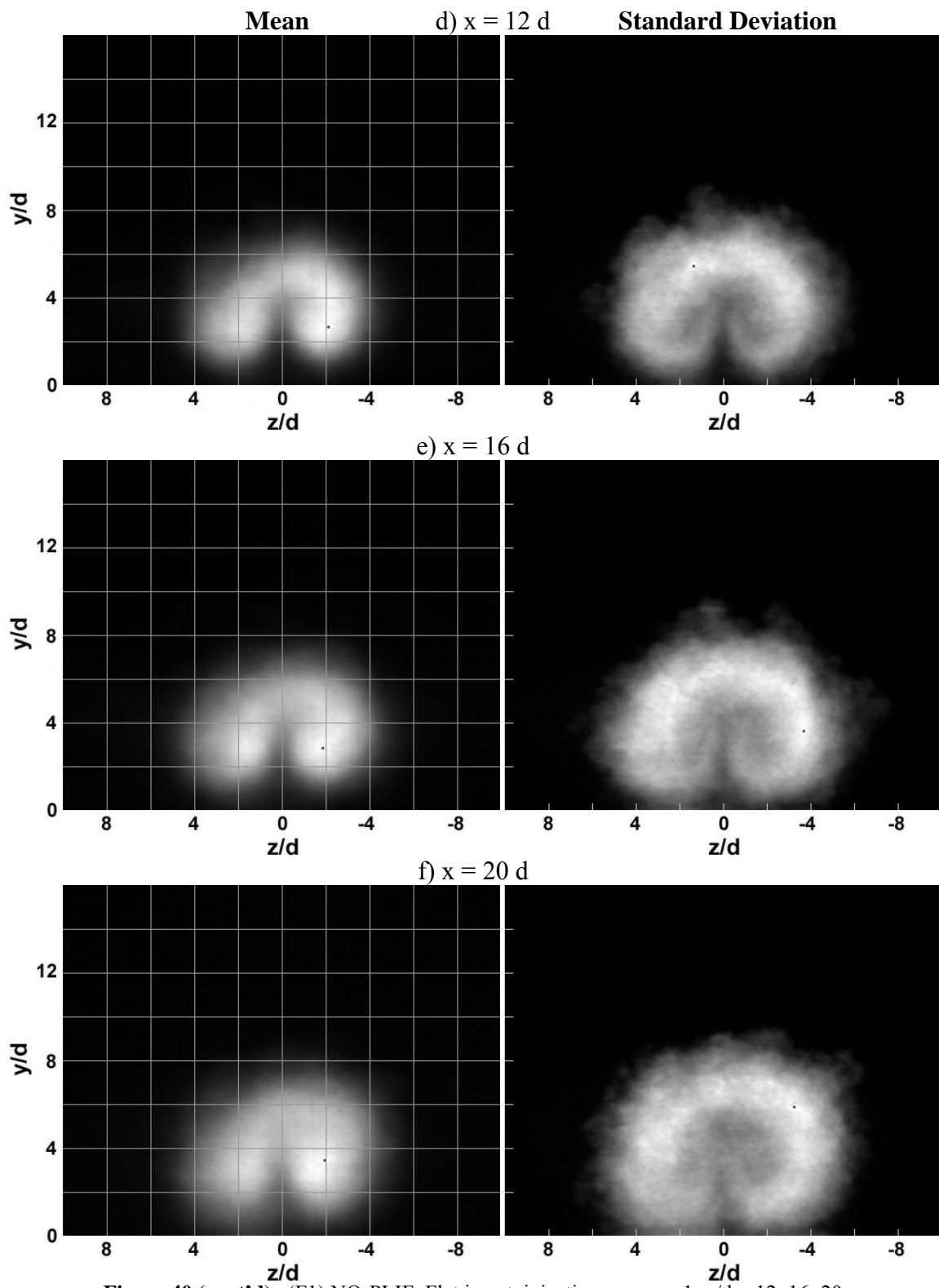
Mean   d) x = 12 d   **Standard Deviation**

e) x = 16 d

f) x = 20 d

Figure 40 (cont'd). (F1) NO-PLIF, Flat insert, injection pressure 1, x/d = 12, 16, 20

Mean   g) x = 24d   **Standard Deviation**

h) x = 32 d

Figure 40 (cont'd). (F1) NO-PLIF, Flat insert, injection pressure 1, x/d = 24, 32

66

Mean   a) x = 0 d   **Standard Deviation**

b) x = 4 d

c) x = 8 d
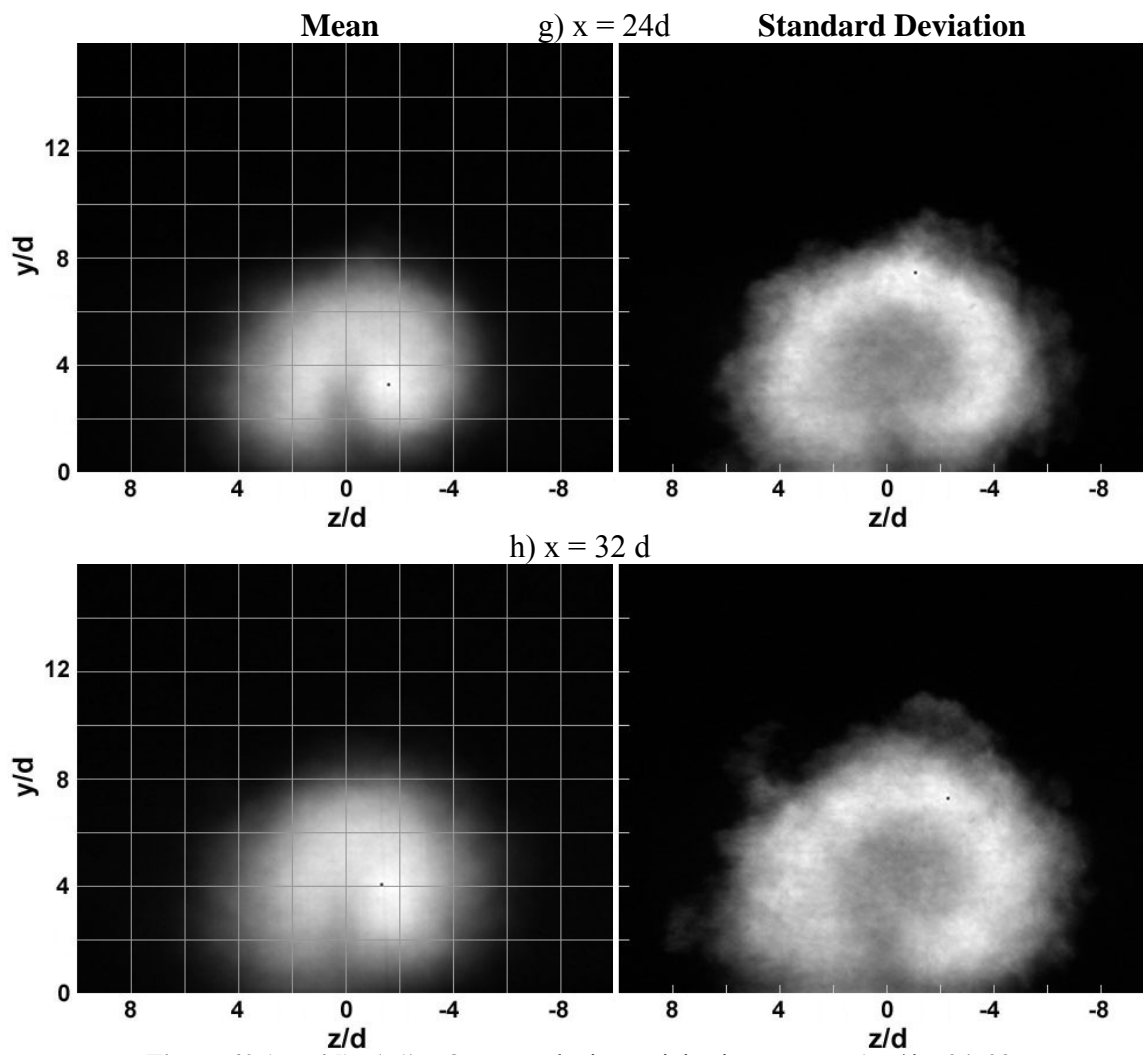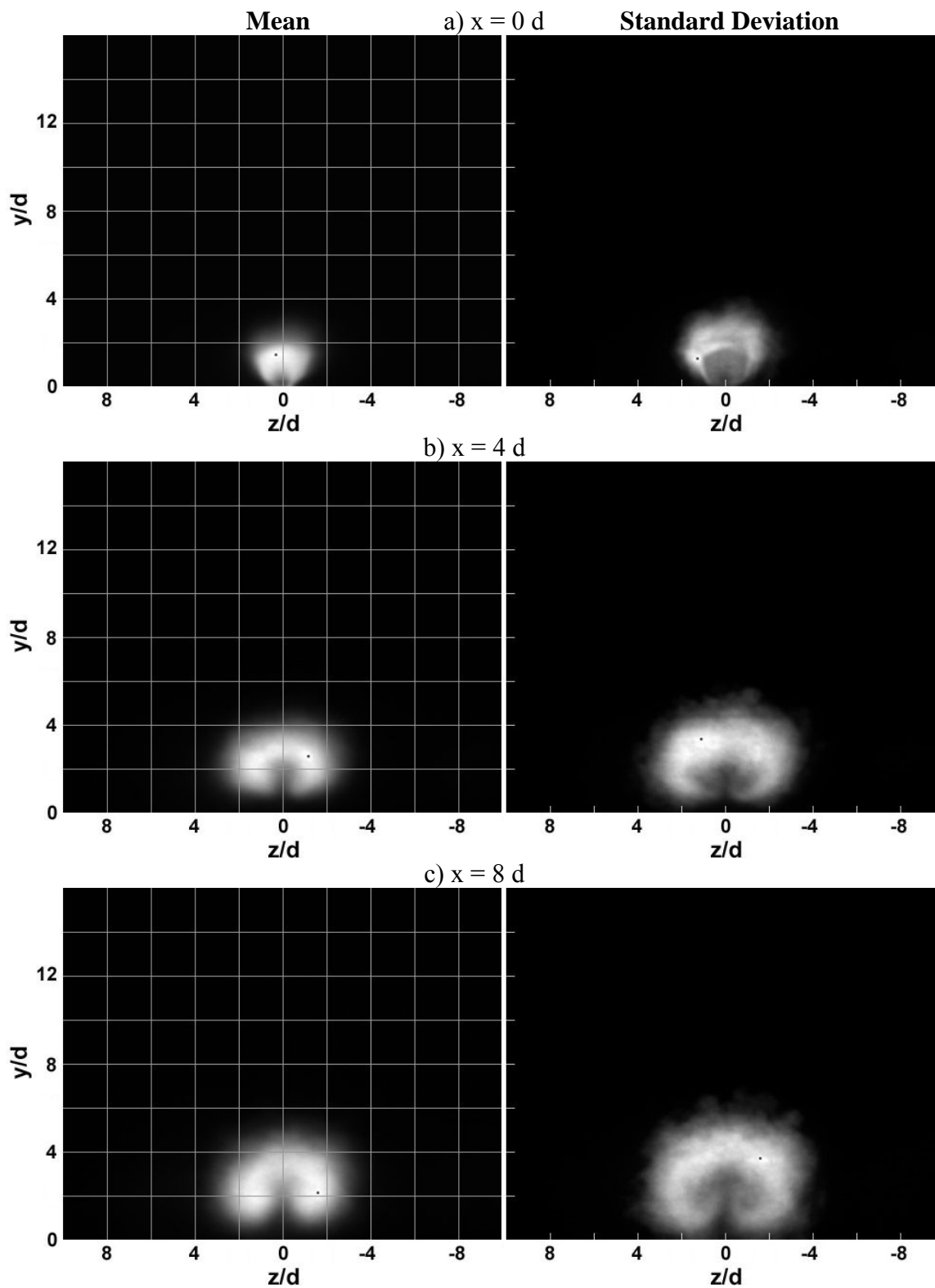
Figure 41. (F2) NO-PLIF, Flat insert, injection pressure 2, x/d = 0, 4, 8
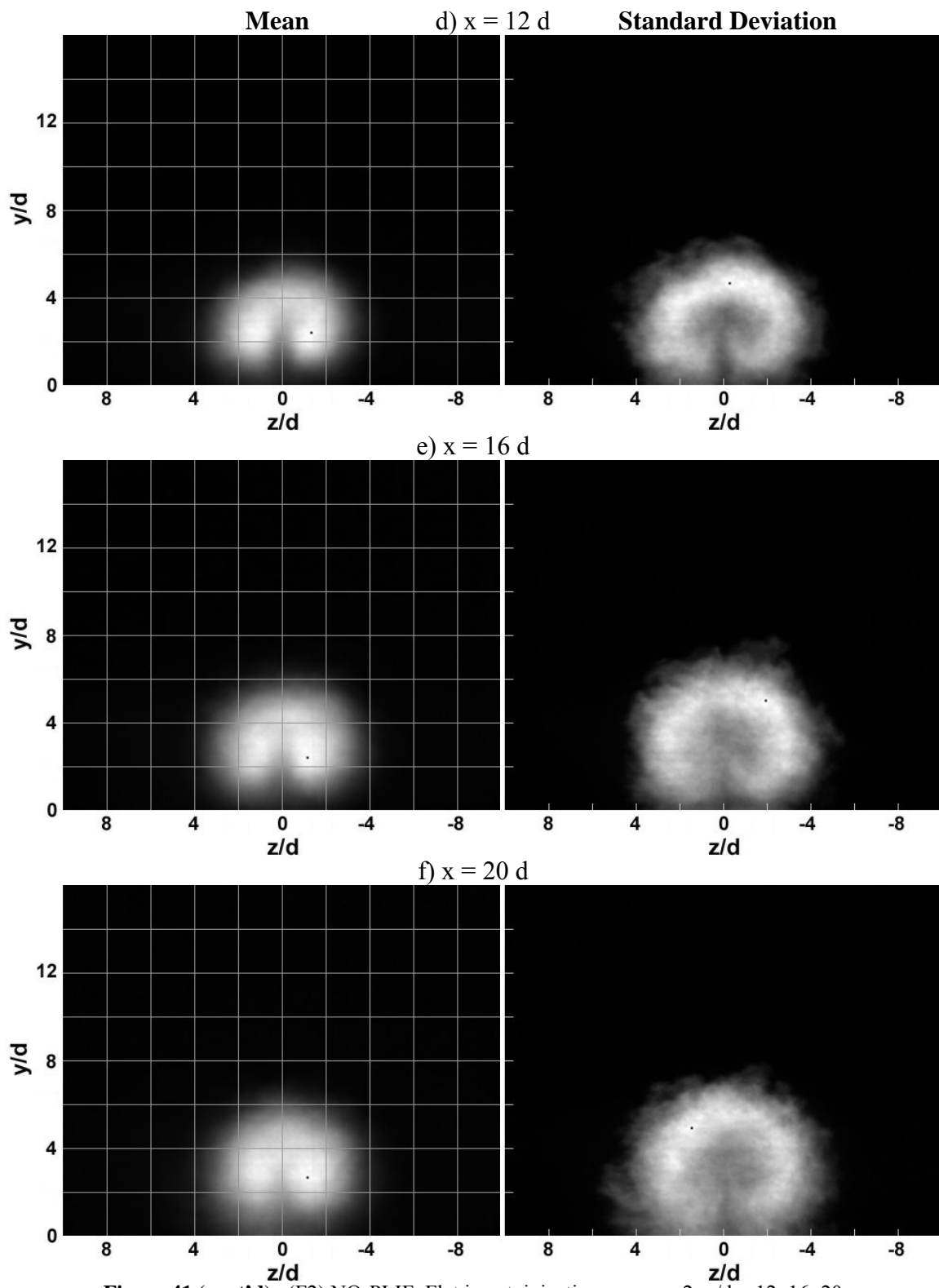
Mean d) x = 12 d **Standard Deviation**

e) x = 16 d

f) x = 20 d

Figure 41 (cont'd). (F2) NO-PLIF, Flat insert, injection pressure 2, x/d = 12, 16, 20

68

Mean   g) x = 24 d   **Standard Deviation**

Figure 41 (cont'd). (F2) NO-PLIF, Flat insert, injection pressure 2, x/d = 24

Mean a) x = 0 d **Standard Deviation**

b) x = 4 d

c) x = 8 d
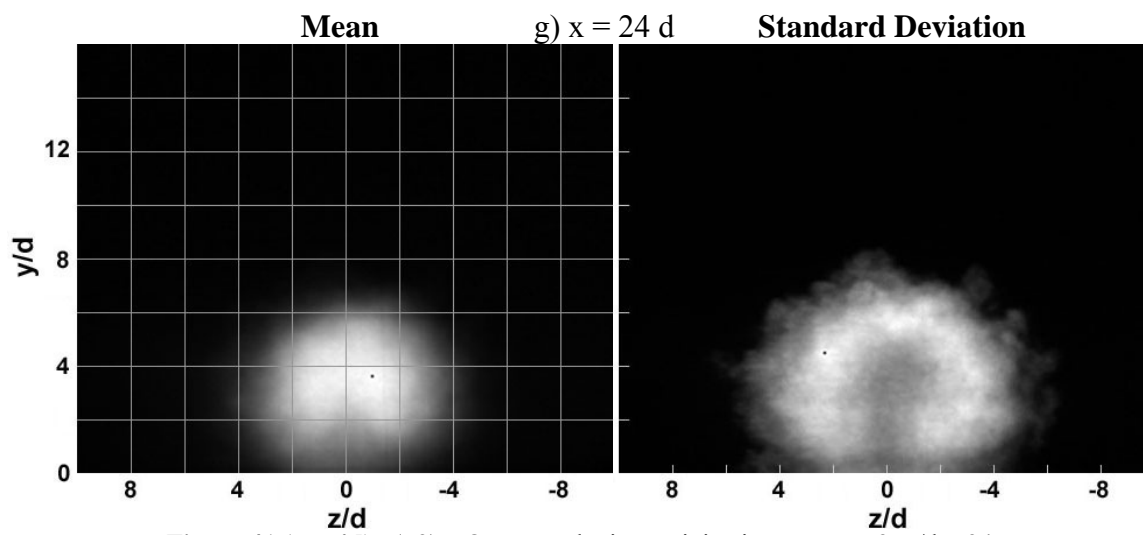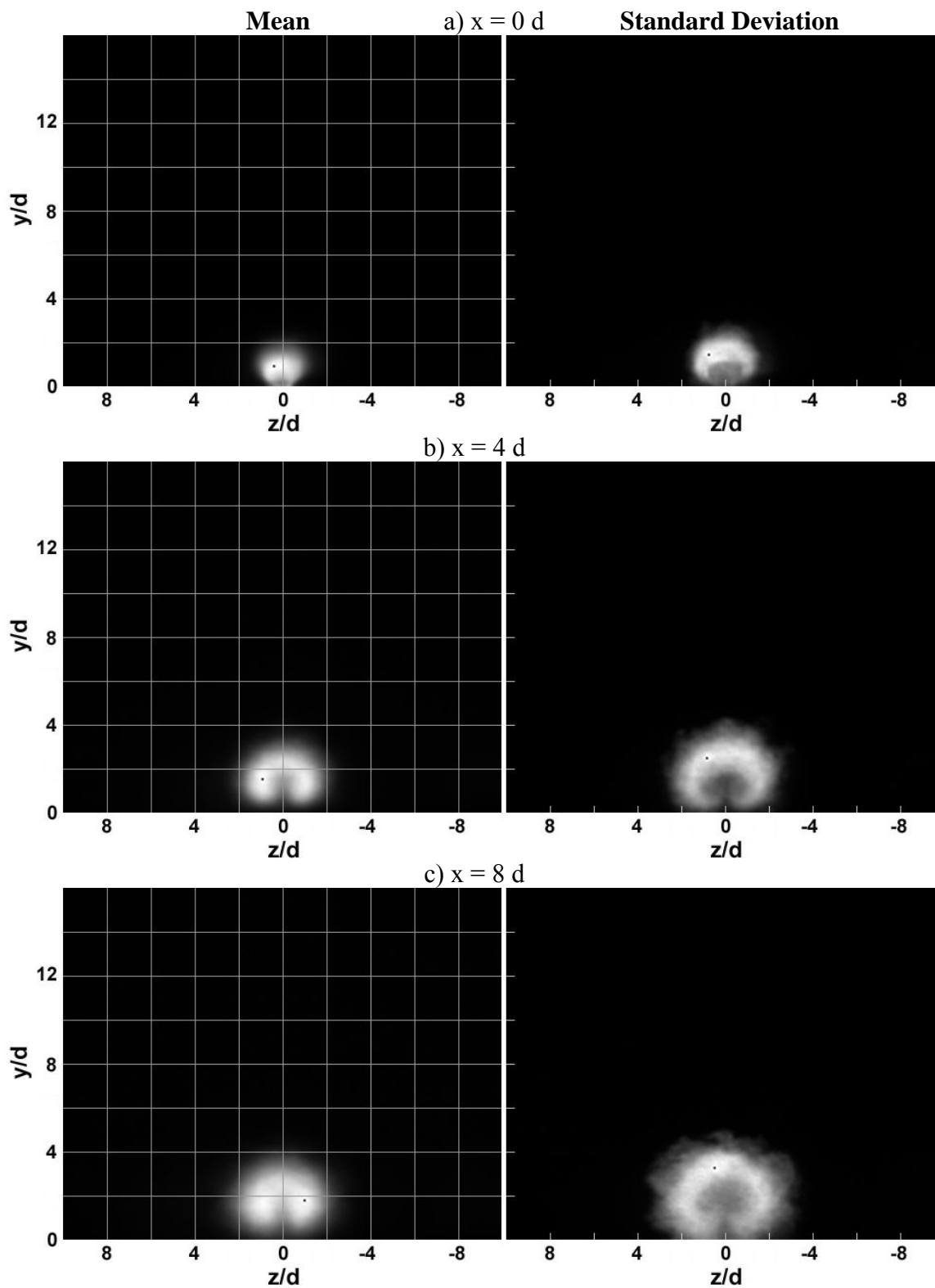
Figure 42. (F3) NO-PLIF, Flat insert, injection pressure 3, x/d = 0, 4, 8

Mean   d) x = 12 d   **Standard Deviation**

e) x = 16 d

f) x = 20 d
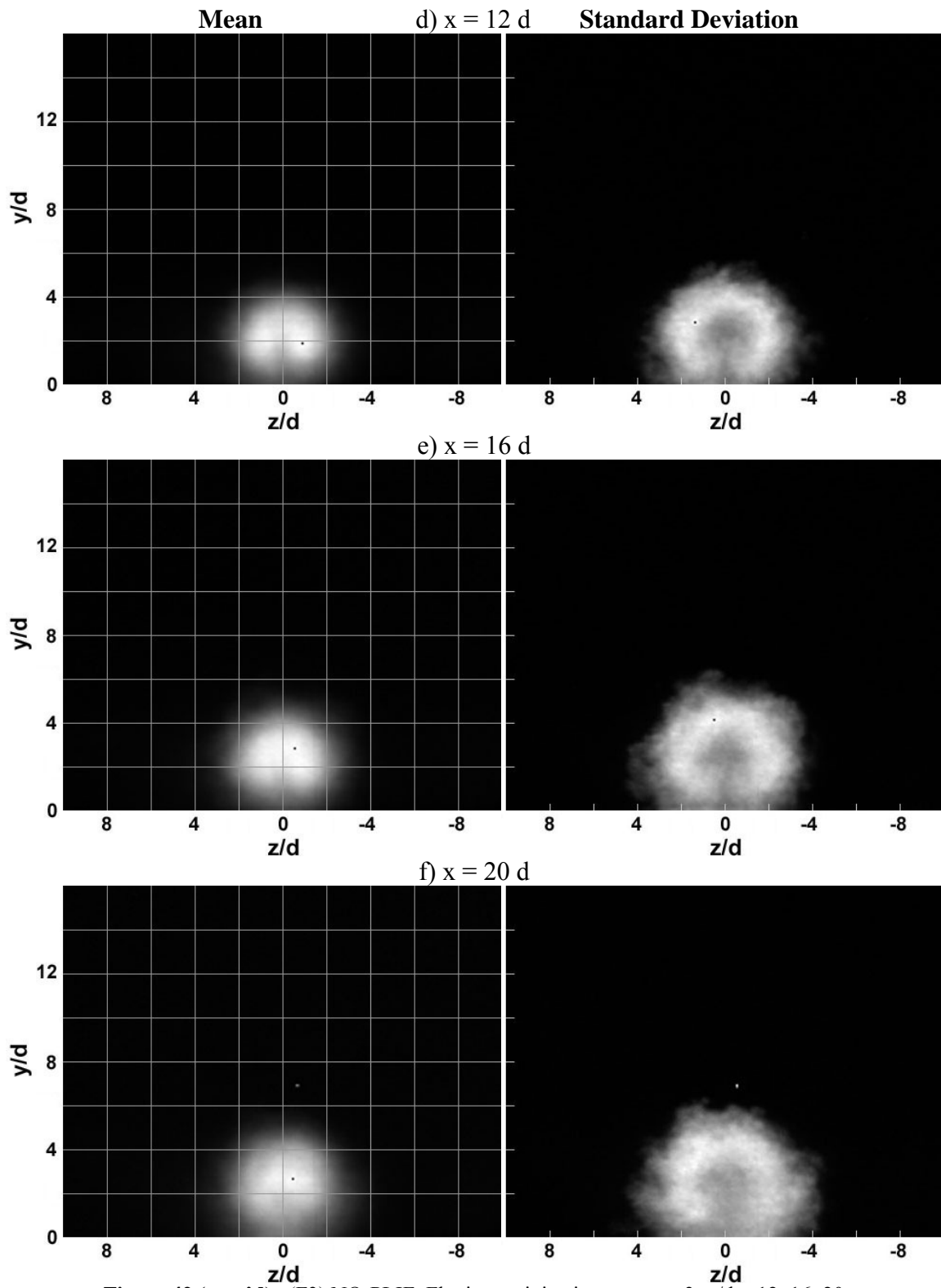
Figure 42 (cont'd). (F3) NO-PLIF, Flat insert, injection pressure 3, x/d = 12, 16, 20

71

When no pylon is installed, the jet exhibits the familiar behavior observed in previous research.[32] At the jet injection location ($x/d = 0$), the jet crowns as it quickly expands, and it is mostly concentrated near the floor. The standard deviation at this location shows a large jet/core interaction over the top of the crown. Figure 40 highlights this well. The fluid then quickly develops into a lifted formation with counter-rotating edges. The mean images show that most of the jet is concentrated in these areas, while the standard deviation illustrates the strong interaction around the side and bottom of the plume. These areas of high interaction (bright white on the standard deviation images) are large and well defined at distances downstream.

As injection pressure decreases from 200 to 50 psia, the formation of the jet into a final shape occurs sooner. In the F1 case, the shape stabilizes at $x/d = 20$, although the size continues to increase (Figure 40(f)). This happens around $x/d = 16$ for F2 (Figure 41(e)) and $x/d = 12$ for F3 (Figure 42(d)). The stronger influence of the freestream at lower q reduces penetration and spread but begins to influence the jet/freestream interaction farther upstream. The higher the injection pressure the farther downstream the jet continues to develop and grow.

Even at high q, some of the jet fluid settles near the floor, such as in Figure 40(h). This could result in fuel pooling in the boundary layer, a condition that can lead to flashback, especially in inlets.[3] Assessment of this condition cannot be completed visually, but software which can create the jet boundaries for each case and measure the floor separation provides a better estimate for each case. That is the subject of the section following the image collages.

NO-PLIF

END VIEW

MEDIUM INSERT

IMAGES
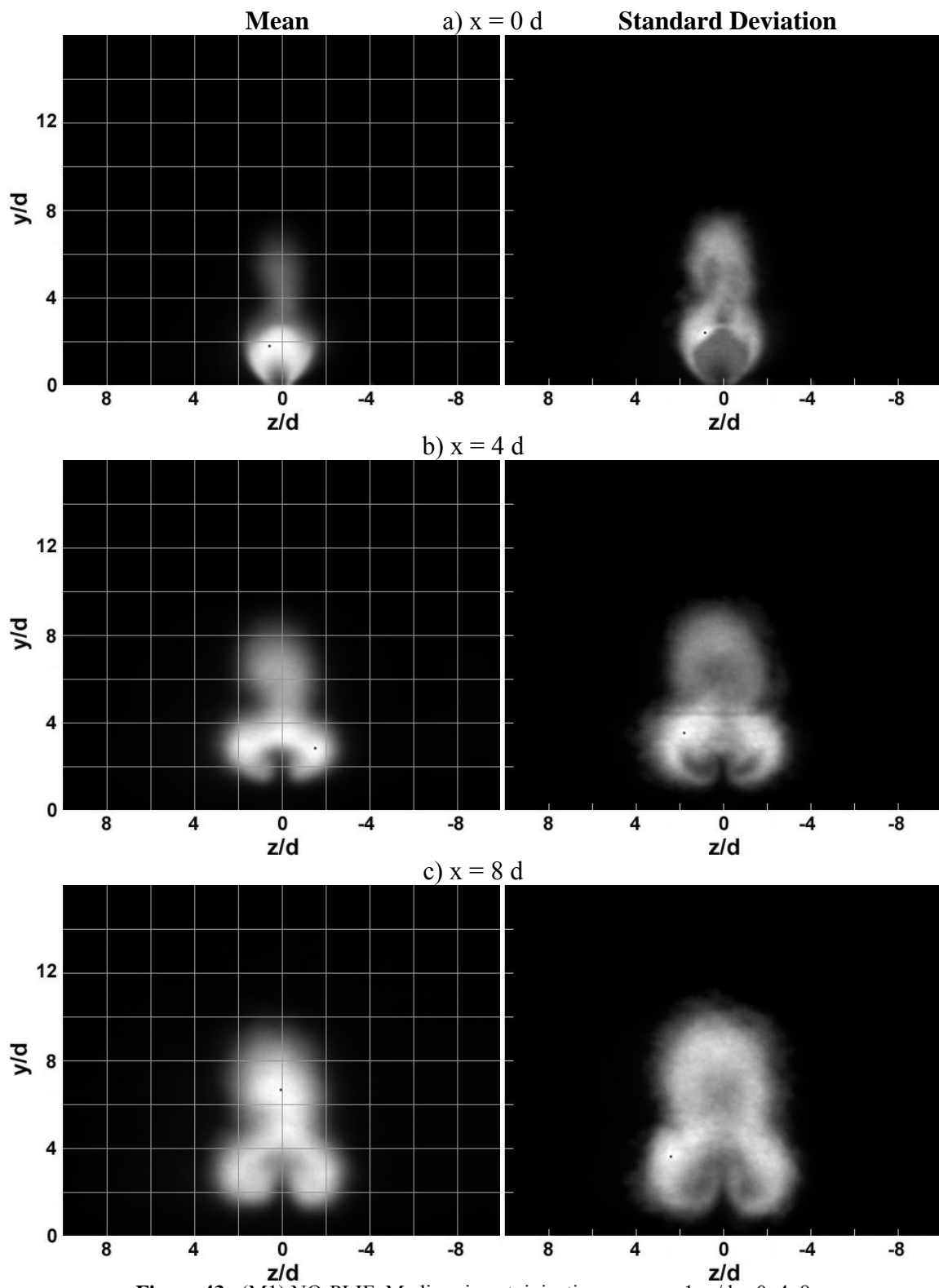
Figure 43. (M1) NO-PLIF, Medium insert, injection pressure 1, x/d = 0, 4, 8
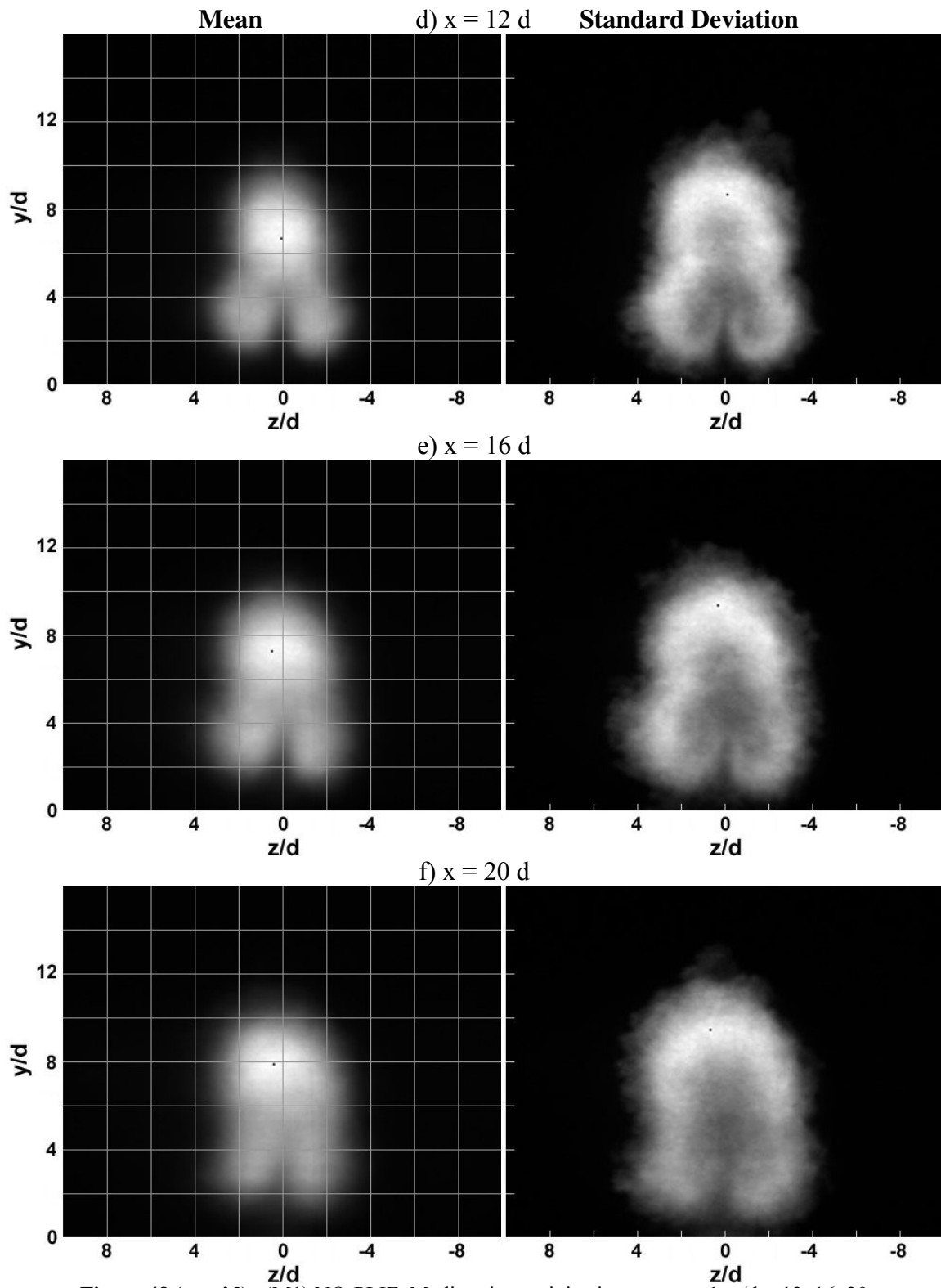
Mean   d) x = 12 d   **Standard Deviation**

e) x = 16 d

f) x = 20 d

Figure 43 (cont'd). (M1) NO-PLIF, Medium insert, injection pressure 1, x/d = 12, 16, 20

75

Mean   g) x = 24 d   **Standard Deviation**

h) x = 32 d

Figure 43 (cont'd). (M1) NO-PLIF, Medium insert, injection pressure 1, x/d = 24, 32

Mean a) x = 0 d **Standard Deviation**

b) x = 4 d

c) x = 8 d
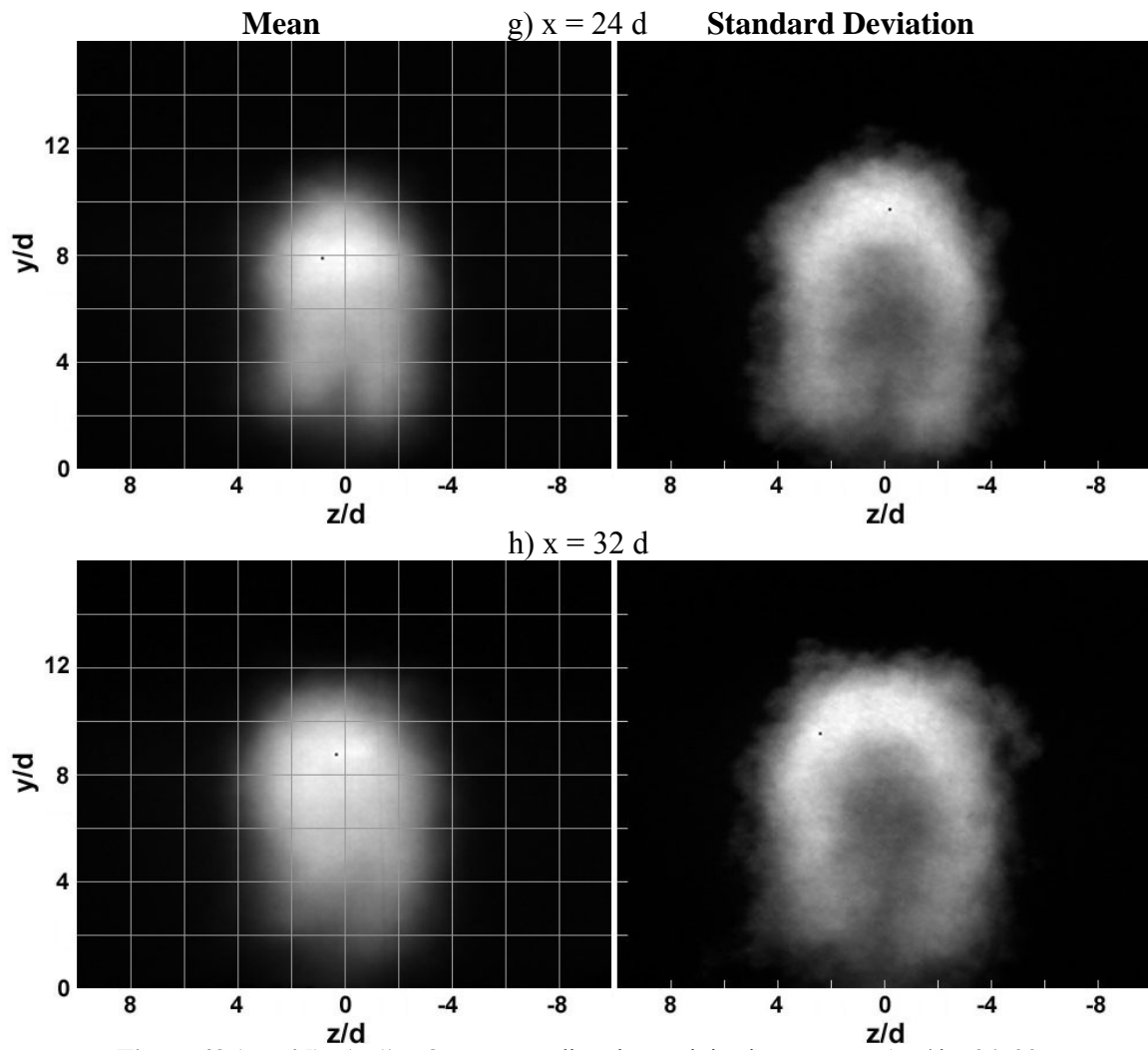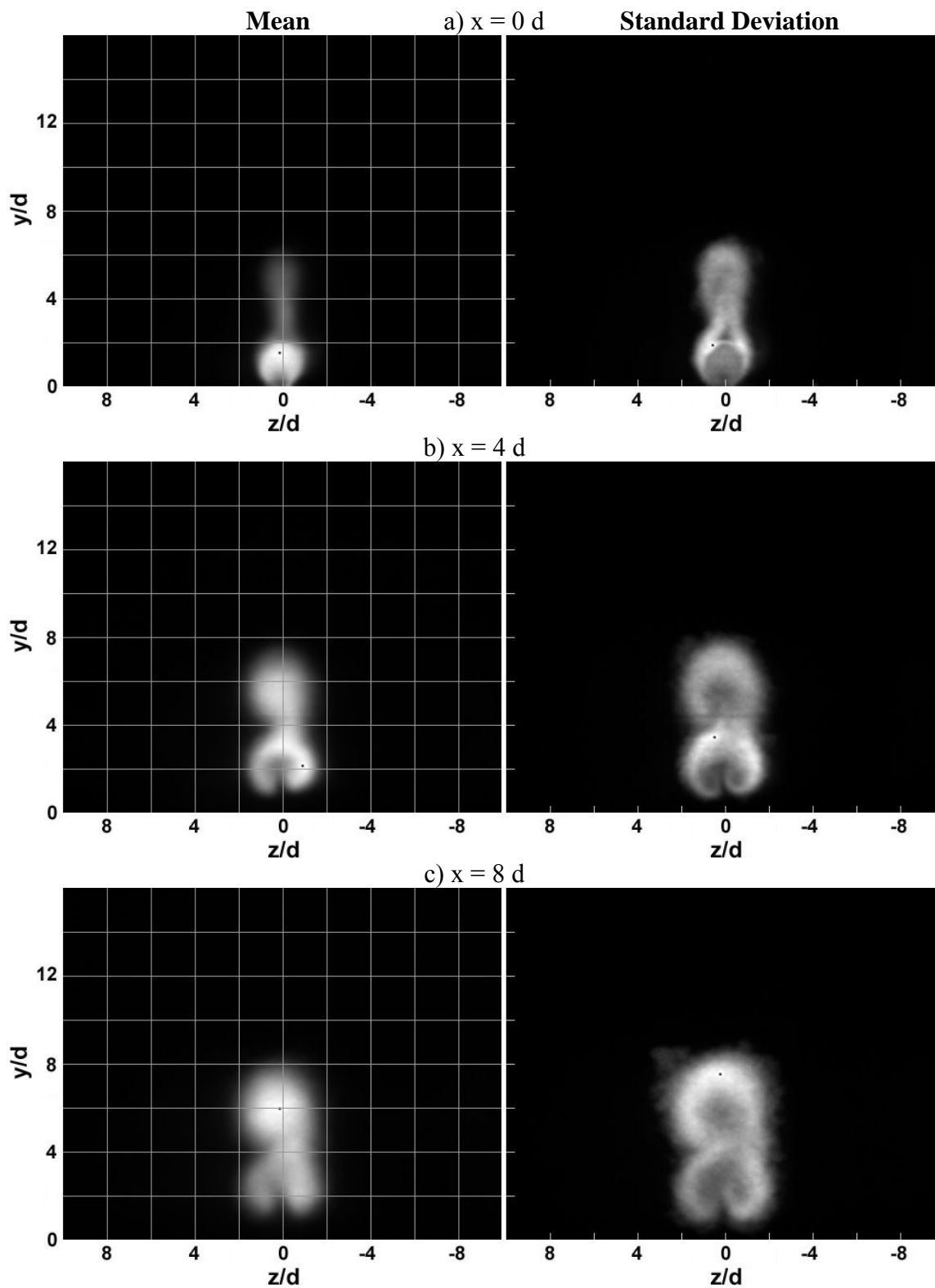
Figure 44. (M2) NO-PLIF, Medium insert, injection pressure 2, x/d = 0, 4, 8
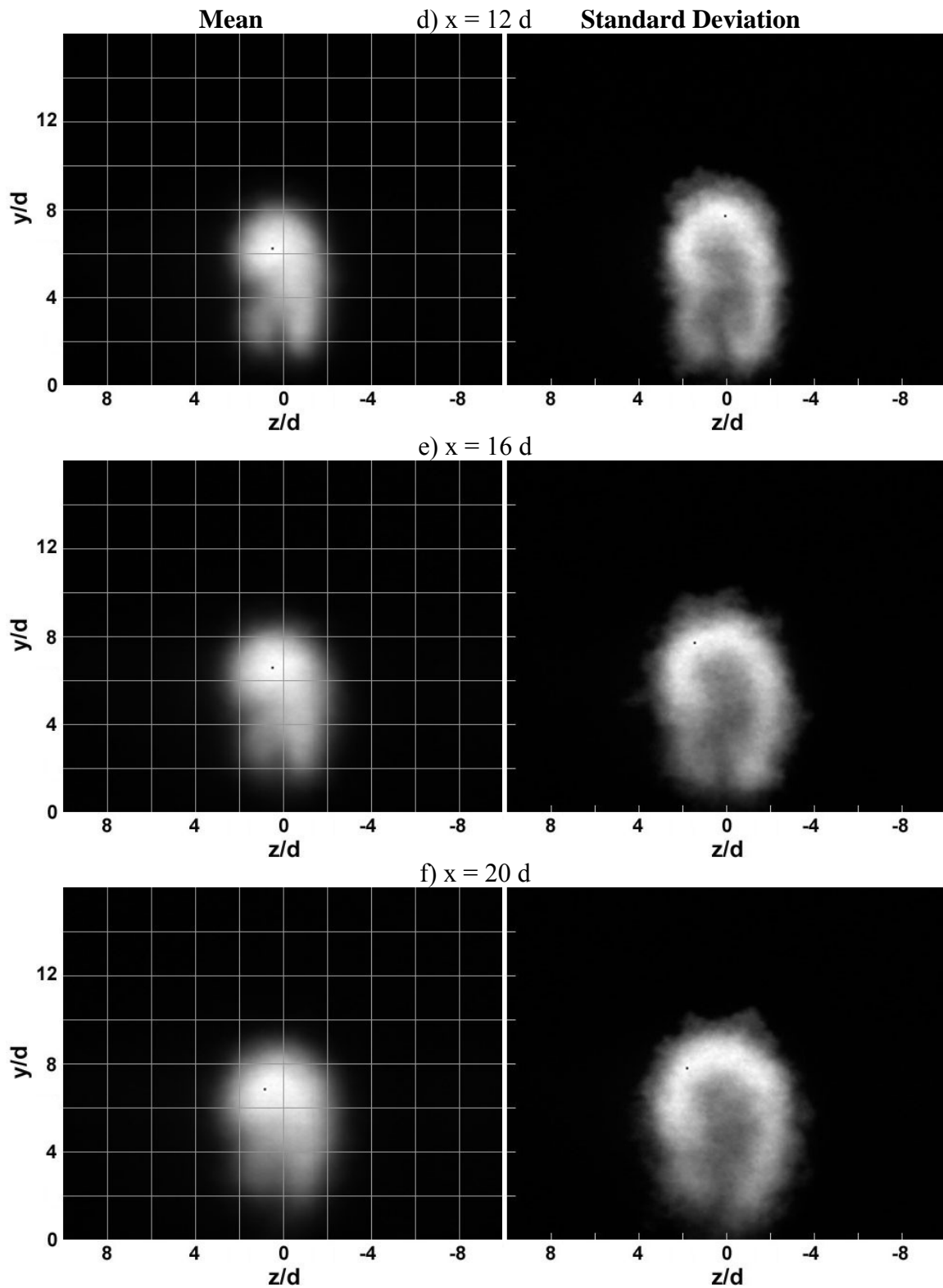
Mean   d) x = 12 d   **Standard Deviation**

e) x = 16 d

f) x = 20 d

Figure 44 (cont'd). (M2) NO-PLIF, Medium insert, injection pressure 2, x/d = 12, 16, 20

78

Mean g) x = 24 d **Standard Deviation**

Figure 44 (cont'd). (M2) NO-PLIF, Medium insert, injection pressure 2, x/d = 24

Mean　　　　　a) x = 0 d　　　　**Standard Deviation**

b) x = 4 d

c) x = 8 d
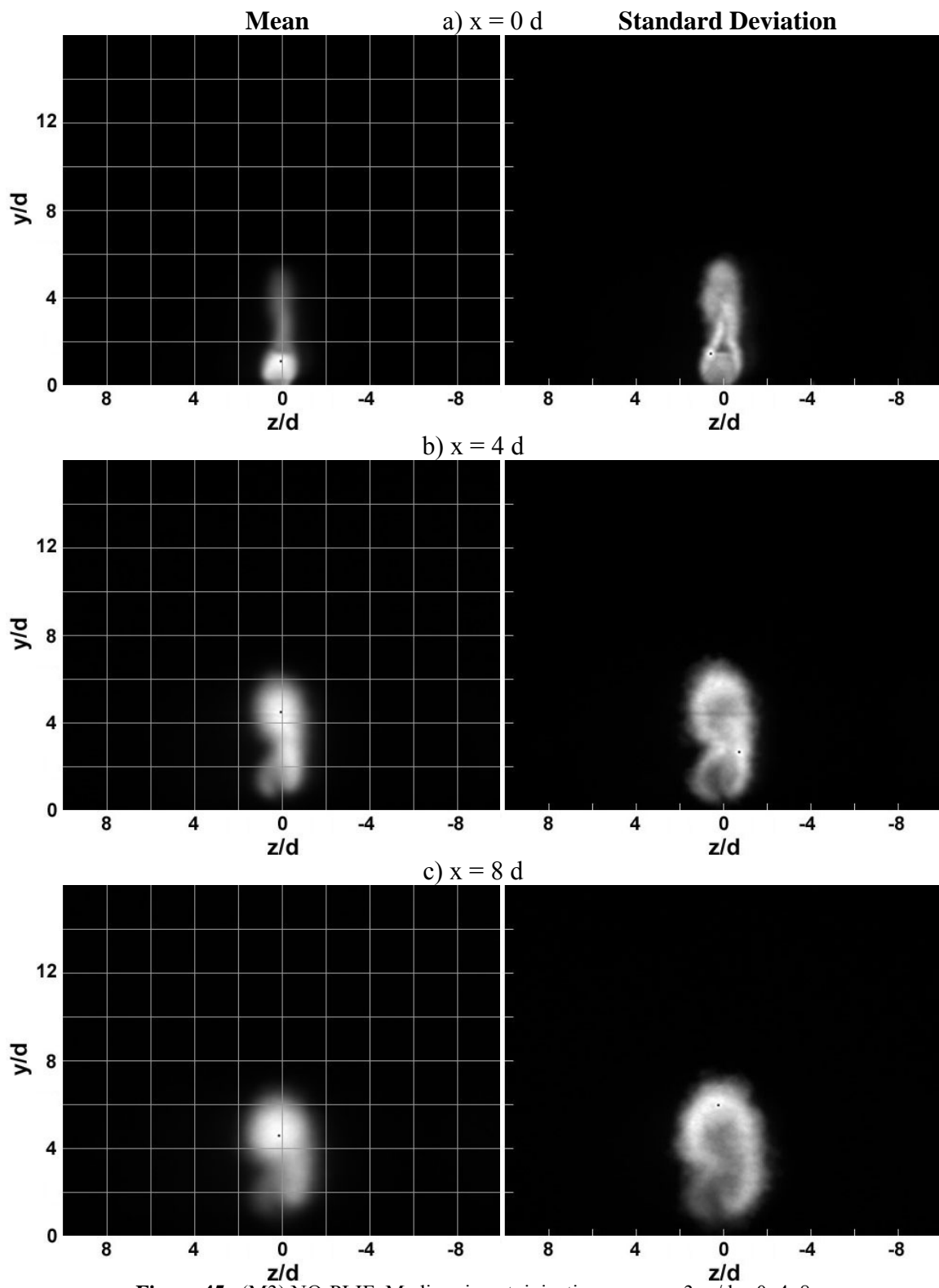
Figure 45. (M3) NO-PLIF, Medium insert, injection pressure 3, x/d = 0, 4, 8

Mean d) x = 12 d **Standard Deviation**

e) x = 16 d

f) x = 20 d

Figure 45 (cont'd). (M3) NO-PLIF, Medium insert, injection pressure 3, x/d = 12, 16, 20

81

When flow is injected behind the Medium pylon, the jet is observed to crown, but with a small amount of NO penetrating past the interaction layer and into the freestream (above the pylon). Figure 43(a) illustrates this. The jet then immediately widens to a thickness greater than the pylon, with a high interaction zone in the base area. By the x/d = 12 location, jet fluid has penetrated into the higher thin area seen before and is more concentrated there (Figure 43(d)). The familiar counter-rotating formations are evident but begin to play less of a role, as the standard deviation shows the interaction zone shifting up to match the lift in jet concentration. By $x/d = 20$, the majority of the jet fluid and interaction are in the upper area, which has become wider and more pronounced (Figure 43(f)).

This three part process (immediate penetration and widening, transfer of fluid concentration away from the floor and counter-rotating areas, settling of the fluid in the now wide upper area) is observable in all three pylon configurations, as will be shown next with the last two pylons. The process suggests that the pylons generally lift fuel from the floor and disperse it higher into the cross-flow, lessening the vortex generation (vortices reduce global mixing as intensity plots show, perhaps due to the centrifugal effect). All pylons also serve to increase the penetration height and leave the fuel higher off the floor over the Flat case. Again, a higher q causes the developments to continue occurring farther downstream. For instance, the fluid settling occurs around $x/d = 12$ for M2 (Figure 44(d)) and $x/d = 8$ for M3 (Figure 45(c)).

At low q the jet is significantly more lifted from the floor than is observed in the Flat case. This is evident by comparing Figures 42(f) and 45(f). This keeps fuel out of the boundary layer.

NO-PLIF

END VIEW

TALL INSERT

IMAGES

Mean   a) x = 0 d   **Standard Deviation**

b) x = 4 d

c) x = 8 d
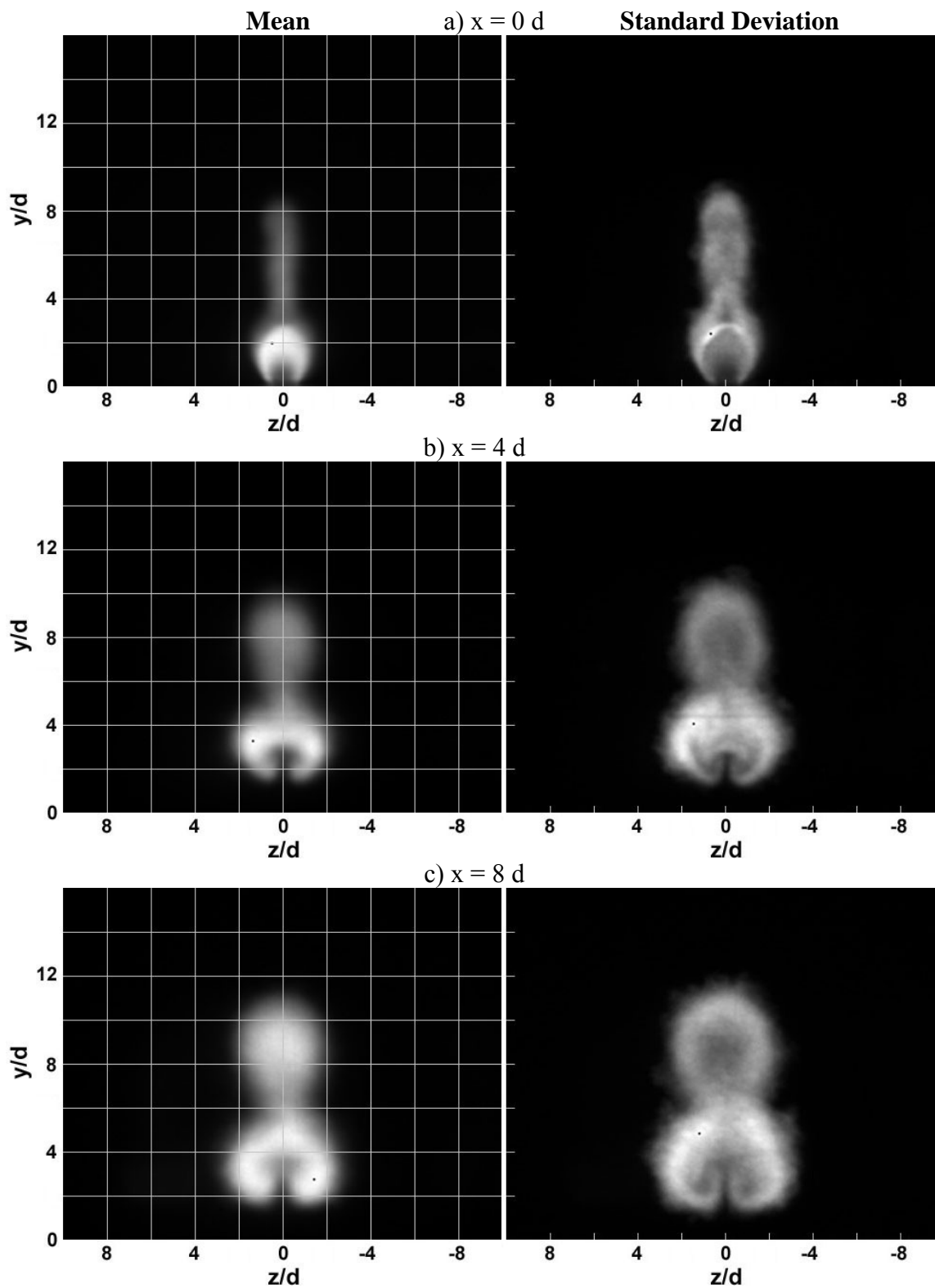
Figure 46. (T1) NO-PLIF, Tall insert, injection pressure 1, x/d = 0, 4, 8
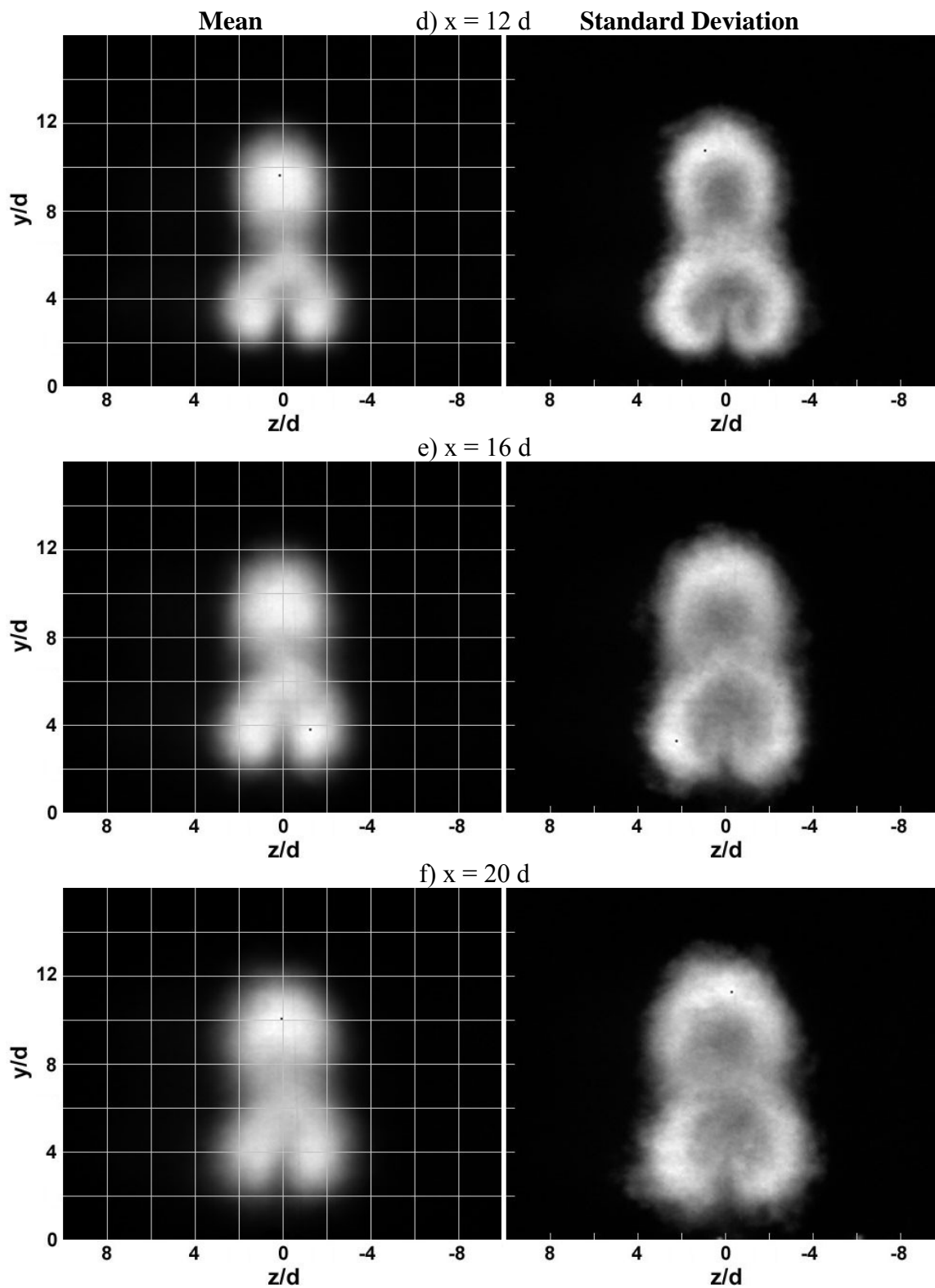
Mean   d) x = 12 d   **Standard Deviation**

e) x = 16 d

f) x = 20 d

Figure 46 (cont'd). (T1) NO-PLIF, Tall insert, injection pressure 1, x/d = 12, 16, 20

Mean   g) x = 24 d   **Standard Deviation**

h) x = 32 d

Figure 46 (cont'd). (T1) NO-PLIF, Tall insert, injection pressure 1, x/d = 24, 32

Mean a) x = 0 d **Standard Deviation**

b) x = 4 d

c) x = 8 d
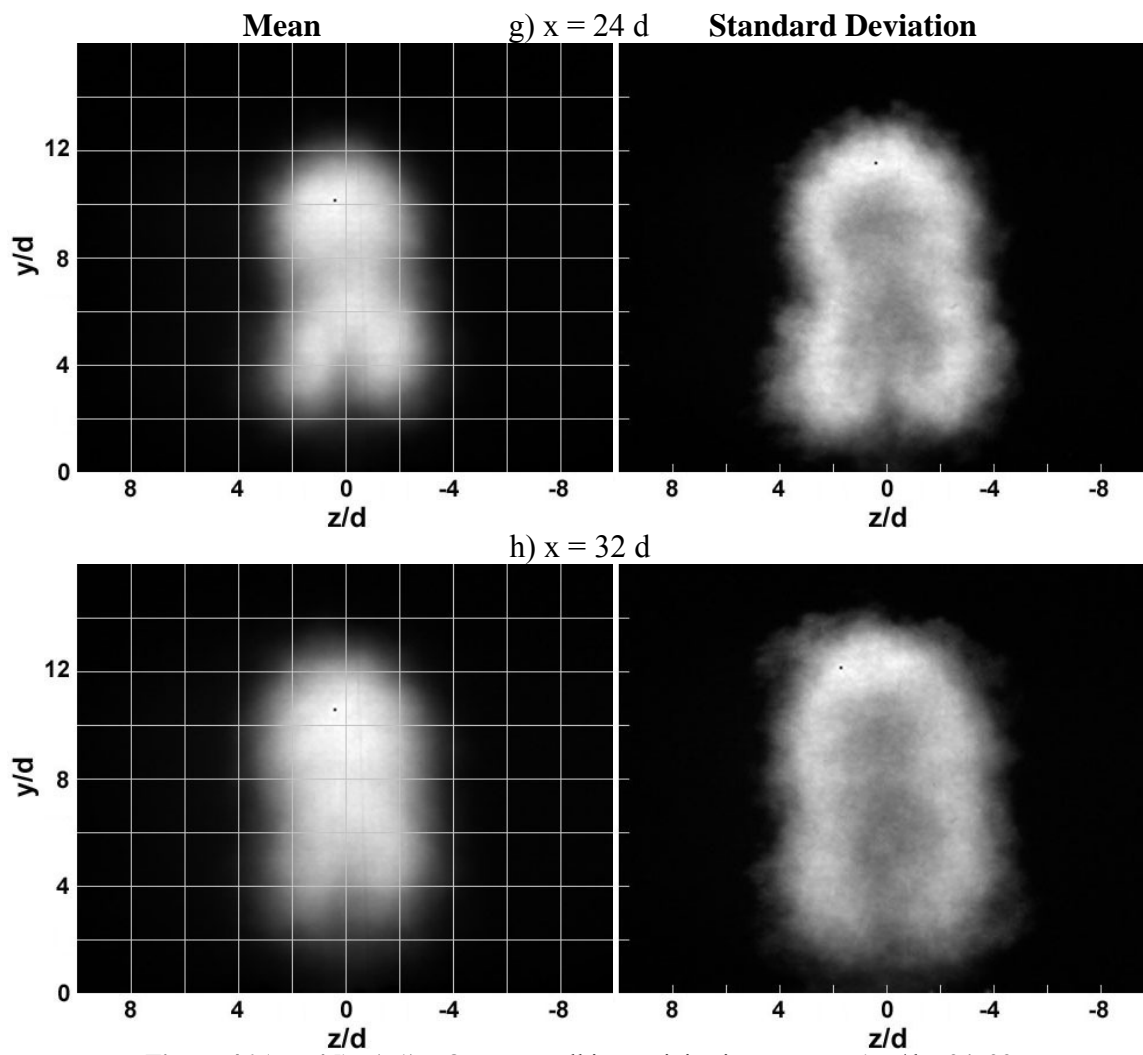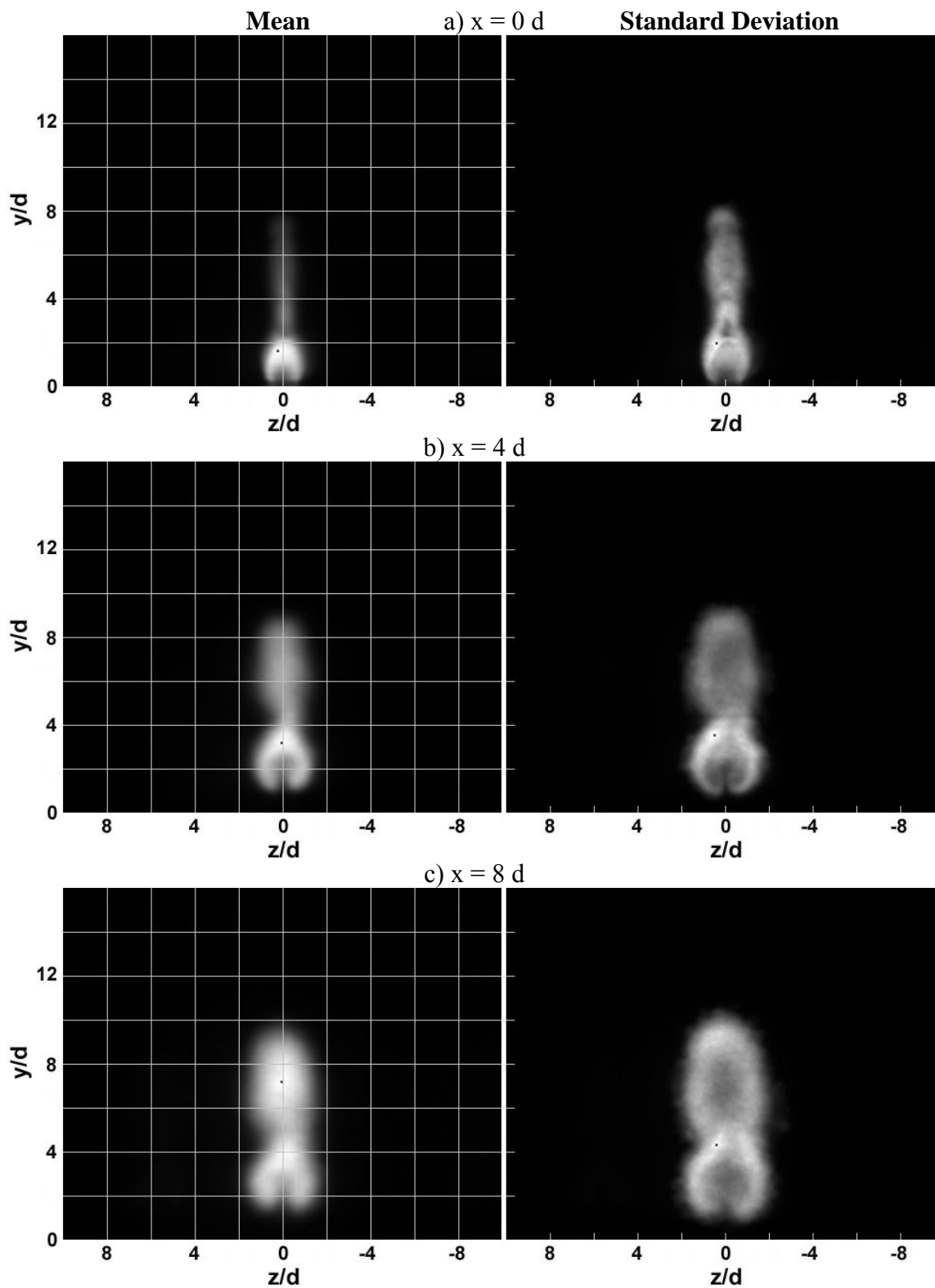
Figure 47. (T2) NO-PLIF, Tall insert, injection pressure 2, x/d = 0, 4, 8
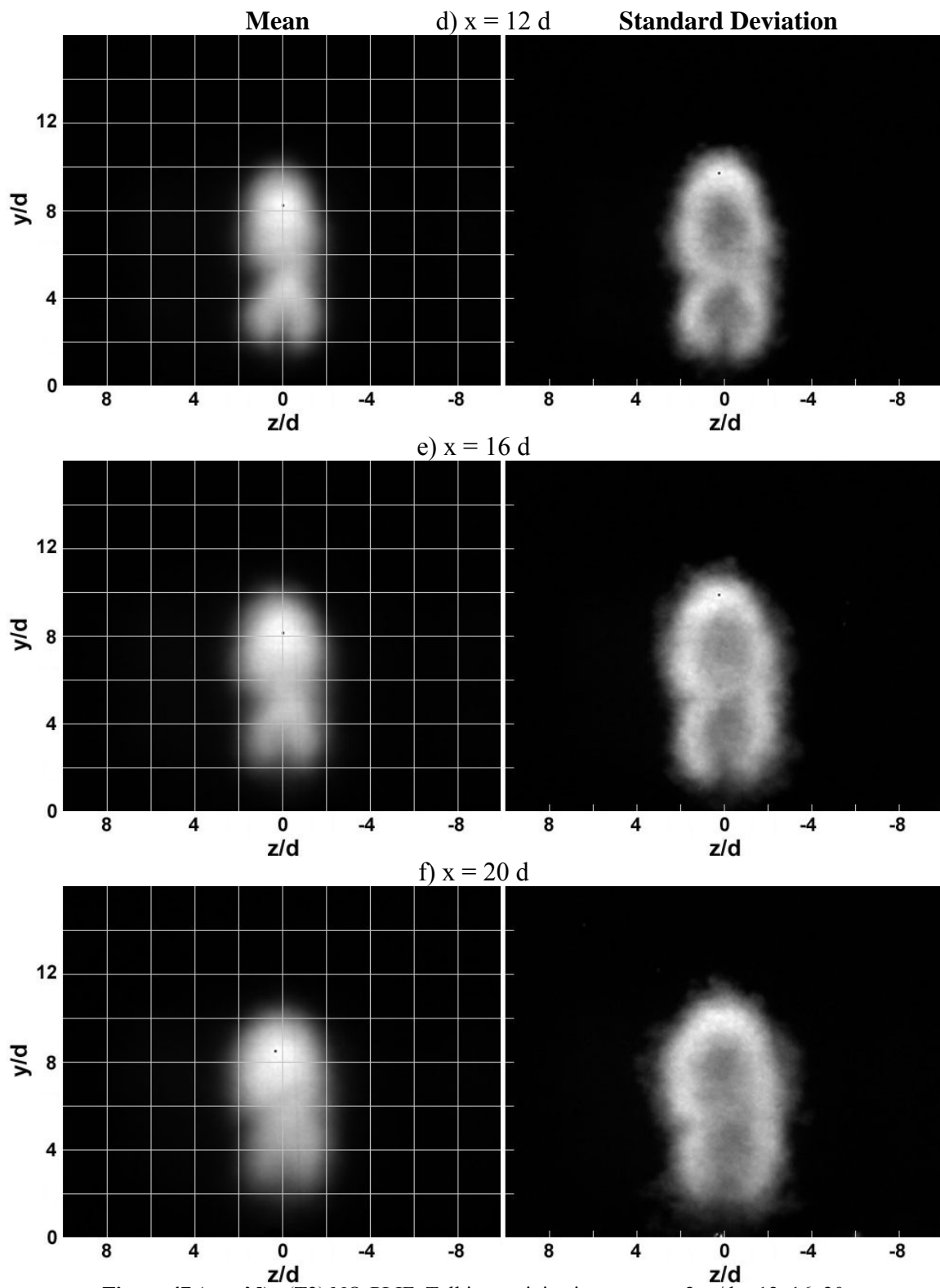
Mean   d) x = 12 d   **Standard Deviation**

e) x = 16 d

f) x = 20 d

Figure 47 (cont'd). (T2) NO-PLIF, Tall insert, injection pressure 2, x/d = 12, 16, 20

Mean   g) x = 24 d   **Standard Deviation**

Figure 47 (cont'd). (T2) NO-PLIF, Tall insert, injection pressure 2, x/d = 24

Mean   a) x = 0 d   **Standard Deviation**

b) x = 4 d

c) x = 8 d
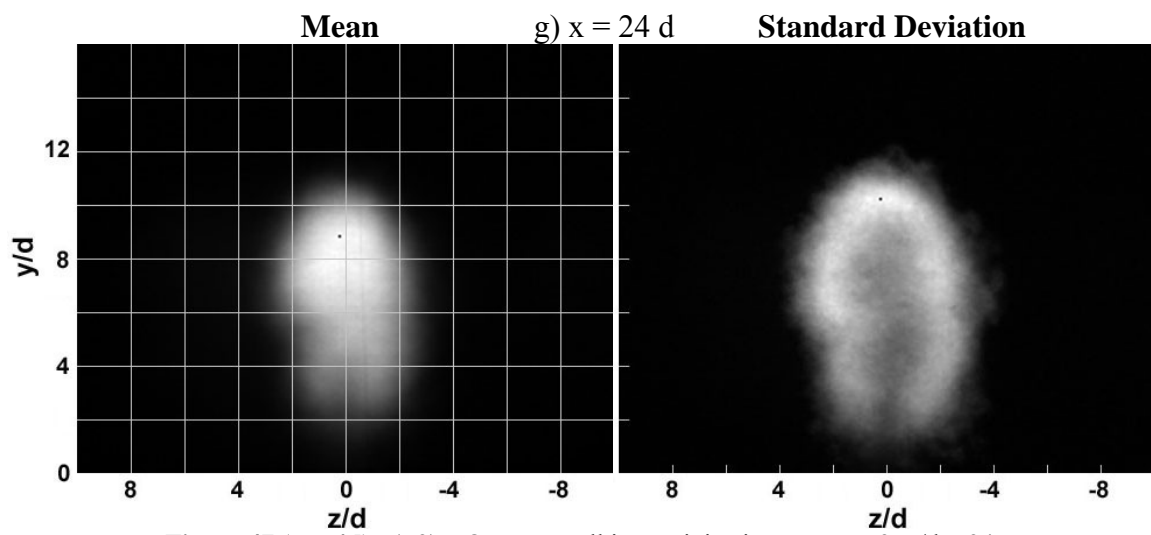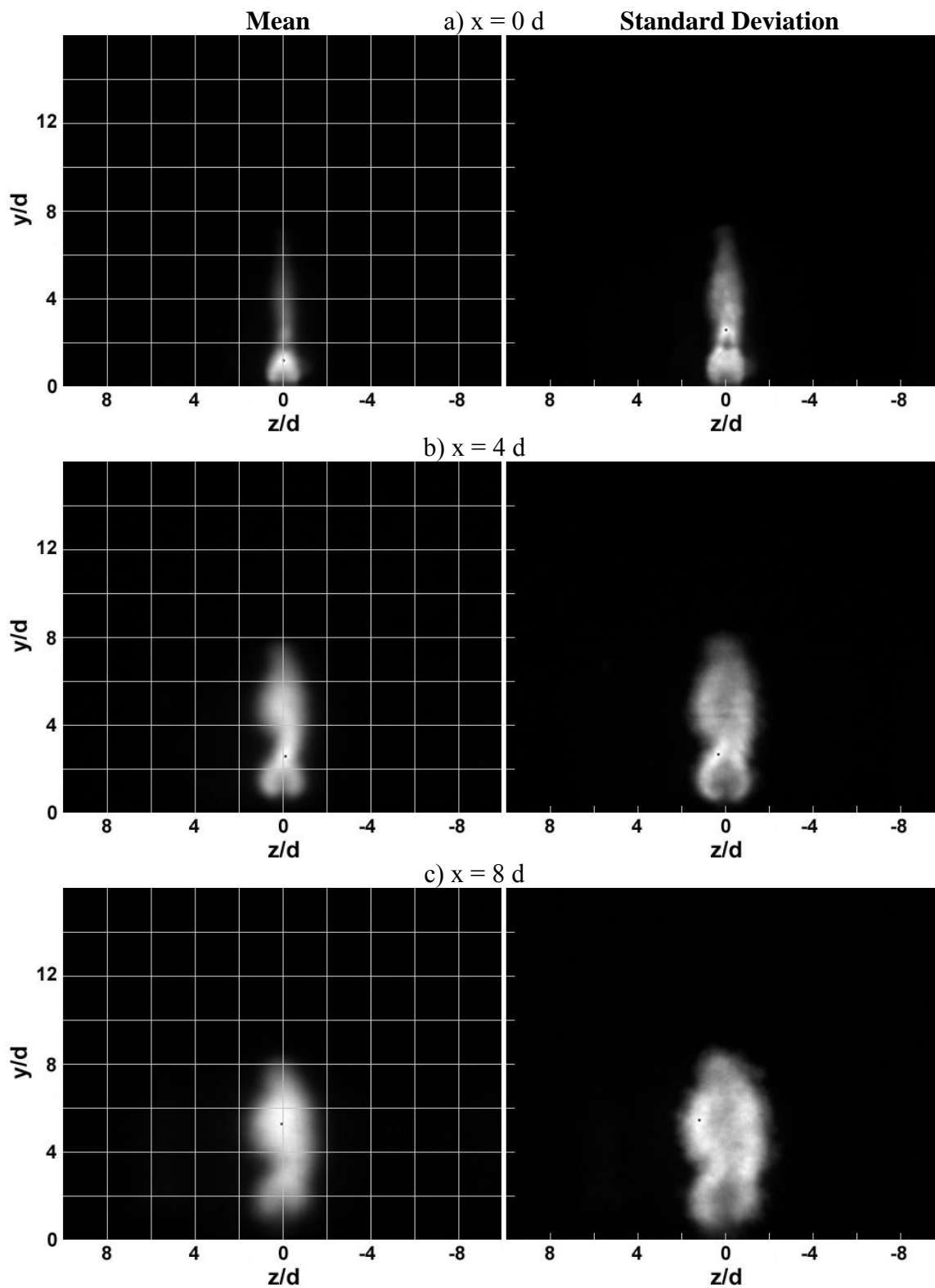
Figure 48. (T3) NO-PLIF, Tall insert, injection pressure 3, x/d = 0, 4, 8

Mean   d) x = 12 d   **Standard Deviation**

e) x = 16 d

f) x = 20 d
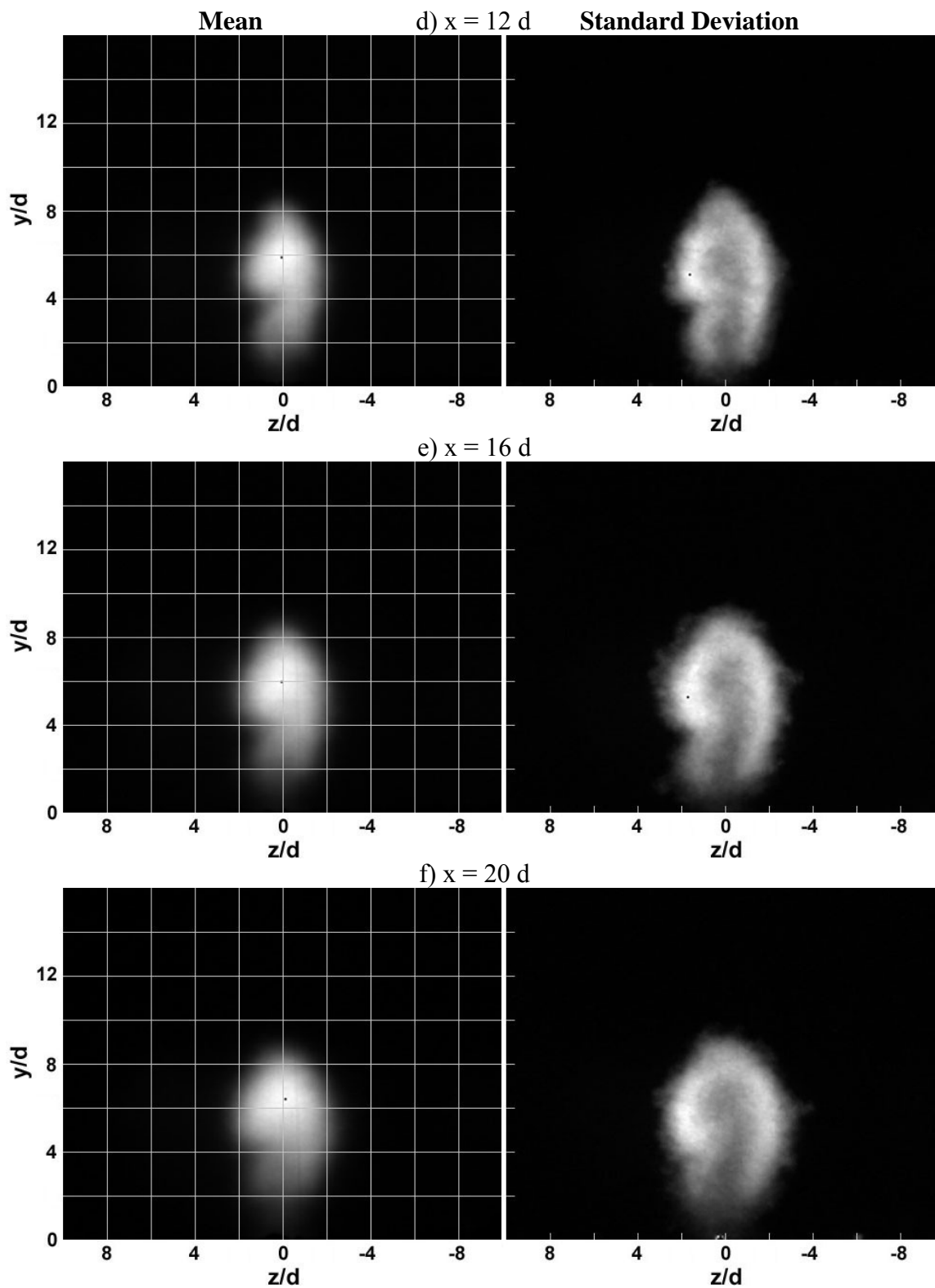
Figure 48 (cont'd). (T3) NO-PLIF, Tall insert, injection pressure 3, x/d = 12, 16, 20

Injection behind the Tall pylon shows immediate penetration past the crown such that the standard deviation shows a high initial level of development in the upper area. The crown does not have as defined of an interaction zone. The base then begins to widen, although not as rapidly as in the Medium case. At x/d = 12, seen in Figure 46(d), there is roughly an equal level of jet concentration and interaction between the upper and lower areas. Here the shape distinctly shows what are almost two independent areas. Downstream, the jet as a whole continues to lift into the freestream. Figure 46(g-h) shows that the counter-rotating flow begins to fade at x/d = 24, and by x/d = 32 more fluid is concentrated in the upper area. This is the trend seen in the Medium case, but the Tall jet does not develop as quickly. The Tall case shows much higher penetration into the freestream. The upper and lower areas are more distinct and continue to develop on their own once formed. This shows that the Tall geometry provides ample room for fuel dispersion initially and downstream, mainly because of its large presence. It is still thin enough to allow vortex generating phenomena to affect the lower area of fuel.

T2 shows a lower to upper transition and a stable formation occurring at x/d = 12 and 20, respectively (Figure 47(d)(f)). The x/d = 24 penetration height is equal to the height achieved at the same distance by the M1 case (Figures 47(g) and 43(g)), which shows how dramatically the Tall pylons affect penetration height. T3 shows an established plume by x/d = 16 (Figure 48(e)). All the Tall cases show a marked increase in penetration height, as well as a large jet cross-section. Development begins to occur farther downstream than with the other pylons.

The Tall pylon also noticeably lifts fuel off the boundary layer through the full range of injection pressures.

NO-PLIF

END VIEW

WIDE INSERT

IMAGES

Mean a) x = 0 d **Standard Deviation**

b) x = 4 d

c) x = 8 d
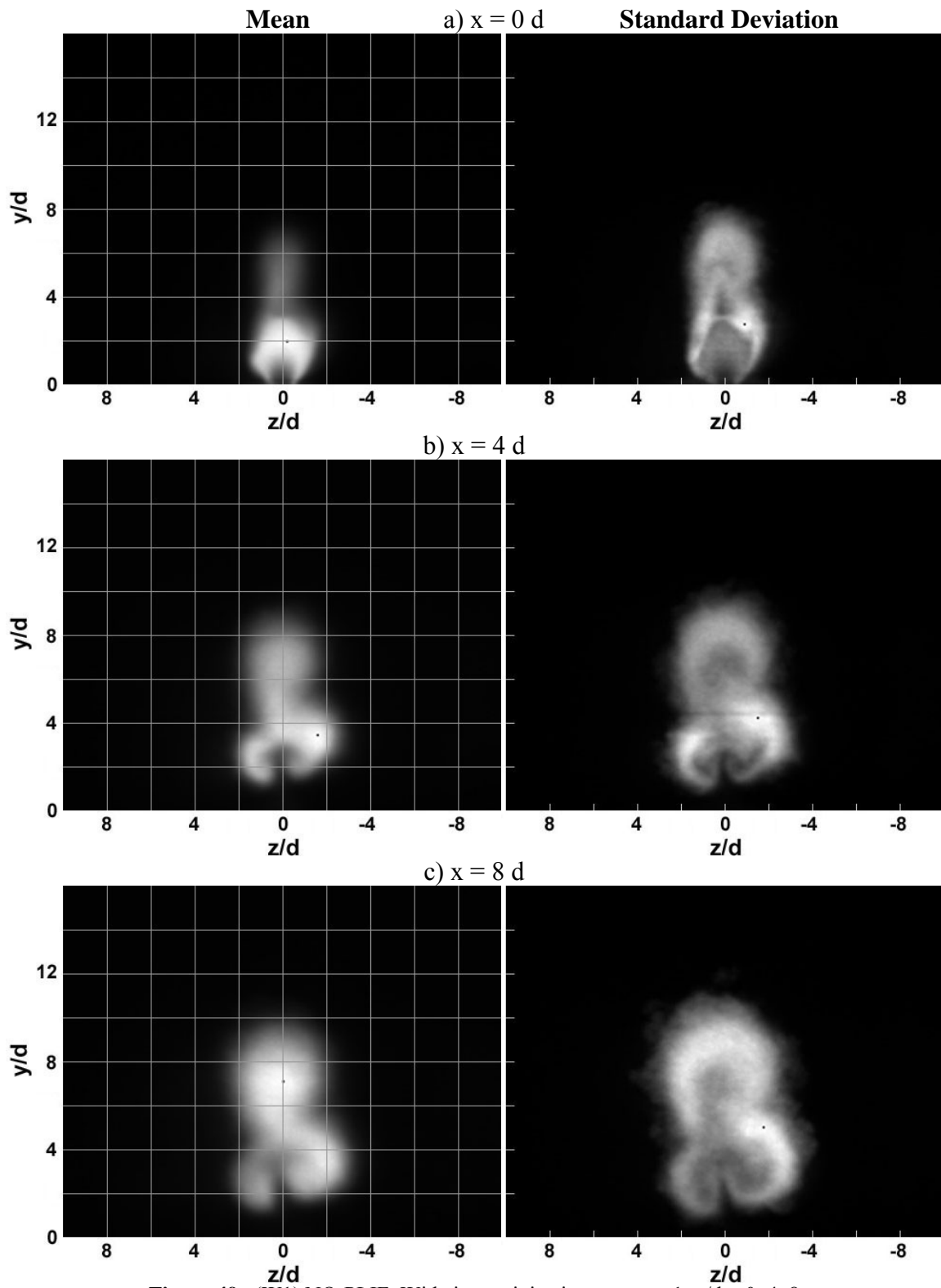
Figure 49. (W1) NO-PLIF, Wide insert, injection pressure 1, x/d = 0, 4, 8
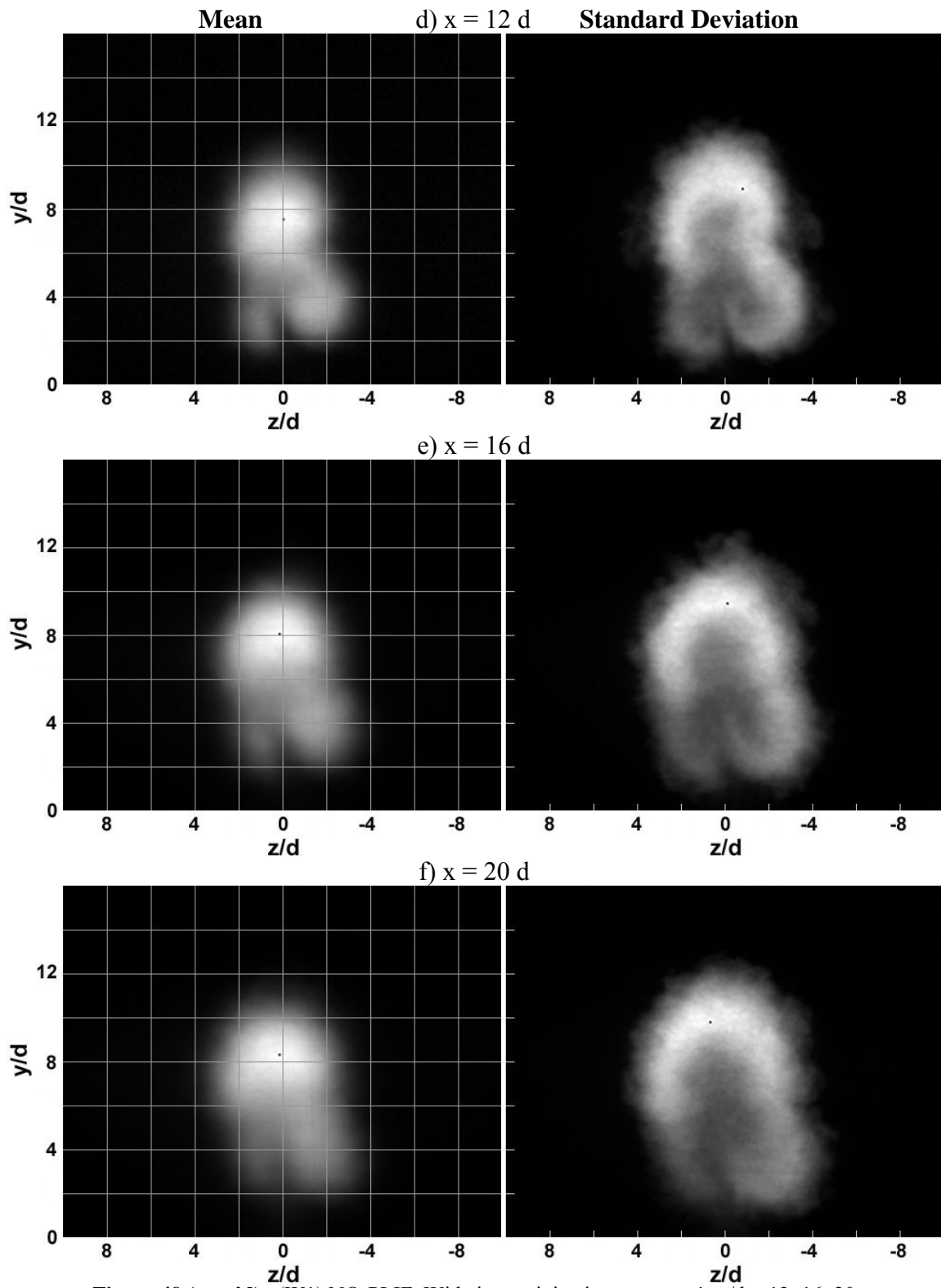
94

Mean   d) x = 12 d   **Standard Deviation**

e) x = 16 d

f) x = 20 d

Figure 49 (cont'd). (W1) NO-PLIF, Wide insert, injection pressure 1, x/d = 12, 16, 20

95

Mean　　　　　g) x = 24 d　　　　**Standard Deviation**

h) x = 32 d

Figure 49 (cont'd). (W1) NO-PLIF, Wide insert, injection pressure 1, x/d = 24, 32

96

Mean   a) x = 0 d   **Standard Deviation**

b) x = 4 d

c) x = 8 d
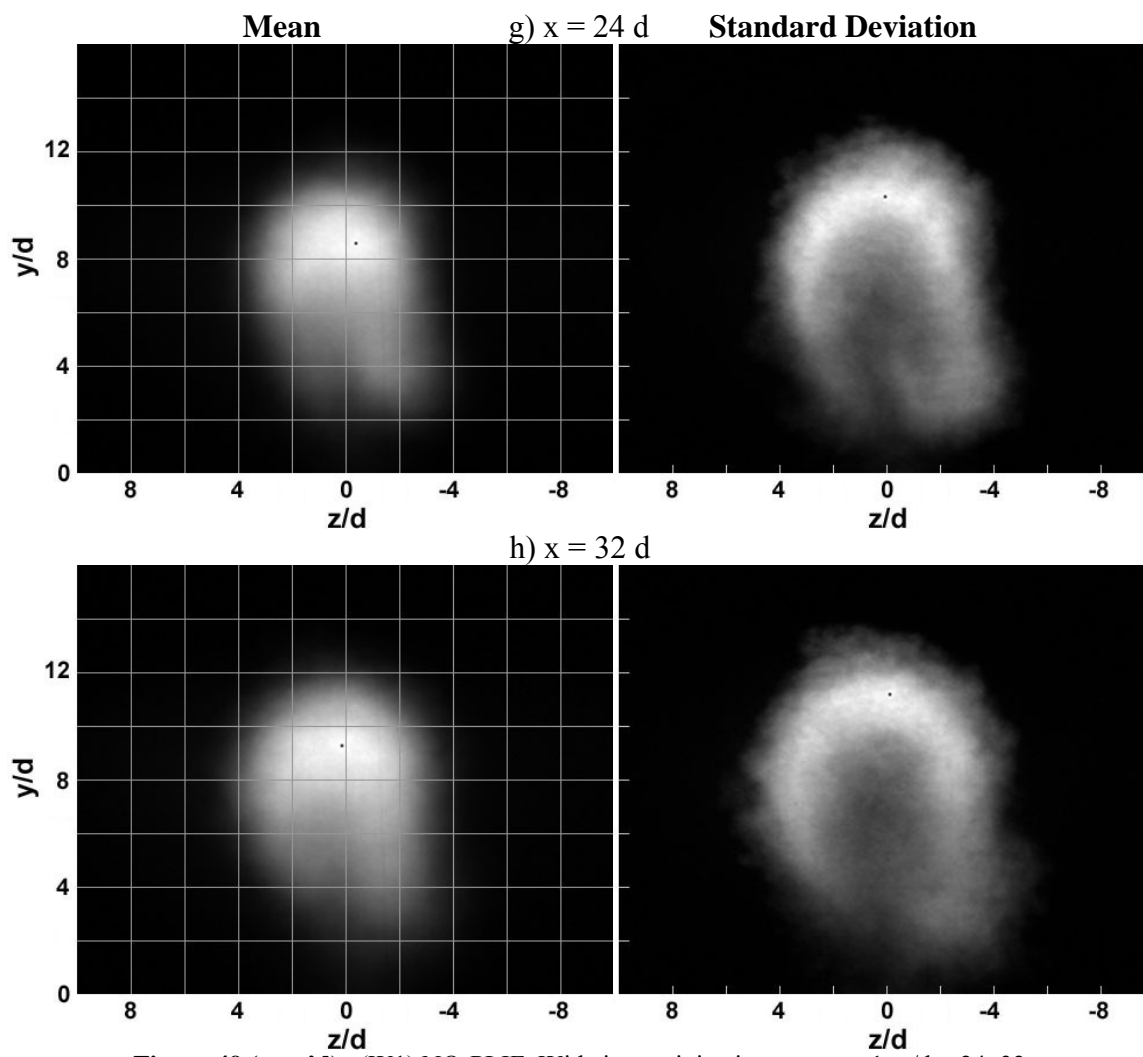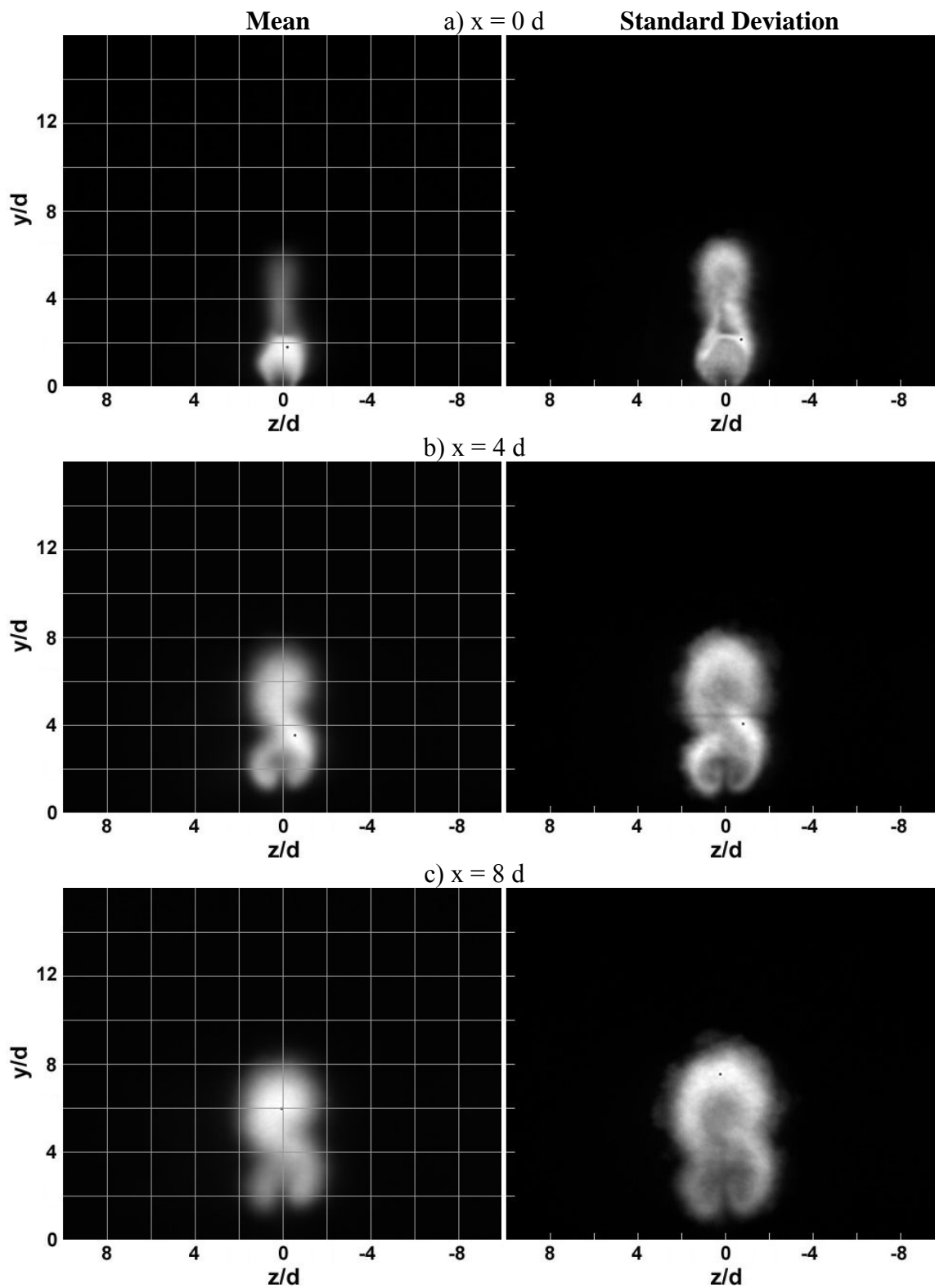
Figure 50. (W2) NO-PLIF, Wide insert, injection pressure 2, x/d = 0, 4, 8

Mean   d) x = 12 d   **Standard Deviation**

e) x = 16 d

f) x = 20 d

Figure 50 (cont'd). (W2) NO-PLIF, Wide insert, injection pressure 2, x/d = 12, 16, 20

Mean   g) x = 24 d   **Standard Deviation**
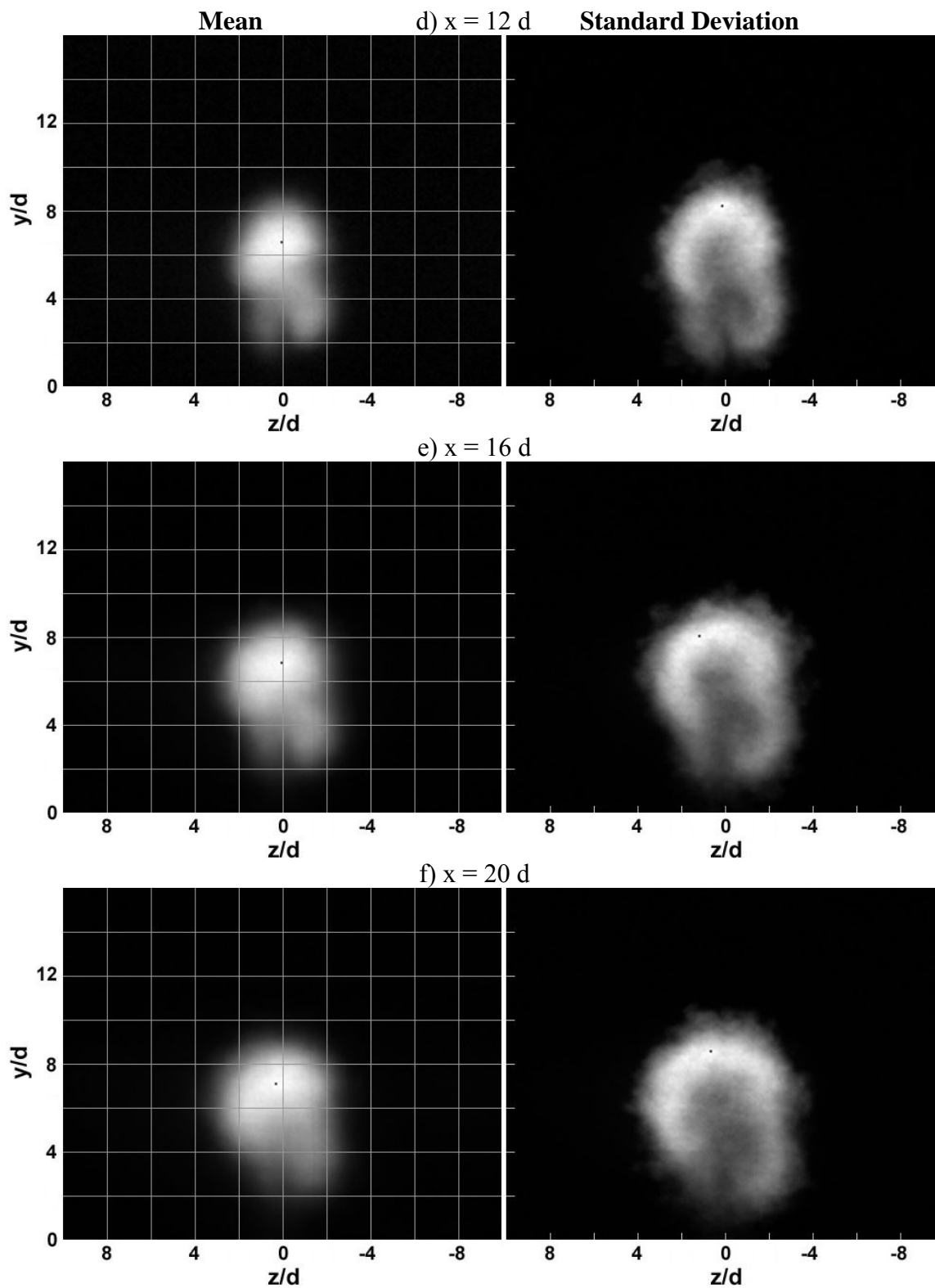
Figure 50 (cont'd). (W2) NO-PLIF, Wide insert, injection pressure 2, x/d = 24

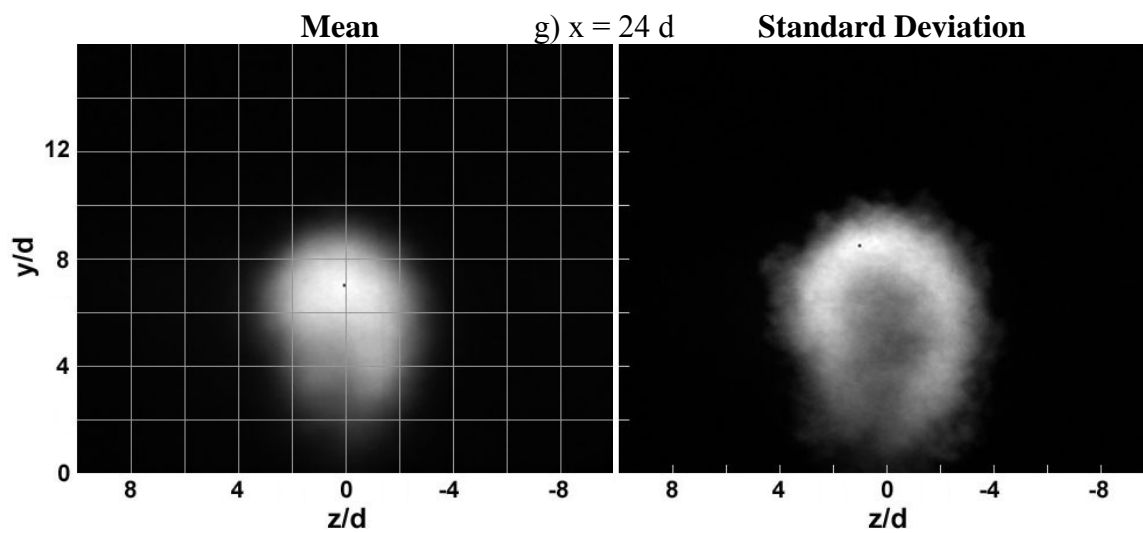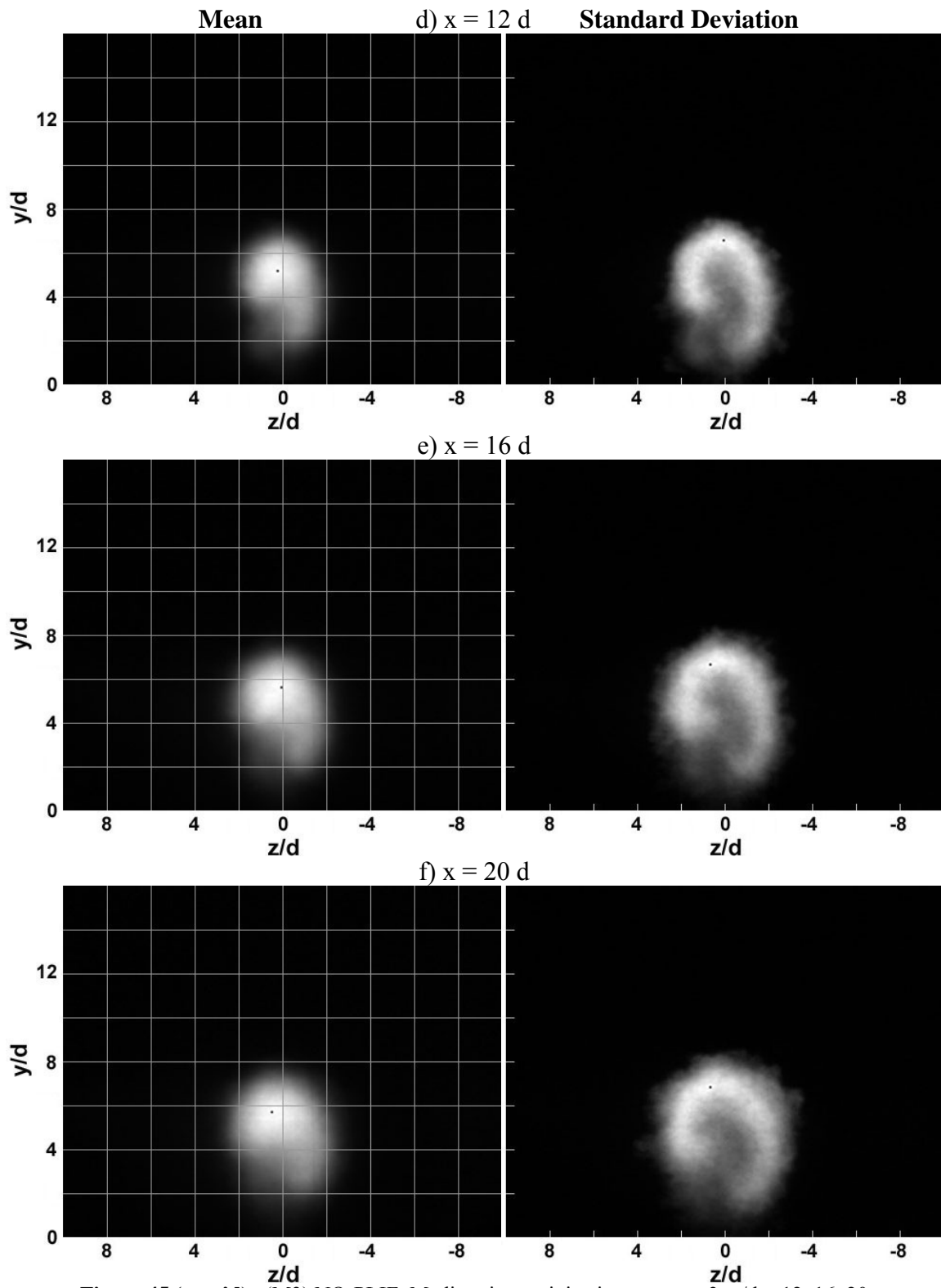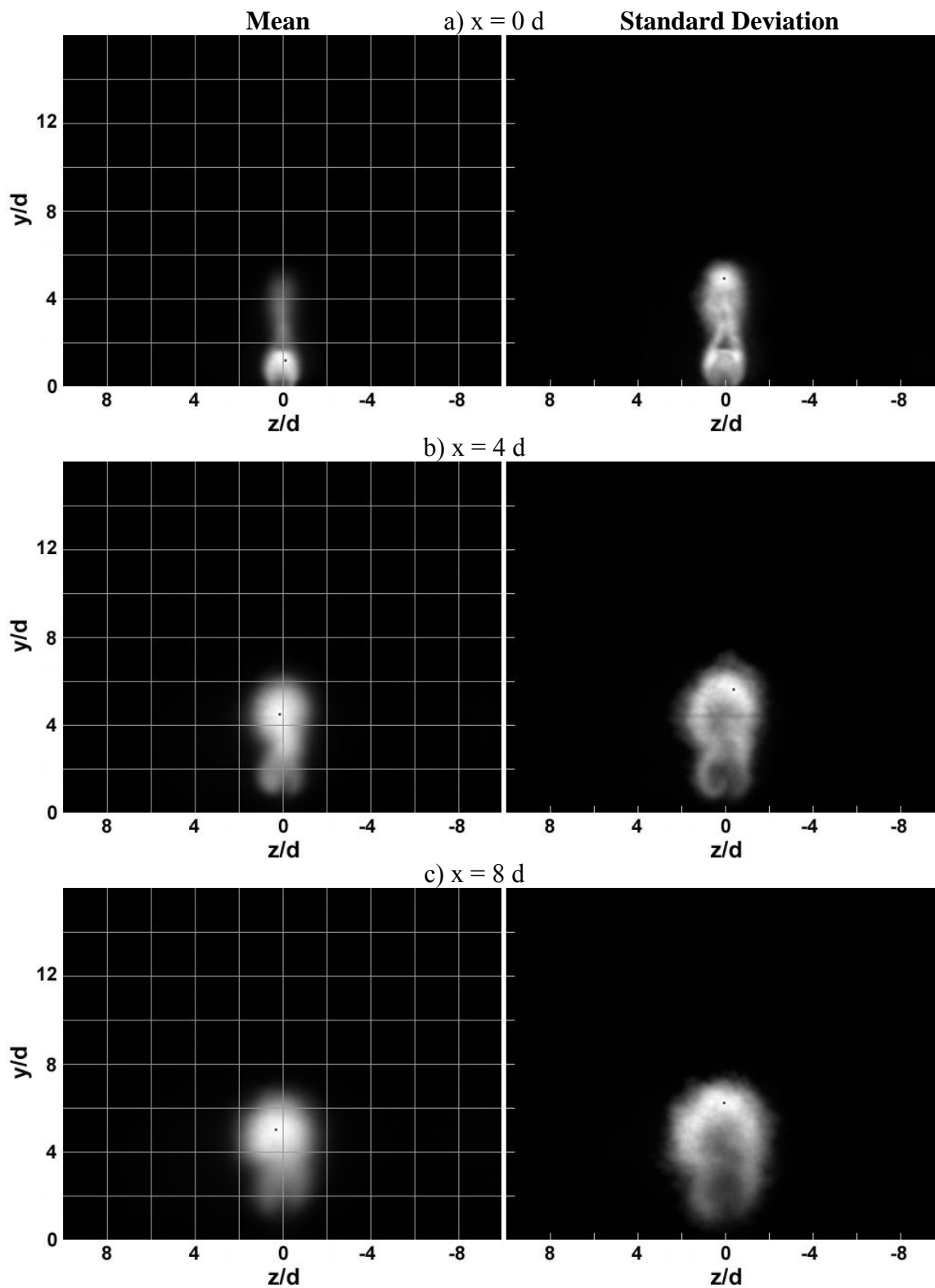**Figure 51.** (W3) NO-PLIF, Wide insert, injection pressure 3, x/d = 0, 4, 8

100

Mean   d) x = 12 d   **Standard Deviation**

e) x = 16 d

f) x = 20 d
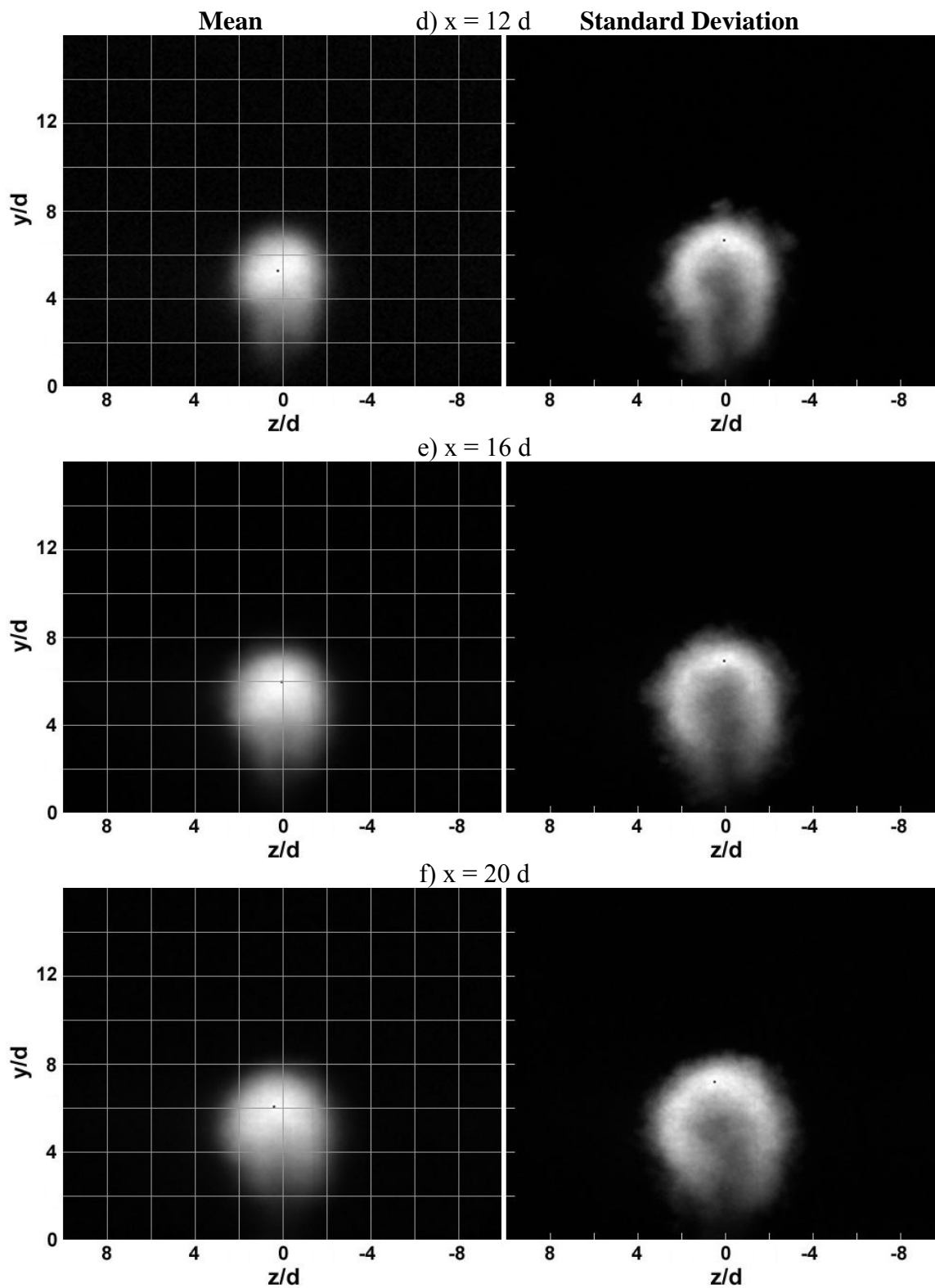
Figure 51 (cont'd). (W3) NO-PLIF, Wide insert, injection pressure 3, x/d = 12, 16, 20

101

Injection behind the Wide pylon exhibits many of the characteristics now established by the Medium and Tall cases. What sets the Wide configuration apart is the rapidness of jet penetration and initial upper area development. Upon injection the jet fluid, as well as the interaction zone, quickly penetrate to a height much higher than the pylon height, and by $x/d = 8$ (Figure 49(c)) the transition from the lower to the upper area begins. As the jet lifts quickly off the floor, it slowly establishes its final form, settling somewhere around $x/d = 24$ (Figure 49(g)). This distance is larger than in the Medium case.

The lower q values yield the same trends. The transition begins at $x/d = 8$ for W2 (Figure 50(c)), which is the same as W1. This occurs very quickly at $x/d = 4$ in W3, shown in Figure 51(b). The fluid settling occurs at $x/d = 16$ for W2 and $x/d = 12$ for W3 (Figure 50(e) and 51(d), respectively). All three injection pressures show the jet transitioning quickly and lifting from the floor, followed by a slow transition to the final form. This is advantageous, for the pylon quickly infuses fuel up into the core flow and then allows it to mix (intensity plots show the most global interaction in the Wide case).

A large floor gap is observed with the Wide pylon. Fuel does not remain in the boundary layer. Once again, this is related to preventing flashback.

An interesting asymmetry is observed in the wide images, as clearly seen in Figure 49(h). Mie scattering images, which will be referenced at a later time, confirm this phenomenon. The most likely explanation is error in fabricating an even injection port or pylon. This is only more confirmed by the shock train images below, which show the same behavior in the Wide case. The discharge coefficient and distance from injection are also noted to be slightly different in the Wide insert.

102

NO-PLIF

END VIEW

BACK PRESSURE

IMAGES

Mean   a) x = 0 d   **Standard Deviation**

c) x = 8 d

e) x = 16 d
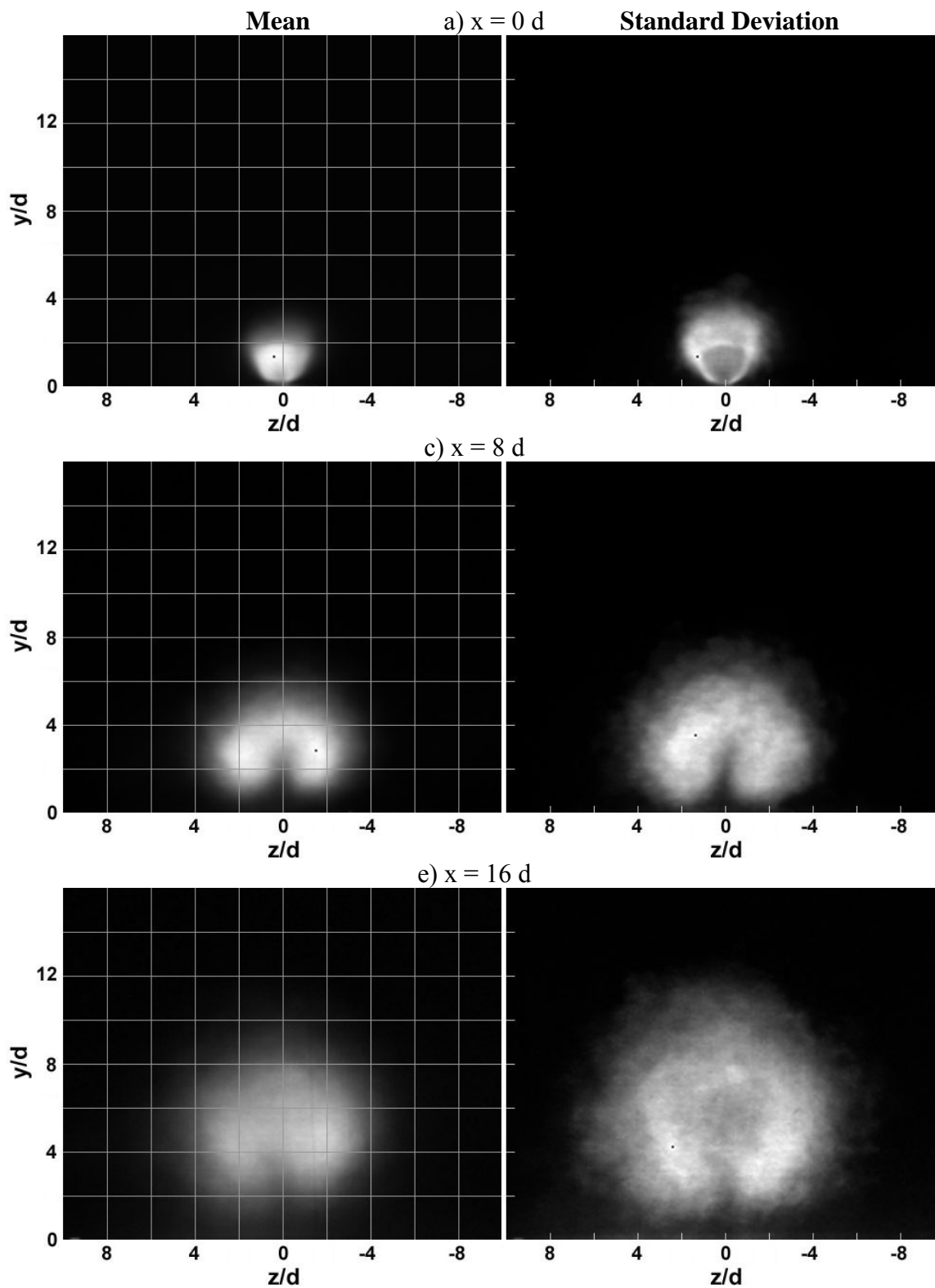
Figure 52. (F2BP) NO-PLIF, Flat insert, injection pressure 2, with shock train

104

Mean a) x = 0 d **Standard Deviation**

c) x = 8 d

e) x = 16 d
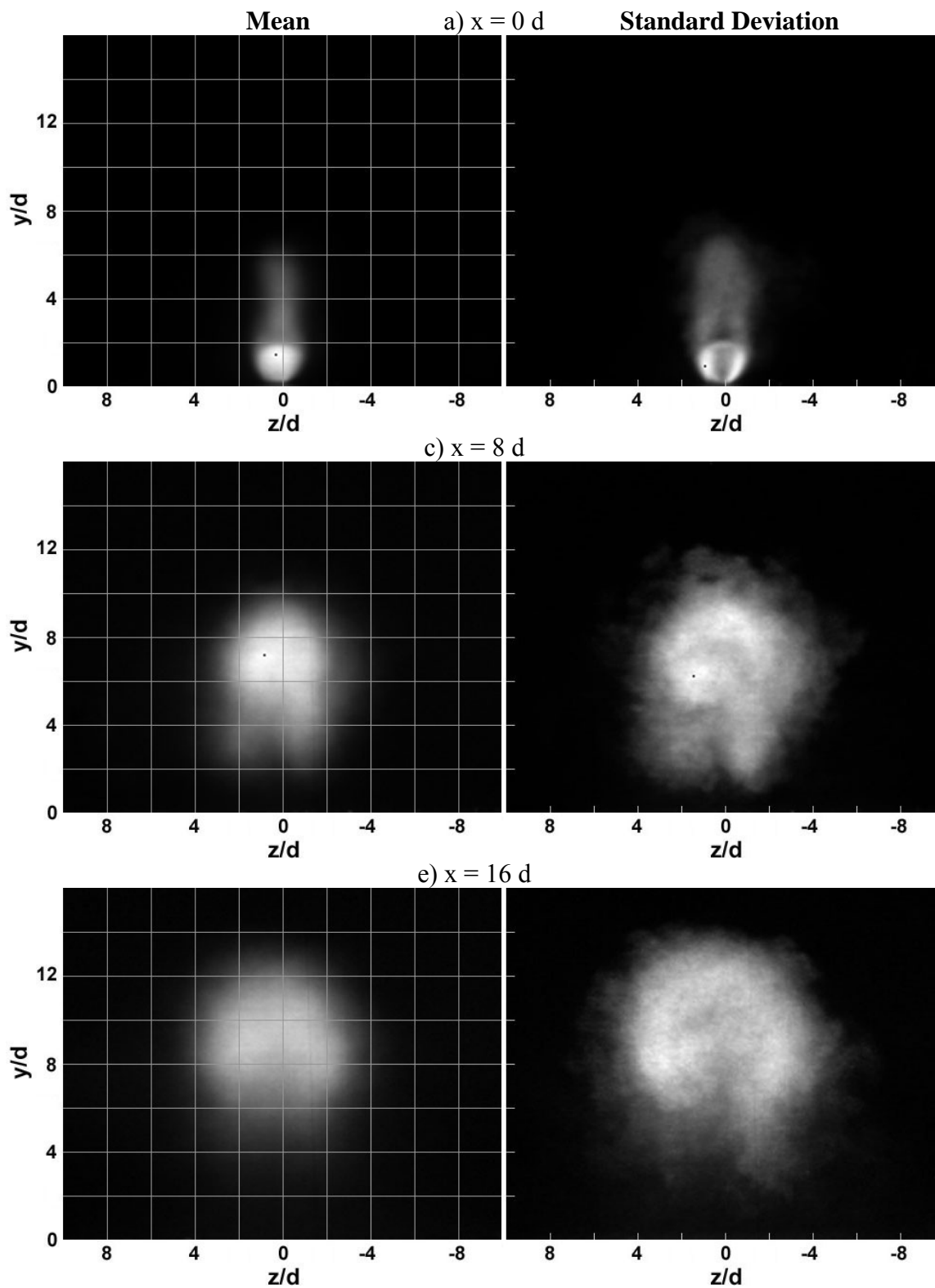
Figure 53. (M2BP) NO-PLIF, Medium insert, injection pressure 2, with shock train

105

Mean   a) x = 0 d   **Standard Deviation**

c) x = 8 d

e) x = 16 d
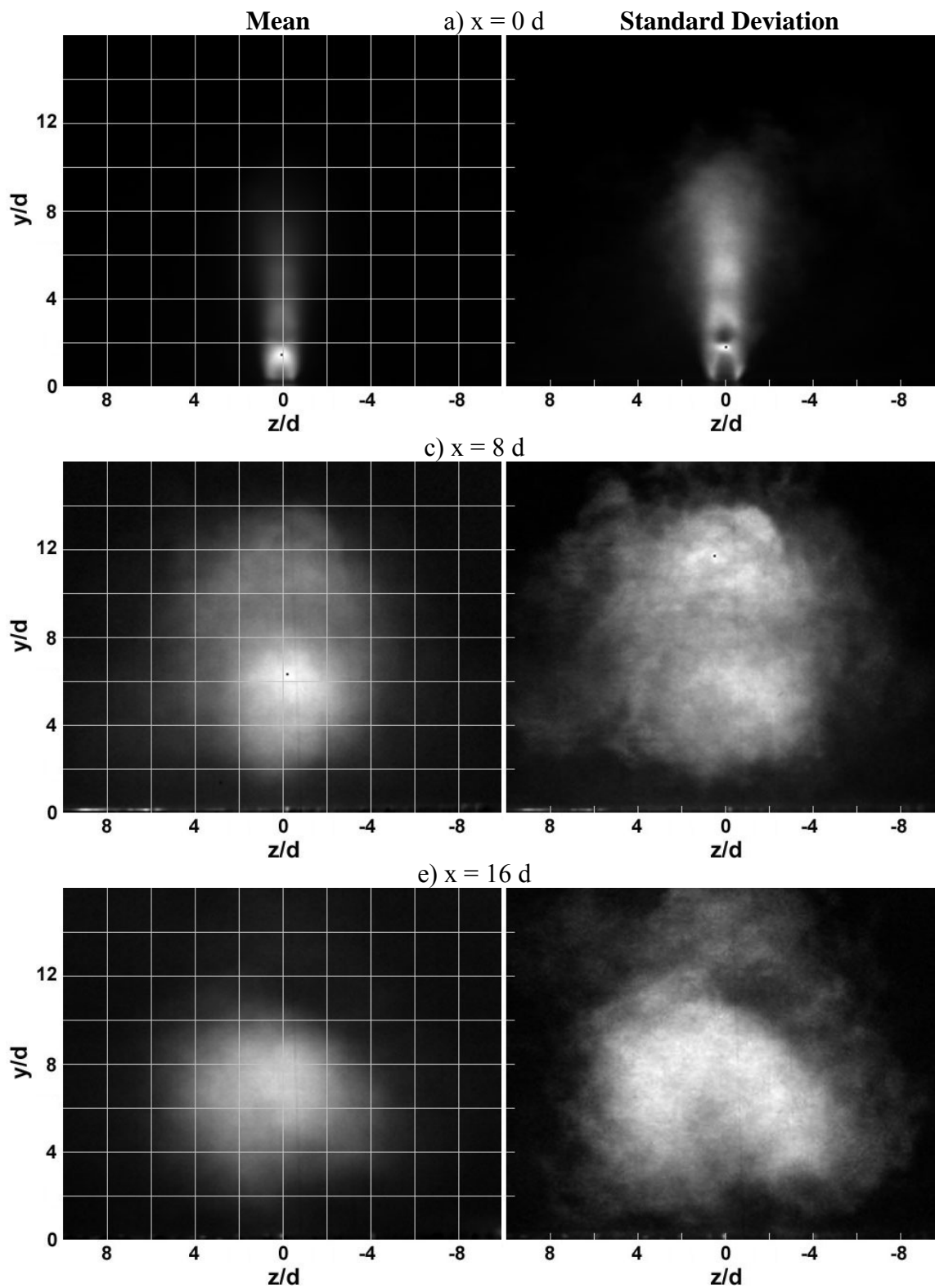
Figure 54. (T2BP) NO-PLIF, Tall insert, injection pressure 2, with shock train

Mean   a) x = 0 d   **Standard Deviation**

c) x = 8 d

e) x = 16 d
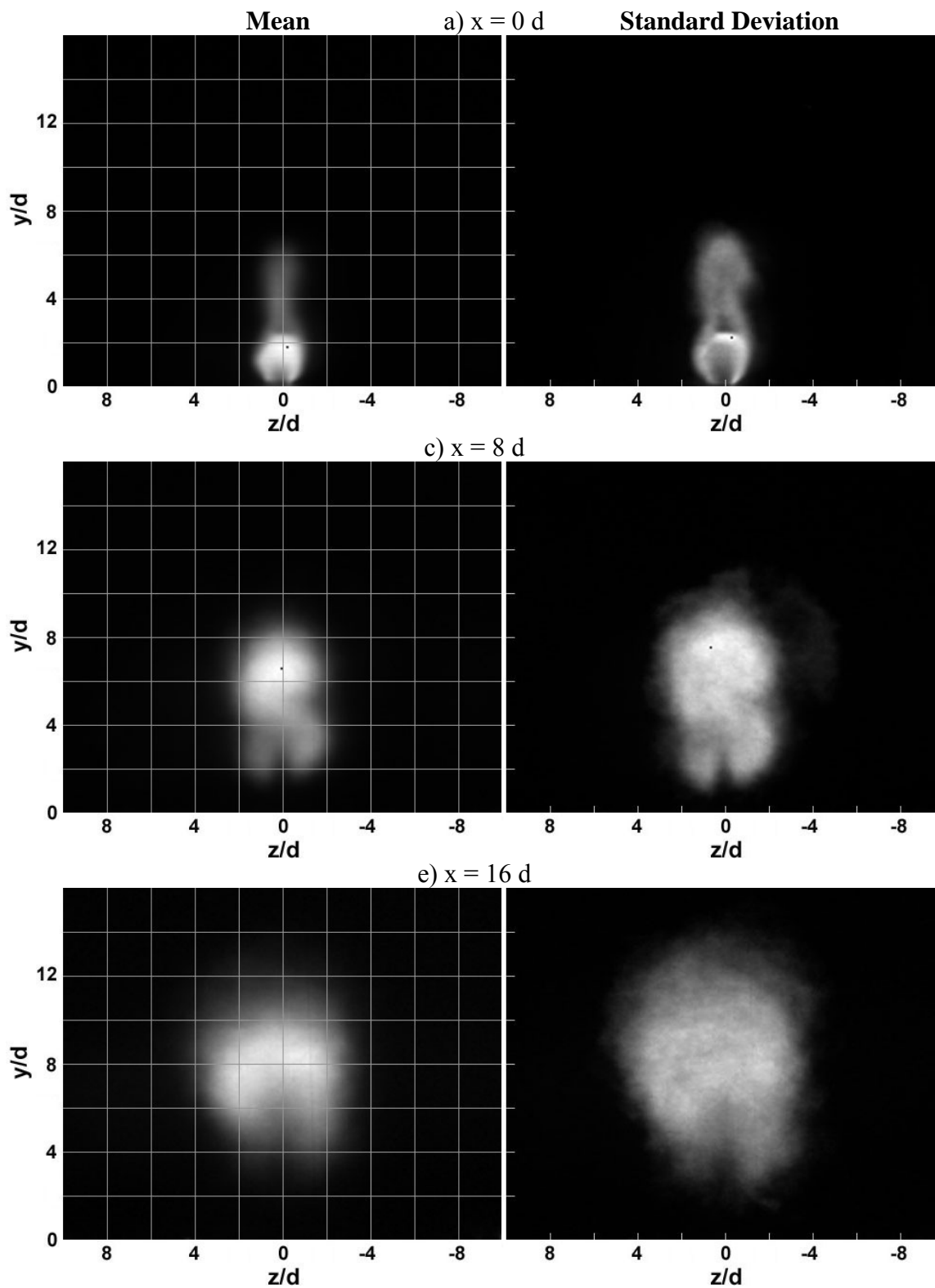
Figure 55. (W2BP) NO-PLIF, Wide insert, injection pressure 2, with shock train

Shock train conditions were simulated with injection pressure 2 (100 psia). An actual value for q was unobtainable for this condition due to the complex nature of this flow and a lack of pressure and velocity measuring capability directly over the injector. The Flat, Medium, and Wide inserts experience the same shock train position. Pressure plots will demonstrate that the beginning of the formation occurs directly over the injection. This region of slightly slower, more turbulent flow causes more dilution and better mixing of the jet fluid. The most noticeable difference in fluid behavior with this condition is the increase in standard deviation activity. The intensity plots show that in general, the fluid concentration and standard deviation strength are of lower values than the non-shock train cases, which means the jet is slightly more diluted and more mixed into the freestream. Within the range of standard deviation behavior, the plumes from the Wide and especially the Medium pylon exhibit much more diverse interaction zones, covering almost the entire extent of the remaining visible fuel jet. The Flat injection contains slightly larger interaction zones as well, but not as high as the pylons.

The Tall case is tested with a higher back pressure, so the shock system is located farther upstream. Pressure plots will show the Tall injection well within the shock train. Within the streamwise distances observed, the intensity plots show more dilution than the other three cases (Figure 34), but the standard deviation intensity actually increases farther downstream (corresponding to the $x/d = 16$ location in Figure 54). The image shows a very large area with a high degree of local interaction. Thus, the complicated flow within the shock train greatly enhances mixing even more so than the beginning of the shock train.

Geometric Comparison of Jet Behavior

Table 4. Pylon versus Flat measurements

		M1	M2	M3	M2BP	T1	T2	T3	T2BP	W1	W2	W3	W2BP
$y_j / y_{j\ FLAT}$	max	1.67	2.03	2.38	1.85	2.06	2.54	2.88	2.31	1.71	2.06	2.35	1.92
	min	1.31	1.42	1.44	1.35	1.49	1.62	1.67	1.37	1.36	1.43	1.49	1.25
$\Delta z / \Delta z_{FLAT}$	max	0.88	0.79	0.82	0.92	0.72	0.70	0.82	1.71	0.76	0.81	0.88	0.79
	min	0.69	0.61	0.66	0.73	0.66	0.55	0.62	0.58	0.70	0.63	0.72	0.66
$A_j / A_{j\ FLAT}$	max	1.13	1.30	1.53	1.36	1.12	1.26	1.42	4.09	1.18	1.40	1.59	1.36
	min	0.90	0.90	0.94	0.88	0.93	0.94	1.02	1.35	0.82	0.91	0.99	0.74
$(A_s/A_j) / (A_s/A_j)_{FLAT}$	max	1.29	0.81	1.27	1.38	1.33	0.86	1.30	1.25	1.43	1.20	0.85	1.16
	min	0.46	0.48	0.46	0.21	0.49	0.32	0.52	0.18	0.35	0.51	0.39	0.19

Data on geometric jet parameters are plotted and presented in this section. Tabulated values for the entire range of testing are found in Appendix F. The plots verify what is determined from the purely visual observations in the previous section. The parameters presented are penetration height (y_j/d), penetration height normalized by pylon height (y_j/h), floor separation (g/d), horizontal jet spread or width ($\Delta z/d$), jet width normalized by pylon width ($\Delta z/W$), 10% or greater visible jet area (A_j/d^2), and 70% or greater local standard deviation fraction (A_s/A_j). A_s/A_j serves to predict the mixing potential for a given location (and its image intensity). Although the value chosen for mixing area seems arbitrary, the important result is the comparison of the mixing to jet area ratio among different inserts. That comparison will show similar trends regardless of the defined mixing area. The jet border is defined at the 10% intensity value for all length measurements. Although the image intensities decrease with streamwise marching (as discussed previously), the local interaction zones can still be characterized on a per image basis.

Figures 56 through 62 contain the plots. After each set a small discussion highlights the pertinent comparisons. Each pylon's maximum and minimum improvement over the Flat case for each injection pressure is presented in Table 4 (these occur at various streamwise locations). In summary, for $q \approx 3.1$, the Tall pylon creates a 105% increase in penetration height and as much as a 34% reduction in jet width. For $q \approx 1.6$, the same pylon causes a maximum y_j increase of 155% and a 45% reduction in width. At $q \approx 0.8$, the Tall pylon causes up to a 190% height improvement and a 38% width reduction. From the standpoint of fuel jet intensifying, the Tall pylon is the most effective, while in the back pressure case it is the Wide pylon. Injection pressure 3

110

exhibits the largest jet height improvement for all pylons. Injection pressure 2 causes the largest width reductions. The Wide and Medium pylons display many similar trends in their maximum abilities. This can be attributed to their physical size being very similar. The Wide pylon is better at providing penetration, whereas it has a slightly lower ability to shrink the lateral spread. Both generally show smaller jet areas and interaction ratios than the Tall pylon (explained later). These maximum and minimum data do not paint the full picture. Further details are discussed with the streamwise plots shown next.

Error in measuring the borders of the images could range up to 10 image pixels when measuring visually.[34] This equates to about 1.7 jet diameters using the NO-PLIF conversion factor discussed in the data reduction section. Using the histogram method of capturing only the brightness values above 10% (or 70% in the standard deviation case), the error reduces to 1 – 2 pixels (0.4 d). The plots are presented without error bars to reduce clutter, noting that all the lines share the same error probability.

(a)

(b)

(c)

(d)
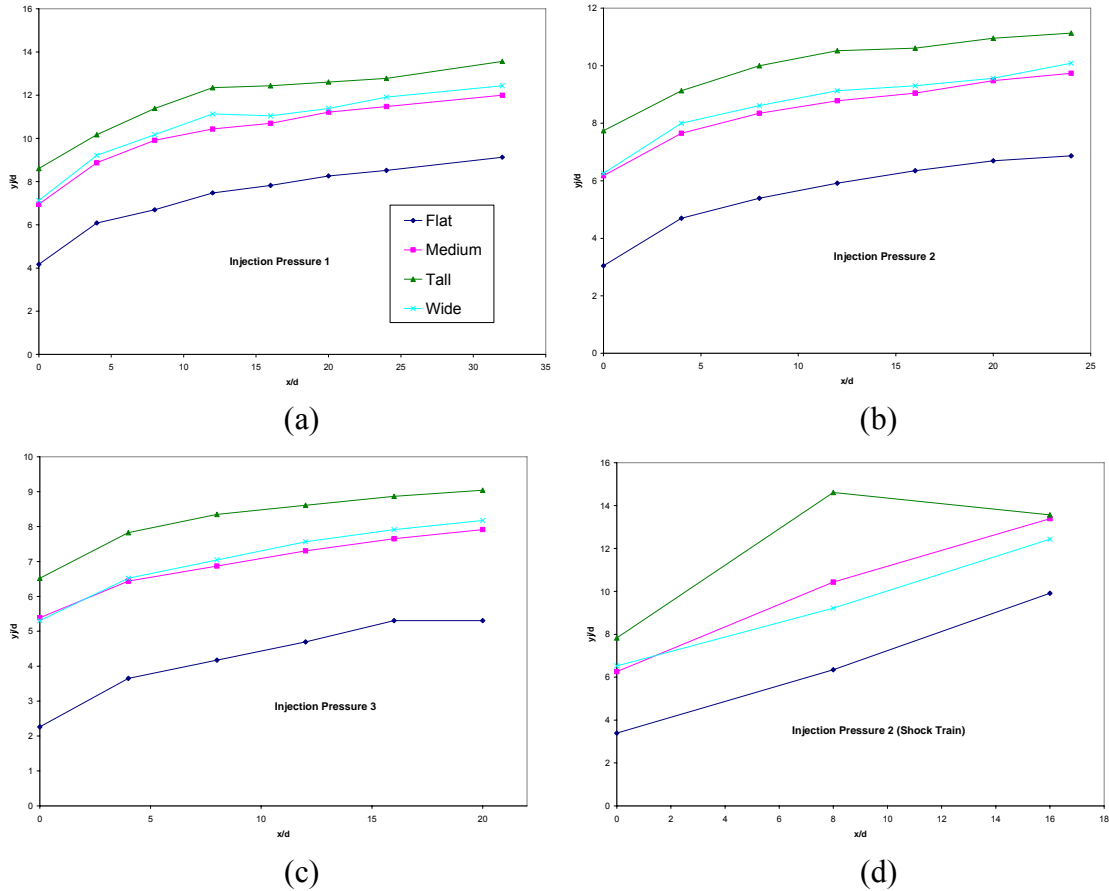
Figure 56. Penetration height (y_j/d) for injection $1 - 3$ and shock train

The Tall pylon shows an overwhelming advantage in pushing the fuel jet into the freestream. The Wide pylon has a slight advantage over the Medium, which actually contradicts the computational predictions by Gouskov et al which would have the Medium pylon providing a slightly higher penetration height.[4] The Tall pylon has a diminished effect downstream in the back pressure case, but as the shock train occurs in a different location than in the other three cases, the Tall pylon will behave differently. All pylons push the jet fluid out higher than Flat injection. Introducing fluid high into the core flow will produce a larger fuel/air mixture over the cavity and may lift the cavity shear layer such as to transfer flameholder energy into the main stream.
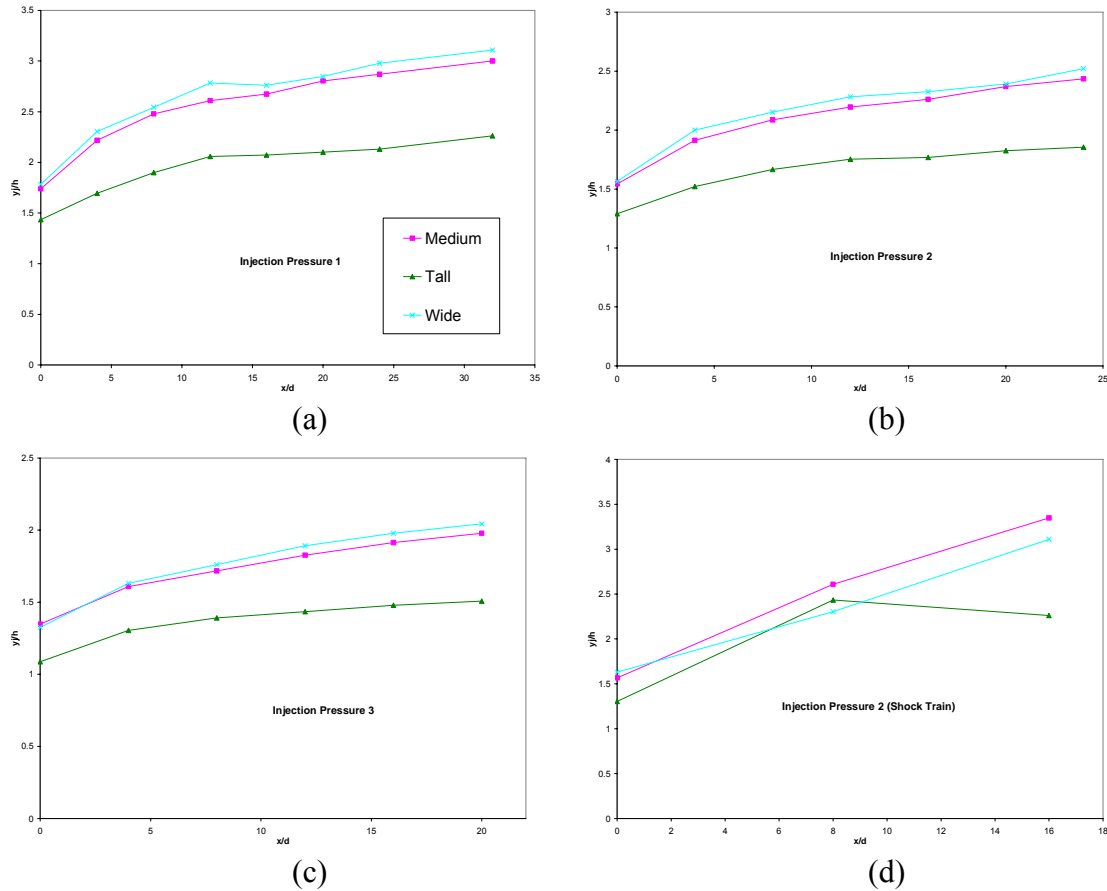
Figure 57. Penetration height with respect to pylon (y_j/h) for injection 1 – 3 and shock train

Only the three pylons are compared with this parameter. The Wide pylon, which is the same height as the Medium pylon, shows a higher self normalized penetration height than its partner, except in the back pressure case. Although the Tall provides more penetration height due solely to its size, design for minimum losses may dictate that a smaller pylon be used that exhibits a better y_j/h. This is more fuel efficient and incurs smaller shock losses. At $x/d = 16$, the Wide and Medium pylons exhibit a self normalized penetration height of greater than 1.5 (the average value observed in previous studies).[2-4] This plot again shows the slight advantage the wide pylon has compared to the Medium pylon, which makes it a better choice given they produce similar losses.

113
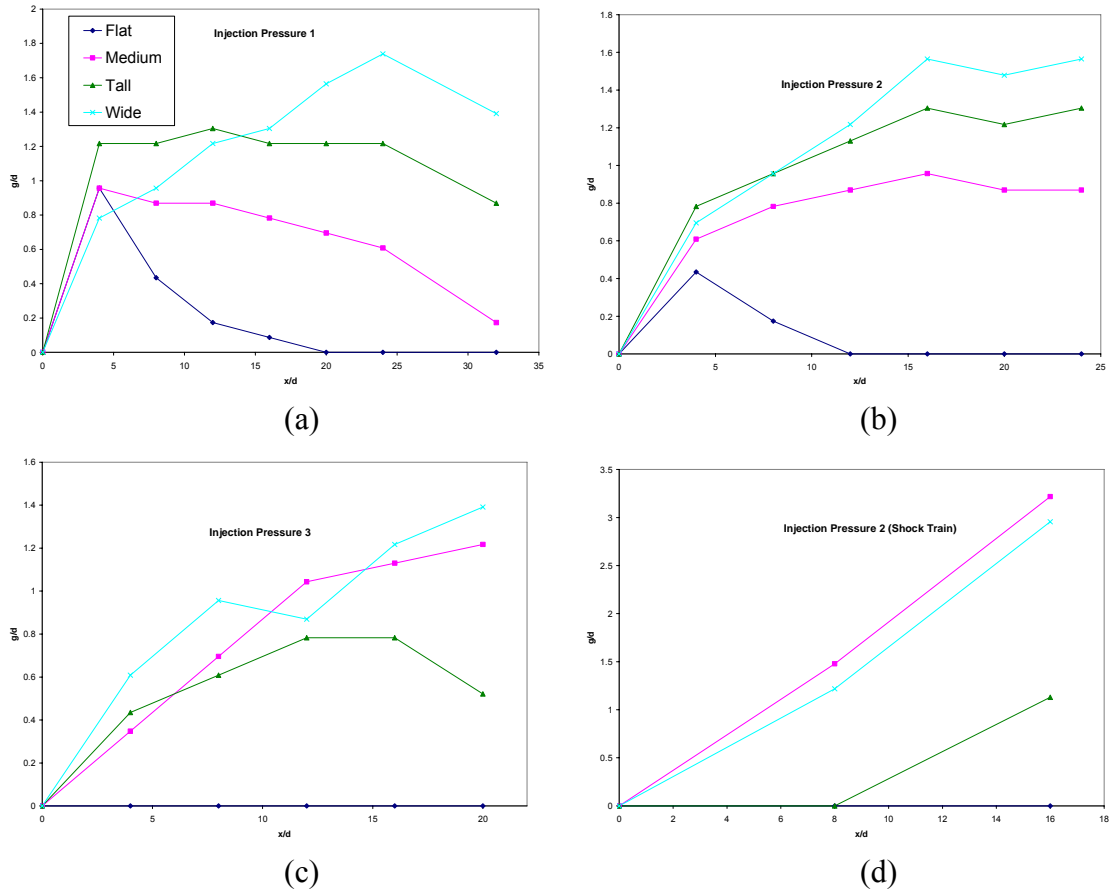
Figure 58. Floor gap (g) for injection 1 – 3 and shock train

Although visually the Flat case appears to lift much of the fuel completely away from the boundary layer, calculations based on the 10% max intensity consideration show that the effective floor gap is completely zero for the F3 and F2BP cases. The jet lifts initially with the higher two injection pressures but then loses its gap farther downstream; this does not guarantee flashback prevention. The Wide pylon is the most effective lifter. The Tall pylon loses its effectiveness as injection pressure is decreased, while the Medium loses effectiveness at higher q values. Both the Medium and Wide pylons exhibit similar lifting characteristics with a shock train present, while the Tall loses effectiveness. All the pylons provide good lifting mechanisms due to cross-stream shear.

114
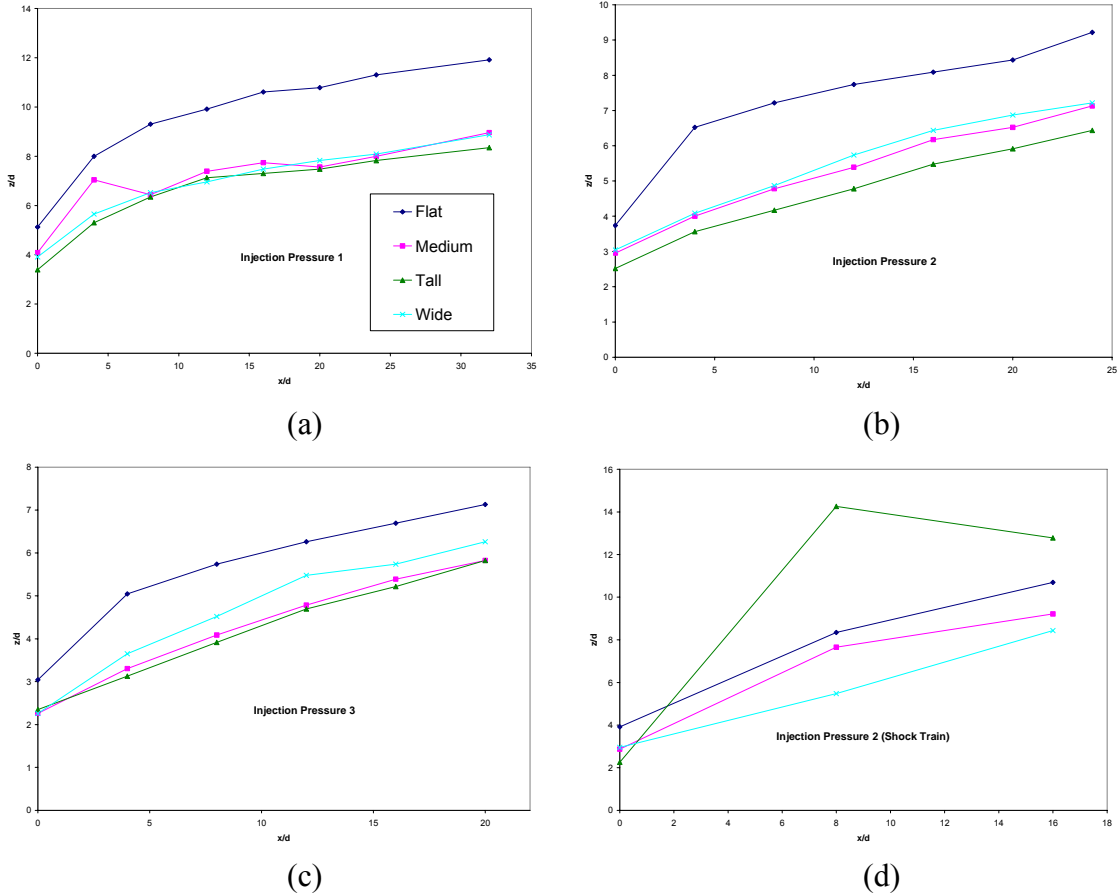
Figure 59. Width ($\Delta z/d$) for injection $1 - 3$ and shock train

Combined with plume height, width affects the area in which mixing potential may exist. The Wide pylon produces only a slightly greater plume width, and only at lower q values. The pylons all distribute the fuel vertically and do not allow it to remain spread out. The Wide pylon shows its influence in the visual images, where its width prevents the free stream from causing the larger vortices seen in the thinner pylons. The Tall pylon provides the thinnest spread, which corresponds to the jet being spread more so along the vertical (y) axis. The Flat case, although it is not able to achieve the same penetration height as the pylons, visually shows a jet that is concentrated on the lower outer boundaries, giving it a larger horizontal spread.

115

(a)

(b)

(c)

(d)
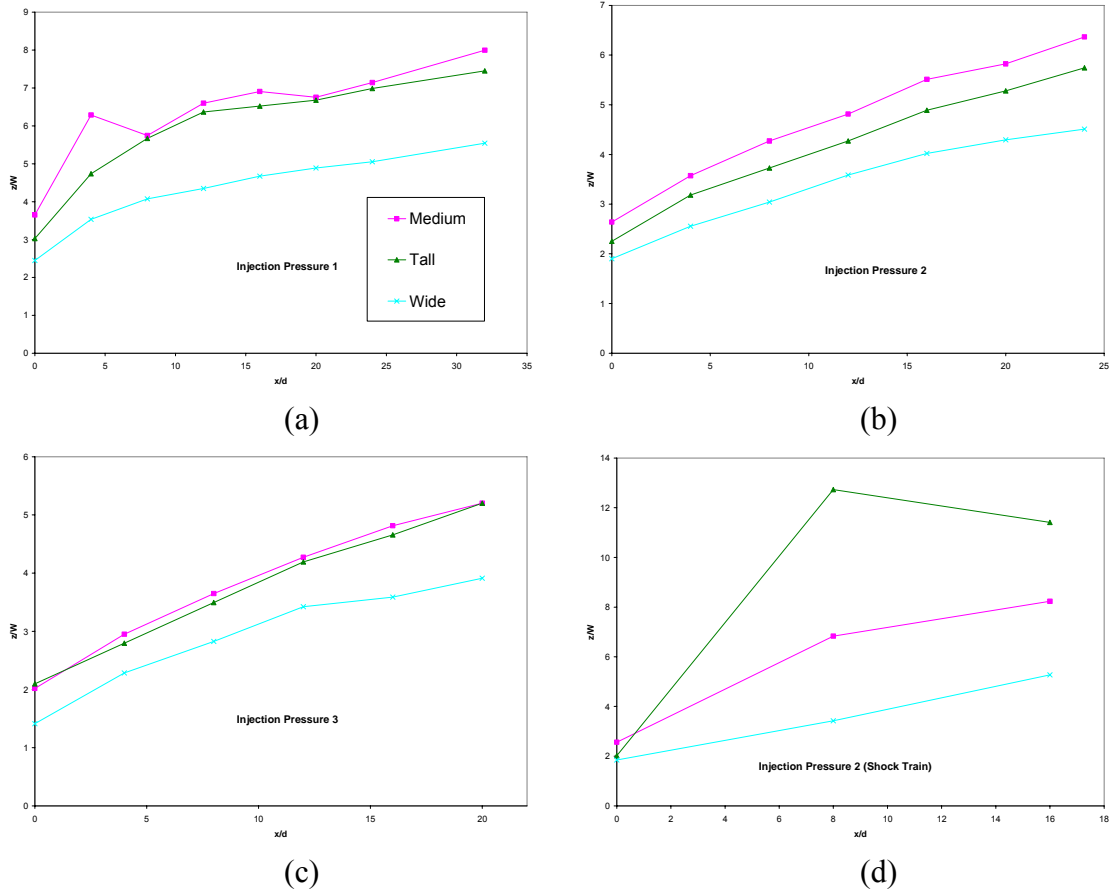
Figure 60. Width with respect to pylon ($\Delta z/W$) for injection $1-3$ and shock train

Normalizing jet width by pylon width results in the Medium pylon having a slight advantage over the Tall pylon in this measurement (both are the same width). This confirms that the Tall pylon distributes fuel more vertically. The wide pylon also lifts fuel into the upper area and does not allow it to spread very much in the spanwise direction. Less of the injected fuel is directly exposed to the freestream, allowing it to penetrate and lift off the floor more than in the other pylons.
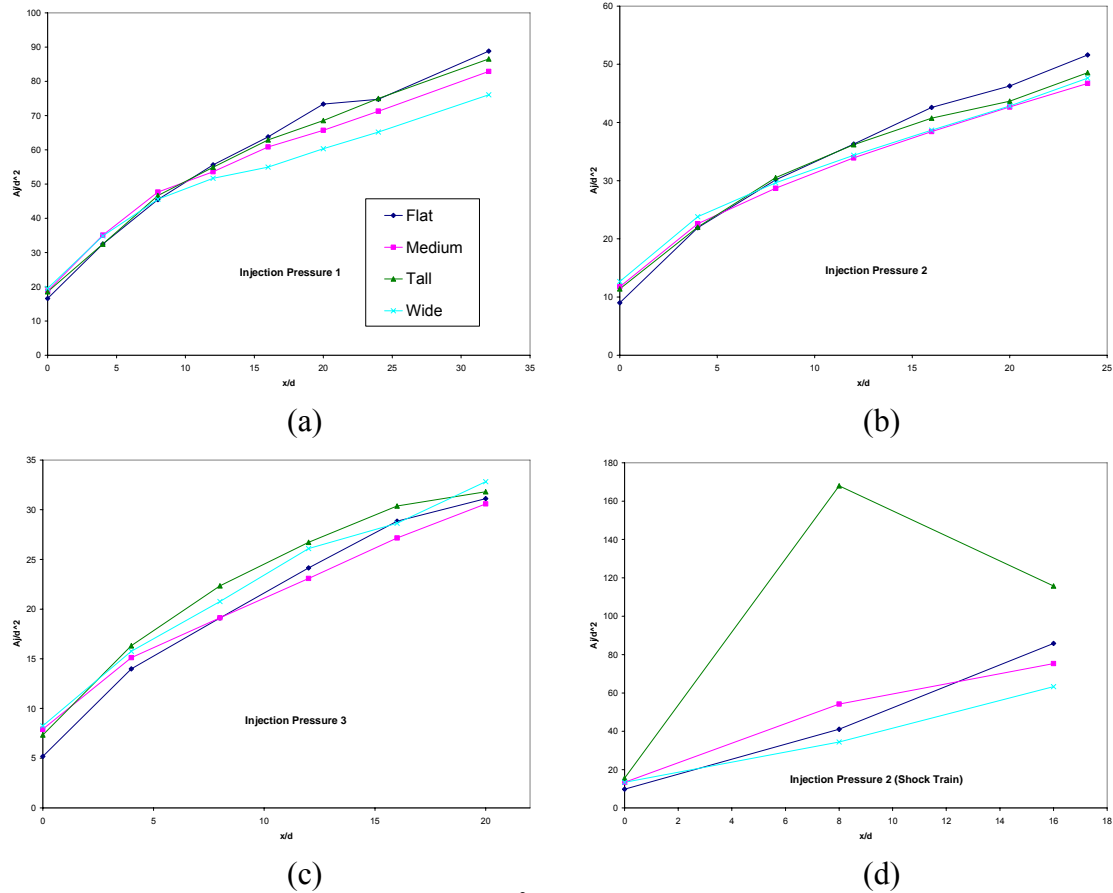
Figure 61. Jet area (Aj/d^2) for injection 1 – 3 and shock train

The measurement of jet area is one composite means to qualitatively predict mixing potential.[34] Intensity results show that the jet is fairly equally diluted into the freestream for all four geometries. At the two higher injection pressures, the Flat case has a larger area than the pylons. The Tall pylon provides the best area of the three pylons, and it overcomes the Flat injection at the lower q, as does the Wide pylon. The back pressure plot demonstrates how the location of the shock train greatly influences the spread and presence of the jet. Because the pylons have less local area but more global interaction (as intensity plots show), it can be supposed that fuel is also mixed into the freestream beyond the scope of the image. The next plots show the local interaction.

117
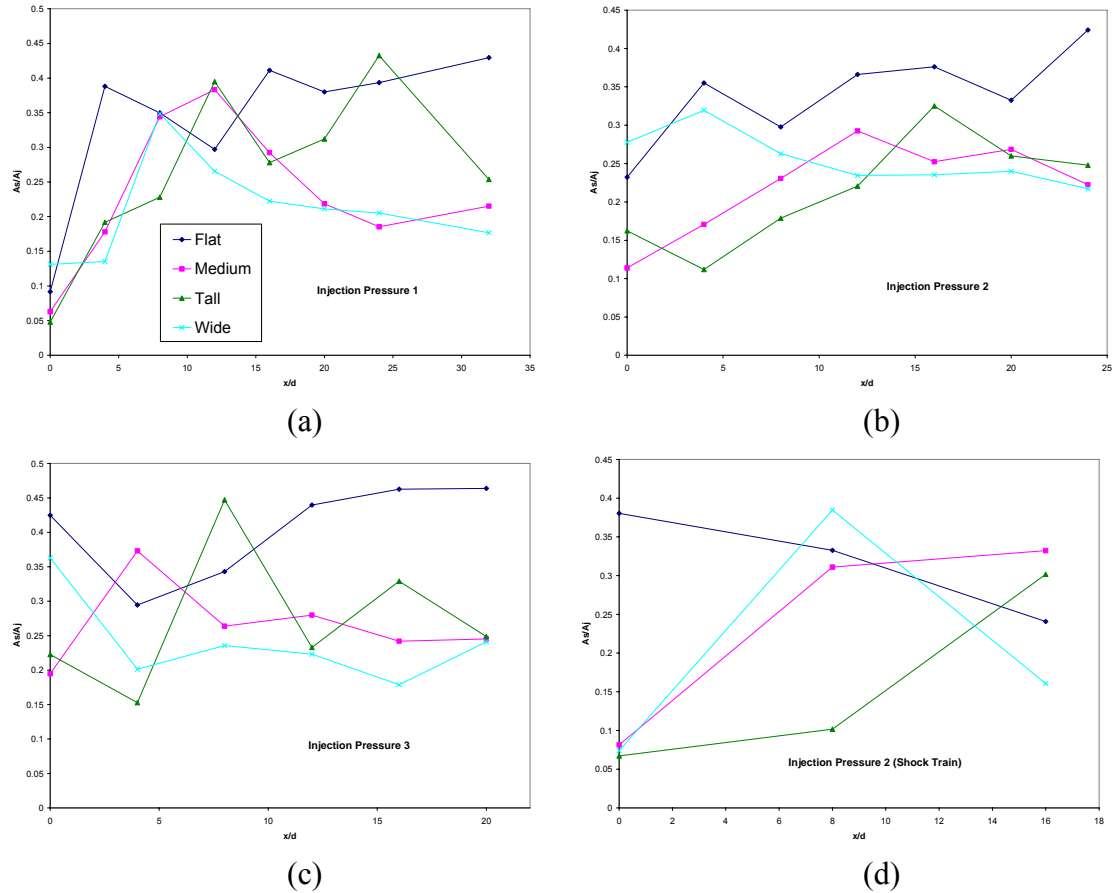
Figure 62. Local standard deviation area fraction (A_s/A_j) for injection 1 – 3 and shock train

The area of high standard deviation (defined as 70% or greater max intensity) varies for the different cases. Flat injection shows a slightly greater local interaction (and area). According to intensity results, the standard deviation normalized intensity is higher for the three pylons over the Flat case at x/d > 16, and injection pressure 1 gives the pylons more normalized standard deviation at x/d = 4. At the lowest and highest injection pressures, the Tall pylon is close to the local capability of the Flat case. At x/d > 16, the Tall pylon outperforms the other two other pylons. None of the pylons exhibit as strong a vortex generation as the Flat case in the images. This results in lower standard deviation in the above graphs. More fuel is exchanged with the freestream.

118

Mie Scattering Results and NO-PLIF Profile View

Appendix G contains supplemental Mie scattering images (instantaneous images in Figures G1 and G2 and end view images in Figures G3 through G14). The raw images display the highly turbulent structures where the jet interacts with the freestream; the unsteadiness of the small bow shocks is also evident. The mean and standard deviation end view images follow many of the same trends as the NO-PLIF images discussed above (including the skew observed in the Wide case), with the addition of visualizing the multiple small shocks that form around the jet and the pylons. Also visible is the boundary layer, which takes the form of a darker region along the section floor, due to viscous effects which affect ice crystal concentration. The thickness of the layer ranges around $1 - 2$ d, and as the NO-PLIF images confirm, the jet fully penetrates through it.

Shock Heights

The Mie scattering end view images show the development of two (sometimes three) shock formations as the image marches downstream. Table 5 displays the heights of the first two shocks for each case, based solely on visual estimation from the end view images. The upper (I) shock emanates along the pylon edge, as profile images will demonstrate. In the Flat case, this shock corresponds to the coincident bow shock that injection into the direct freestream creates. A secondary shock (II) begins to form around the jet boundary and becomes observable around $x/d = 8 - 12$. Shock widths were not measured due to a camera range that was too small to observe their full spanwise extent. The small range also resulted in some of the heights being unreadable in the larger shock (I) for injection pressures 1 and 2. T3 did not have Mie imagery collected at $x/d = 20$.

Table 5. Shock heights measured from Mie end view images

x/d	F1 I	F1 II	M1 I	M1 II	T1 I	T1 II	W1 I	W1 II	F2 I	F2 II	M2 I	M2 II
0	6.5		9		10.5		9.5		5		8	
4	11		12.5		14		13.5		9		12	
8	14.5		16		17.5		16.5		12.5	5	15	7
12	18.5	7.5	19	9	20.5	9.5	20	9	16	7.5	18	9
16	21.5	9.5	22.5	11	23.5	13	23	12	19.5	10	21	11
20		11.5	25	14.5		14		14	23	12	24	13.5
24		14.5		16.5		16.5		16	25	14		15
32		19		20.5		21		20				

x/d	T2 I	T2 II	W2 I	W2 II	F3 I	F3 II	M3 I	M3 II	T3 I	T3 II	W3 I	W3 II
0	10		8		4		7		9.5		6	
4	13		12		8		10.5		12.5		10	
8	16		15.5	7	11.5	5	14	6.5	16		13	7
12	19	9	18.5	9	14.5	7	17	8.5	18.5	9	16	8.5
16	22	11	21.5	11	18	9.5	20	10.5	22	11	20	10.5
20	24.5	13	24	13.5	21	12	23.5	13			23	13
24		15.5		15.5								

The Medium and Wide pylons create shocks that are slightly stronger than the Flat case. The lower the injection pressure (3 being the lowest), the farther away from Flat values they become. For injection pressures 1 and 2, the Wide pylon creates somewhat stronger shocks (than the Medium), and at injection pressure 3 the Medium creates the stronger shocks. The Tall pylon generates the largest shock heights for all

120

injection pressures. Based on only this data, the Tall pylon may not be a desirable geometry due to the overwhelmingly larger shocks it creates compared to the no pylon instance.

Profile Views

The following images are taken from the profile configuration, and each shows the general development of the jet in one picture. Figures 63 through 66 show the comparison in shock formations between the F1, M1, M3, and M0 conditions. The M0 case (Figure 63) displays some small but prominent shocks forming in the area of the pylon. Most noticeable is a shock continuing off the upper tip of the pylon and remaining at roughly the same angle as the pylon (~30°). This is termed shock I in the previous section.

When fuel is injected at the low q value, it has no effect on the development and merely remains behind the tip shock. When fuel is injected such as in the F1 case (Figure 65), the resulting shock is higher than the pylon alone or the pylon with injection pressure 3. When the M1 case is applied (Figure 66), the fuel causes the tip shock to rise to approximately the same height as in F1 (actually slightly higher as Table 5 shows). Thus, almost the same shock system occurs in F1 and M1, while M1 provides more fuel penetration. These approximate shock heights correlate with the Mie scattering end view images. Knowing that the Wide case produces similar shocks to the Medium pylon and similar penetration heights, both these options appear suitable over the Tall pylon.
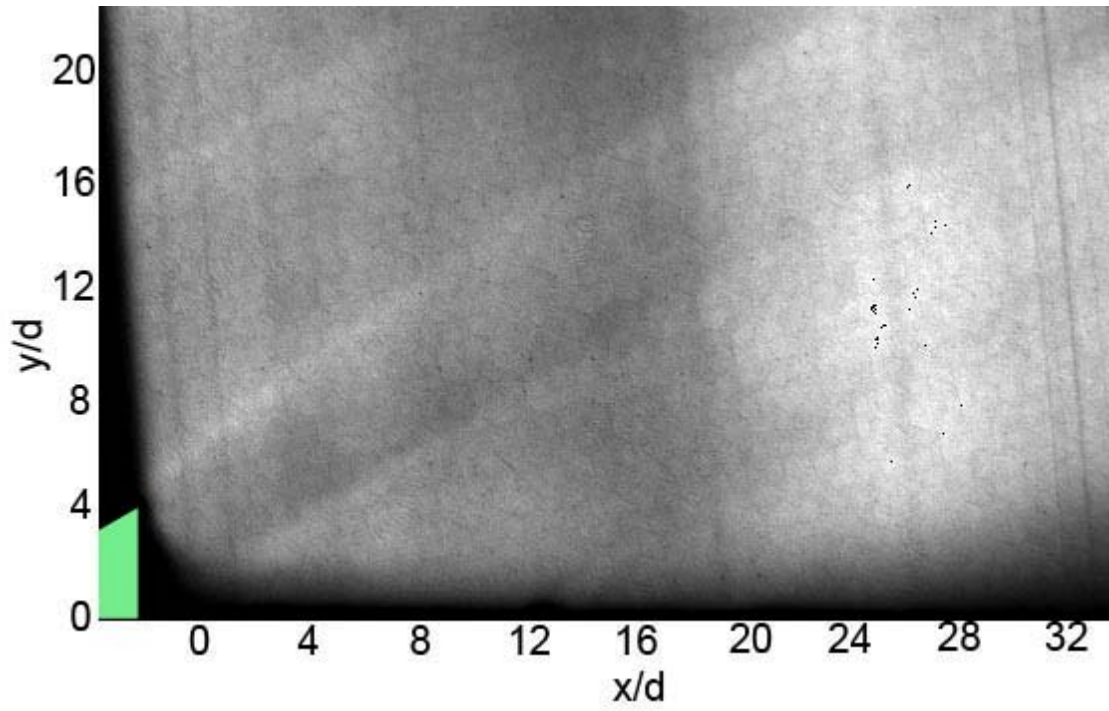
Figure 63. M0 case, Mie scatter profile view
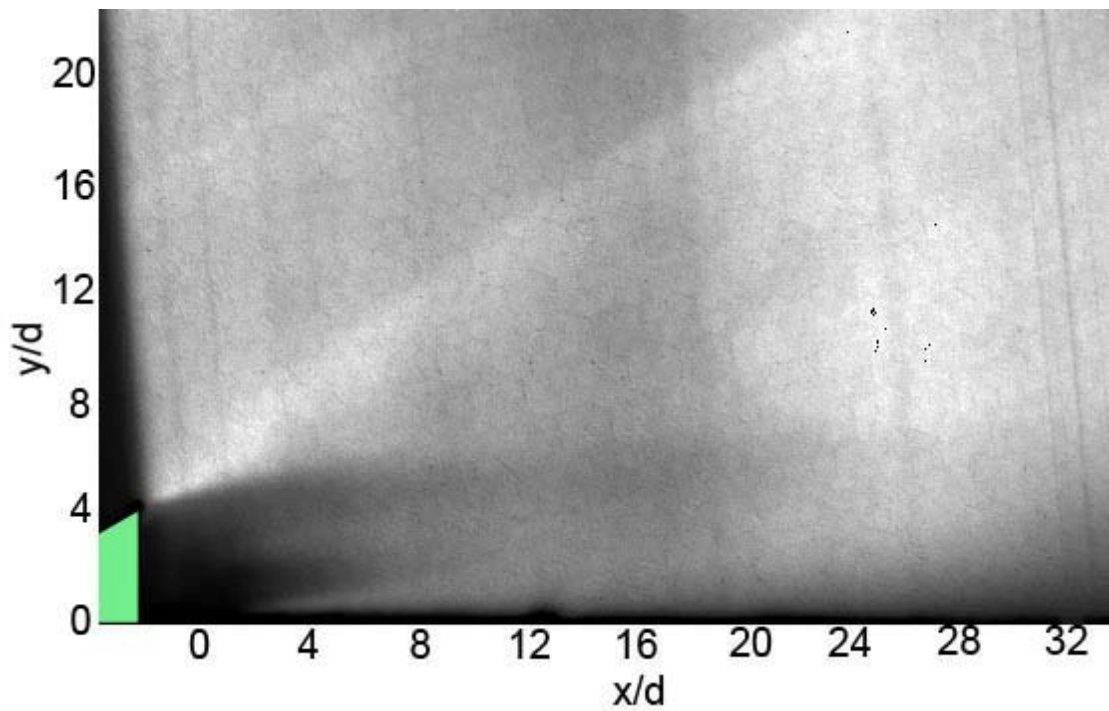
Figure 64. M3 case, Mie scatter profile view
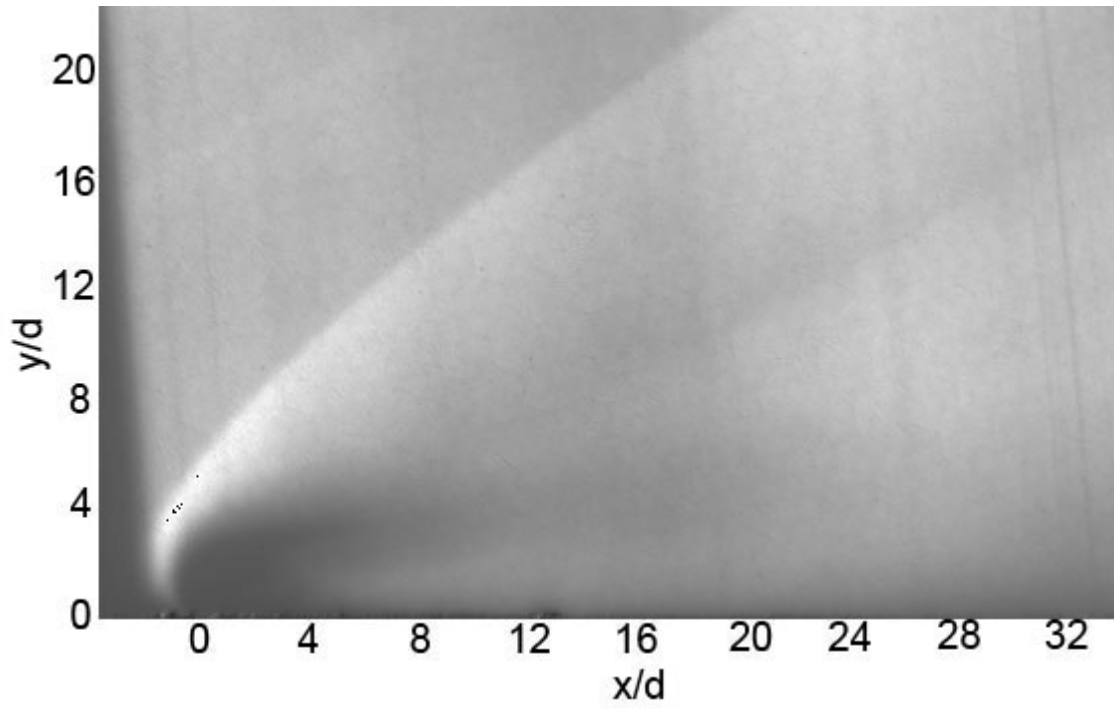
Figure 65. F1 case, Mie scatter profile view
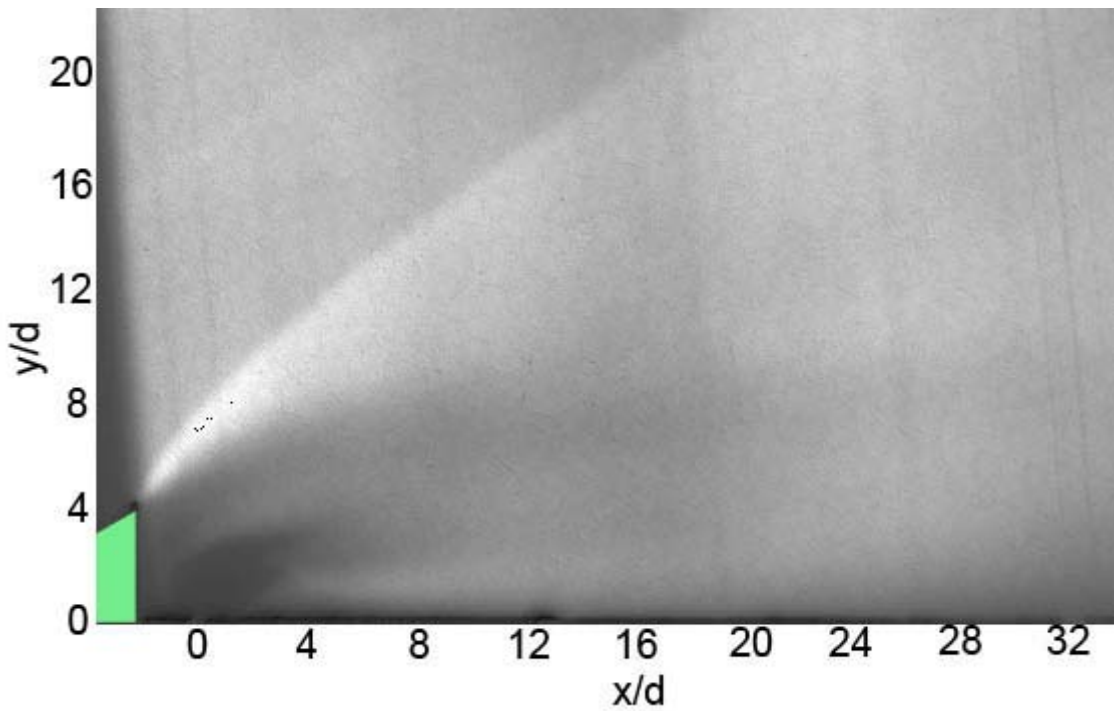
Figure 66. M1 case, Mie scatter profile view

123

The NO-PLIF profile views (Figures 67 through 72) provide a visual representation of intensity reduction as well as a side-by-side comparison for penetration height between the Medium and the Flat injection. The Flat image correlates with other studies that observe similar jets under the same imaging methods.[40] The barrel shock and mach disc are visible and can be compared to Figure 6. The pylon injection closely resembles the trend observed in liquid jet pylon studies.[2] The fluid is lifted beyond the height of the pylon and eventually settles at a certain height. This higher presence of fuel may interact with the shear layer over the cavity, but current data cannot support any hypotheses concerning actual shear layer behavior. For all three injection pressures, the pylon case outperforms the no pylon case by a noticeable margin.

The largest improvement in penetration height in these examples is in the M3 case (Figure 72). Visually there is a clear improvement of over 100%. Table 4 confirms this with a maximum value of 138% increase.

Shocks are barely visible in these profile images, both averaged and raw (see Appendix F for raw image). This occurs because the UG-5 filter employed for NO-PLIF does not completely block out all the scattering at 226 nm. The shocks that are clearly visible in the Mie images therefore make themselves slightly apparent in the PLIF pictures.
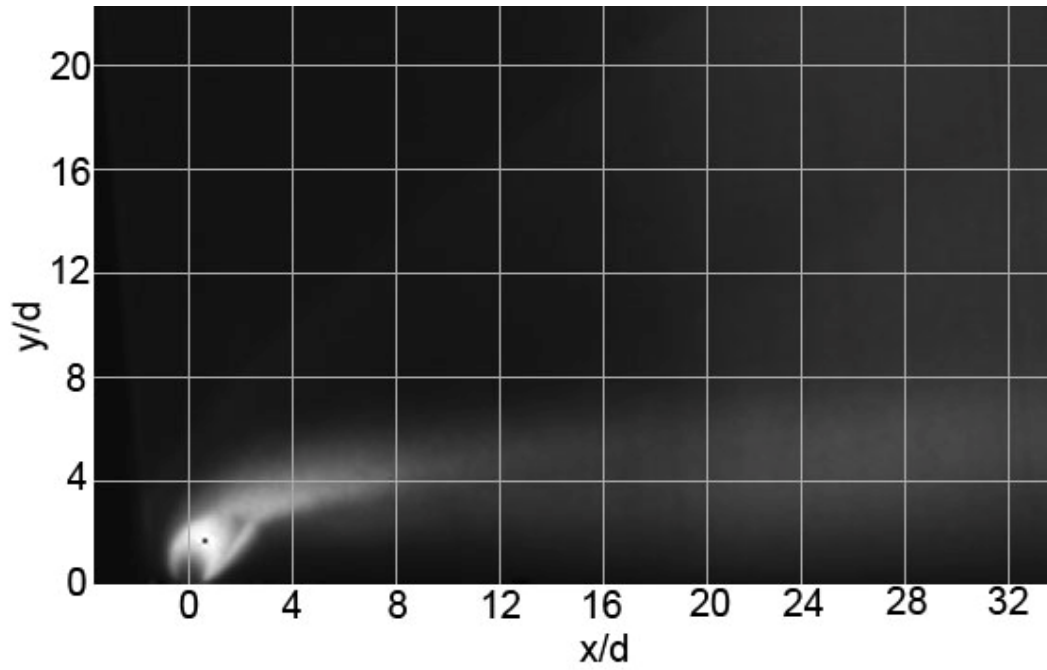
Figure 67. F1 case, NO-PLIF profile view
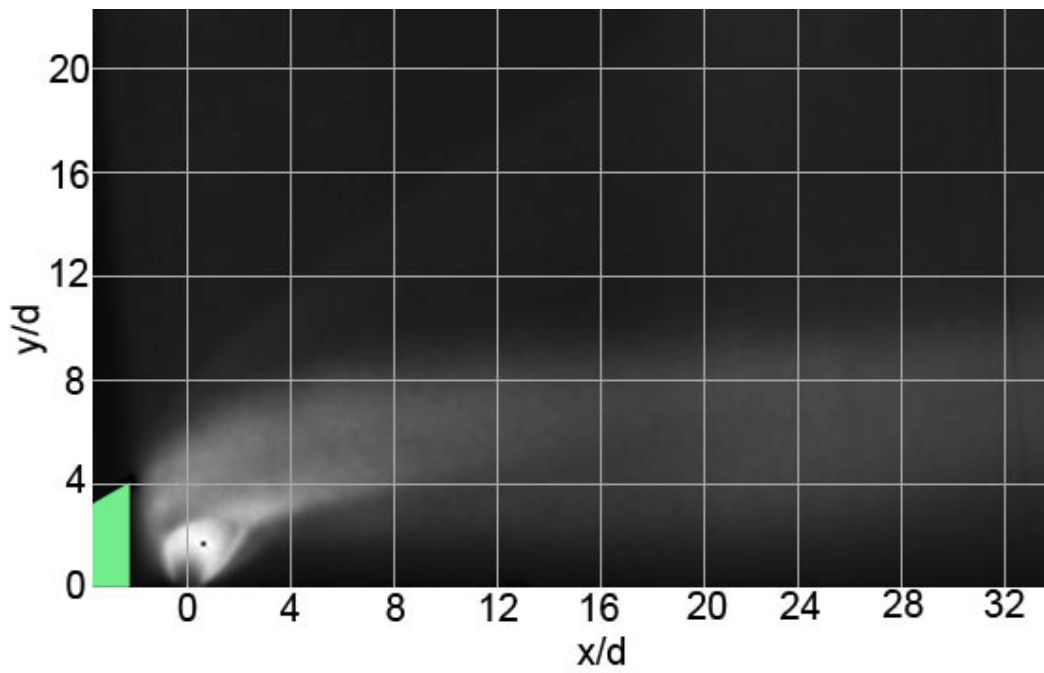
Figure 68. M1 case, NO-PLIF profile view
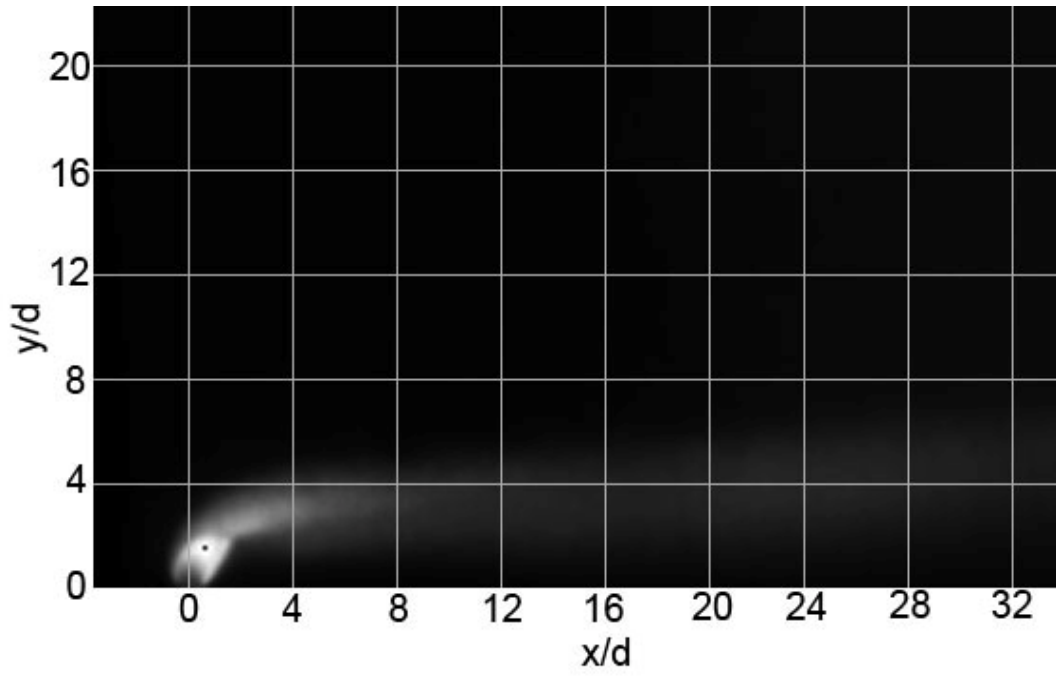
Figure 69. F2 case, NO-PLIF profile view
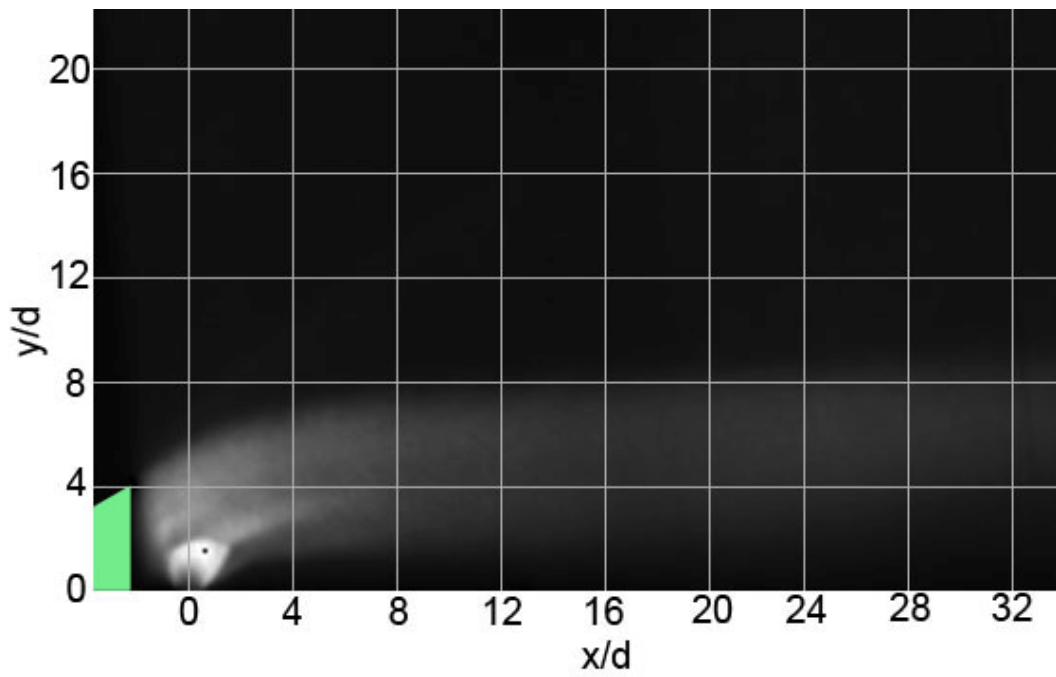
Figure 70. M2 case, NO-PLIF profile view
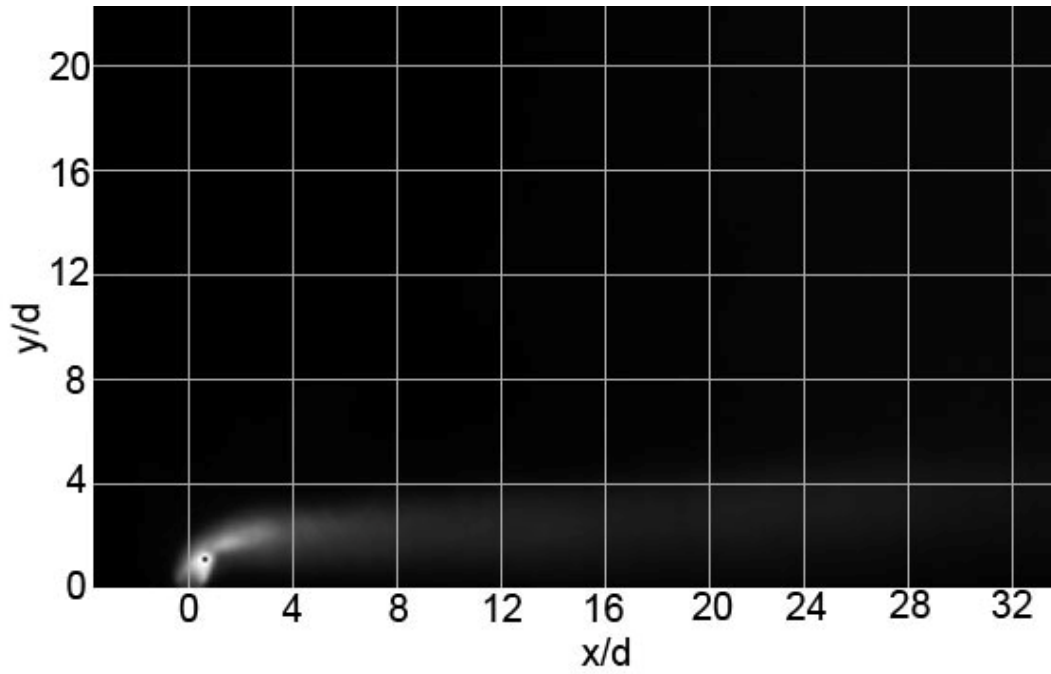
Figure 71. F3 case, NO-PLIF profile view
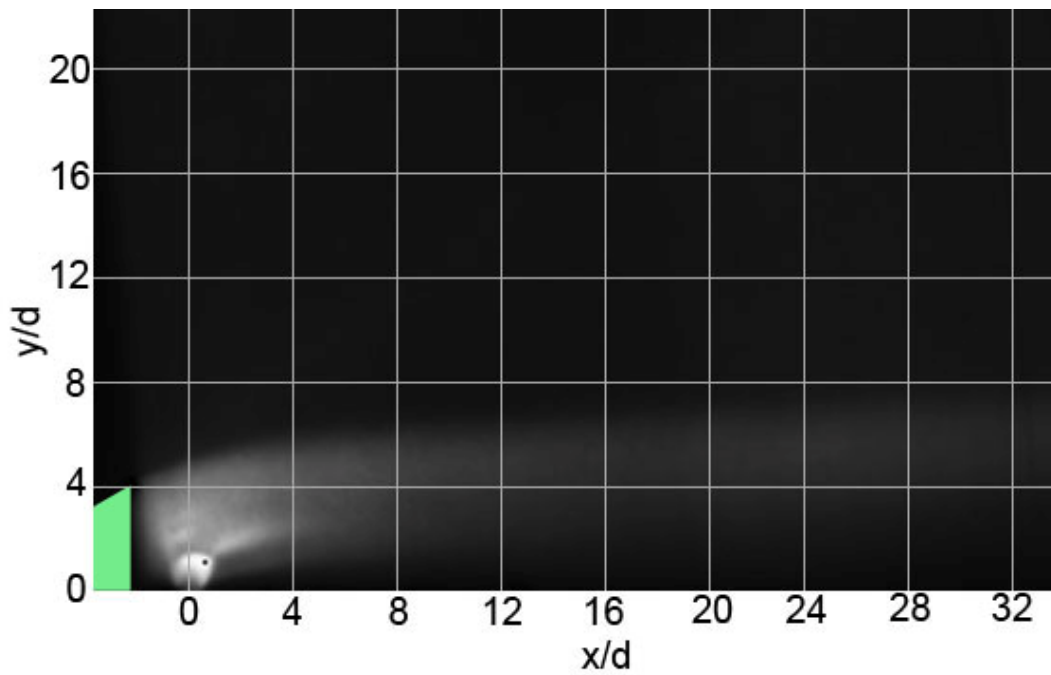
Figure 72. M3 case, NO-PLIF profile view

Wall Pressure Data

Graphs of wind tunnel wall pressure are presented as Figures 73 through 82. They represent the static pressure captured by the taps in the top and bottom walls of the test section. The test section floor is sketched in all the graphs, highlighting the location of the cavity and pylon in each case with respect to the taps. Reference data for the plots is found in Appendix H.

Injection both in the Flat case and behind pylons has a large effect on the floor pressure downstream of the injection site, as seen by comparing Figure 73 with the other plots. While bottom wall tap #6 shows an increase in baseline static pressure right before the flow reaches the cavity, the injection cases cause this pressure to drop and remain relatively lower over the cavity. The same effect is carried through the cavity region and seen downstream of the cavity in bottom tap #11, which also has a marked decrease in static pressure when injection is used.

Injection results show that the top wall taps of interest are #11, #12 – #14, and #16. For any given insert, static pressure is injection pressure independent until tap #11 (located at $x/d = 38.5$, approximately over the 90 degree cavity step). Here the tap shows a higher static pressure at the injection 1 case ($q \approx 3.1$). Over the cavity (taps #12 – #14), injection 2 and 3 ($q \approx 1.6$ and 0.8 respectively) become dominant in increasing static pressure, with injection 1 having the lowest effect. At tap #16 ($x/d = 118$, beyond the cavity), injection 1 again produces the highest static pressure. When comparing different inserts, the cavity area is also of interest. For injection 1, tap #11 (at the cavity leading edge) experiences the highest static pressure increase with the T then W insert, followed

by a smaller effect by the M then F configuration. Injection 3 sees the inserts having an effect in the opposite order (F, M, W, T), but this time over the cavity at tap #12. Injection 2 shows consistent static pressures in front of and over the cavity that are independent of the insert chosen. For all three injections, tap #16 exhibits the original dependence observed in tap #11 (static pressure increases in the progression F, M, W, and T). To summarize, the areas over the front cavity step and also downstream of the cavity experience higher static pressure with the Tall (and Wide) inserts and at q equal to 3.1, while the areas over the main cavity have a higher static pressure increase from the Flat insert at the lower q values. These observations may be related to bow shock effects on the top surface.

The bottom wall individual taps of interest (noting that tap #5 is disconnected in the installation diagram and thus does not appear on the plots) are #9 – #10, #15 – #16, and #19 – #20. The first observation is that there is hardly any dependence on the type of insert along the entire bottom wall; both the Flat and the three pylon configurations produce the same bottom wall pressures for a given injection. Only injection pressures make an impact, which is observed on the taps listed above. These affected taps are all located downstream of the cavity. Taps #9, #15, and #19 show the highest static pressure with injection 1, while taps #10, #16, and #20 produce the lower static pressure with injection 1. This implies that once a certain q is reached (between 1.6 and 3.1), injection pressure effects are observed on the bottom wall downstream of the cavity. Also of interest is the sharp pressure rise between taps #11 and #12 seen in all cases (located at 2.7 L downstream of the end of the cavity). This and the small oscillatory pressure variations show that the cavity is creating impingent pressure effects farther downstream.

The last few pressure taps on the top wall show the beginning of the cavity-caused phenomena described above. When graphed together (top of Figure 82), the top wall is seen to experience cavity-caused pressure changes about 1.7 L before the bottom wall. The top wall pressure taps run out before the sharp pressure rise (shown by the bottom wall instrumentation) is detected.

The back pressure comparison plot (bottom of Figure 82) shows that both top and bottom wall are equally affected when the shock train moves over the cavity. The Tall pylon back pressure condition encounters the shocks farther upstream than the other inserts. This explains why the T2BP image data shows different trends than the other back pressure images.
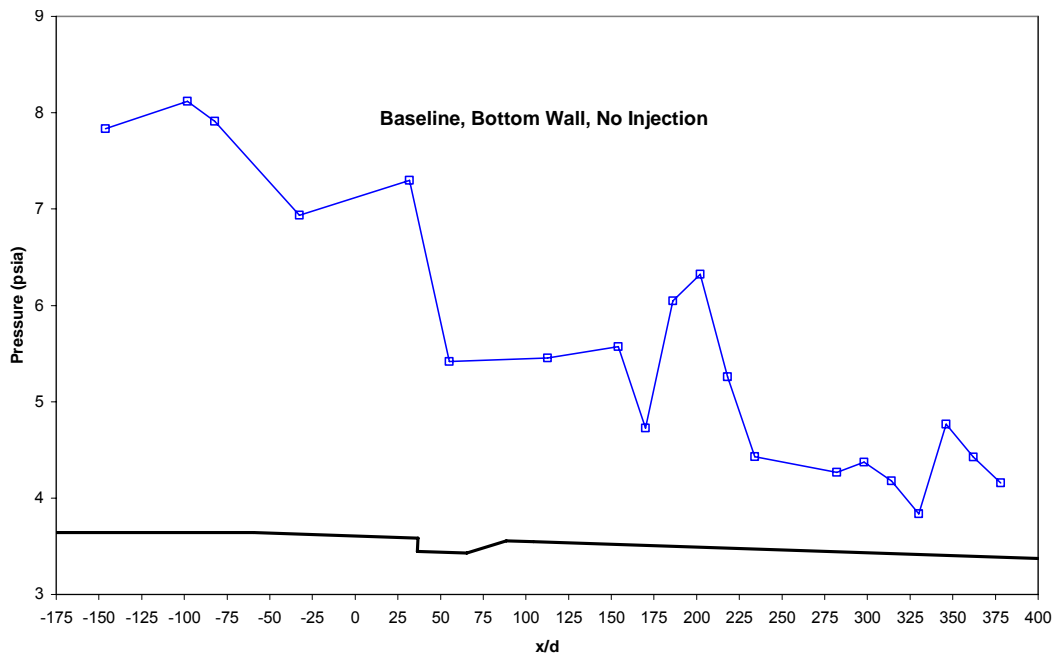
Figure 73. Baseline pressure readings on bottom wall
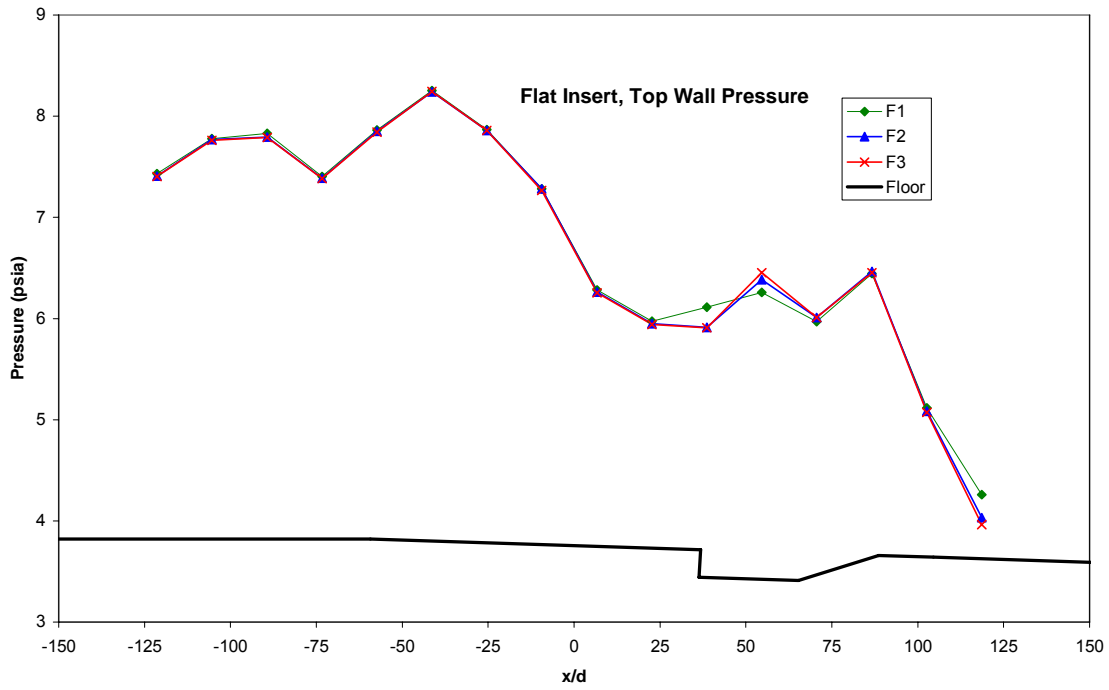
(a)
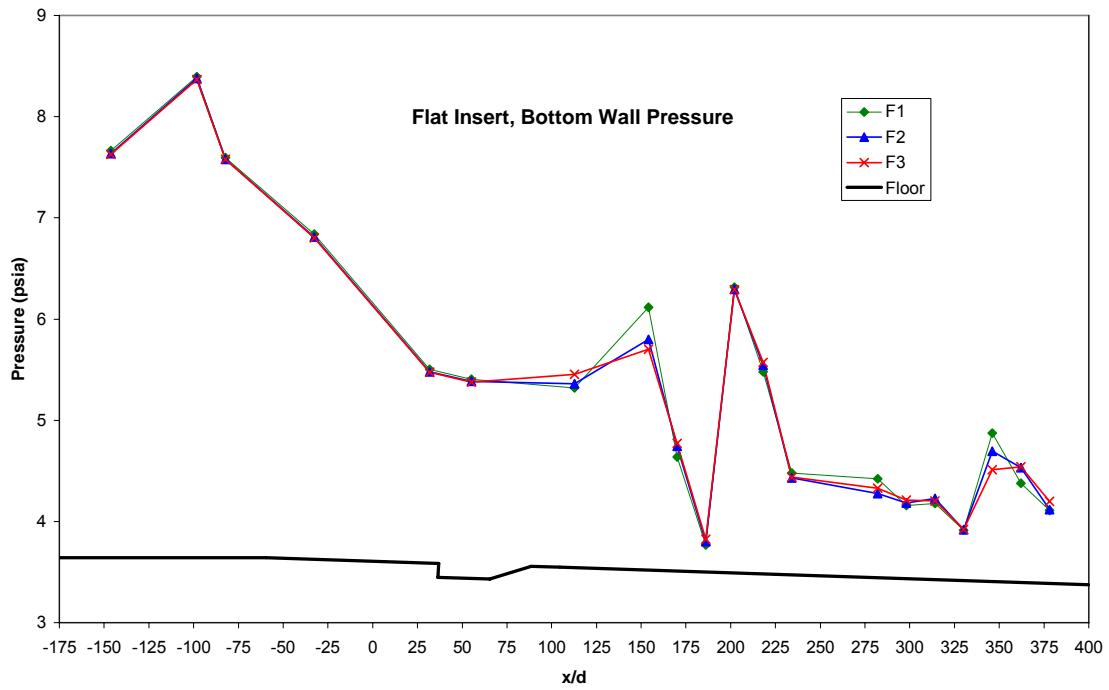
(b)

Figure 74. Flat insert wall readings at each injection pressure

131
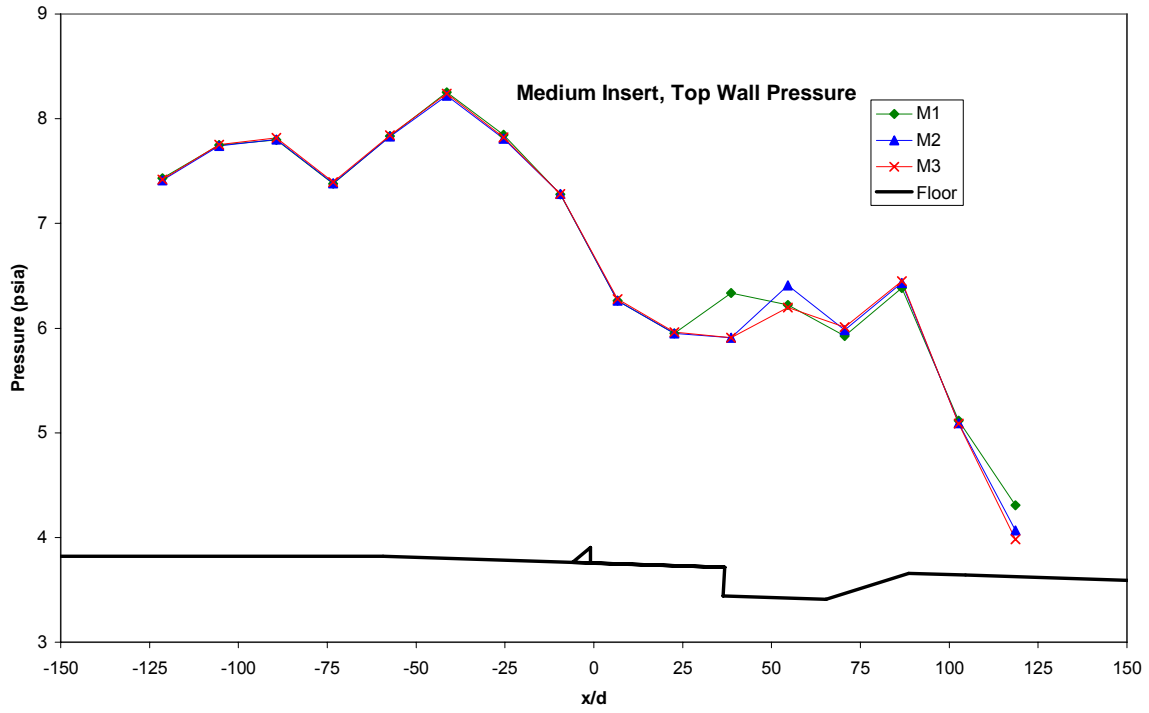
(a)
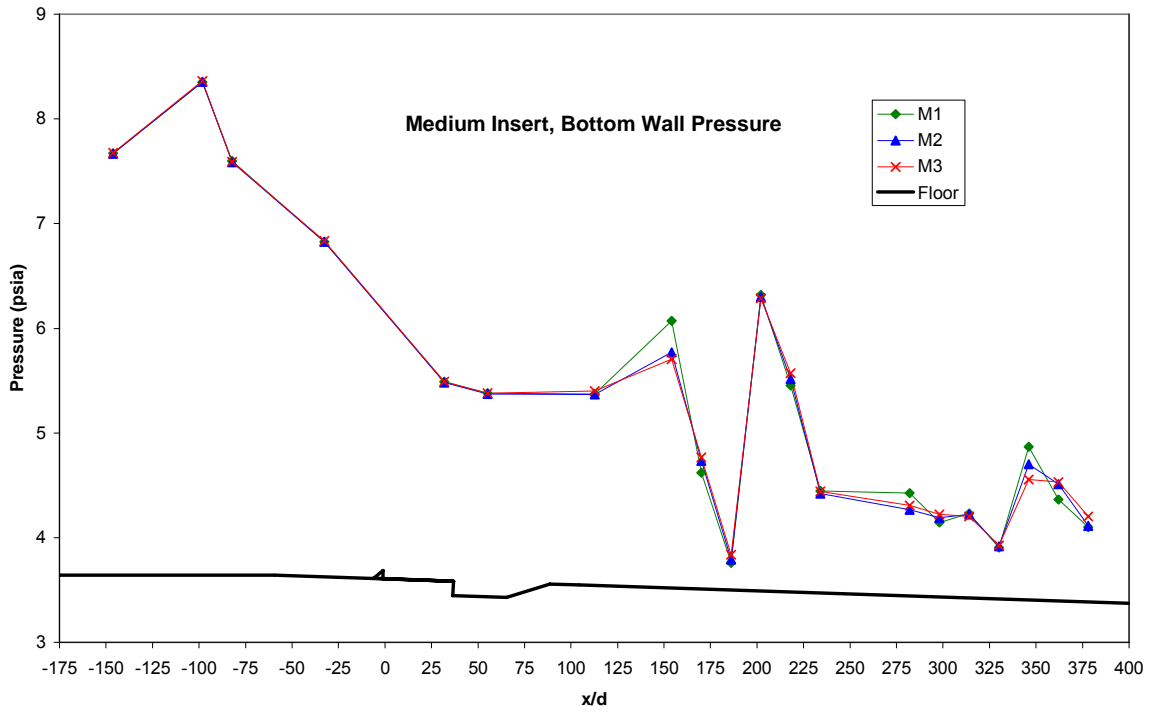
(b)

Figure 75. Medium insert wall readings at each injection pressure

132
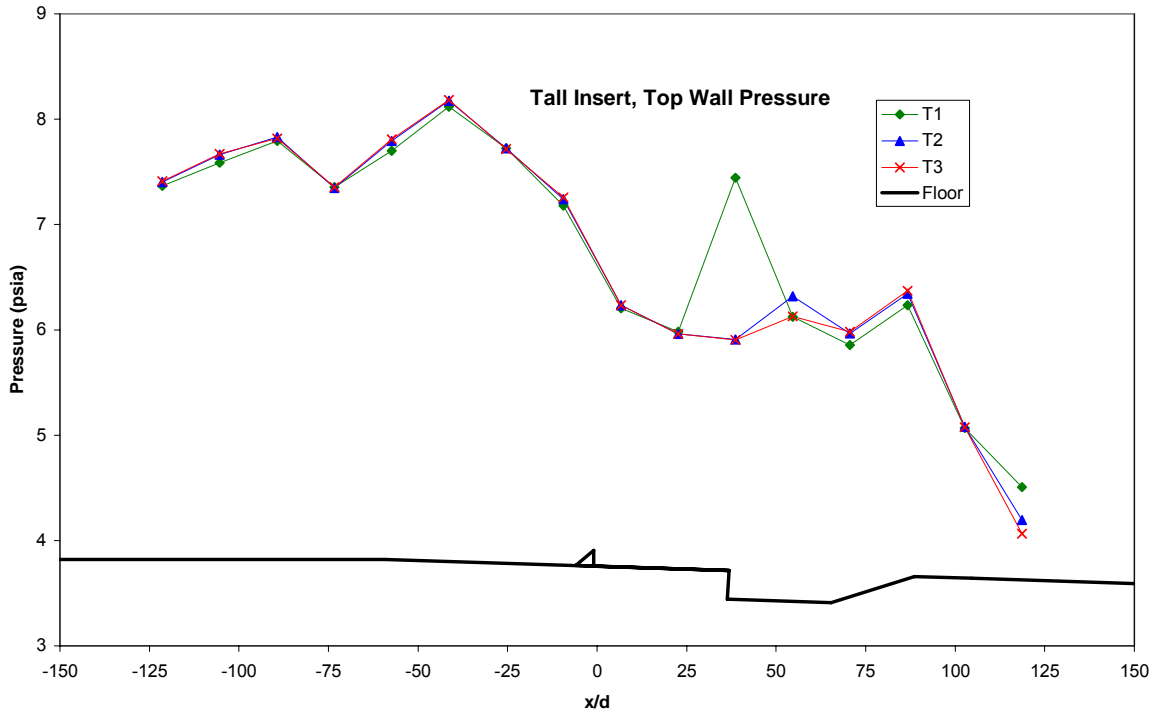
(a)
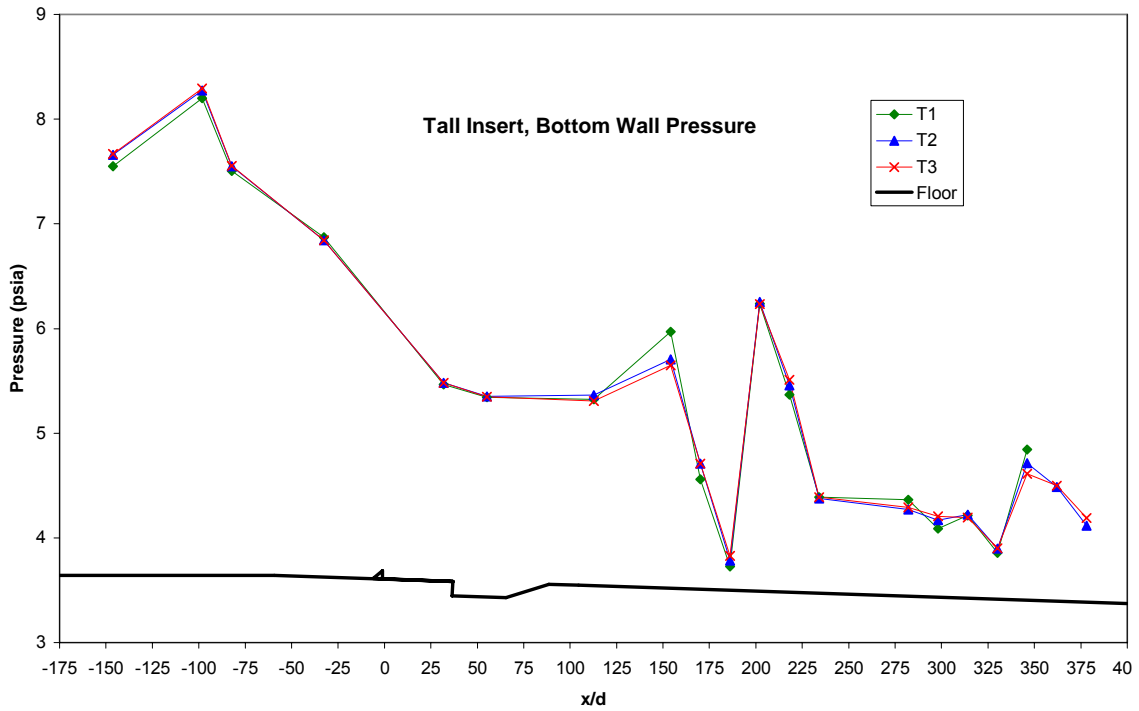
(b)

Figure 76. Tall insert wall readings at each injection pressure

133
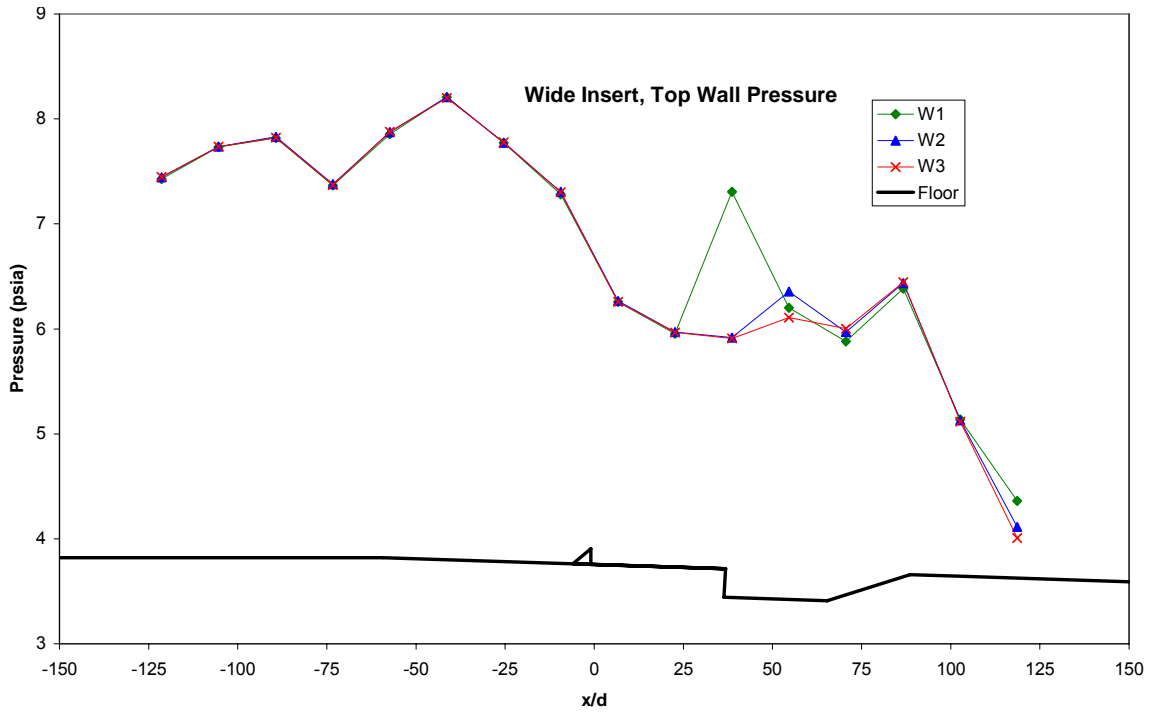
(a)
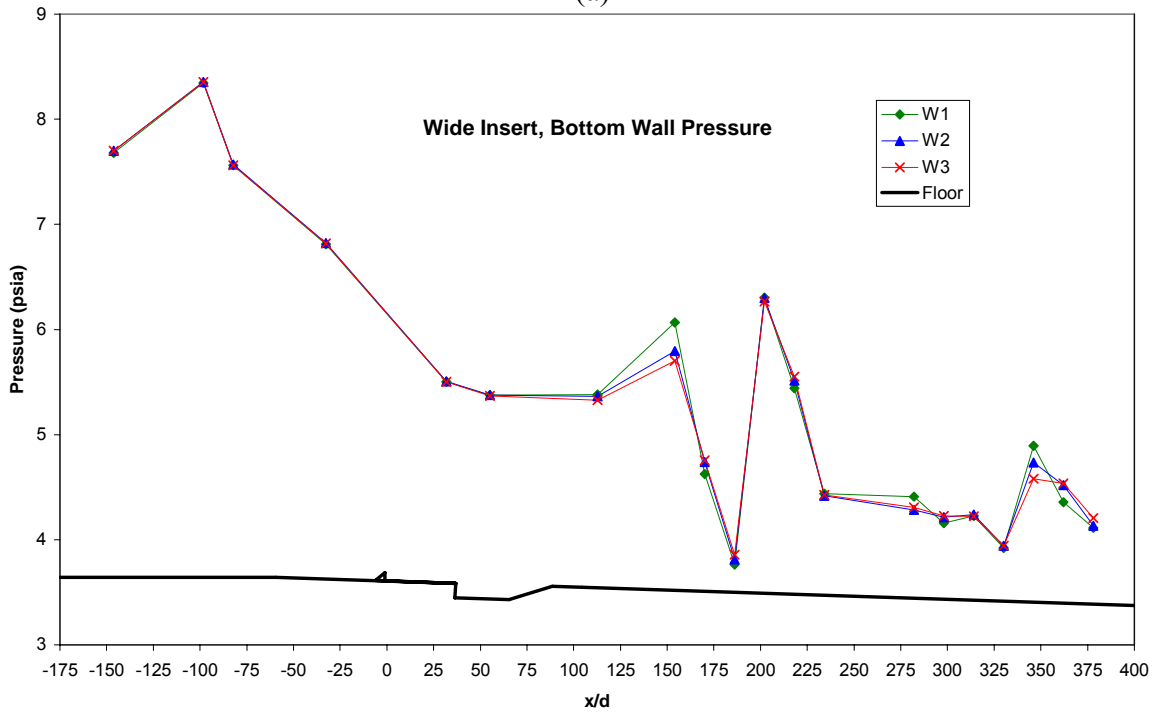
(b)

Figure 77. Wide insert wall readings at each injection pressure
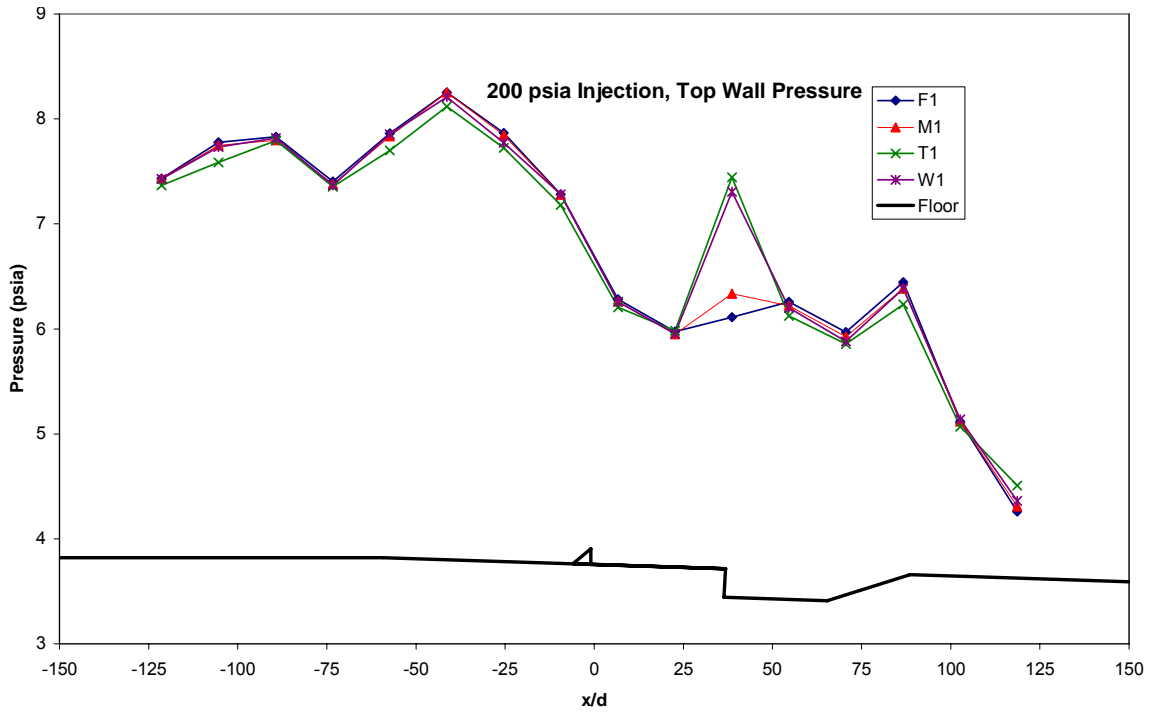
(a)
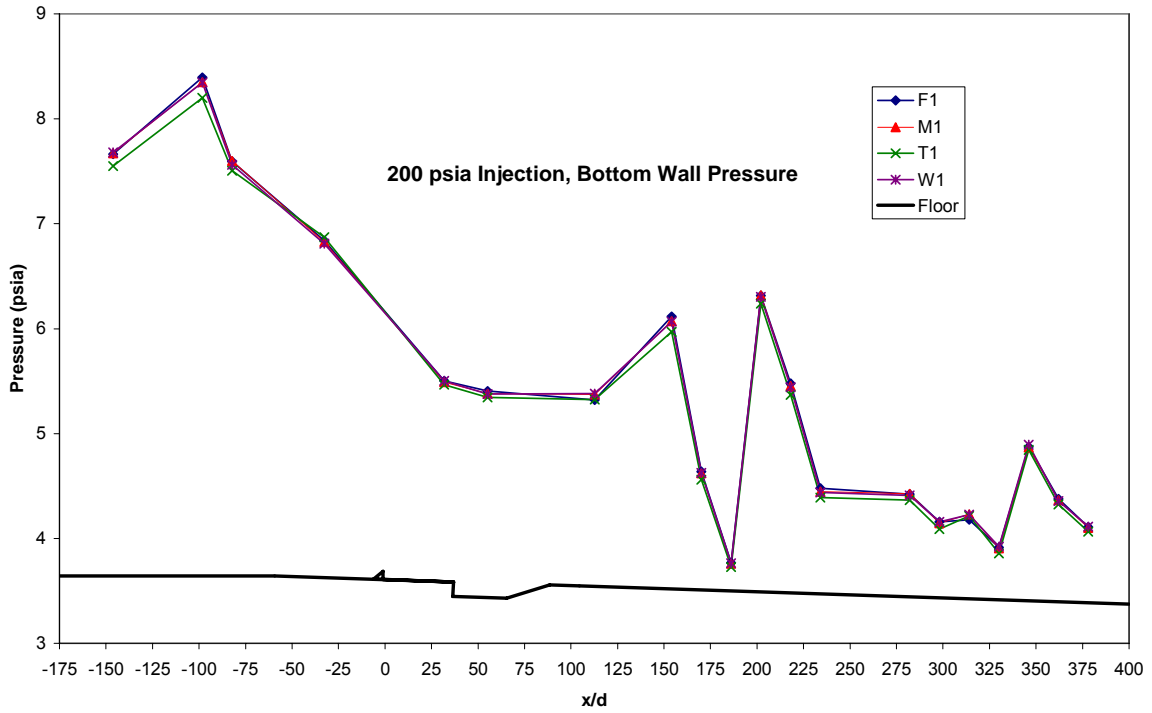
(b)

Figure 78. Injection pressure 1 wall readings for each insert

135
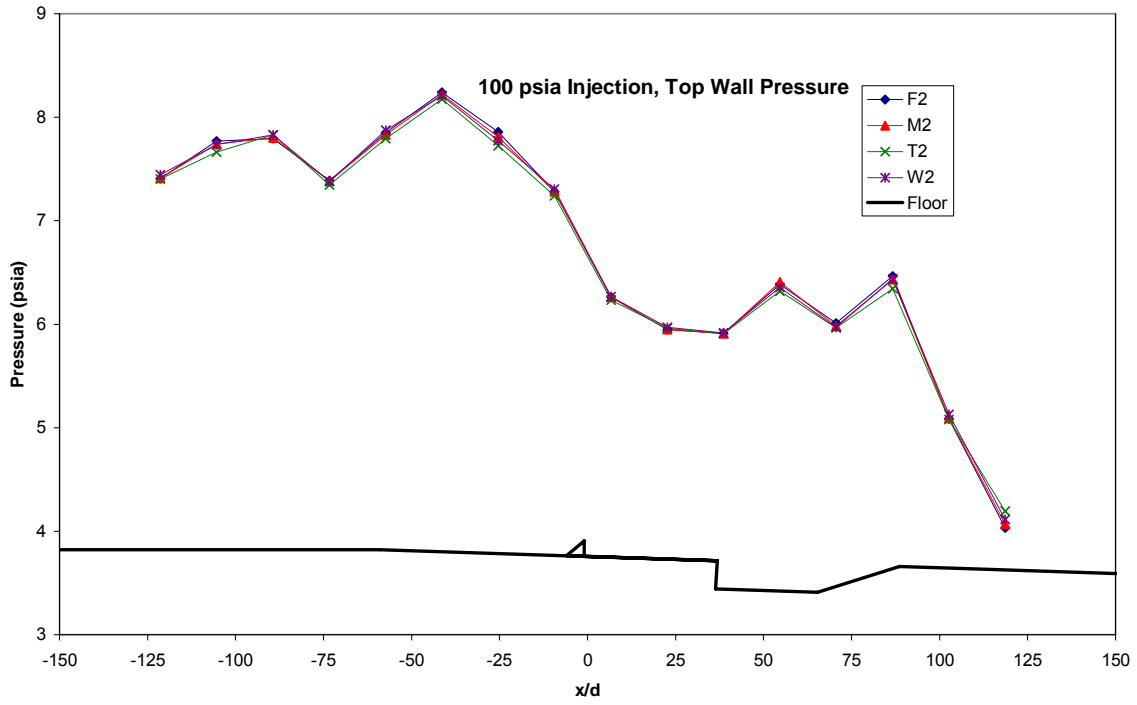
(a)

(b)

Figure 79. Injection pressure 2 wall readings for each insert
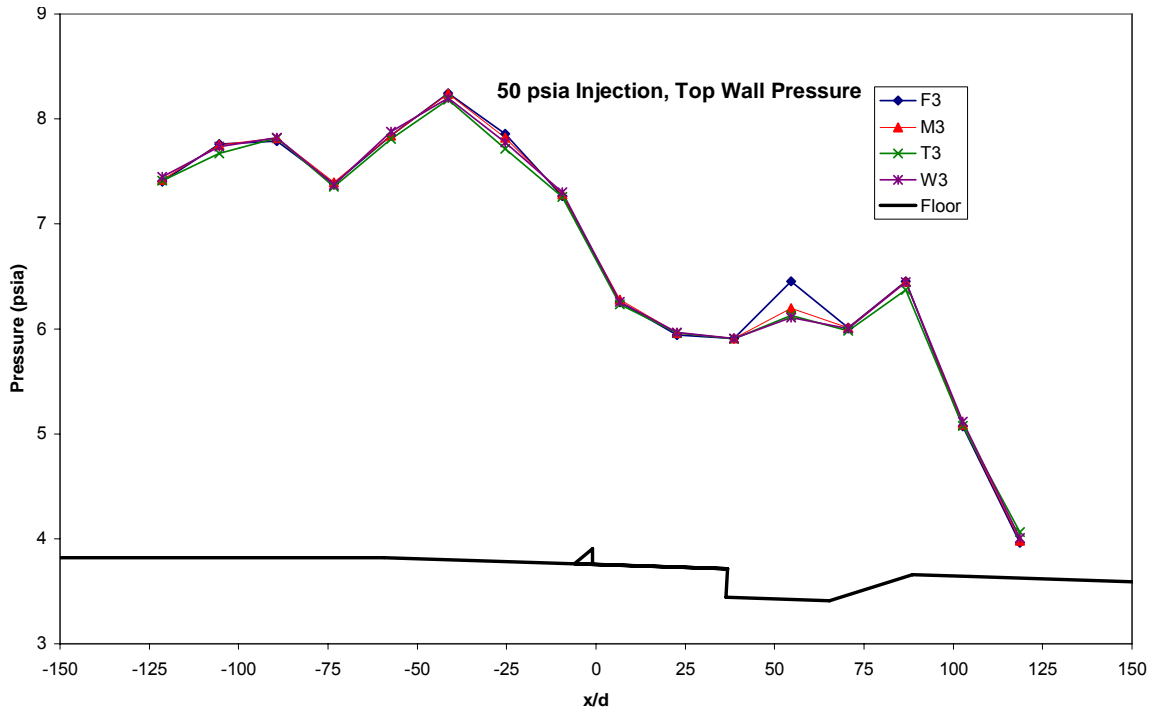
(a)
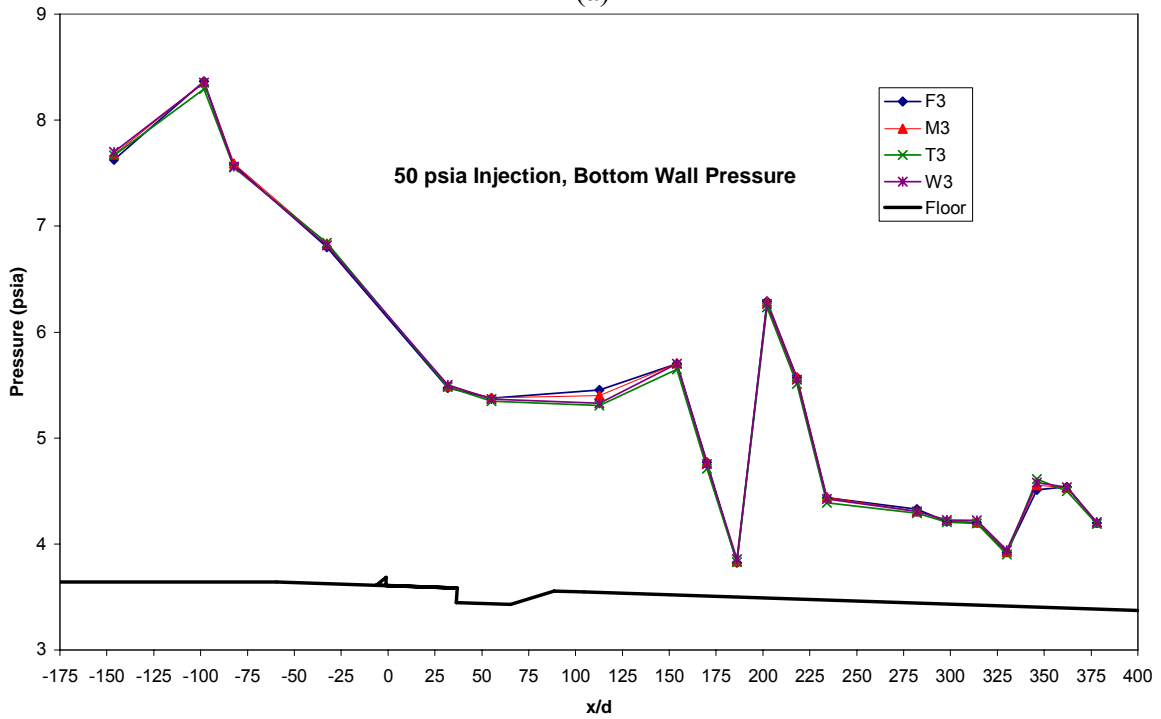
(b)

Figure 80. Injection pressure 3 wall readings for each insert
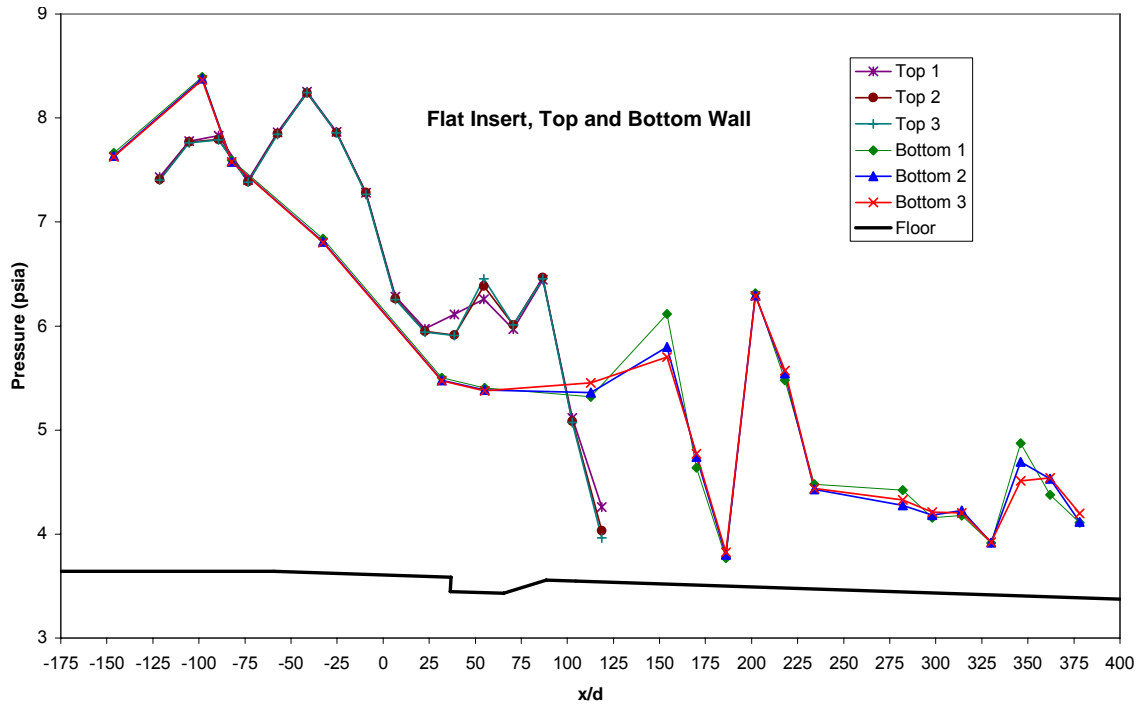
Figure 81. Top and bottom wall comparison for Flat injection
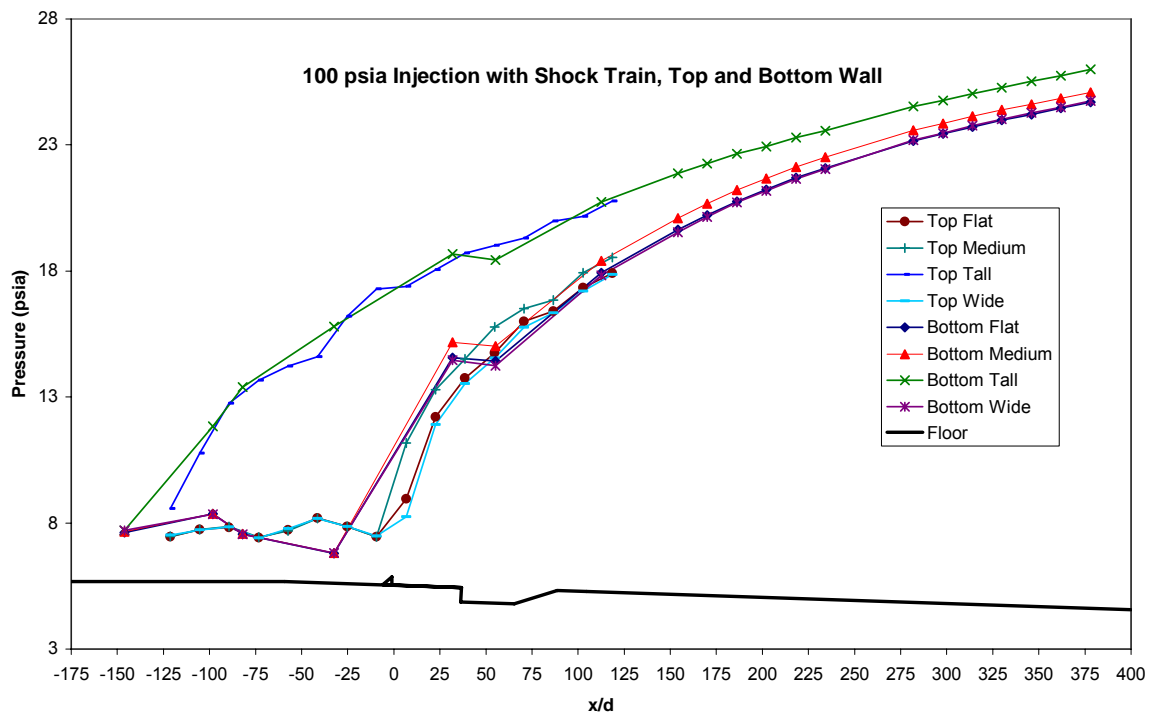
Figure 82. Tap readings for the different inserts during high back pressure flow

138

Summary of Data Collected

The following results have been presented in this paper in the various forms detailed:

A) Intensity reductions – Figures 32 through 39, Appendix E

B) NO-PLIF end views – Figures 40 through 55

C) End view geometry – Figures 56 through 62, Table 4, Appendix F

D) Mie scattering end views – Appendix G

E) Bow shock characterization – Table 5

F) Mie scattering Medium / Flat profile view – Figures 63 through 66

G) NO-PLIF Flat / Medium profile view – Figures 67 through 72

H) Pressure data – Figures 73 through 82, Appendix H

Total time devoted in the laboratory collecting raw data was estimated at 20 hours over three sessions.

V. Conclusions and Recommendations

Experiment Overview

Three pylons were installed in turn upstream of a transverse circular injector in order to qualify any improvements that they made on fueling. Tests were conducted in a Mach 2 flow environment within a test section simulated to act like a supersonic combustor. The injection took place upstream of a cavity flameholder similar in design to cavities employed in functional scramjets. Data was acquired both visually and through the use of static pressure measurements. Twelve configurations were tested in "scramjet" mode with completely supersonic flow. Four configurations were tested with back pressure increased so that shock trains formed and simulated "ramjet" mode. Two additional readings (one baseline with no obstructions and one with a pylon obstruction but no injection) were also conducted.

Results have been presented as a compilation of images, tables and plots that characterize jet properties seen in the images, image intensity comparisons, and tunnel wall pressure trends. This data correlates with past experiments that studied penetration behind pylons and presents some interesting findings concerning optimal pylon geometry.

Synopsis of Results

Mean intensity plots showed that the jet mixes into the freestream fairly consistently with a 95% dilution by the last streamwise readings. Standard deviation intensities demonstrated that more interaction was taking place in the farfield with pylons

140

than without (it was highest in the Wide case). With a high enough injection pressure, pylons created a high intensity of standard deviation directly downstream of injection.

Raw images from both the Mie scattering and the NO-PLIF runs display large, turbulent structures that demonstrate a considerable opportunity for mixing interaction. This information is not intuitive from the averaged images.

Flat injection showed solid development of counter-rotating vortices, a wide profile, the largest jet area, and the most local standard deviation

Medium pylon injection creates an initially wide jet, and the vortices are not as much an influence. Fluid eventually moves to the top formation. The higher the injection pressure the longer it takes to develop. The Medium pylon causes the most jet width normalized by pylon width. At then higher injection pressures it has the lowest floor clearance of the three pylons.

The Tall pylon immediately penetrates past the crown, but development of the remainder of the average structure is slower than the other pylons. This pylon is a very effective fuel penetrator that causes the highest vertical penetration and width reduction of all the inserts. It provides a considerable floor clearance (only behind the Wide pylon) and contains the same or better jet area as the Flat case. The Tall also creates a significant amount of local standard deviation.

The Wide pylon demonstrates immediate penetration followed by a very slow development relative to the other pylons. Its causes very high fuel heights when normalized by pylon height, and the second largest total fuel height. Injection behind this pylon quickly lifts from the floor, suggesting a significant baroclinic torque or cross-stream shear effect. The floor gap is the highest of the pylons in the farfield. This pylon

141

also exhibits medium to low standard deviation compared to the other inserts, suggesting that its vortices are not as much as an influence.

The shock train, on the average, increased the standard deviation and vertical and lateral spread of all injection cases. The more upstream the shock train (or the more within the shock train that injection occurs), the higher the standard deviation, both locally and on the intensity scale. Mixing potential is high in this regime.

The Medium and Wide pylons create similar bow shock magnitudes that are slightly higher than the Flat injection. The Tall pylon causes much larger shocks. High q injection behind the Medium pylon produced almost as low shock heights as the same q injection with no pylon. Low q injection behind the Medium pylon did not affect the shock heights present when there was no injection. The pylon effectively shielded the entire jet, allowing it to achieve high penetration.

The Tall pylon increased top wall static pressure ahead of and behind the cavity at high injection pressures, while the Flat insert increased the top wall pressures directly over the cavity at low injection pressures. In general, the highest q raised the static pressure before and aft of the cavity, while the lowest injection pressure raised static pressure directly over the cavity.

Along the bottom wall pylon type had no effect, but higher injection pressures show oscillatory static pressure effects downstream of the cavity, possibly caused by cavity shock interactions.

Conclusions of Research

All the pylons provided more penetration and less lateral spread than the Flat injection. All the pylons lifted the fuel off the floor at all values of q, suggesting that flashback is preventable using this injection method. The pylons showed less local standard deviation activity (seen in the images), but intensity plots show that all the pylons were interacting with and diluting into the freestream at the same level or more than in the Flat case.

The Tall pylon was designed to be of a larger scale than the other two pylons. It was based on the optimal geometry obtained from a computational study. The greater size of this pylon (more than its shape) is what effected the large penetration height. Unfortunately, $h/d = 6$ created stronger shocks than the other three cases. Based on shock heights alone, the Tall incurred between a $10 - 50\%$ additional drag penalty compared to the smaller pylons. Pylon height should be kept to a value of 4 d or below to minimize losses.

The Wide pylon was the best performer overall. It lifted the fuel jet away from the boundary layer quickly and established a good penetration height. In the shock train case it provided the greatest penetration effect. This pylon was designed with the second best geometry suggested by computational research but performed better than the Medium pylon of the same height (designed with the optimal suggested geometry). Further profile analysis would probably yield a similar shock trend as exhibited by the Medium pylon, as suggested by end view shock measurements.

The lowest q resulted in fuel being completely shielded behind the pylons and having no additional effect on shock losses. This injection pressure achieved the most

drastic pylon aided fuel height increase over Flat injection. The Wide pylon at the low q (0.83) enhanced penetration height by 135% (105% for q = 1.67, 70% for q = 3.34).

Pressure readings demonstrated that the larger pylon (Tall) as well as the highest injection pressure caused the highest pressure increases upstream of the cavity, suggesting a possible loss parameter. These pressure changes might have an important effect on the cavity shear layer. The cavity itself experiences pressure variations even without the high back pressure condition. High q injection upstream of the cavity is communicated through this area and measures downstream, another indication that higher injection pressures affect the shear layer.

Mixing potential was present through observations of the raw images, as well as evidenced by the vortices observed in all the cases. The pylons showed a higher standard deviation intensity but had less developed counter-rotating vortices than the Flat case, suggesting that the structures, although they contribute to local interaction, do not promote as much dilution and freestream exchange, as intensity plots confirm.

Significance of Research

This experiment has shown that pylons are a viable option for injecting fuel and preventing flashback, and from a first look additional losses with the Wide and Medium pylons are minimal. Lower injection pressures experience the best enhancement and cause the least pressure and shock disturbances. This knowledge may lead to experiments that aim to optimize injection strengths and pylon shapes and sizes to provide excellent mixing potential. The road ahead will combine pylon injection, cavity

144

injection, and ignition to attempt to couple these systems into a single combustion strategy.

Recommendations for Future Action

More research has to be conducted to visualize and characterize the effect of pylon-aided injection over the flameholding cavity. This could be achieved with traditional visual systems such as Schlieren or shadowgraph, as well as more intricate pressure tap placement in the cavity region.

A more in depth shock analysis may be performed with current image data, or with reruns that position the camera to capture more of the shock formations. Standard deviations from the Mie scattering and NO-PLIF images could also be compared to observe what overlap exists.

A computational fluid dynamics (CFD) analysis is in order to further characterize the intricate formation that occurred behind pylon injection and observed with end view NO-PLIF imagery and to verify that the Wide pylon is indeed more optimal than the Medium for increasing penetration height. This could be combined with a concentration study to quantify mixing behind pylons and over the cavity and elimination of fuel existence on the floor.

A pitot rake should be employed to measure total pressure losses and begin to quantify efficiency comparisons between different pylons. A method to calculate q in shock train conditions would also be desirable.

Any of the inserts may be installed at the original location used for this study or in Fixture B just upstream of the cavity to be used in combustion studies. These studies

would attempt to lift the shear layer out of the cavity and seed the air stream above it with mixed fuel/air.

Further in the future, the pylons may be combined with non-circular/transverse injectors (e.g., angled or swirled) to create complex mixing and penetration effects which could be used in conjunction with reactive studies.

Summary

This study aims to contribute to the development of more efficient fueling strategies for dual-mode scramjet combustors. The Air Force has a high interest in optimizing these engines, and the current research has yielded conclusions that favorably impact this goal. This research also confirmed the usefulness of the imaging equipment utilized and demonstrated its potential. The value of computational studies was also validated, as hardware design would not have been possible without a theoretical starting point. Follow-up studies and additional data analysis will be performed after the writing of this report in preparation for several conference presentations later this year.

Appendix A – Hardware Specifics
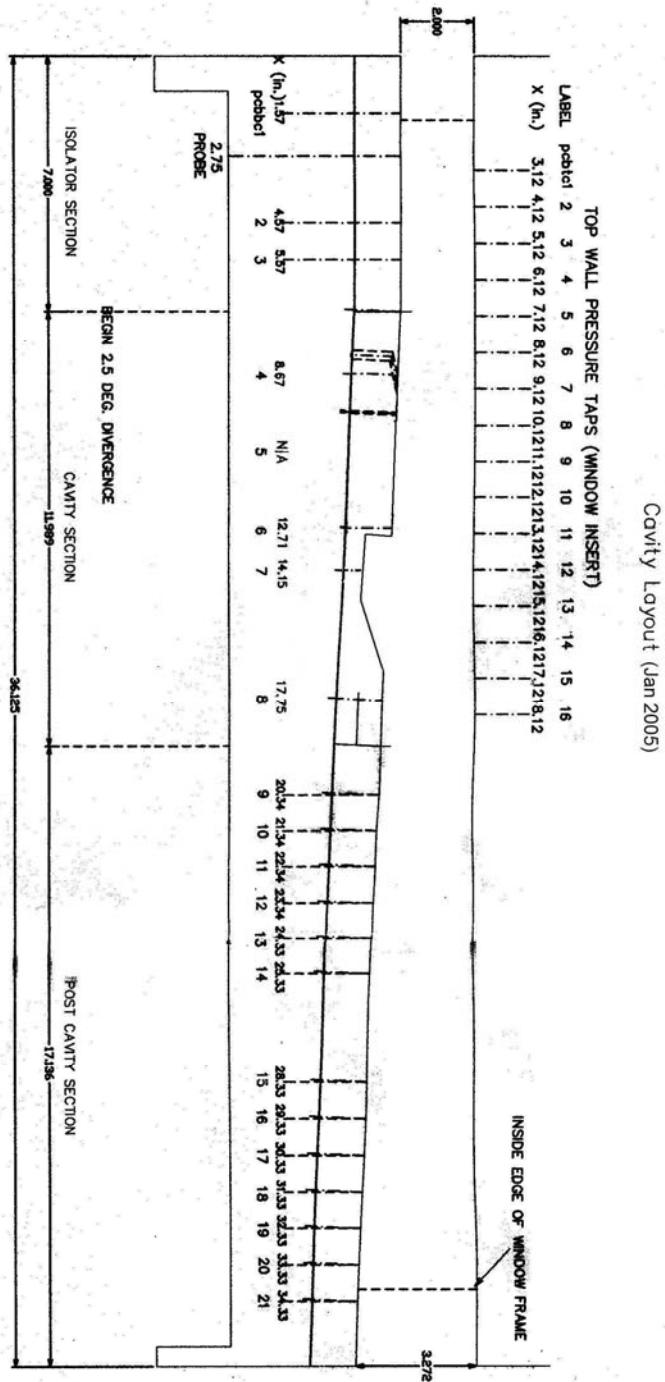
Figure A1. Pressure tap placement in test section
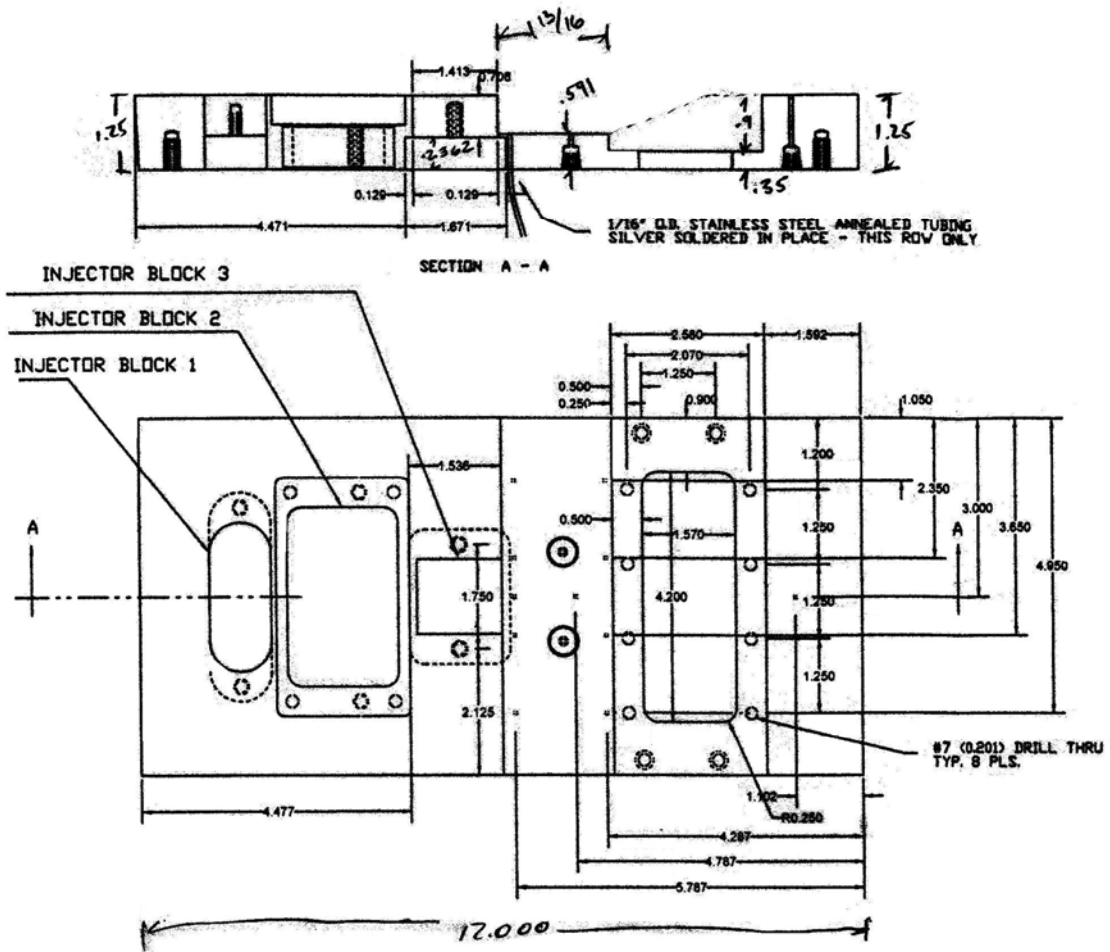
Figure A2. Detailed cavity section with insert points highlighted

Note: Fixtures A and B (which are compatible with pylon inserts) install into "Injector Block 2" and "Injector Block 3", respectively.
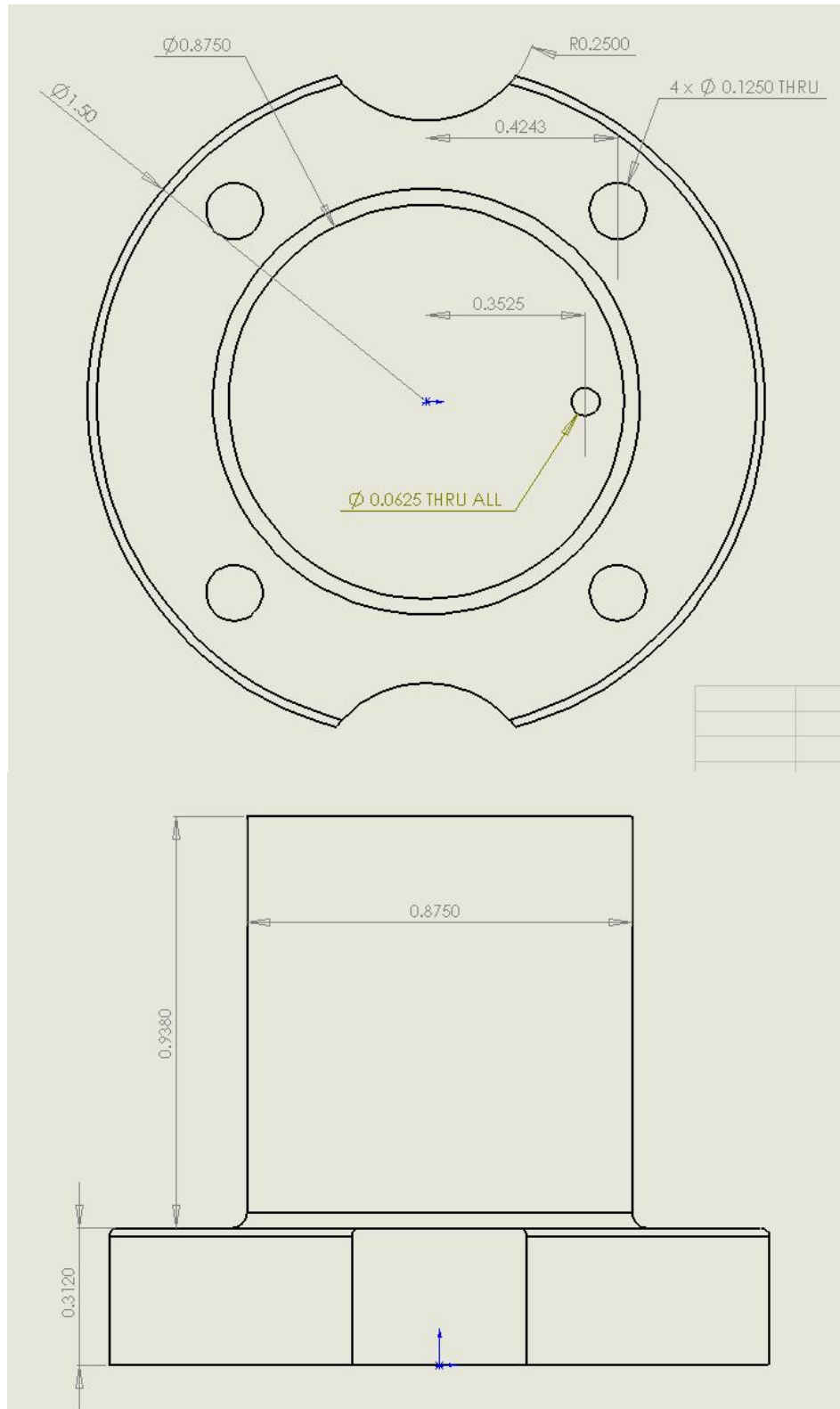
Figure A3. Pylon insert dimensions

Discharge Coefficient

The discharge coefficient (C_D) is a mass flow rate loss parameter attributed to any particular injector. During a C_D evaluation, Tylan[®] equipment is integrated into the injection line to measure true flow rates in standard liters per minute (SLPM). A standard liter is a volumetric liter converted by the following expression:

$$SL = L \cdot \frac{\rho_{std}}{\rho_j} \tag{B1}$$

where ρ_{std} is standard atmospheric density (1.185 kg/m^3 in SI units) and ρ_j is calculated from measured pressure and temperature. SLPM can therefore be converted to the familiar $\dot{m}$ convention (mass per second) via

$$\dot{m} = SLPM \cdot \left(\frac{\rho_j}{\rho_{std}} \right) \cdot \frac{1 \cdot m^3}{1000 \cdot L} \cdot \rho_j \cdot \frac{60 \cdot s}{\min} \tag{B2}$$

assuming SI units again. In this method a "true" value of mass flow rate is acquired.

The real experiment does not utilize a flowmeter. To simulate actual experiment measurements, injection pressure and temperature are measured concurrently with the

Tylan® readings. With knowledge that the nozzle is choked and a value for injection area (A), the mass flow parameter may be used to calculate mass flow rate using uncorrected temperature and pressure information (from the tube):

$$\dot{m} = \frac{P \cdot A}{\sqrt{R \cdot T \cdot \left[1 - \left(\dfrac{\gamma - 1}{\gamma}\right)\right]}}$$

(B3)

where the standard properties for air at room temperature are assumed for the specific gas constant (R) and the ratio of specific heats (γ).

Experimental error is going to yield a value for $\dot{m}$ greater than the true Tylan® measured value. The discharge coefficient is therefore

$$C_D = \frac{\dot{m}_{true}}{\dot{m}_{calculated}}$$

(B4)

and each injector will have a unique value for it. An average is usually taken from the same pressures used in real testing; this is a way to check for consistency over the range of injection conditions that will be in the experiment. Figure B1 shows the configuration used to find C_D.
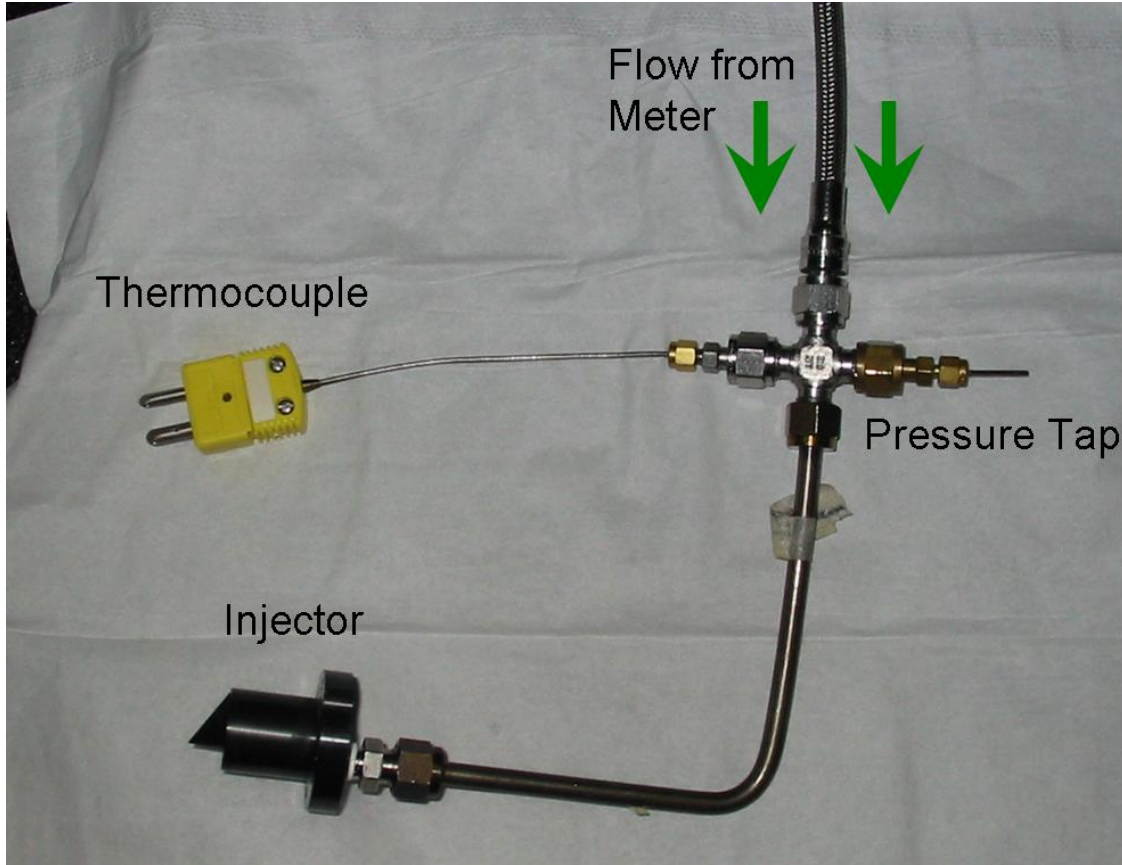
Figure B1. Discharge coefficient test setup

Dynamic Pressure Ratio

The same equations used to derive the discharge coefficient can also be applied to the dynamic pressure ratio development. The three injection pressures used for each insert are measured as total pressures (P_{0j}) in the tube. Because each insert has its own C_D value, there are twelve total values of q calculated. The values of q for this experiment are found in Table 2. If C_D were not considered, only three q values would result (presented as uncorrected values). The first step in calculating the dynamic

pressure ratio is to reduce the measured tube total pressures to static pressures with

knowledge that the nozzle is choked:

$$P = \frac{P_0}{\left[1 + \left(\frac{\gamma - 1}{2}\right)\right]^{\left(\frac{\gamma}{\gamma - 1}\right)}} \tag{B5}$$

Temperature is a measured quantity; thus, reapplying Equation B3 yields a

calculated value for $\dot{m}$. A simple rearrangement of Equation B4 allows the true $\dot{m}$ to be

determined:

$$C_D \cdot \dot{m}_{calculated} = \dot{m}_{true} \tag{B4-ii}$$

This value for $\dot{m}$ may be used in Equation 3, rested below, to determine the

dynamic pressure ratio, q.

$$q = \frac{\left(\frac{\dot{m}_{true}^2}{\rho \cdot A^2}\right)_{jet}}{(\gamma \cdot P \cdot M^2)_{core}} \tag{1}$$

An interesting thing to note is that the injection temperature (T_j) has no effect on

q. It only affects the mass flow rate of the fuel jet.

Appendix C – Laser Imaging Addendum

Author: Dr. Campbell Carter, AFRL

This routine calculates the relative NO LIF signal for a **constant mole fraction of NO** in terms of local T (Kelvins) and P (atm). The signal varies due to 1) ground state population fraction (Boltzmann fraction FB(T)), 2) total number density, 3) the laser-transition overlap integral g(T,P), and 4) electronic quenching Q(T,P):

$$\text{Signal} = \text{Const.} * XNO * FB(J,T) * (P/T) * g(T,P)/(Q(T,P))$$

First, calculate the Boltzmann fraction for the probed ground state:

Plank (erg*s)   speed of light (cm/s)   Boltzmann (erg/molecules*K)

$$h := 6.626196 \cdot 10^{-27} \qquad cl := 2.9979250 \cdot 10^{10} \qquad k := 1.380622 \cdot 10^{-16} \text{ CGS unit system}$$

Rotational and vibrational constants (wavenumbers, cm^{-1}) for calculating the ground state population (Boltzmann fraction, FB)

$$A := 123.0372 \qquad Bv := 1.69619 \qquad we := 1904.405 \qquad wexe := 14.187$$

Describe the Boltzmann population fraction of the pumped level for the NO X state with a simplified Boltzmann fraction calculation.

$$Qr(T) = \left[\exp\left[\frac{-h \cdot cl}{k} \cdot \frac{(A - 3.5 \cdot Bv)}{2 \cdot T} \right] + \exp\left[\frac{-h \cdot cl}{k} \cdot \frac{(0.5 \cdot Bv - A)}{2 \cdot T} \right] \right] \cdot \frac{k \cdot T}{h \cdot cl \cdot Bv} \qquad \text{Rotational partition function}$$

$$Qv(T) := \sum_{vi = 0}^{20} \exp\left[\frac{-h \cdot cl}{k} \cdot \frac{we \cdot (vi + 0.5) - wexe \cdot (vi + 0.5)^2}{T} \right] \qquad \text{Vibrational partition function}$$

$$\alpha(JI) := \left(\frac{\frac{A}{Bv} - 2}{2} \right)^2 + (JI + 0.5)^2 - 1 \qquad \begin{array}{l}\text{Define F1 and F2, rotational term energies for the two spin}\\\text{split levels. Ignore centrifugal stretching (i.e., the Dv term)}\end{array}$$

$$F1(JI) := Bv \cdot \left[(JI + 0.5)^2 - 1 - \sqrt{\alpha(JI)} \right] \qquad F2(JI) := Bv \cdot \left[(JI + 0.5)^2 - 1 + \sqrt{\alpha(JI)} \right]$$

$$FB1(JI, T) := \frac{(2 \cdot JI + 1) \cdot \exp\left(\frac{-h \cdot cl}{k} \cdot \frac{F1(JI) + we \cdot 0.5 - wexe \cdot 0.25}{T} \right)}{2 \cdot Qv(T) \cdot Qr(T)} \qquad \begin{array}{l}\text{Boltzmann population}\\\text{fractions for two spin split}\\\text{states}\end{array}$$

$$FB2(JI, T) := \frac{(2 \cdot JI + 1) \cdot \exp\left(\frac{-h \cdot cl}{k} \cdot \frac{F2(JI) + we \cdot 0.5 - wexe \cdot 0.25}{T} \right)}{2 \cdot Qv(T) \cdot Qr(T)}$$

Calculate the quenching rate (1/s) in terms of T (K) and P (atm). Consider air to be composed of O2, N2 (though N2 is a very poor quencher of NO at low T), and a small amount of H2O. CO2, H2O, and NO are efficient quenchers of A-state NO but should be in low concentration: $XCO_2 = 350$ ppm and $XNO < 1000$ ppm (unless we've doped too much); XH_2O will depend on how dry the incoming air is (it has been dried so maybe $XH_2O = 1000$ ppm) and its cross section is 4 to 5 times that of O2. Really, only the O2 quenching matters much, unless temperatures are > 1000 K (at which time the contribution from N2 begins to play a part)

Cross sections are in terms of m^2 (from published sources)

$$\sigma N2(T) := 0.88 \cdot 10^{-16} \cdot \exp\left(-4.9 \cdot \frac{300}{T}\right) + 48 \cdot 10^{-16} \cdot \exp\left(-32 \cdot \frac{300}{T}\right) \qquad \sigma O2 := 25 \cdot 10^{-16}$$

$$\sigma H2O(T) := 123 \cdot 10^{-16} \cdot \left(\frac{293}{T}\right)^{0.65} \qquad a\,mu := 1.6605 \cdot 10^{-24} \qquad pconv := 1.01325 \cdot 10^{6}$$

$$ZN2(T, P) := 0.79 \cdot \frac{(P \cdot pconv)}{k \cdot T} \cdot \sigma N2(T) \cdot \left[\frac{(8 \cdot k \cdot T)}{\pi \cdot \dfrac{a\,mu \cdot (28 \cdot 30)}{28 + 30}}\right]^{0.5}$$

The terms involved are the mole fraction, the total number density (the product of these two is the collider species number density), the collision cross section, and the reduced-mass collision velocity.

$$ZO2(T, P) := 0.21 \cdot \frac{(P \cdot pconv)}{k \cdot T} \cdot \sigma O2 \cdot \left[\frac{(8 \cdot k \cdot T)}{\pi \cdot \dfrac{a\,mu \cdot (32 \cdot 30)}{32 + 30}}\right]^{0.5}$$

$$ZH2O(T, P) := 0.001 \cdot \frac{(P \cdot pconv)}{k \cdot T} \cdot \sigma H2O(T) \cdot \left[\frac{(8 \cdot k \cdot T)}{\pi \cdot \dfrac{a\,mu \cdot (18 \cdot 30)}{18 + 30}}\right]^{0.5}$$

I am assuming that the air has 1000 ppm of H2O. The answer is not sensitive to this value

Now, sum the contributions. The last term accounts for the natural lifetime of the A state from fluorescence (i.e., 210 ns lifetime)

$$Q(T, P) := ZN2(T, P) + ZO2(T, P) + ZH2O(T, P) + \frac{1}{(210 \cdot 10^{-9})}$$

Now calculate the dependence on the laser-transition overlap integral. Describe the collisional broadening of the transition with the Hummer formulation of the Voigt profile, v(x, y). Here, x is the frequency unit and y is the broadening coefficient.

$$t := \begin{pmatrix} 0.314240376 \\ 0.947788391 \\ 0.159768264 \cdot 10^{1} \\ 0.227950708 \cdot 10^{1} \\ 0.302063703 \cdot 10^{1} \\ 0.388972490 \cdot 10^{1} \end{pmatrix} \qquad c := \begin{pmatrix} 0.101172805 \cdot 10^{1} \\ -0.75197147 \\ 0.12557727 \cdot 10^{-1} \\ 0.100220082 \cdot 10^{-1} \\ -0.242068135 \cdot 10^{-3} \\ 0.500848061 \cdot 10^{-6} \end{pmatrix} \qquad s := \begin{pmatrix} 0.1393237 \cdot 10^{1} \\ 0.231152406 \\ -0.155351466 \\ 0.621836624 \cdot 10^{-2} \\ 0.919082986 \cdot 10^{-4} \\ -0.627525958 \cdot 10^{-6} \end{pmatrix}$$

$$v1(x, y) := \sum_{n=0}^{5} \left[c_n \cdot \left[\frac{y + 1.5}{(|x| - t_n)^2 + (y + 1.5)^2} + \frac{y + 1.5}{(|x| + t_n)^2 + (y + 1.5)^2} \right] - s_n \cdot \left[\frac{|x| - t_n}{(|x| - t_n)^2 + (y + 1.5)^2} - \frac{|x| + t_n}{(|x| + t_n)^2 + (y + 1.5)^2} \right] \right]$$

$$v2(x, y) := \exp(-x^2) + y \cdot \sum_{n=0}^{5} \left[\frac{c_n \cdot \left[(|x| - t_n)^2 - 1.5 \cdot (1.5 + y) \right] + s_n \cdot (3 + y) \cdot (|x| - t_n)}{\left[(|x| - t_n)^2 + (y + 1.5)^2 \right] \cdot \left[(|x| - t_n)^2 + 2.25 \right]} + \frac{c_n \cdot \left[(|x| + t_n)^2 - 1.5 \cdot (1.5 + y) \right] - s_n \cdot (3 + y) \cdot (|x| + t_n)}{\left[(|x| + t_n)^2 + (y + 1.5)^2 \right] \cdot \left[(|x| + t_n)^2 + 2.25 \right]} \right]$$

155

$v(x, y) := if[(y > 0.85) + [x < (18.1 \cdot y + 1.65)], v1(x, y), v2(x, y)]$ Here's the Voigt function

Now calculate inputs to the Voigt function (also known as the complex error function); relative error of this formulation is very low, about 1 part per million.

$v0 := 44300$ line center (wavenumbers $= cm^{-1}$)

$\Delta D(T) := 1.307 \cdot 10^{-7} \cdot v0 \cdot \sqrt{T}$ Doppler linewidth (wavenumbers)

$\Delta C(T, P) := 0.585 \cdot P \cdot \left(\dfrac{295}{T}\right)^{0.75}$ Collisional linewidth (wavenumbers), assuming collisons N2 [Chang et al., JQSRT 47, p. 375, 1992]

$aC(T, P) := 0.83256 \dfrac{\Delta C(T, P)}{\Delta D(T)}$ $aL(T, \Delta L) := \dfrac{\Delta L}{\Delta D(T)}$ Nondimensionalize the collisional and laser linewidths with the Doppler width

g(T, P) is the so-called overlap integral and accounts for changes in coupling of laser radiation and the transition. We have assumed the laser spectral irradiance function is described by a Gaussian relation with a linewidth given above (ΔL). This allows us to write the overlap integral in the form below (rather than carrying out the integration of the normalized lineshape functions). Note that we are neglecting collisional line-shift.

The first argument for the v function is "0" to indicate that the laser is tuned to line center of the transition.

$$g(T, P, \Delta L) := \left(\dfrac{1}{\sqrt{1 + aL(T, \Delta L)^2}}\right) \dfrac{1.66511}{\sqrt{\pi} \cdot \Delta D(T)} \cdot v\left(\dfrac{0}{\sqrt{1 + aL(T, \Delta L)^2}}, \dfrac{aC(T, P)}{\sqrt{1 + aL(T, \Delta L)^2}}\right)$$

$Tref := 250$ $Pref := 0.45$ These are just convenient reference conditions so that we can reference the signal to some condition

LIF signal dependence:

    Signal   = Const. * XNO * FB(J,T) * (P/T) * g(T,P,ΔL)/(Q(T,P))
          = Const. * XNO * F LIF(T,P)

If one knows T and P, then the relative NO mole fraction can be obtained by dividing the measured signal counts by "F LIF(T,P)"

This equation assumes linear fluorescence behavior and we may have some saturation behavior (a mix of linear and saturated behaviors)!

$$F\_LIF(T, P, \Delta L) := (FB1(6.5, T)) \cdot \frac{g(T, P, \Delta L)}{Q(T, P)} \cdot \frac{P}{T}$$

Consider a range of temperatures but constant pressure (Pref):

T := 100, 110 .. 1000

$\dfrac{F\_LIF(T, Pref, 0.1)}{F\_LIF(Tref, Pref, 0.1)}$

P := 0.1, 0.11 .. 1
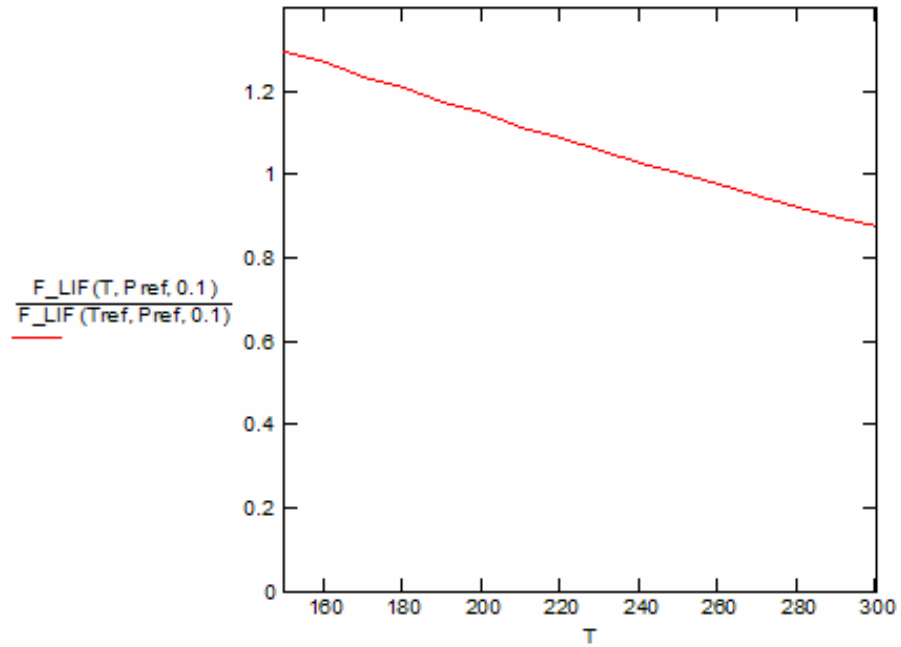
$\dfrac{F\_LIF(Tref, P, 0.1)}{F\_LIF(Tref, Pref, 0.1)}$
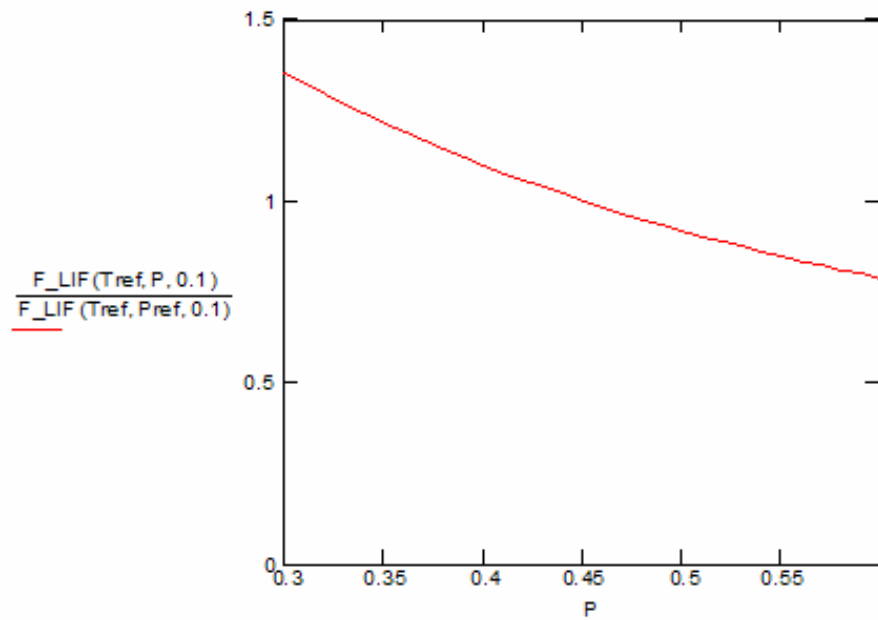
Appendix D – Test Matrix

Table D1. Test matrix

Run	Hardware	Back Pressure	Injection Pressure	Instrument	Run	Hardware	Back Pressure	Injection Pressure	Instrument
1	Flat	Low	1	Pressure	9	Tall	Low	1	Pressure
	Flat	Low	1	Mie		Tall	Low	1	Mie
	Flat	Low	1	NO-PLIF		Tall	Low	1	NO-PLIF
2	Flat	Low	2	Pressure	10	Tall	Low	2	Pressure
	Flat	Low	2	Mie		Tall	Low	2	Mie
	Flat	Low	2	NO-PLIF		Tall	Low	2	NO-PLIF
3	Flat	Low	3	Pressure	11	Tall	Low	3	Pressure
	Flat	Low	3	Mie		Tall	Low	3	Mie
	Flat	Low	3	NO-PLIF		Tall	Low	3	NO-PLIF
4	Flat	High	2	Pressure	12	Tall	High	2	Pressure
	Flat	High	2	NO-PLIF		Tall	High	2	NO-PLIF
5	Medium	Low	1	Pressure	13	Wide	Low	1	Pressure
	Medium	Low	1	Mie		Wide	Low	1	Mie
	Medium	Low	1	NO-PLIF		Wide	Low	1	NO-PLIF
6	Medium	Low	2	Pressure	14	Wide	Low	2	Pressure
	Medium	Low	2	Mie		Wide	Low	2	Mie
	Medium	Low	2	NO-PLIF		Wide	Low	2	NO-PLIF
7	Medium	Low	3	Pressure	15	Wide	Low	3	Pressure
	Medium	Low	3	Mie		Wide	Low	3	Mie
	Medium	Low	3	NO-PLIF		Wide	Low	3	NO-PLIF
8	Medium	High	2	Pressure	16	Wide	High	2	Pressure
	Medium	High	2	NO-PLIF		Wide	High	2	NO-PLIF

Appendix E – NO Intensity Values

Table E1. Mean image maximum intensity values

x/d	F1 intensity	F1 normalized	F2 intensity	F2 normalized	F2BP intensity	F2BP normalized	F3 intensity	F3 normalized
0	1.52	1.000	2.05	1.000	1.95	1.000	1.69	1.000
4	0.44	0.289	0.4	0.195			0.3	0.178
8	0.22	0.145	0.19	0.093	0.12	0.062	0.14	0.083
12	0.12	0.079	0.12	0.059			0.09	0.053
16	0.1	0.066	0.1	0.049	0.04	0.021	0.07	0.041
20	0.1	0.066	0.1	0.049			0.08	0.047
24	0.08	0.053	0.08	0.039				
32	0.06	0.039						

x/d	M1 intensity	M1 normalized	M2 intensity	M2 normalized	M2BP intensity	M2BP normalized	M3 intensity	M3 normalized
0	1.51	1.000	2.04	1.000	1.63	1.000	1.88	1.000
4	0.36	0.238	0.34	0.167			0.26	0.138
8	0.19	0.126	0.2	0.098	0.07	0.043	0.15	0.080
12	0.14	0.093	0.13	0.064			0.1	0.053
16	0.11	0.073	0.11	0.054	0.04	0.025	0.08	0.043
20	0.13	0.086	0.12	0.059			0.08	0.043
24	0.11	0.073	0.1	0.049				
32	0.08	0.053						

x/d	T1 intensity	T1 normalized	T2 intensity	T2 normalized	T2BP intensity	T2BP normalized	T3 intensity	T3 normalized
0	1.09	1.000	1.74	1.000	1.58	1.000	1.78	1.000
4	0.29	0.266	0.29	0.167			0.21	0.118
8	0.13	0.119	0.13	0.075	0.03	0.019	0.1	0.056
12	0.08	0.073	0.09	0.052			0.07	0.039
16	0.07	0.064	0.08	0.046	0.02	0.013	0.06	0.034
20	0.08	0.073	0.08	0.046			0.07	0.039
24	0.08	0.073	0.07	0.040				
32	0.06	0.055						

x/d	W1 intensity	W1 normalized	W2 intensity	W2 normalized	W2BP intensity	W2BP normalized	W3 intensity	W3 normalized
0	1.48	1.000	1.72	1.000	1.52	1.000	1.6	1.000
4	0.37	0.250	0.29	0.169			0.23	0.144
8	0.2	0.135	0.17	0.099	0.13	0.086	0.12	0.075
12	0.14	0.095	0.11	0.064			0.08	0.050
16	0.12	0.081	0.09	0.052	0.04	0.026	0.06	0.038
20	0.13	0.088	0.1	0.058			0.06	0.038
24	0.11	0.074	0.08	0.047				
32	0.08	0.054						

Table E2. Standard deviation image maximum intensity values

x/d	F1 intensity	normalized	F2 intensity	normalized	F2BP intensity	normalized	F3 intensity	normalized
0	943	1.000	1143	1.000	1067	1.000	972	1.000
4	849	0.900	1114	0.975			1012	1.041
8	680	0.721	734	0.642	515	0.483	518	0.533
12	503	0.533	481	0.421			345	0.355
16	374	0.397	389	0.340	175	0.164	273	0.281
20	302	0.320	301	0.263			210	0.216
24	249	0.264	244	0.213				
32	197	0.209						

x/d	M1 intensity	normalized	M2 intensity	normalized	M2BP intensity	normalized	M3 intensity	normalized
0	899	1.000	877	1.000	1619	1.000	705	1.000
4	898	0.999	788	0.899			496	0.704
8	604	0.672	509	0.580	263	0.162	369	0.523
12	437	0.486	394	0.449			296	0.420
16	381	0.424	338	0.385	130	0.080	260	0.369
20	339	0.377	299	0.341			221	0.313
24	318	0.354	278	0.317				
32	261	0.290						

x/d	T1 intensity	normalized	T2 intensity	normalized	T2BP intensity	normalized	T3 intensity	normalized
0	598	1.000	678	1.000	1086	1.000	664	1.000
4	565	0.945	638	0.941			429	0.646
8	403	0.674	366	0.540	153	0.141	224	0.337
12	273	0.457	280	0.413			205	0.309
16	251	0.420	221	0.326	182	0.168	163	0.245
20	211	0.353	197	0.291			148	0.223
24	195	0.326	175	0.258				
32	180	0.301						

x/d	W1 intensity	normalized	W2 intensity	normalized	W2BP intensity	normalized	W3 intensity	normalized
0	682	1.000	643	1.000	842	1.000	599	1.000
4	774	1.135	553	0.860			475	0.793
8	525	0.770	430	0.669	352	0.418	344	0.574
12	444	0.651	361	0.561			280	0.467
16	375	0.550	315	0.490	187	0.222	221	0.369
20	340	0.499	272	0.423			179	0.299
24	303	0.444	231	0.359				
32	266	0.390						

Note: Highlighted regions show higher than expected standard deviation intensities.
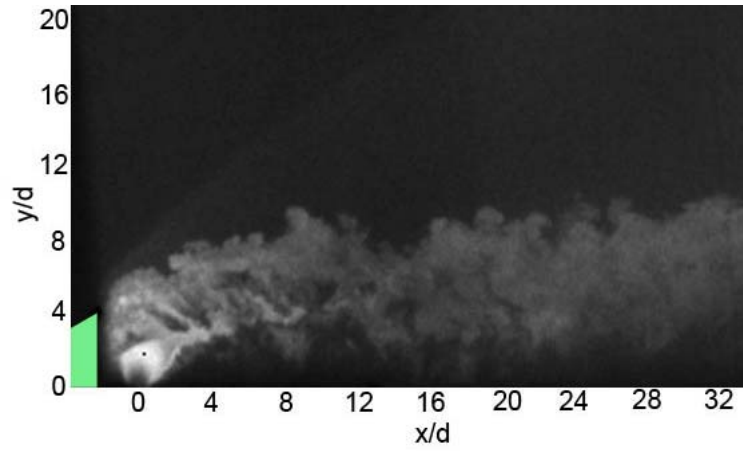
Figure F1. Instantaneous NO-PLIF profile view, Medium pylon

Flat

Medium

Tall

Wide
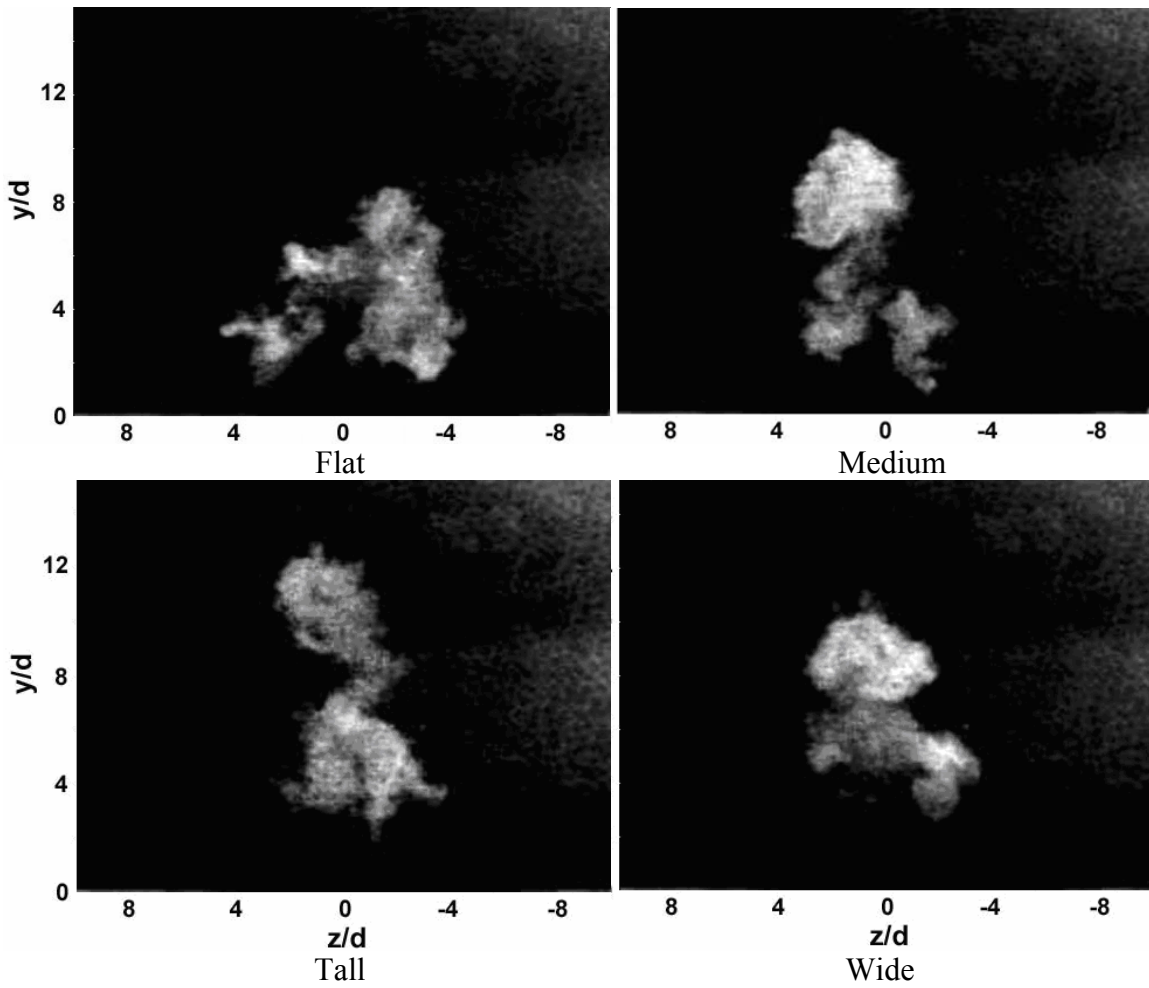
Figure F2. Instantaneous NO-PLIF end view images (x/d = 16)

Table F1. F1 geometry

F1	x = 0 d	4	8	12	16	20	24	32
yj (inches)	0.26	0.38	0.42	0.47	0.49	0.52	0.53	0.57
yj/d	4.17	6.09	6.70	7.48	7.83	8.26	8.52	9.13
Δy (inches)	0.26	0.32	0.39	0.46	0.48	0.52	0.53	0.57
Δy/d	4.17	5.13	6.26	7.30	7.74	8.26	8.52	9.13
g/d	0.00	0.96	0.43	0.17	0.09	0.00	0.00	0.00
Δz (inches)	0.32	0.50	0.58	0.62	0.66	0.67	0.71	0.74
Δz/d	5.13	8.00	9.30	9.91	10.61	10.78	11.30	11.91
Aj (in2)	0.06	0.13	0.18	0.22	0.25	0.29	0.29	0.35
Aj/d2	16.61	32.50	45.47	55.64	63.76	73.38	74.76	88.85
As/Aj	0.09	0.39	0.35	0.30	0.41	0.38	0.39	0.43

Table F2. F2 geometry

F2	x = 0 d	4	8	12	16	20	24
yj (inches)	0.19	0.29	0.34	0.37	0.40	0.42	0.43
yj/d	3.04	4.70	5.39	5.91	6.35	6.70	6.87
Δy (inches)	0.19	0.27	0.33	0.37	0.40	0.42	0.43
Δy/d	3.04	4.26	5.22	5.91	6.35	6.70	6.87
g/d	0.00	0.43	0.17	0.00	0.00	0.00	0.00
Δz (inches)	0.23	0.41	0.45	0.48	0.51	0.53	0.58
Δz/d	3.74	6.52	7.22	7.74	8.09	8.43	9.22
Aj (in2)	0.04	0.09	0.12	0.14	0.17	0.18	0.20
Aj/d2	9.02	21.91	30.13	36.29	42.59	46.27	51.61
As/Aj	0.23	0.36	0.30	0.37	0.38	0.33	0.42

Table F3. F3 and F2BP geometry

F3	x = 0 d	4	8	12	16	20
yj (inches)	0.14	0.23	0.26	0.29	0.33	0.33
yj/d	2.26	3.65	4.17	4.70	5.30	5.30
Δy (inches)	0.14	0.23	0.26	0.29	0.33	0.33
Δy/d	2.26	3.65	4.17	4.70	5.30	5.30
g/d	0.00	0.00	0.00	0.00	0.00	0.00
Δz (inches)	0.19	0.32	0.36	0.39	0.42	0.45
Δz/d	3.04	5.04	5.74	6.26	6.70	7.13
Aj (in2)	0.02	0.05	0.07	0.09	0.11	0.12
Aj/d2	5.18	13.99	19.11	24.14	28.85	31.11
As/Aj	0.42	0.29	0.34	0.44	0.46	0.46

F2BP	x = 0 d	4	8
yj (inches)	0.21	0.40	0.62
yj/d	3.39	6.35	9.91
Δy (inches)	0.21	0.40	0.62
Δy/d	3.39	6.35	9.91
g/d	0.00	0.00	0.00
Δz (inches)	0.24	0.52	0.67
Δz/d	3.91	8.35	10.70
Aj (in2)	0.04	0.16	0.34
Aj/d2	9.82	41.05	85.82
As/Aj	0.38	0.33	0.24

Table F4. M1 geometry

M1	x = 0 d	4	8	12	16	20	24	32
yj (inches)	0.43	0.55	0.62	0.65	0.67	0.70	0.72	0.75
yj/d	6.96	8.87	9.91	10.43	10.70	11.22	11.48	12.00
yj/h	1.74	2.22	2.48	2.61	2.67	2.80	2.87	3.00
Δy (inches)	0.43	0.49	0.57	0.60	0.62	0.66	0.68	0.74
Δy/d	6.96	7.91	9.04	9.57	9.91	10.52	10.87	11.83
g/d	0.00	0.96	0.87	0.87	0.78	0.70	0.61	0.17
Δz (inches)	0.26	0.44	0.40	0.46	0.48	0.47	0.50	0.56
Δz/d	4.09	7.04	6.43	7.39	7.74	7.57	8.00	8.96
Δz/W	3.65	6.29	5.75	6.60	6.91	6.75	7.14	8.00
Aj (in2)	0.07	0.14	0.19	0.21	0.24	0.26	0.28	0.32
Aj/d2	18.77	35.09	47.69	53.61	60.84	65.69	71.27	82.93
As/Aj	0.06	0.18	0.34	0.38	0.29	0.22	0.19	0.22

Table F5. M2 geometry

M2	x = 0 d	4	8	12	16	20	24
yj (inches)	0.39	0.48	0.52	0.55	0.57	0.59	0.61
yj/d	6.17	7.65	8.35	8.78	9.04	9.48	9.74
yj/h	1.54	1.91	2.09	2.20	2.26	2.37	2.43
Δy (inches)	0.39	0.44	0.47	0.49	0.51	0.54	0.55
Δy/d	6.17	7.04	7.57	7.91	8.09	8.61	8.87
g/d	0.00	0.61	0.78	0.87	0.96	0.87	0.87
Δz (inches)	0.18	0.25	0.30	0.34	0.39	0.41	0.45
Δz/d	2.96	4.00	4.78	5.39	6.17	6.52	7.13
Δz/W	2.64	3.57	4.27	4.81	5.51	5.82	6.37
Aj (in2)	0.05	0.09	0.11	0.13	0.15	0.17	0.18
Aj/d2	11.76	22.59	28.70	33.91	38.44	42.65	46.71
As/Aj	0.11	0.17	0.23	0.29	0.25	0.27	0.22

Table F6. M3 and M2BP geometry

M3	x = 0 d	4	8	12	16	20	M2BP	x = 0 d	4	8
yj (inches)	0.34	0.40	0.43	0.46	0.48	0.49	yj (inches)	0.39	0.65	0.84
yj/d	5.39	6.43	6.87	7.30	7.65	7.91	yj/d	6.26	10.43	13.39
yj/h	1.35	1.61	1.72	1.83	1.91	1.98	yj/h	1.57	2.61	3.35
Δy (inches)	0.34	0.38	0.39	0.39	0.41	0.42	Δy (inches)	0.39	0.56	0.64
Δy/d	5.39	6.09	6.17	6.26	6.52	6.70	Δy/d	6.26	8.96	10.17
g/d	0.00	0.35	0.70	1.04	1.13	1.22	g/d	0.00	1.48	3.22
Δz (inches)	0.14	0.21	0.26	0.30	0.34	0.36	Δz (inches)	0.18	0.48	0.58
Δz/d	2.26	3.30	4.09	4.78	5.39	5.83	Δz/d	2.87	7.65	9.22
Δz/W	2.02	2.95	3.65	4.27	4.81	5.20	Δz/W	2.56	6.83	8.23
Aj (in2)	0.03	0.06	0.07	0.09	0.11	0.12	Aj (in2)	0.05	0.21	0.29
Aj/d2	7.92	15.12	19.12	23.08	27.15	30.58	Aj/d2	13.38	54.20	75.30
As/Aj	0.19	0.37	0.26	0.28	0.24	0.25	As/Aj	0.08	0.31	0.33

Table F7. T1 geometry

T1	x = 0 d	4	8	12	16	20	24	32
yj (inches)	0.54	0.64	0.71	0.77	0.78	0.79	0.80	0.85
yj/d	8.61	10.17	11.39	12.35	12.43	12.61	12.78	13.57
yj/h	1.43	1.70	1.90	2.06	2.07	2.10	2.13	2.26
Δy (inches)	0.54	0.56	0.64	0.69	0.70	0.71	0.72	0.79
Δy/d	8.61	8.96	10.17	11.04	11.22	11.39	11.57	12.70
g/d	0.00	1.22	1.22	1.30	1.22	1.22	1.22	0.87
Δz (inches)	0.21	0.33	0.40	0.45	0.46	0.47	0.49	0.52
Δz/d	3.39	5.30	6.35	7.13	7.30	7.48	7.83	8.35
Δz/W	3.03	4.74	5.67	6.37	6.52	6.68	6.99	7.45
Aj (in2)	0.07	0.13	0.18	0.21	0.25	0.27	0.29	0.34
Aj/d2	18.54	32.49	46.65	54.91	62.88	68.56	74.99	86.53
As/Aj	0.05	0.19	0.23	0.39	0.28	0.31	0.43	0.25

Table F8. T2 geometry

T2	x = 0 d	4	8	12	16	20	24
yj (inches)	0.48	0.57	0.63	0.66	0.66	0.68	0.70
yj/d	7.74	9.13	10.00	10.52	10.61	10.96	11.13
yj/h	1.29	1.52	1.67	1.75	1.77	1.83	1.86
Δy (inches)	0.48	0.52	0.57	0.59	0.58	0.61	0.61
Δy/d	7.74	8.35	9.04	9.39	9.30	9.74	9.83
g/d	0.00	0.78	0.96	1.13	1.30	1.22	1.30
Δz (inches)	0.16	0.22	0.26	0.30	0.34	0.37	0.40
Δz/d	2.52	3.57	4.17	4.78	5.48	5.91	6.43
Δz/W	2.25	3.18	3.73	4.27	4.89	5.28	5.75
Aj (in2)	0.04	0.09	0.12	0.14	0.16	0.17	0.19
Aj/d2	11.41	22.03	30.53	36.17	40.75	43.65	48.56
As/Aj	0.16	0.11	0.18	0.22	0.33	0.26	0.25

Table F9. T3 and T2BP geometry

T3	x = 0 d	4	8	12	16	20		T2BP	x = 0 d	4	8
yj (inches)	0.41	0.49	0.52	0.54	0.55	0.57		yj (inches)	0.49	0.91	0.85
yj/d	6.52	7.83	8.35	8.61	8.87	9.04		yj/d	7.83	14.61	13.57
yj/h	1.09	1.30	1.39	1.43	1.48	1.51		yj/h	1.30	2.43	2.26
Δy (inches)	0.41	0.46	0.48	0.49	0.51	0.53		Δy (inches)	0.49	0.91	0.78
Δy/d	6.52	7.39	7.74	7.83	8.09	8.52		Δy/d	7.83	14.61	12.43
g/d	0.00	0.43	0.61	0.78	0.78	0.52		g/d	0.00	0.00	1.13
Δz (inches)	0.15	0.20	0.24	0.29	0.33	0.36		Δz (inches)	0.14	0.89	0.80
Δz/d	2.35	3.13	3.91	4.70	5.22	5.83		Δz/d	2.26	14.26	12.78
Δz/W	2.10	2.80	3.49	4.19	4.66	5.20		Δz/W	2.02	12.73	11.41
Aj (in2)	0.03	0.06	0.09	0.10	0.12	0.12		Aj (in2)	0.06	0.66	0.45
Aj/d2	7.33	16.32	22.34	26.72	30.37	31.80		Aj/d2	15.58	167.98	115.78
As/Aj	0.22	0.15	0.45	0.23	0.33	0.25		As/Aj	0.07	0.10	0.30

Table F10. W1 geometry

W1	x = 0 d	4	8	12	16	20	24	32
yj (inches)	0.45	0.58	0.64	0.70	0.69	0.71	0.74	0.78
yj/d	7.13	9.22	10.17	11.13	11.04	11.39	11.91	12.43
yj/h	1.78	2.30	2.54	2.78	2.76	2.85	2.98	3.11
Δy (inches)	0.45	0.53	0.58	0.62	0.61	0.61	0.64	0.69
Δy/d	7.13	8.43	9.22	9.91	9.74	9.83	10.17	11.04
g/d	0.00	0.78	0.96	1.22	1.30	1.57	1.74	1.39
Δz (inches)	0.24	0.35	0.41	0.43	0.47	0.49	0.51	0.55
Δz/d	3.91	5.65	6.52	6.96	7.48	7.83	8.09	8.87
Δz/W	2.45	3.53	4.08	4.35	4.67	4.89	5.05	5.54
Aj (in2)	0.08	0.14	0.18	0.20	0.21	0.24	0.25	0.30
Aj/d2	19.56	34.87	45.56	51.67	54.98	60.33	65.17	76.08
As/Aj	0.13	0.14	0.35	0.27	0.22	0.21	0.21	0.18

Table F11. W2 geometry

W2	x = 0 d	4	8	12	16	20	24
yj (inches)	0.39	0.50	0.54	0.57	0.58	0.60	0.63
yj/d	6.26	8.00	8.61	9.13	9.30	9.57	10.09
yj/h	1.57	2.00	2.15	2.28	2.33	2.39	2.52
Δy (inches)	0.39	0.46	0.48	0.49	0.48	0.51	0.53
Δy/d	6.26	7.30	7.65	7.91	7.74	8.09	8.52
g/d	0.00	0.70	0.96	1.22	1.57	1.48	1.57
Δz (inches)	0.19	0.26	0.30	0.36	0.40	0.43	0.45
Δz/d	3.04	4.09	4.87	5.74	6.43	6.87	7.22
Δz/W	1.90	2.55	3.04	3.59	4.02	4.29	4.51
Aj (in2)	0.05	0.09	0.12	0.13	0.15	0.17	0.19
Aj/d2	12.66	23.80	29.63	34.35	38.68	42.83	47.62
As/Aj	0.28	0.32	0.26	0.23	0.24	0.24	0.22

Table F12. W3 and W2BP geometry

W3	x = 0 d	4	8	12	16	20	W2BP	x = 0 d	4	8
yj (inches)	0.33	0.41	0.44	0.47	0.49	0.51	yj (inches)	0.41	0.58	0.78
yj/d	5.30	6.52	7.04	7.57	7.91	8.17	yj/d	6.52	9.22	12.43
yj/h	1.33	1.63	1.76	1.89	1.98	2.04	yj/h	1.63	2.30	3.11
Δy (inches)	0.33	0.37	0.38	0.42	0.42	0.42	Δy (inches)	0.41	0.50	0.59
Δy/d	5.30	5.91	6.09	6.70	6.70	6.78	Δy/d	6.52	8.00	9.48
g/d	0.00	0.61	0.96	0.87	1.22	1.39	g/d	0.00	1.22	2.96
Δz (inches)	0.14	0.23	0.28	0.34	0.36	0.39	Δz (inches)	0.18	0.34	0.53
Δz/d	2.26	3.65	4.52	5.48	5.74	6.26	Δz/d	2.96	5.48	8.43
Δz/W	1.41	2.28	2.83	3.42	3.59	3.91	Δz/W	1.85	3.42	5.27
Aj (in2)	0.03	0.06	0.08	0.10	0.11	0.13	Aj (in2)	0.05	0.13	0.25
Aj/d2	8.25	15.77	20.76	26.09	28.64	32.82	Aj/d2	13.38	34.43	63.25
As/Aj	0.36	0.20	0.24	0.22	0.18	0.24	As/Aj	0.07	0.38	0.16

Appendix G – Mie Scattering Image Data Supplement
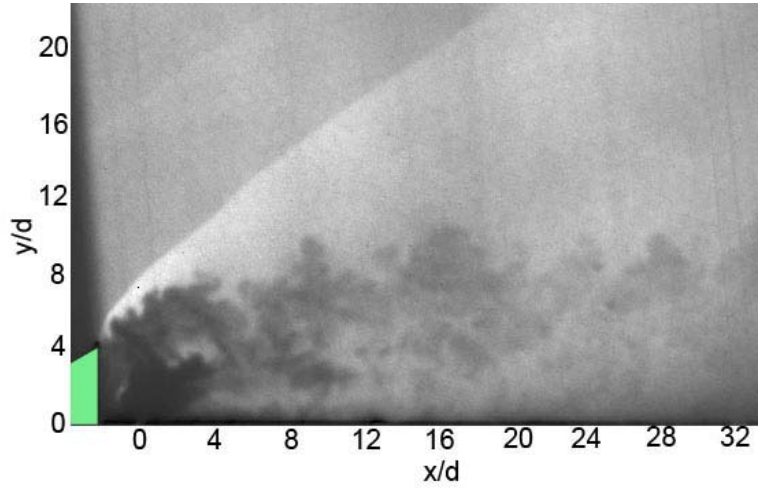
Figure G1. Instantaneous Mie scattering profile view image, Medium pylon

Flat

Medium

Tall

Wide
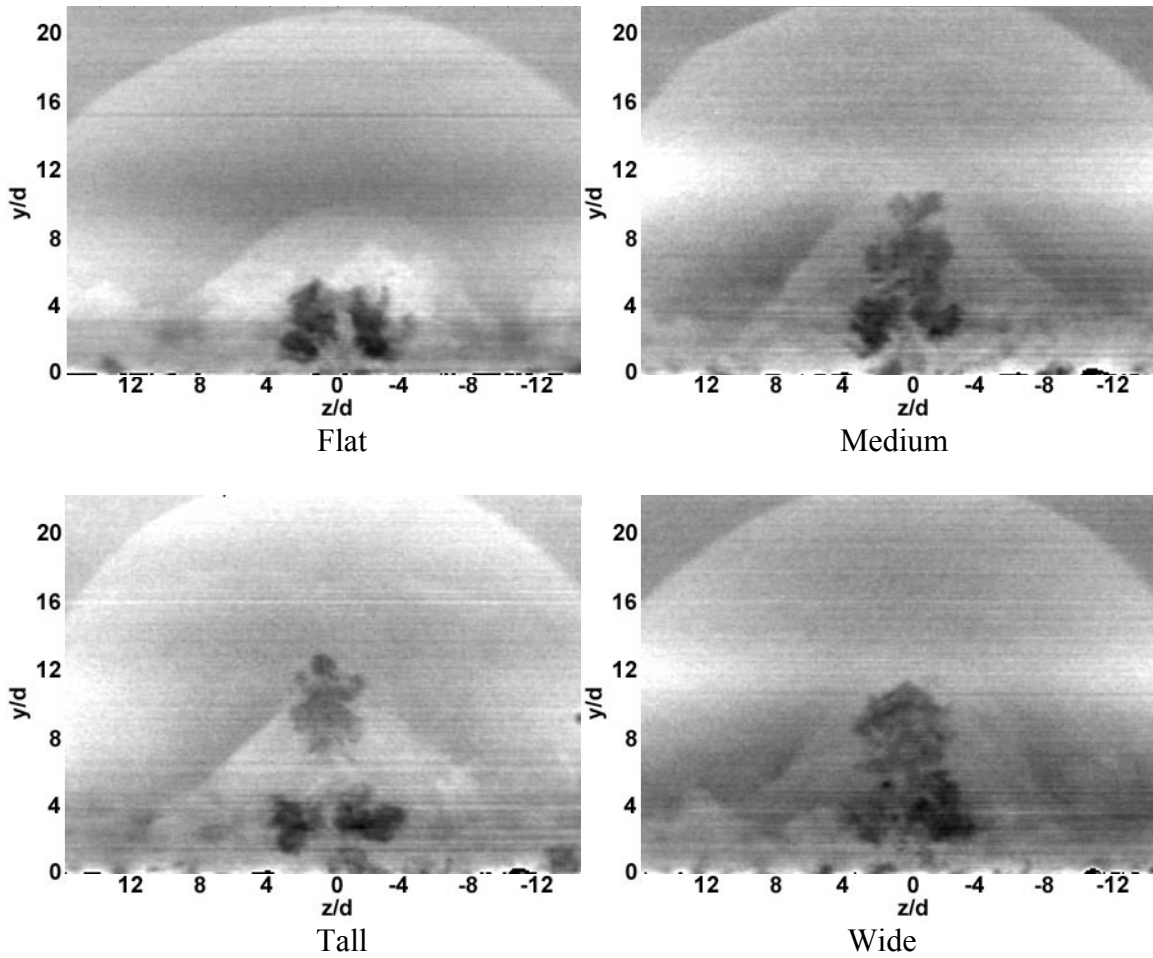
Figure G2. Instantaneous Mie scattering end view images (x/d = 16)

MIE SCATTER

END VIEW

FLAT INSERT

IMAGES

Figure G3. (F1) Mie Scatter, Flat insert, injection pressure 1, x/d = 0, 4, 8

Mean   d) x = 12 d   **Standard Deviation**

e) x = 16 d

f) x = 20 d

Figure G3 (cont'd). (F1) Mie scatter, Flat insert, injection pressure 1, x/d = 12, 16, 20

Mean   g) x = 24 d   **Standard Deviation**

h) x = 32 d

Figure G3 (cont'd). (F1) Mie scatter, Flat insert, injection pressure 1, x/d = 24, 32

a) x = 0 d

b) x = 4 d

c) x = 8 d
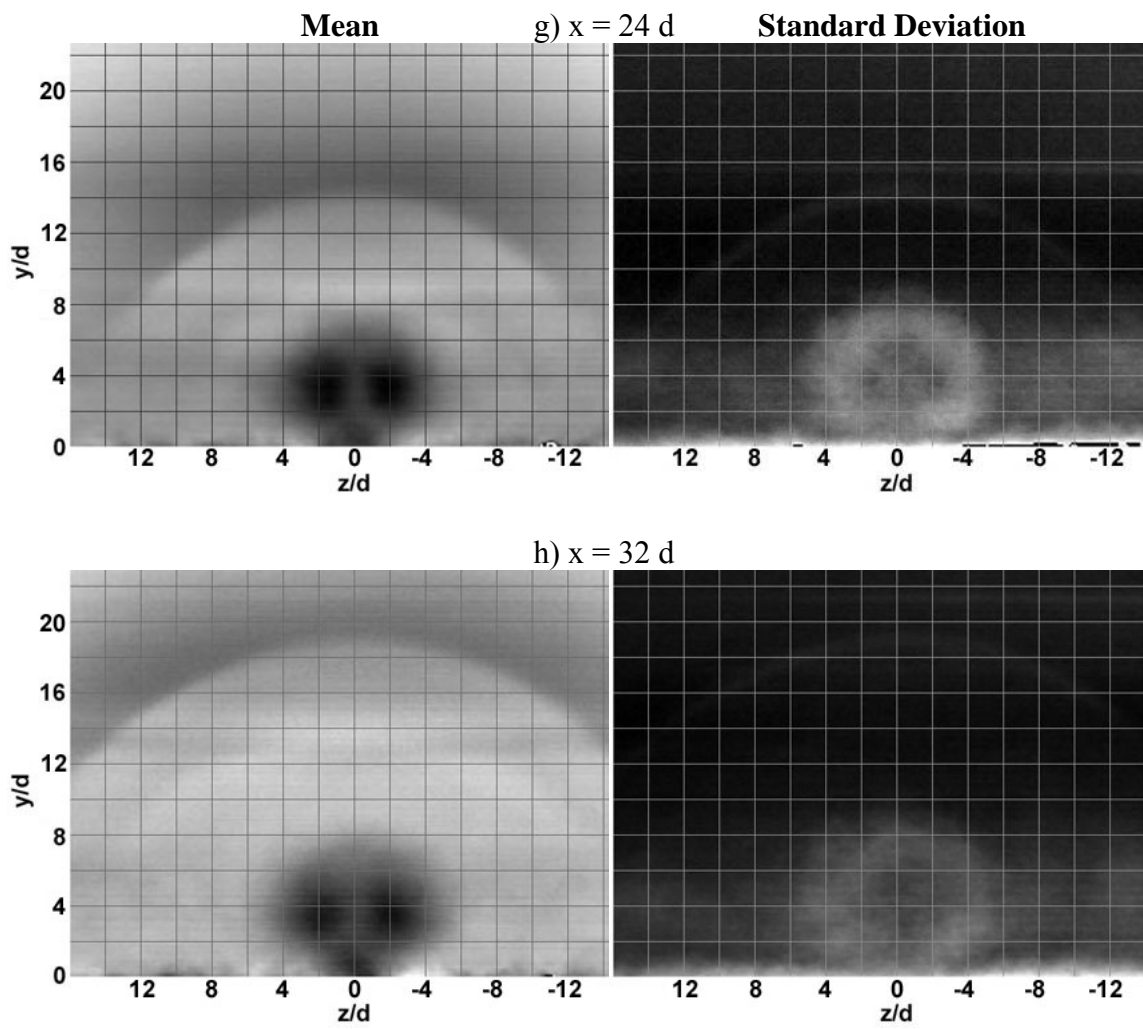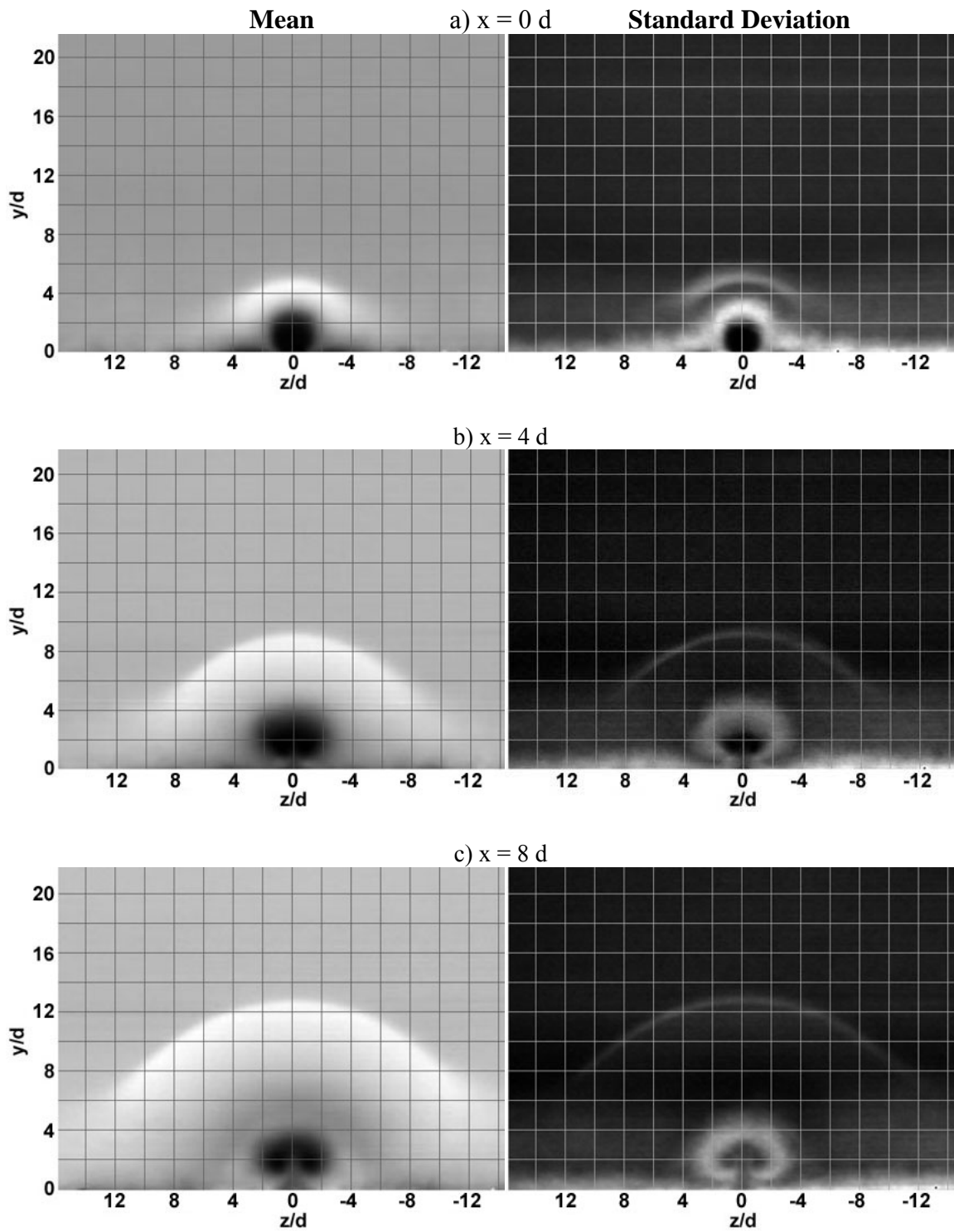
Figure G4. (F2) Mie scatter, Flat insert, injection pressure 2, x/d = 0, 4, 8
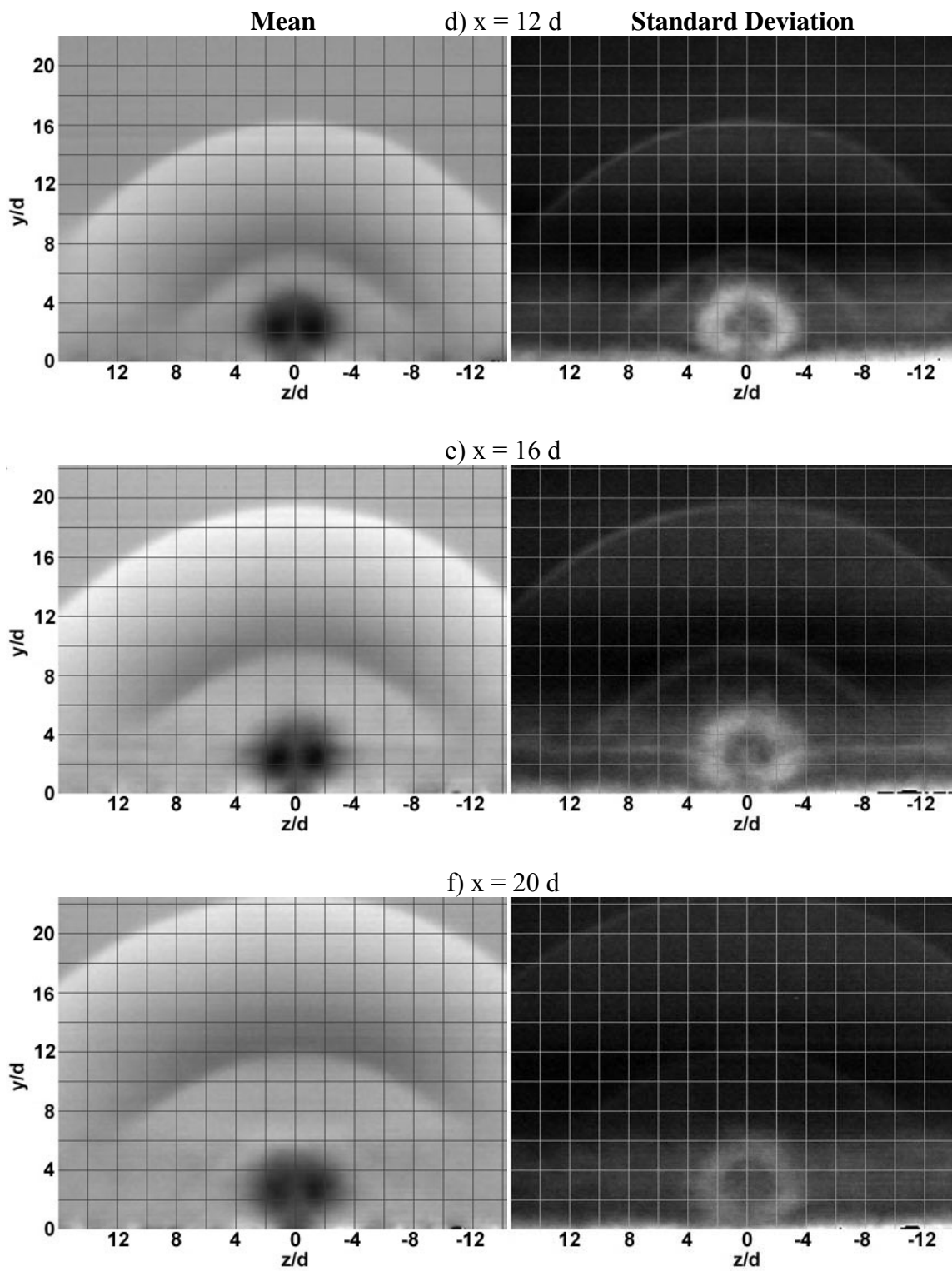
Mean   d) x = 12 d   **Standard Deviation**

e) x = 16 d

f) x = 20 d

Figure G4 (cont'd). (F2) Mie scatter, Flat insert, injection pressure 2, x/d = 12, 16, 20
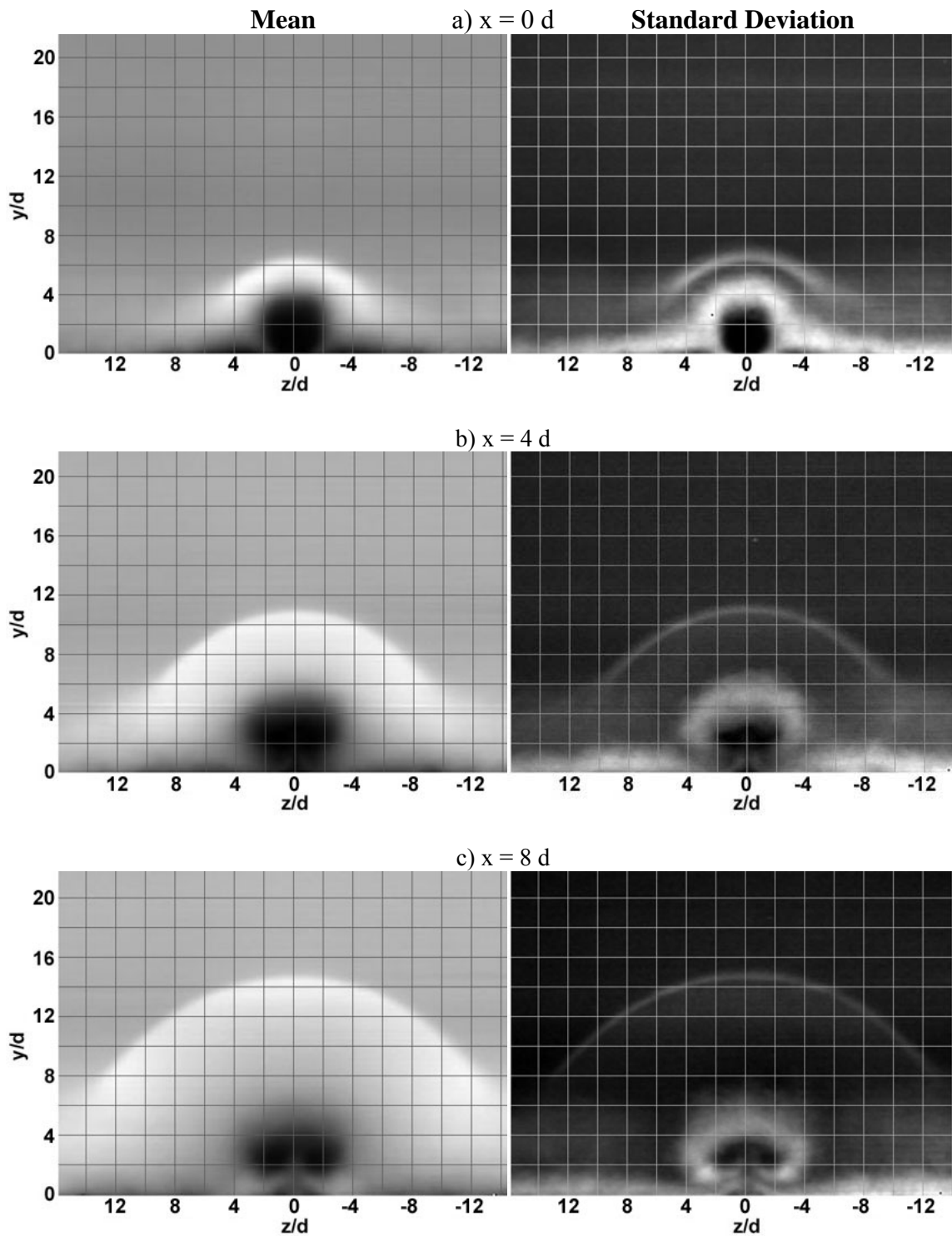
174

Mean   g) x = 24 d   **Standard Deviation**

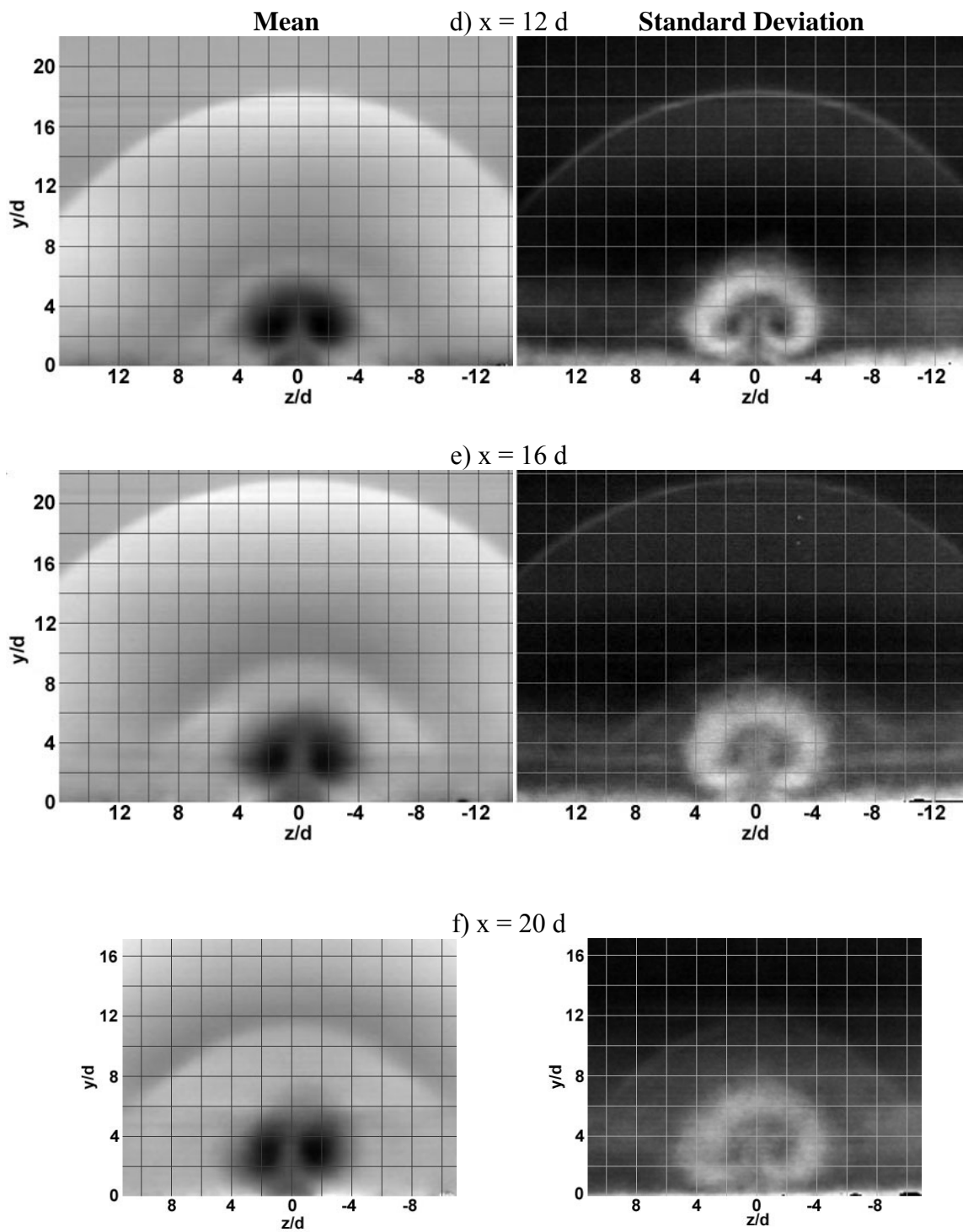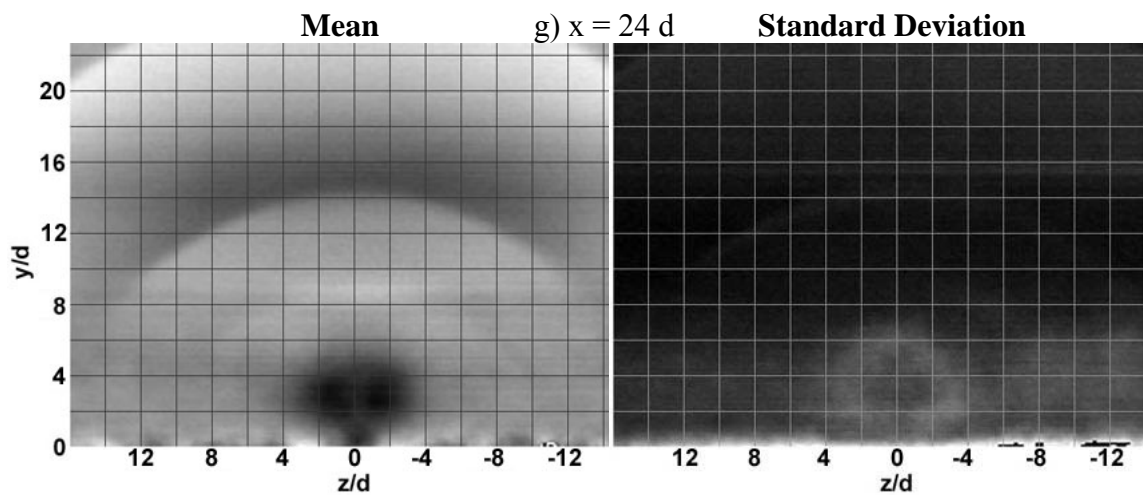**Figure G4 (cont'd).** (F2) Mie scatter, Flat insert, injection pressure 2, x/d = 24
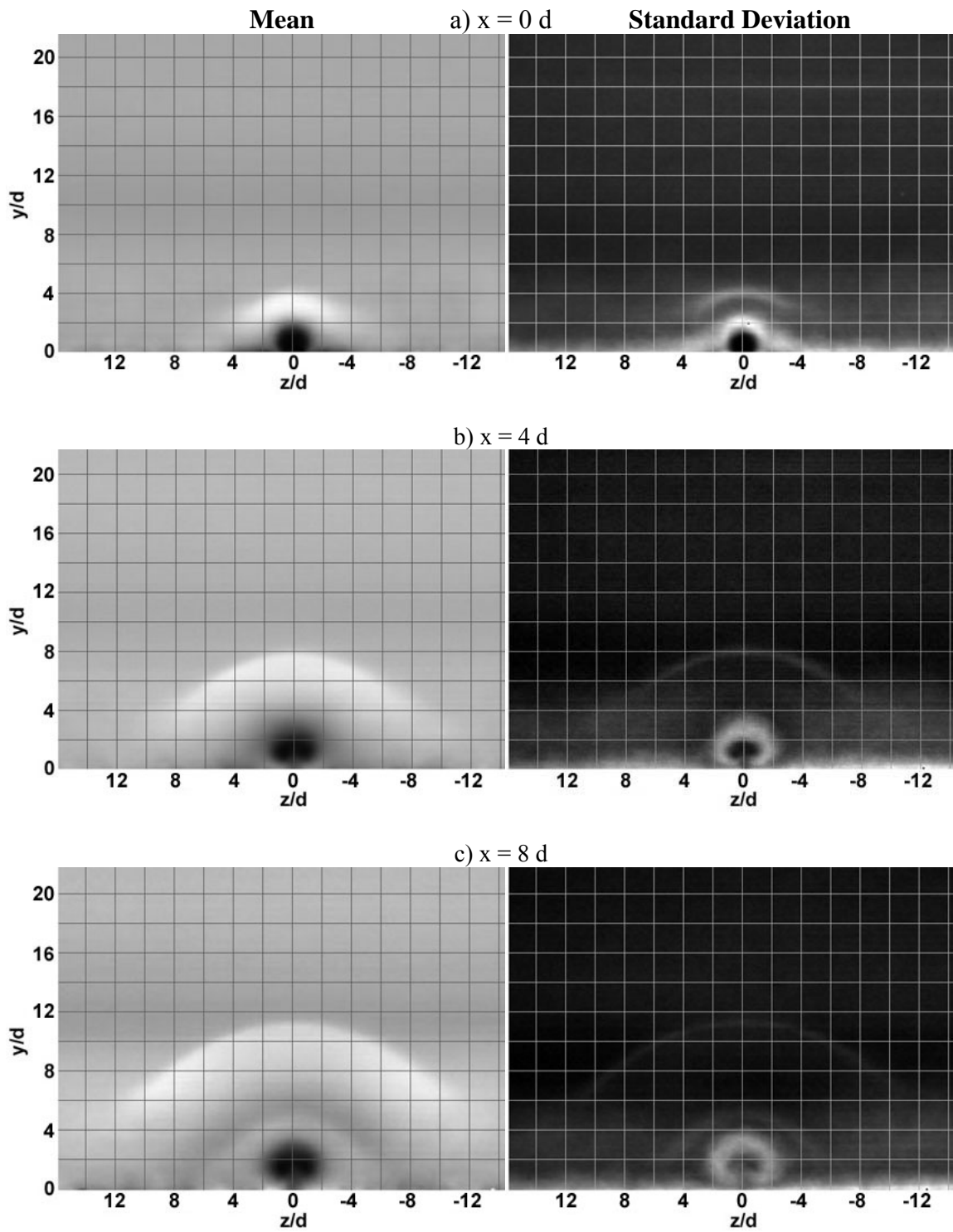
Figure G5. (F3) Mie scatter, Flat insert, injection pressure 3, x/d = 0, 4, 8

Mean   d) x = 12 d   **Standard Deviation**

e) x = 16 d

f) x = 20 d
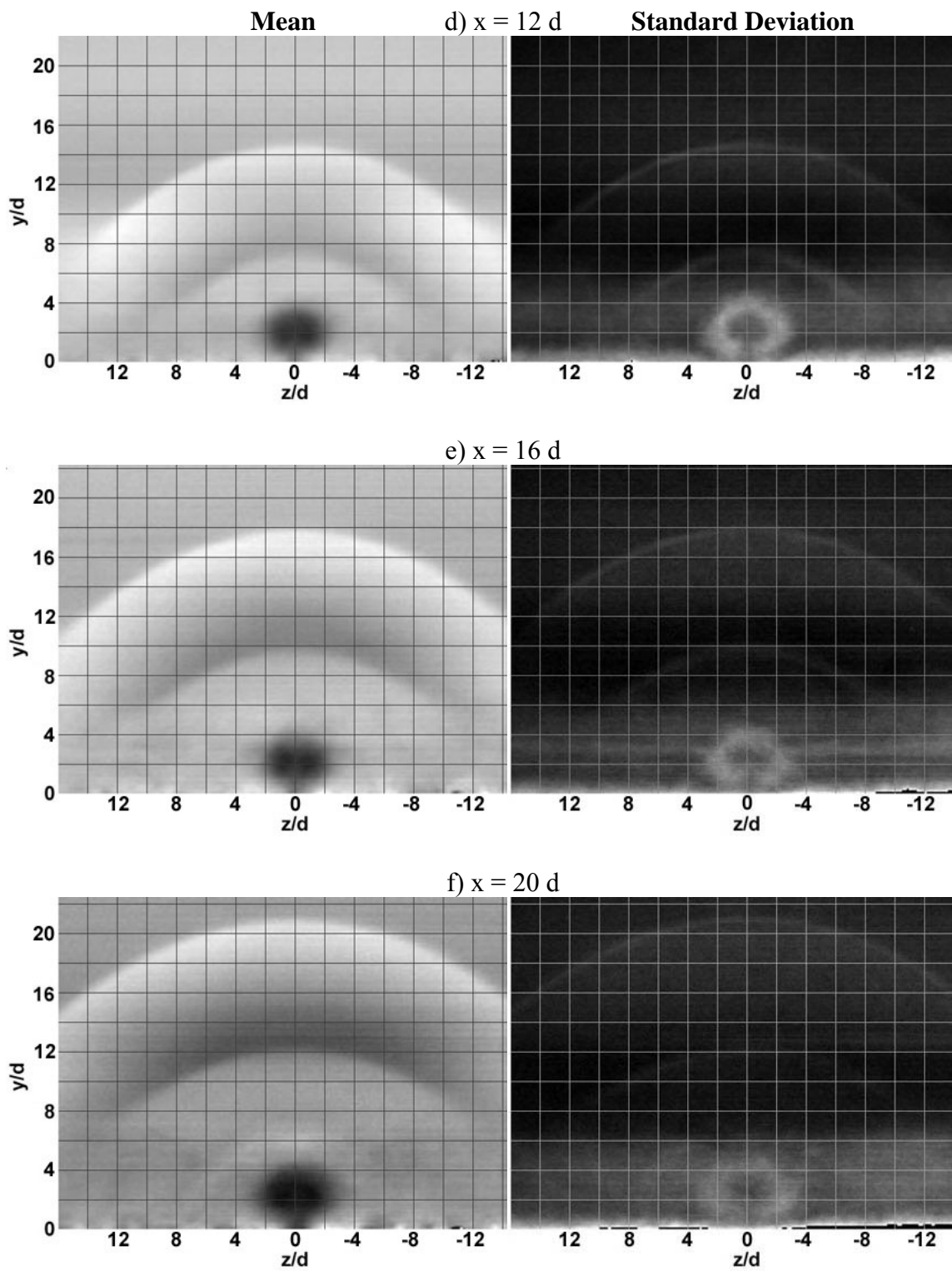
Figure G5 (cont'd). (F3) Mie scatter, Flat insert, injection pressure 3, x/d = 12, 16, 20

MIE SCATTER

END VIEW

MEDIUM INSERT

IMAGES
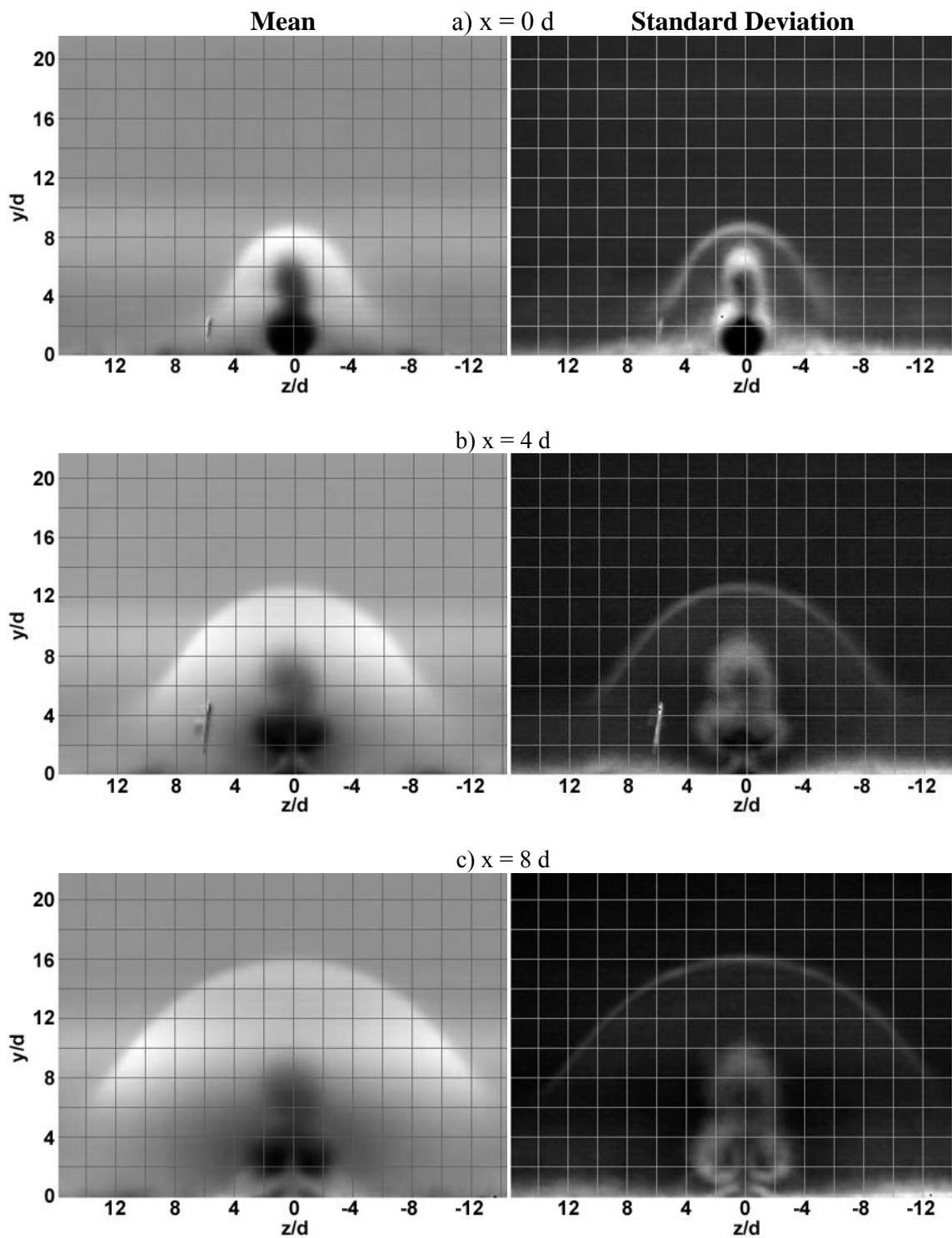
Figure G6. (M1) Mie scatter, Medium insert, injection pressure 1, x/d = 0, 4, 8
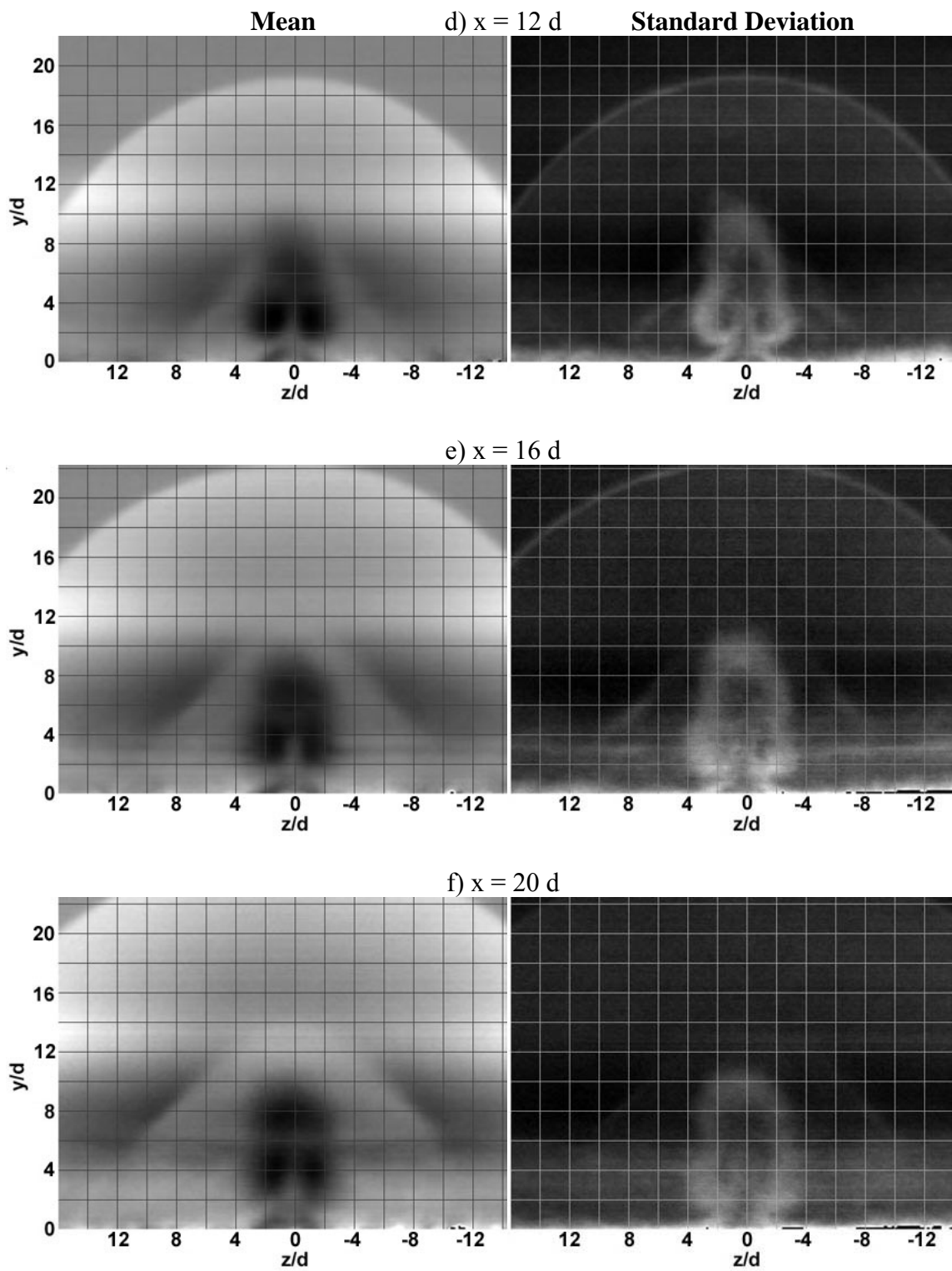
179

Mean d) x = 12 d **Standard Deviation**

e) x = 16 d

f) x = 20 d

Figure G6 (cont'd). (M1) Mie scatter, Medium insert, injection pressure 1, x/d = 12, 16, 20

Mean g) x = 24 d **Standard Deviation**

h) x = 32 d

Figure G6 (cont'd). (M1) Mie scatter, Medium insert, injection pressure 1, x/d = 24, 32

Mean   a) x = 0 d   **Standard Deviation**

b) x = 4 d

c) x = 8 d
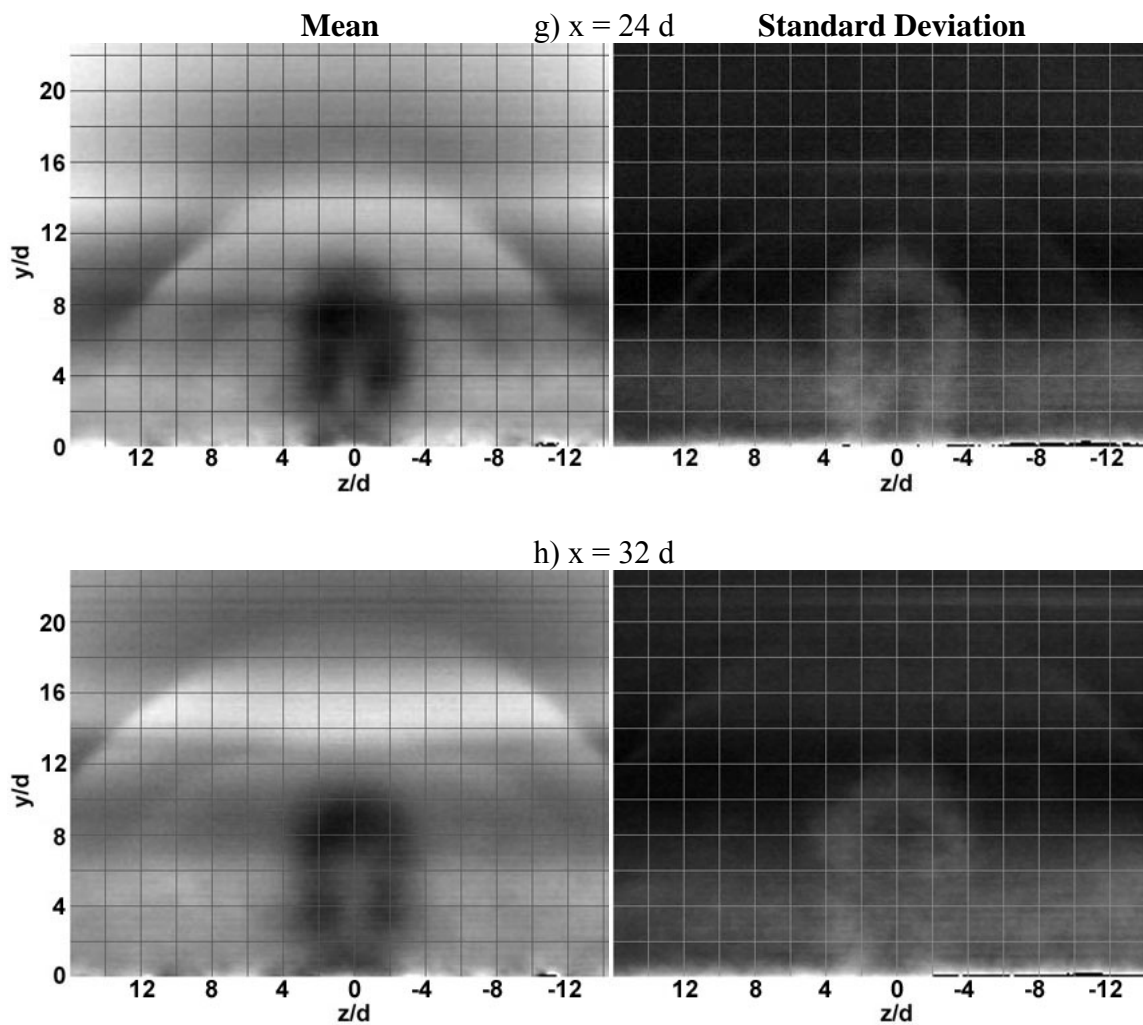
Figure G7. (M2) Mie scatter, Medium insert, injection pressure 2, x/d = 0, 4, 8

Mean d) x = 12 d **Standard Deviation**

e) x = 16 d

f) x = 20 d

Figure G7 (cont'd). (M2) Mie scatter, Medium insert, injection pressure 2, x/d = 12, 16, 20

183

Mean   g) x = 24 d   **Standard Deviation**

Figure G7 (cont'd). (M2) Mie scatter, Medium insert, injection pressure 2, x/d = 24

Mean a) x = 0 d **Standard Deviation**

b) x = 4 d

c) x = 8 d
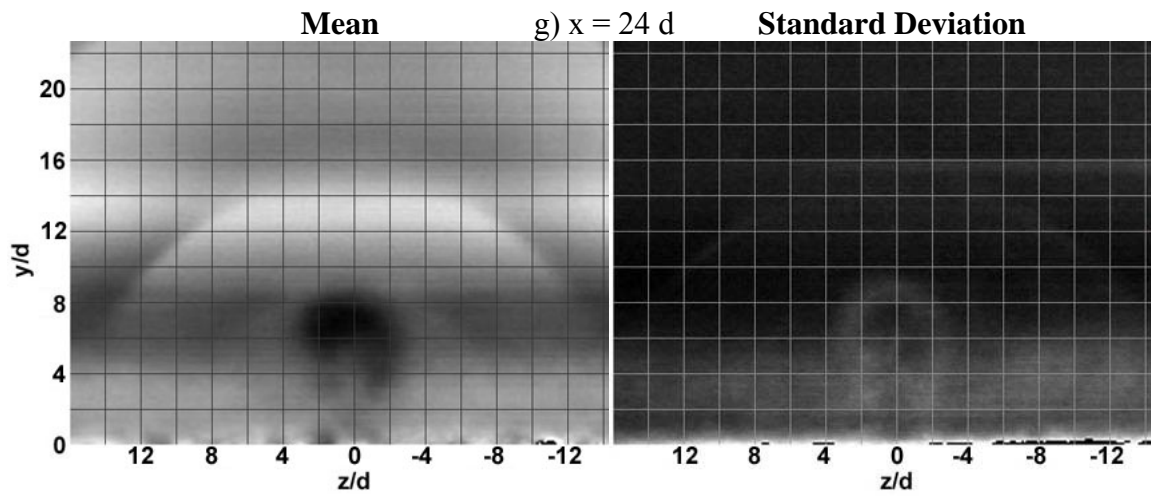
Figure G8. (M3) Mie scatter, Medium insert, injection pressure 3, x/d = 0, 4, 8

185

Mean   d) x = 12 d   **Standard Deviation**

e) x = 16 d

f) x = 20 d
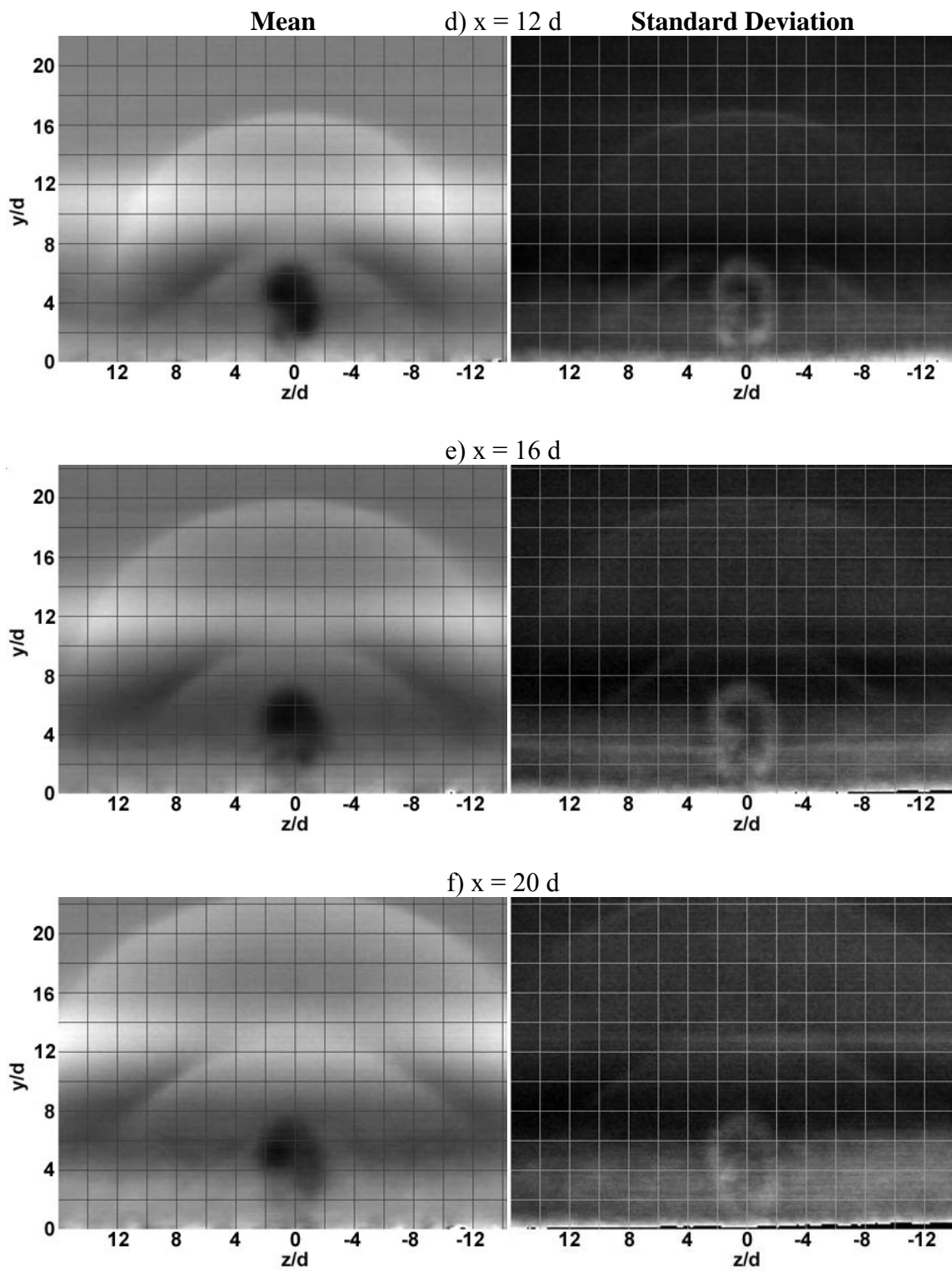
Figure G8 (cont'd). (M3) Mie scatter, Medium insert, injection pressure 3, x/d = 12, 16, 20

186

MIE SCATTER

END VIEW

TALL INSERT

IMAGES

Mean   a) x = 0 d   **Standard Deviation**

b) x = 4 d

c) x = 8 d
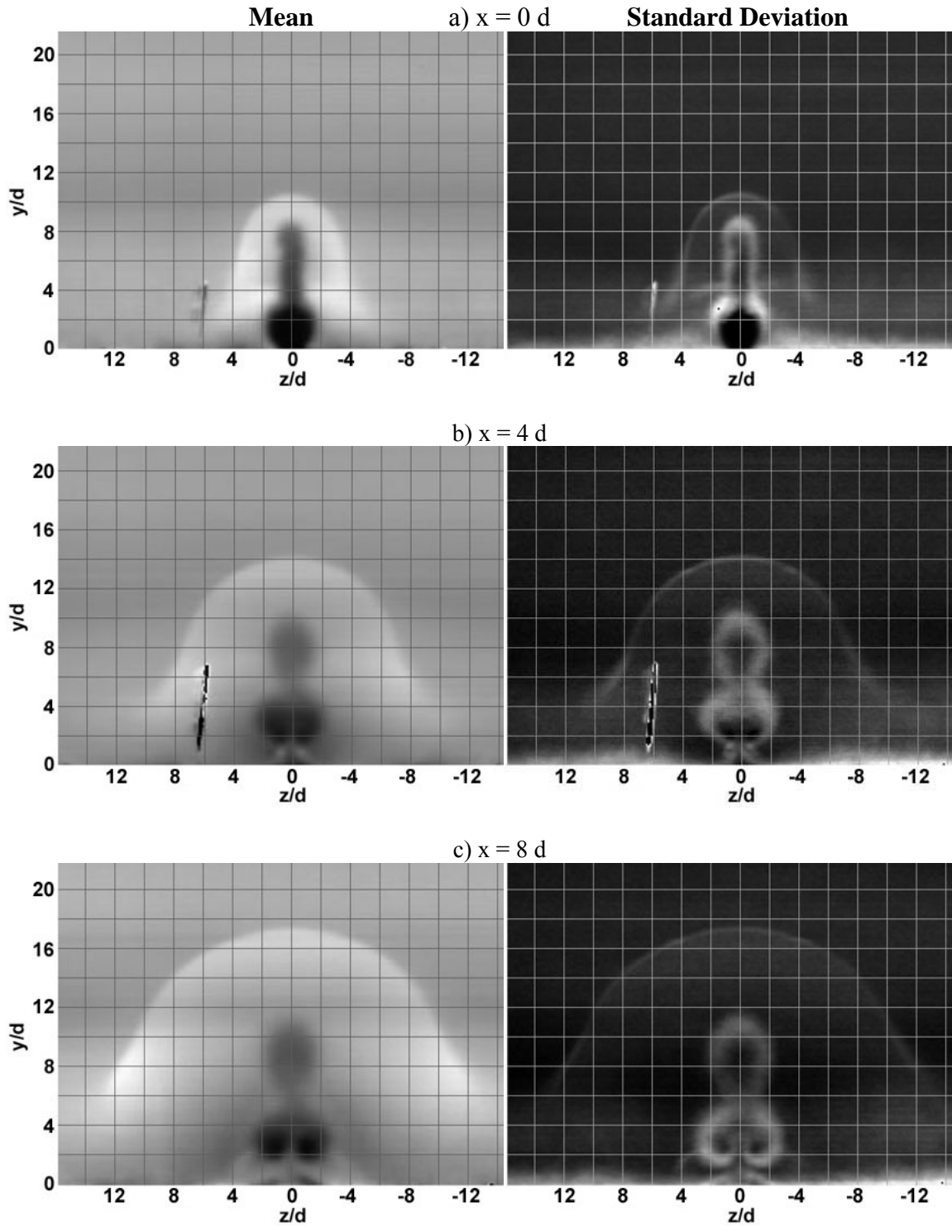
Figure G9. (T1) Mie scatter, Tall insert, injection pressure 1, x/d = 0, 4, 8
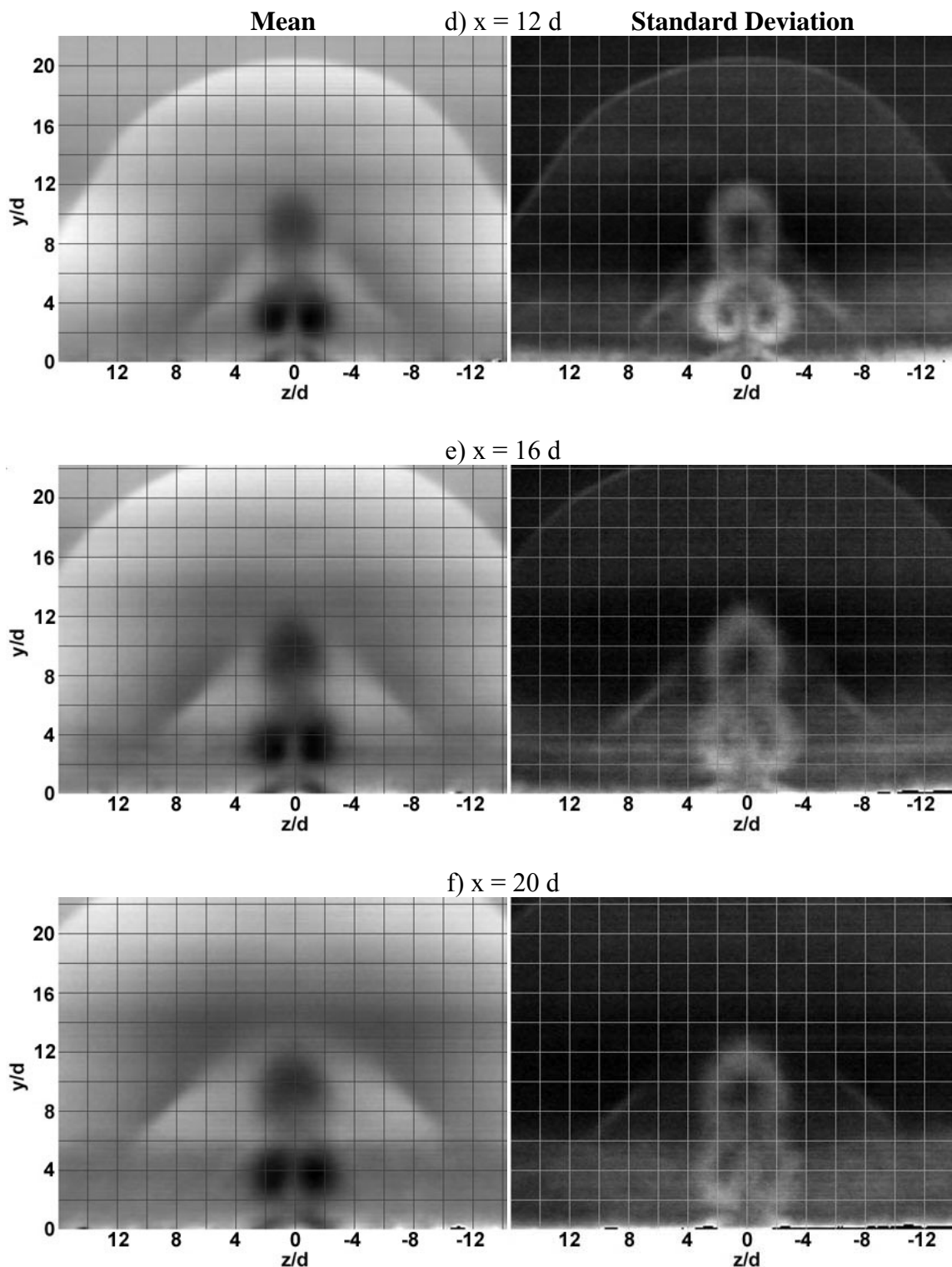
    UAppendix G

Mean   d) x = 12 d   **Standard Deviation**

e) x = 16 d

f) x = 20 d

Figure G9 (cont'd). (T1) Mie scatter, Tall insert, injection pressure 1, x/d = 12, 16, 20

Mean   g) x = 24 d   **Standard Deviation**

h) x = 32 d

Figure G9 (cont'd). (T1) Mie scatter, Tall insert, injection pressure 1, x/d = 24, 32

Mean a) x = 0 d **Standard Deviation**

b) x = 4 d

c) x = 8 d
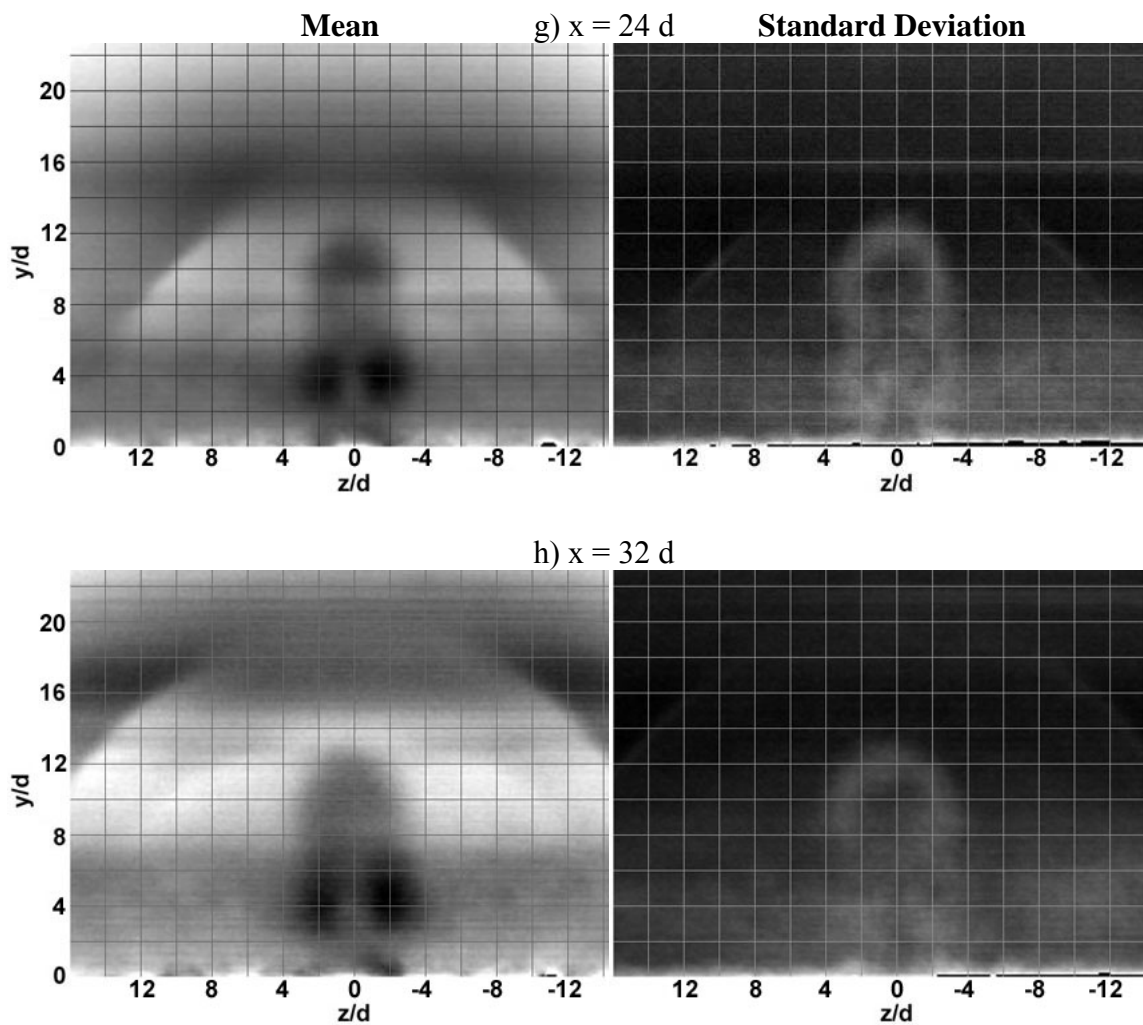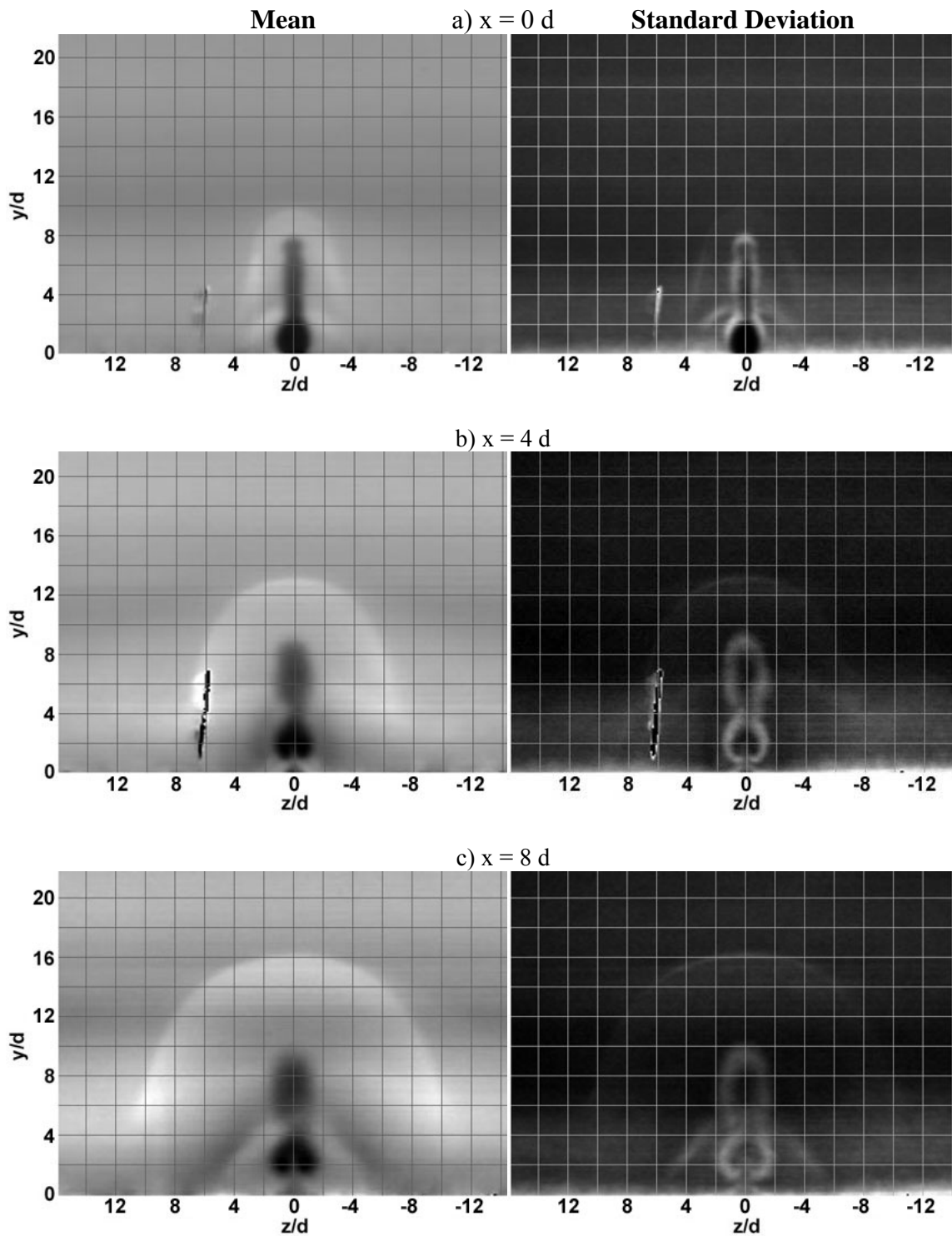
Figure G10. (T2) Mie scatter, Tall insert, injection pressure 2, x/d = 0, 4, 8

UAppendix G

Mean   d) x = 12 d   **Standard Deviation**

e) x = 16 d

f) x = 20 d
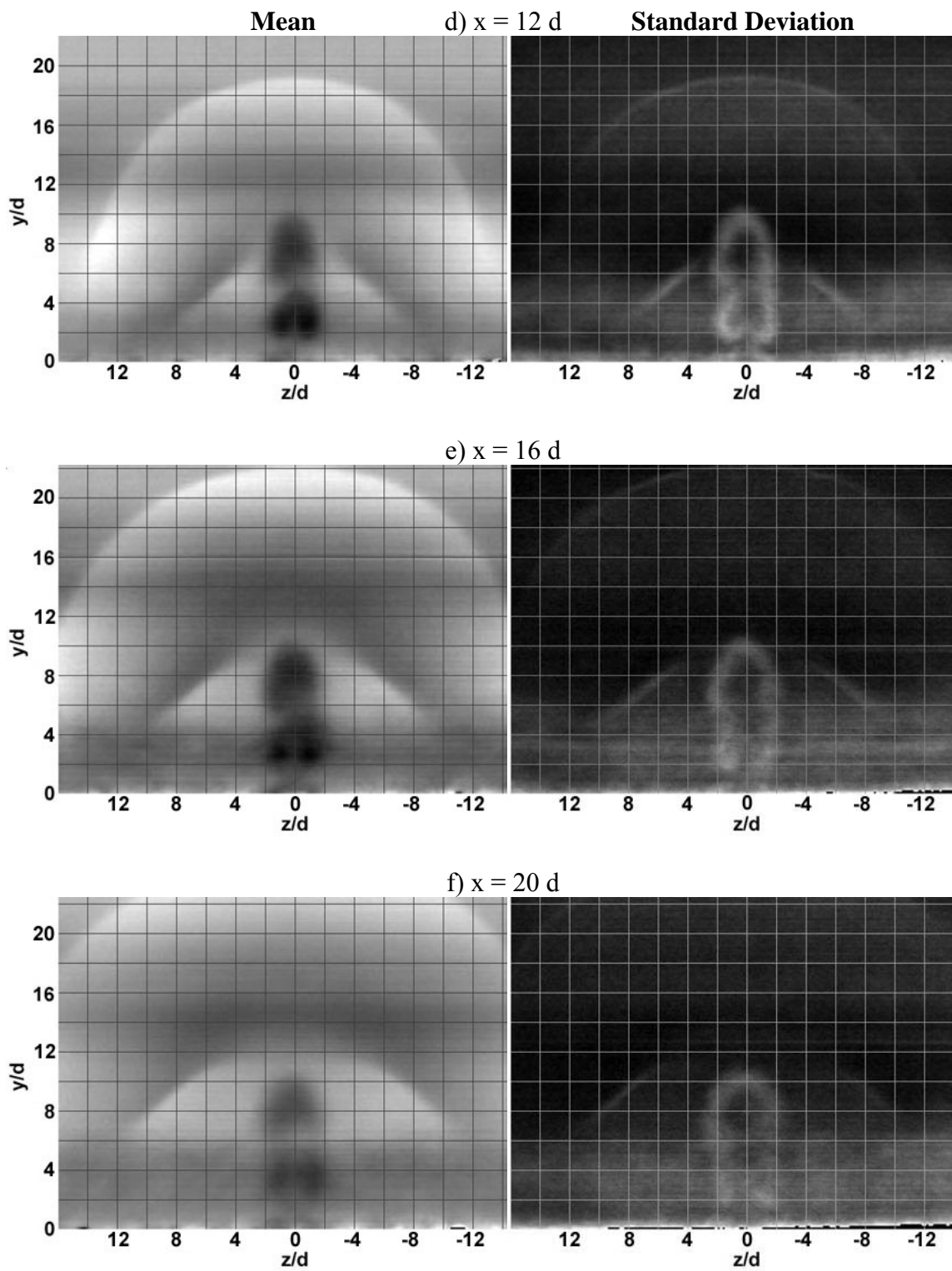
Figure G10 (cont'd). (T2) Mie scatter, Tall insert, injection pressure 2, x/d = 12, 16, 20

Figure G10 (cont'd). (T2) Mie scatter, Tall insert, injection pressure 2, x/d = 24

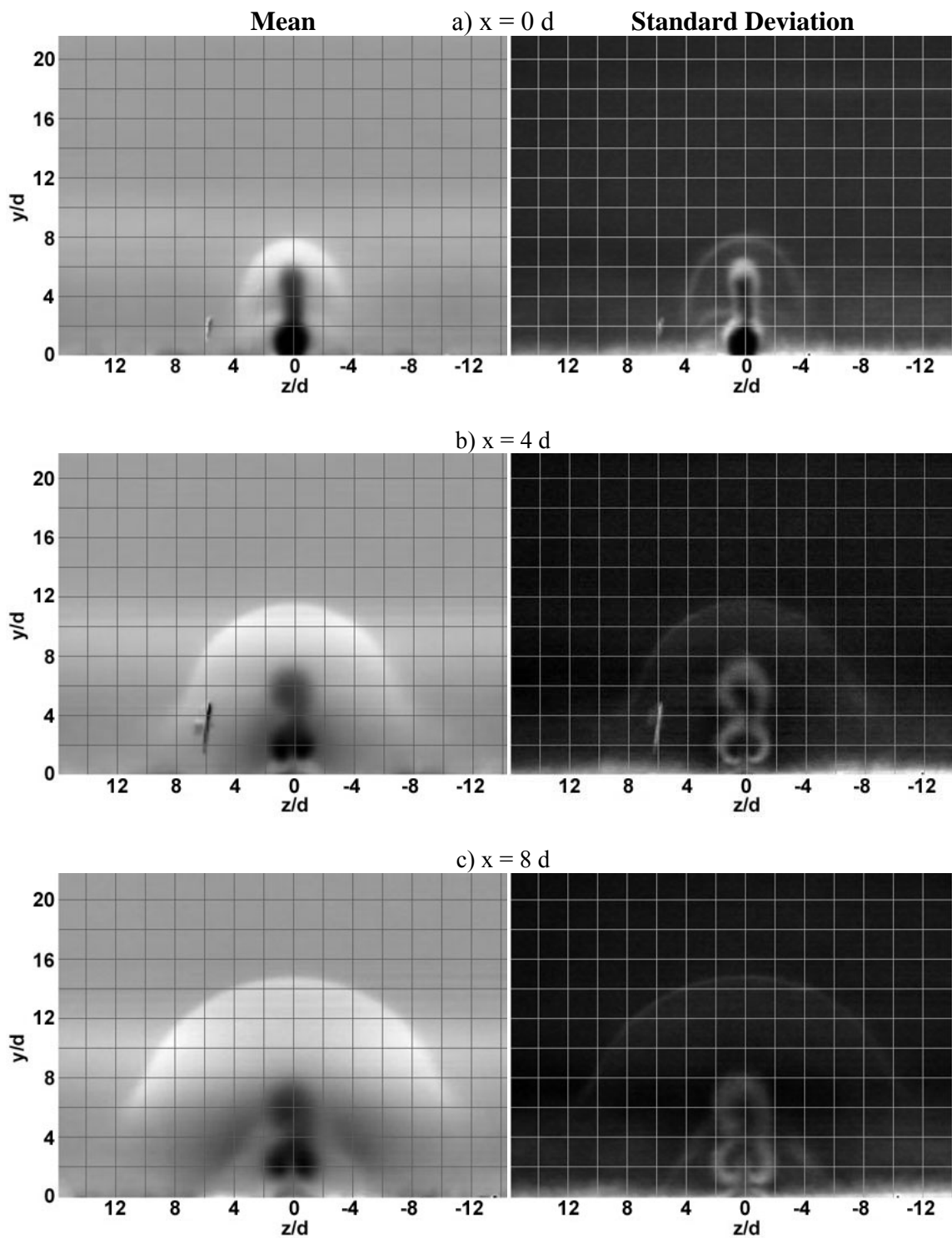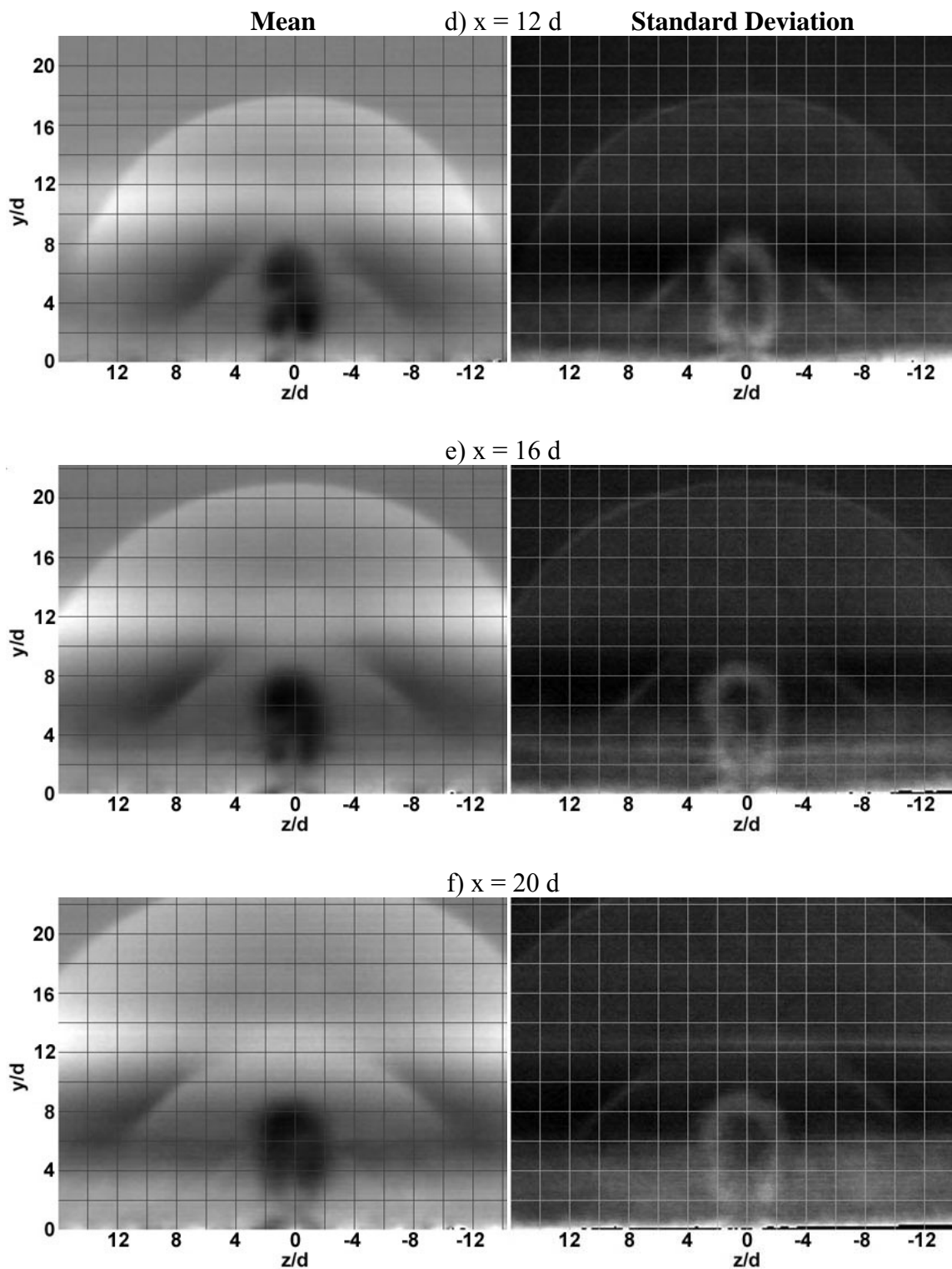*UAppendix G*

Mean   a) x = 0 d   **Standard Deviation**

b) x = 4 d

c) x = 8 d
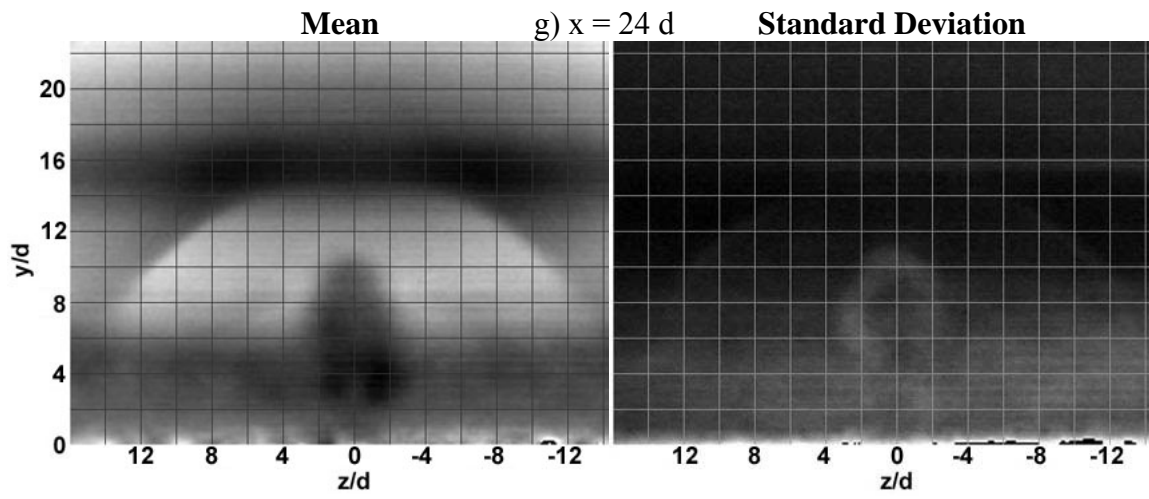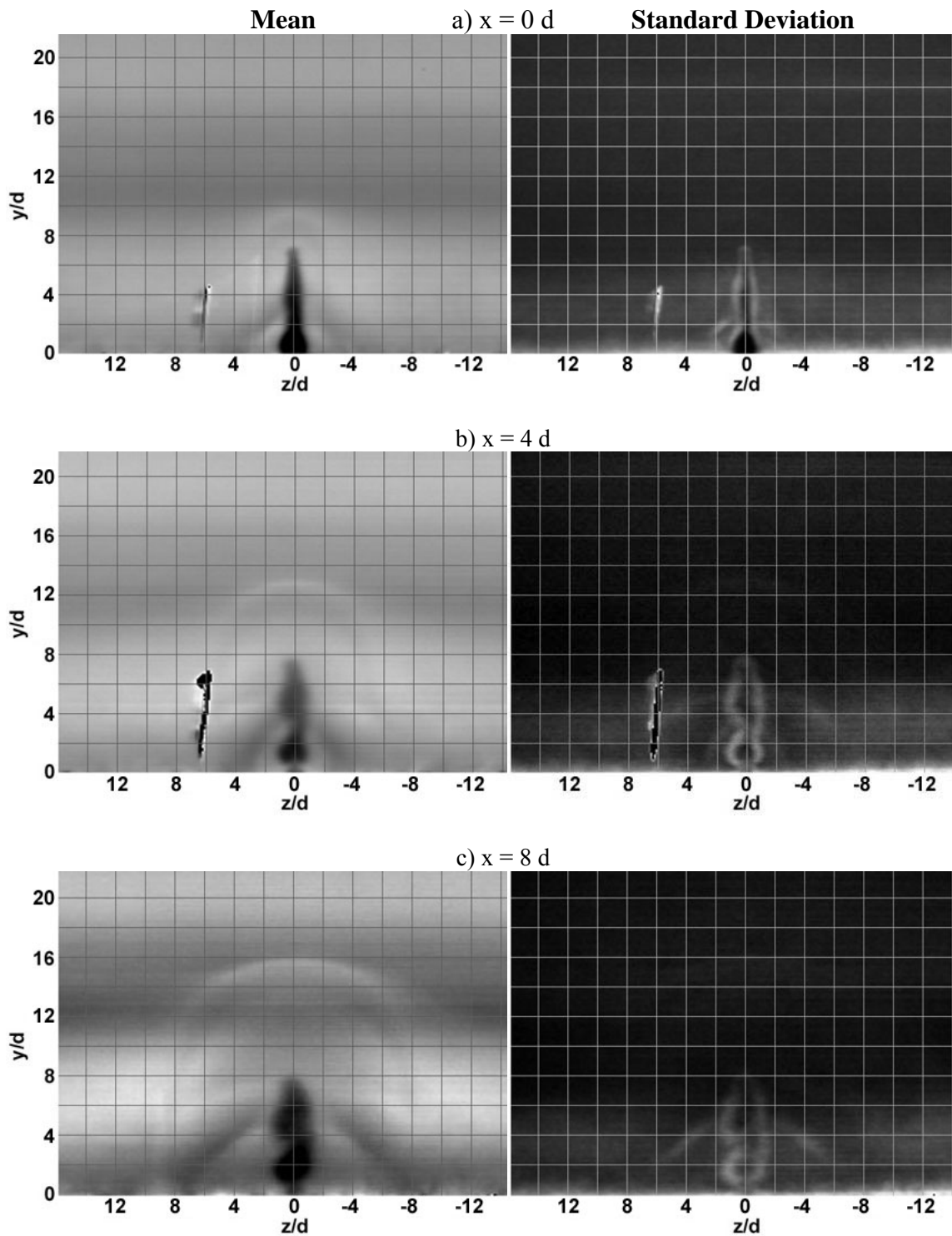
Figure G11. (T3) Mie scatter, Tall insert, injection pressure 3, x/d = 0, 4, 8

Mean   d) x = 12 d   **Standard Deviation**

e) x = 16 d
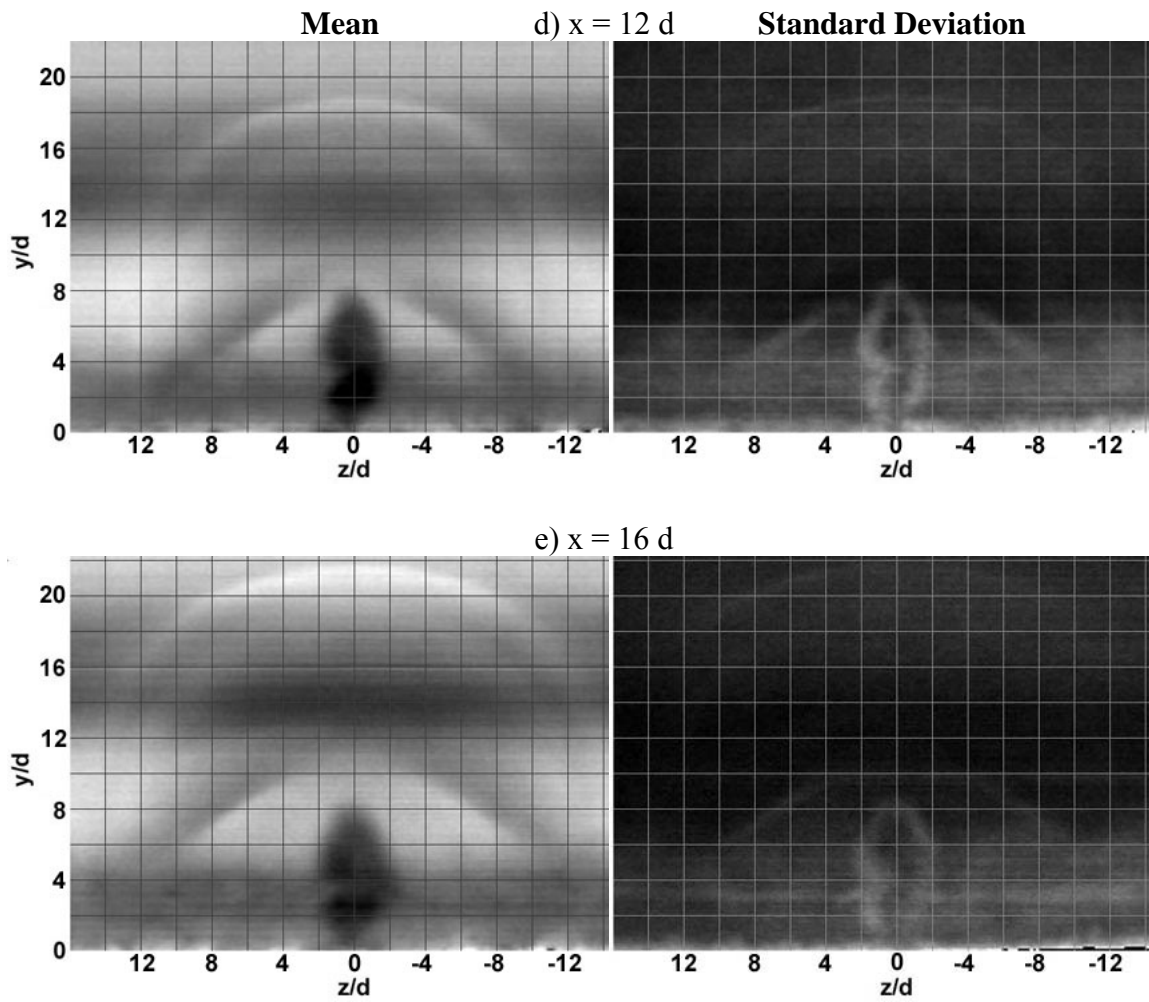
Figure G11 (cont'd). (T3) Mie scatter, Tall insert, injection pressure 3, x/d = 12, 16

MIE SCATTER

END VIEW

WIDE INSERT

IMAGES

Mean a) x = 0 d **Standard Deviation**

b) x = 4 d

c) x = 8 d
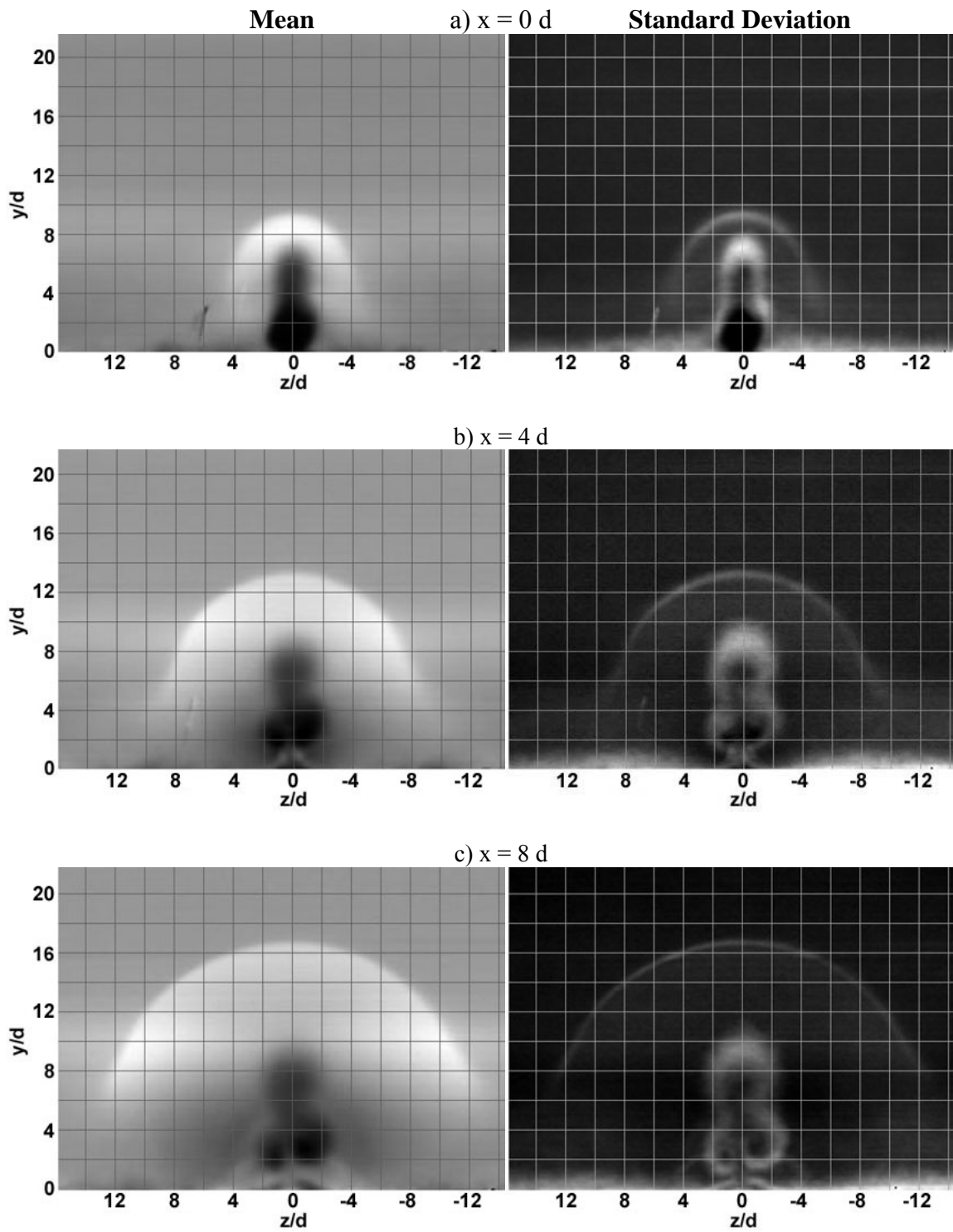
Figure G12. (W1) Mie scatter, Wide insert, injection pressure 1, x/d = 0, 4, 8
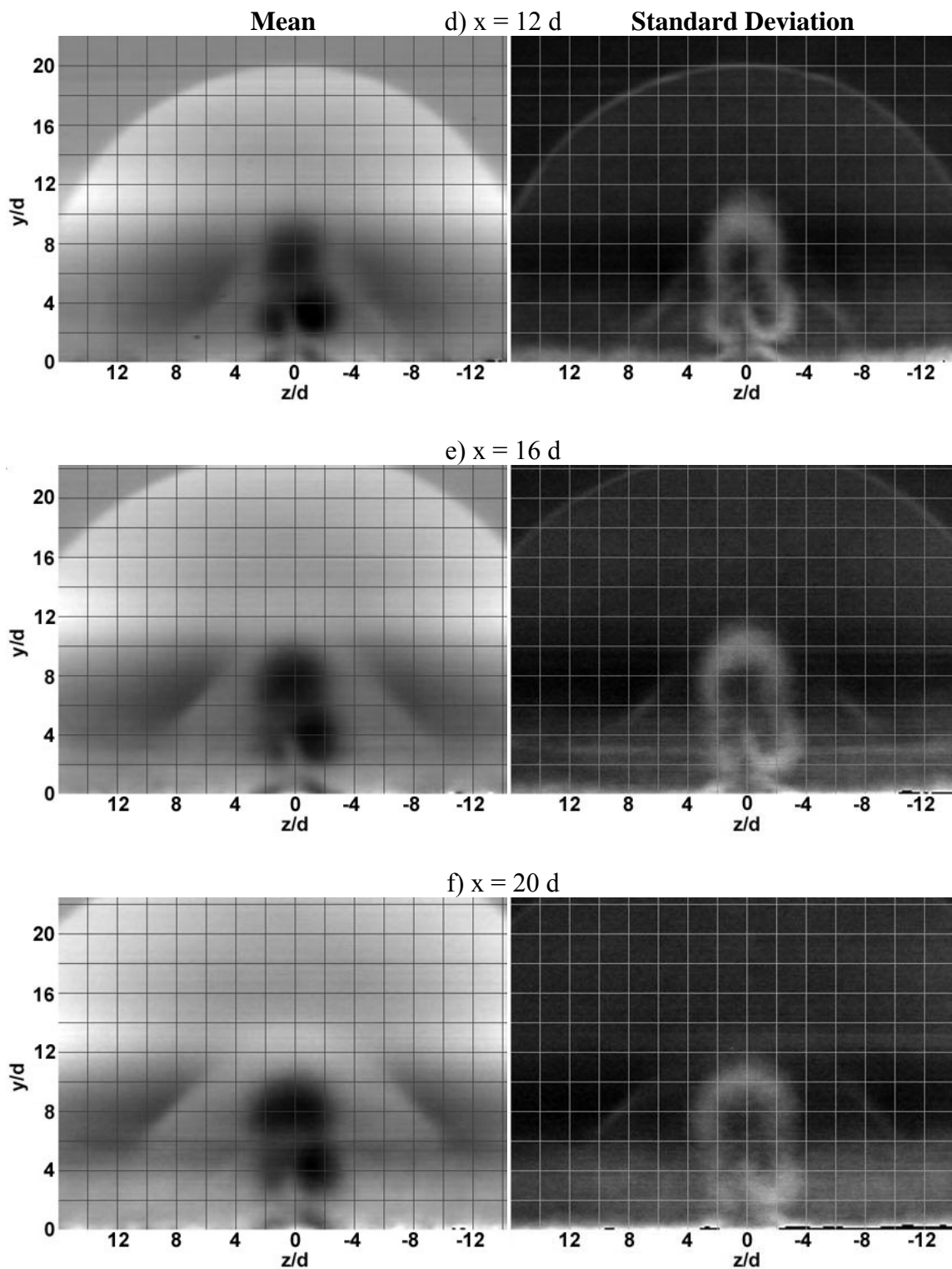
197

Mean   d) x = 12 d   **Standard Deviation**

e) x = 16 d

f) x = 20 d

Figure G12 (cont'd). (W1) Mie scatter, Wide insert, injection pressure 1, x/d = 12, 16, 20

Mean g) x = 24 d **Standard Deviation**

h) x = 32 d

Figure G12 (cont'd). (W1) Mie scatter, Wide insert, injection pressure 1, x/d = 24, 32

Mean   a) x = 0 d   **Standard Deviation**

b) x = 4 d

c) x = 8 d
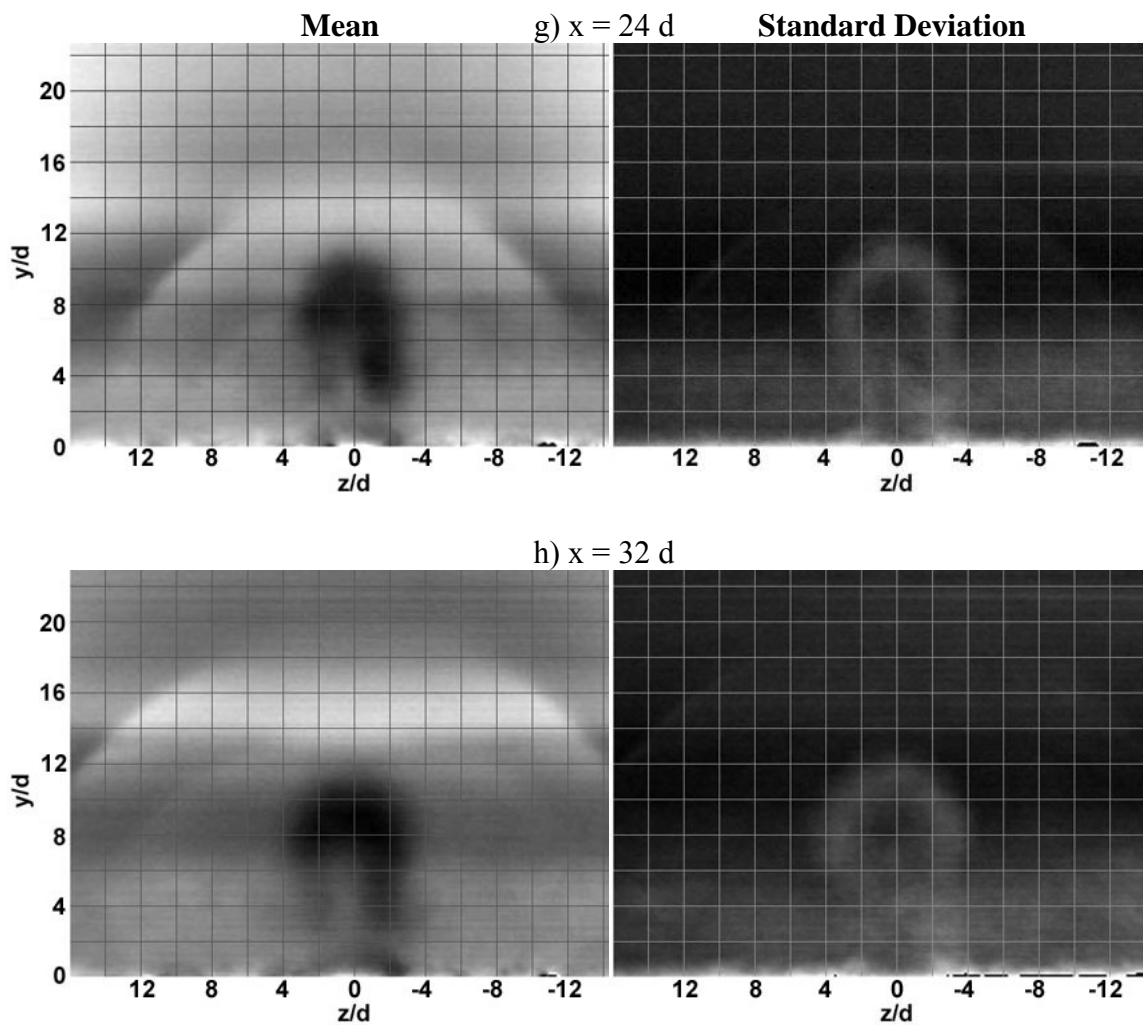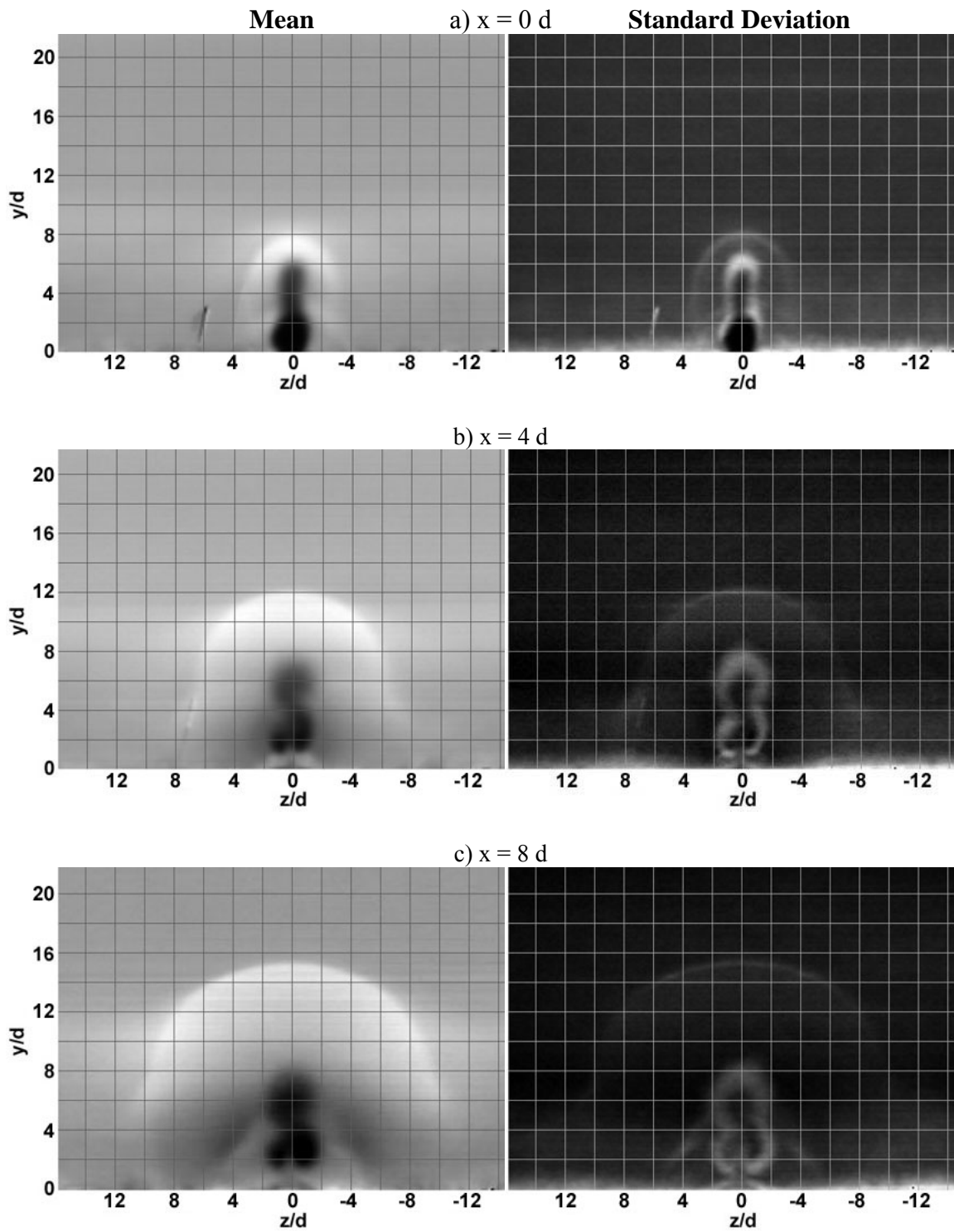
Figure G13. (W2) Mie scatter, Wide insert, injection pressure 2, x/d = 0, 4, 8

200

Mean   d) x = 12 d   **Standard Deviation**

e) x = 16 d

f) x = 20 d

Figure G13 (cont'd). (W2) Mie scatter, Wide insert, injection pressure 2, x/d = 12, 16, 20

201

Mean g) x = 24 d **Standard Deviation**

Figure G13 (cont'd). (W2) Mie scatter, Wide insert, injection pressure 2, x/d = 24

Mean   a) x = 0 d   Standard Deviation

b) x = 4 d

c) x = 8 d
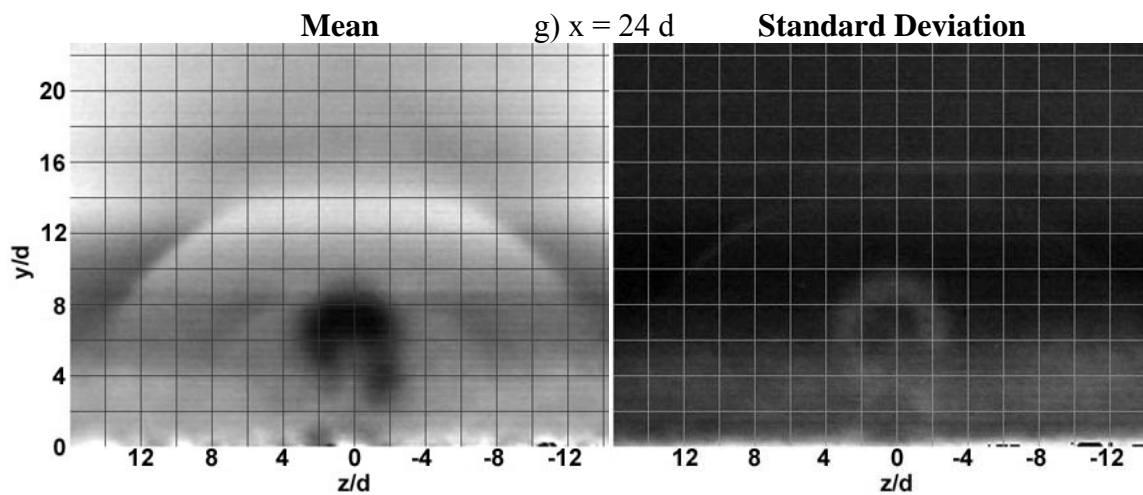
Figure G14. (W3) Mie scatter, Wide insert, injection pressure 3, x/d = 0, 4, 8

Mean   d) x = 12 d   **Standard Deviation**

e) x = 16 d

f) x = 20 d
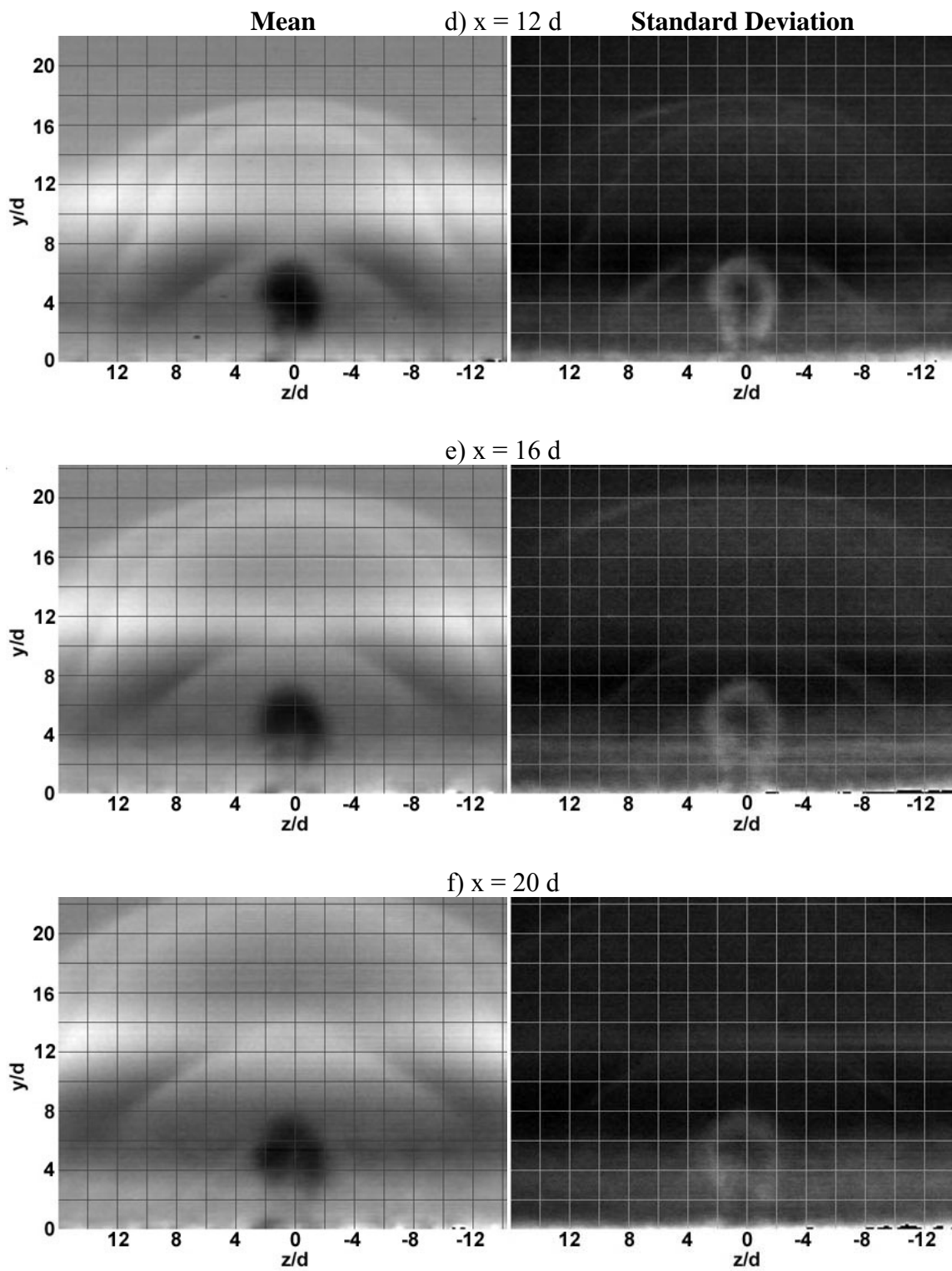
Figure G14 (cont'd). (W3) Mie scatter, Wide insert, injection pressure 3, x/d = 12, 16, 20

Appendix H – Wall Pressure Data

Table H1. Flat insert wall pressures (psia), including baseline (no injection)

Tap	F1 Bottom	F1 Top	F2 Bottom	F2 Top	F3 Bottom	F3 Top	F2BP Bottom	F2BP Top	Baseline Bottom
#1	7.66	7.43	7.64	7.41	7.63	7.40	7.62	7.45	7.83
#2	8.39	7.78	8.38	7.77	8.37	7.76	8.36	7.75	8.12
#3	7.59	7.83	7.58	7.80	7.58	7.79	7.56	7.83	7.91
#4	6.84	7.40	6.81	7.39	6.80	7.38	6.79	7.42	6.94
#5		7.86		7.85		7.84		7.73	
#6	5.50	8.25	5.48	8.24	5.48	8.24	14.57	8.19	7.30
#7	5.40	7.87	5.38	7.86	5.38	7.86	14.43	7.86	5.42
#8	5.32	7.28	5.36	7.28	5.45	7.26	17.94	7.45	5.45
#9	6.12	6.28	5.80	6.26	5.70	6.26	19.63	8.96	5.57
#10	4.64	5.97	4.74	5.95	4.77	5.94	20.21	12.21	4.73
#11	3.77	6.11	3.80	5.91	3.83	5.91	20.76	13.76	6.05
#12	6.31	6.26	6.30	6.38	6.29	6.45	21.22	14.74	6.32
#13	5.48	5.97	5.54	6.01	5.57	6.01	21.70	16.00	5.26
#14	4.48	6.44	4.43	6.46	4.44	6.45	22.08	16.40	4.43
#15	4.42	5.12	4.27	5.09	4.33	5.07	23.16	17.34	4.27
#16	4.16	4.26	4.18	4.03	4.21	3.96	23.44	17.92	4.37
#17	4.18		4.23		4.20		23.72		4.18
#18	3.91		3.92		3.92		23.98		3.84
#19	4.87		4.70		4.51		24.21		4.77
#20	4.38		4.53		4.54		24.46		4.43
#21	4.11		4.12		4.20		24.71		4.16

Table H2. Medium insert wall pressures (psia)

Tap	M1 Bottom	M1 Top	M2 Bottom	M2 Top	M3 Bottom	M3 Top	M2BP Bottom	M2BP Top
#1	7.67	7.43	7.67	7.41	7.68	7.42	7.66	7.48
#2	8.35	7.75	8.35	7.74	8.36	7.75	8.36	7.74
#3	7.60	7.80	7.58	7.80	7.59	7.82	7.56	7.85
#4	6.83	7.38	6.83	7.38	6.84	7.40	6.81	7.43
#5		7.83		7.83		7.84		7.69
#6	5.49	8.25	5.48	8.22	5.49	8.24	15.17	8.18
#7	5.38	7.85	5.37	7.81	5.38	7.82	15.01	7.86
#8	5.37	7.28	5.37	7.28	5.40	7.28	18.41	7.45
#9	6.07	6.26	5.77	6.26	5.71	6.28	20.10	11.17
#10	4.62	5.95	4.73	5.95	4.77	5.96	20.67	13.30
#11	3.76	6.33	3.79	5.91	3.84	5.91	21.21	14.50
#12	6.32	6.22	6.30	6.41	6.29	6.20	21.66	15.77
#13	5.45	5.93	5.51	5.98	5.57	6.01	22.13	16.50
#14	4.44	6.38	4.42	6.43	4.44	6.45	22.51	16.84
#15	4.43	5.12	4.27	5.09	4.31	5.09	23.59	17.93
#16	4.15	4.31	4.19	4.07	4.22	3.98	23.86	18.54
#17	4.23		4.22		4.20		24.14	
#18	3.91		3.92		3.93		24.39	
#19	4.87		4.70		4.56		24.61	
#20	4.36		4.51		4.53		24.85	
#21	4.10		4.11		4.20		25.09	

Table H3. Tall insert wall pressures (psia)

Tap	T1 Bottom	T1 Top	T2 Bottom	T2 Top	T3 Bottom	T3 Top	T2BP Bottom	T2BP Top
#1	7.55	7.37	7.66	7.40	7.68	7.42	7.71	8.57
#2	8.20	7.59	8.27	7.66	8.36	7.75	11.84	10.76
#3	7.50	7.79	7.55	7.83	7.59	7.82	13.39	12.74
#4	6.87	7.35	6.84	7.35	6.84	7.40	15.79	13.66
#5		7.70		7.79		7.84		14.23
#6	5.46	8.12	5.48	8.17	5.49	8.24	18.67	14.59
#7	5.35	7.72	5.35	7.72	5.38	7.82	18.44	16.20
#8	5.32	7.18	5.37	7.24	5.40	7.28	20.74	17.29
#9	5.97	6.20	5.71	6.23	5.71	6.28	21.87	17.39
#10	4.56	5.98	4.71	5.96	4.77	5.96	22.27	18.05
#11	3.73	7.45	3.78	5.91	3.84	5.91	22.64	18.71
#12	6.24	6.12	6.26	6.32	6.29	6.20	22.95	19.01
#13	5.37	5.85	5.46	5.97	5.57	6.01	23.29	19.30
#14	4.39	6.23	4.38	6.35	4.44	6.45	23.57	19.98
#15	4.37	5.07	4.27	5.08	4.31	5.09	24.52	20.16
#16	4.09	4.51	4.17	4.19	4.22	3.98	24.77	20.77
#17	4.21		4.22		4.20		25.04	
#18	3.86		3.90		3.93		25.27	
#19	4.84		4.72		4.56		25.53	
#20	4.32		4.49		4.53		25.75	
#21	4.06		4.12		4.20		26.01	

Table H4. Wide insert wall pressures (psia)

Tap	W1 Bottom	W1 Top	W2 Bottom	W2 Top	W3 Bottom	W3 Top	W2BP Bottom	W2BP Top
#1	7.68	7.43	7.70	7.44	7.70	7.45	7.70	7.51
#2	8.34	7.73	8.35	7.74	8.35	7.74	8.35	7.73
#3	7.56	7.82	7.57	7.83	7.56	7.82	7.56	7.84
#4	6.81	7.37	6.82	7.38	6.82	7.37	6.80	7.40
#5		7.85		7.87		7.88		7.78
#6	5.50	8.21	5.51	8.21	5.50	8.20	14.45	8.18
#7	5.38	7.77	5.38	7.77	5.37	7.78	14.24	7.85
#8	5.38	7.28	5.36	7.30	5.33	7.30	17.83	7.48
#9	6.07	6.26	5.80	6.27	5.70	6.26	19.53	8.24
#10	4.62	5.95	4.74	5.97	4.75	5.97	20.15	11.91
#11	3.76	7.30	3.81	5.91	3.86	5.91	20.72	13.53
#12	6.30	6.20	6.30	6.36	6.27	6.11	21.18	14.55
#13	5.44	5.88	5.51	5.97	5.55	6.00	21.66	15.77
#14	4.44	6.38	4.42	6.44	4.43	6.44	22.04	16.34
#15	4.41	5.14	4.28	5.13	4.31	5.12	23.20	17.20
#16	4.16	4.36	4.21	4.11	4.23	4.01	23.47	17.87
#17	4.23		4.24		4.22		23.78	
#18	3.92		3.94		3.94		24.01	
#19	4.89		4.74		4.58		24.27	
#20	4.36		4.52		4.54		24.49	
#21	4.11		4.13		4.21		24.75	

Bibliography

[1]Gruber, M.R., Donbar, J.M., and Carter, C.D., "Mixing and Combustion Studies Using Cavity-Based Flameholders in a Supersonic Flow," ISABE Paper 2003-1204, September 2003.

[2]Livingston, T., and Segal, C., "Penetration and Spreading of Liquid Jets in an External-Internal Compression Inlet," *AIAA Journal*, Vol. 38, No.6, 2000, pp. 989-994.

[3]Owens, M.G., Mullagiri, S., and Segal, S., "Effects of Fuel Preinjection on Mixing in Mach 1.6 Airflow," *Journal of Propulsion and Power*, Vol. 17, No. 3, 2001, pp. 605-610.

[4]Gouskov, O., Kopchenov, V., and Vinogradov, V., "Numerical Researches of Gaseous Fuel Pre-Injection in Hypersonic 3-D Inlet," AIAA Paper 2000-3599, July 2000.

[5]McClinton, C.R., Hunt, J.L., and Ricketts, R.H., "Airbreathing Hypersonic Technology Vision Vehicles and Development Dreams," AIAA Paper 99-4978, November 1999.

[6]Rogers, R.C., Capriotti, D.P., and Guy, R.W., "Experimental Supersonic Combustion Research at NASA Langley," AIAA Paper 98-2506, June 1998.

[7]Tishkoff, J.M, Drummond, J.P, Edwards, T., and Nejad, A.S., "Future Directions of Supersonic Combustion Research – Air Force/NASA Workshop on Supersonic Combustion," AIAA Paper 97-1017, January 1997.

[8]Seiner, J.N., Dash, S.M., and Kenzakowski, D.C., "Historical Survey on Enhanced Mixing in Scramjet Engines," *Journal of Propulsion and Power*, Vol. 17, No. 6, 2001, pp. 1273-1286.

[9]Billig, F.S., "Research on Supersonic Combustion," *Journal of Propulsion and Power*, Vol. 9, No. 4, 1993, pp. 499-514.

[10]Sabelnikov, V.A., Voloschenko, O.V., Ostras, V.N., and Sermanov, V.N., "Gasdynamics of Hydrogen-Fueled Scramjet Combustors," AIAA Paper 93-2145, June 1993.

[11]Owens, M.G., Mullagiri, S., and Segal, C., "Thermal Choking Analyses in a Supersonic Combustor," *Journal of Propulsion and Power*, Vol. 17, No.3, 2001, pp.611-616.

[12]Baurle, R.A., and Eklund, D.R., "Analysis of Dual-Mode Hydrocarbon Scramjet Operation at Mach 4 - 6.5," *Journal of Propulsion and Power*, Vol. 18, No. 5, 2002, pp. 990-1002.

[13]Roy, G.D., "Subsonic and Supersonic Mixing and Combustion Enhancement," ISABE Paper 91-7093, September 1991.

[14]Tomioka, S., Nagata, H., and Segawa, D., "Effect of Combustion on Mixing Process in a Supersonic Combustor," ISABE Paper 91-7094, September 1991.

[15]Stone, C., and Menon, S., "Simulation of Fuel-Air Mixing and Combustion in a Trapped-Vortex Combustor," AIAA Paper 2000-0478, January 2000.

[16]Mathur, T., "Supersonic Combustion Experiments with a Cavity-Based Fuel Injector," *Journal of Propulsion and Power*, Vol. 17, No. 6, 2001, pp. 1305-1312.

[17]Hsu, K.-Y., and Goss, L.P., "Characteristics of a Trapped-Vortex Combustor," *Journal of Propulsion and Power*, Vol. 14, No. 1, 1998, pp. 57-65.

[18]Ben-Yakar, A., and Hanson, R.K., "Cavity Flameholders for Ignition and Flame Stabilization in Scramjets: An Overview," *Journal of Propulsion and Power*, Vol. 17, No. 4, 2001, pp. 869-877.

[19]Yu, K., Wilson, K.J., Smith, R.A., and Schadow, K.C., "Experimental Investigation on Dual-Purpose Cavity in Supersonic Reacting Flows," AIAA Paper 98-0723, January 1998.

[20]Yu, K.H., Wilson, K.J., and Schadow, K.C., "Effect of Flame-Holding Cavities on Supersonic Combustion Performance," AIAA Paper 99-2638, June 1999.

[21]Burnes, R., Parr, T.P., and Wilson, K.J., "Investigation of Supersonic Mixing Control Using Cavities: Effect of Fuel Injection Location," AIAA Paper 2000-3618, July 2000.

[22]Franke, M.E., and Carr, D.L., "Effect of Geometry on Open Cavity Flow-Induced Pressure Oscillations," AIAA Paper 75-492, March 1975.

[23]Katta, V.R., "Study on Trapped-Vortex Combustor – Effect of Injection on Flow Dynamics," *Journal of Propulsion and Power*, Vol. 14, No. 3, 1998, pp. 273-281.

[24]Baurle, R.A., Tam, C.-J., and Dasgupta, S., "Analysis of Unsteady Cavity Flows for Scramjet Applications," AIAA Paper 2000-3617, July 2000.

[25]Gruber, M.R., Baurle, R.A., Mathur, T., Hsu, K.-Y., "Fundamental Studies of Cavity-Based Flameholder Concepts for Supersonic Combustors," *Journal of Propulsion and Power*, Vol. 17, No. 1, 2001, pp.146-153.

[26]Ben-Yakar, A., and Hanson, R.K., "Supersonic Combustion of Cross-Flow Jets and Influence of Cavity Flame-Holders," AIAA Paper 99-0484, January 1999.

[27]Gruber, M.R., Jackson, K., Mathur, T., and Billig, F., "Experiments with a Cavity-Based Fuel Injector for Scramjet Applications," ISABE Paper 99-7154, September 1999.

[28]Riggins, D. W., and McClinton, C.R., "Analysis of Losses in Supersonic Mixing and Reacting Flows," AIAA Paper 91-2266, June 1991.

[29]Lee, M.P., McMillin, B.K., Palmer, J.L., and Hanson, R.K., "Planar Fluorescence Imaging of a Transverse Jet in a Supersonic Cross Flow," *Journal of Propulsion and Power*, Vol. 8, No. 4, 1992, pp. 729-735.

[30]Hermanson, J.C., and Winter, M., "Mie Scattering Imaging of Transverse, Sonic Jet in Supersonic Flow," *AIAA Journal*, Vol. 31, No. 1, 1993, pp. 129-132.

[31]VanLerberghe, W.M., Santiago, J.G., Dutton, J.C., and Lucht, R.P., "Mixing of a Sonic Transverse Jet Injected into a Supersonic Flow," *AIAA Journal*, Vol. 38, No.3, 2000, pp. 470-479.

[32]Cortelezzi, L., and Karagozian, A.R., "On the Formation of the Counter-rotating Vortex Pair in Transverse Jets," *Journal of Fluids*, Vol. 446, 2001, pp. 347-373.

[33]Papamoschou, D., and Hubbard, D.G., "Visual Observations of Supersonic Transverse Jets," *Experiments in Fluids*, Vol. 14, 1993, pp. 468-471.

[34]Gruber, M.R., Nejad, A.S., Chen, T.H., and Dutton, J.C., "Transverse Injection from Circular and Elliptic Nozzles into a Supersonic Cross Flow," *Journal of Propulsion and Power*, Vol. 16, No. 3, 2000, pp. 449-457.

[35]Orth, R.C., Schetz, J.A., and Billig, F.S., "The Interaction and Penetration of Gaseous Jets in Supersonic Flow," NASA CR-1386, July 1969.

[36]Arai, T., and Schetz, J.A., "Injection of Bubbling Liquid Jets from Multiple Injectors into a Supersonic Stream," AIAA Paper 92-5060, December 1992.

[37]Northam, G.B., Greenberg, I., and Byington, C.S., "Evaluation of Parallel Injector Configurations for Supersonic Combustion," AIAA Paper 89-2525, July 1989.

[38]Gutmark, E.J., Schadow, K.C., and Yu, K.H., "Mixing Enhancement in Supersonic Free Shear Flows," *Annual Review of Fluid Mechanics*, Vol. 27, 1995, pp. 375-417.

[39]Drummond, J.P., and Carpenter, M.H., "Mixing and Mixing Enhancement in Supersonic Reacting Flowfields," *Progress in Astronautics and Aeronautics*, Vol. 137 (High Speed Propulsion Systems), Ch. 7, 1991, pp. 383-455.

[40]Murugappan, S., and Gutmark, E., "Control of a Transverse Supersonic Jet Injection into a Supersonic Cross-Stream," AIAA Paper 2004-1204, January 2004.

[41]Murugappan, S., and Gutmark, E., "Control of Penetration and Mixing of an Excited Supersonic Jet into a Supersonic Cross-Stream," AIAA Paper 2005-0612, January 2005.

[42]Marble, F.E., Hendricks, G.J., Zukoski, E.E., "Progress Toward Shock Enhancement of Supersonic Combustion Processes," AIAA Paper 87-1880, June 1987.

[43]Menon, S., "Shockwave Induced Mixing Enhancement in Scramjet Combustors," AIAA Paper 89-0104, January 1989.

[44]Marble, F.E., Zukoski, E.E., Jacobs, J.W., Hendrick, G.J., Waitz, I.A., "Shock Enhancement of and Control of Hypersonic Mixing and Combustion," AIAA Paper 90-1981, April 1990.

[45]Northam, G.B., Capriotti, D.P., Byington, C.S., and Greenberg, I., "Supersonic Mixing and Combustion in Scramjets," ISABE Paper 91-7095, September 1991.

[46]Yang, J., Kubota, T., and Zukoski, E.E., "An Analytical and Computational Investigation of Shock Induced Vortical Flows," AIAA Paper 92-0316, January 1992.

[47]Yang, J., Kubota, T., and Zukoski, E.E., "Application of Shock-Induced Mixing to Supersonic Combustion," *AIAA Journal*, Vol. 31, No. 5, 1993, pp. 854-862.

[48]Riggins, D.W., "Vortex Generation and Mixing in Three-Dimensional Supersonic Combustors," *Journal of Propulsion and Power*, Vol. 11, No. 3, 1995, pp. 419-426.

[49]Riggins, D.W., "Investigation of Scramjet Injection Strategies for High mach Number Flows," *Journal of Propulsion and Power*, Vol. 11, No. 3, 1995, pp. 409-418.

[50]Sislian, J.P., and Schumacher, J., "Fuel/air Mixing Enhancement by Cantilevered Ramp Injectors in Hypersonic Flows," ISABE Paper 99-7155, September 1999.

[51]Kalkhoran, I.J., and Smart, M.K., "Aspects of Shockwave induced Vortex Breakdown," *Progress in Aerospace Sciences*, Vol. 36, 2000, pp. 63-95.

[52]Waitz, I.A., Marble, F.E., and Zukoski, E.E., "Vorticity Generation by Contoured Wall Injectors," AIAA Paper 92-3550, July 1992.

[53]Huh, H., and Driscoll, J.F., "Measured Effects of Shock Waves on Supersonic Hydrogen-Air Flames," AIAA Paper 96-3035, July 1996.

[54]Gruber, M.R., and Nejad, A.S., "New Supersonic Combustion Research Facility," *Journal of Propulsion and Power*, Vol. 11, No. 5, 1995, pp. 1080-1083.

Vita

Second Lieutenant Daniel R. Montes was born in San Juan, Puerto Rico. He graduated from Keith Country Day School in Rockford, Illinois. He then immediately entered undergraduate studies at the United States Air Force Academy in Colorado Springs, Colorado where he graduated with a Bachelor of Science degree in Astronautical Engineering in May 2003. Upon graduation he was commissioned as a Second Lieutenant in the United States Air Force.

In August 2003, he entered the Graduate School of Engineering and Management, Air Force Institute of Technology for his first assignment. There he is studying under the Department of Aeronautics and Astronautics and sequencing in air-breathing and rocket propulsion. Upon graduation, he will be assigned to the AFRL Munitions Directorate in Eglin AFB, Florida.

REPORT DOCUMENTATION PAGE

1. REPORT DATE (DD-MM-YYYY)	2. REPORT TYPE	3. DATES COVERED (From – To)
21-03-2005	Master's Thesis	Aug 2003 - Mar 2005

4. TITLE AND SUBTITLE	5a. CONTRACT NUMBER
Mixing Effects of Pylon-aided Fuel Injection Located Upstream of a Flameholding Cavity in Supersonic Flow	5b. GRANT NUMBER
	5c. PROGRAM ELEMENT NUMBER
6. AUTHOR(S)	5d. PROJECT NUMBER
Montes, Daniel R., Second Lieutenant, USAF	5e. TASK NUMBER
	5f. WORK UNIT NUMBER

7. PERFORMING ORGANIZATION NAMES(S) AND ADDRESS(S)	8. PERFORMING ORGANIZATION REPORT NUMBER
Air Force Institute of Technology Graduate School of Engineering and Management (AFIT/EN) 2950 Hobson Way, Building 640 WPAFB OH 45433-8865	AFIT/GAE/ENY/05-M12

9. SPONSORING/MONITORING AGENCY NAME(S) AND ADDRESS(ES)	10. SPONSOR/MONITOR'S ACRONYM(S)
Gruber, M. R. AFRL/PRAS 1950 Fifth Street Wright-Patterson Air Force Base, Ohio 45433	11. SPONSOR/MONITOR'S REPORT NUMBER(S)

12. DISTRIBUTION/AVAILABILITY STATEMENT

APPROVED FOR PUBLIC RELEASE; DISTRIBUTION UNLIMITED.

13. SUPPLEMENTARY NOTES

14. ABSTRACT

The Air Force Research Lab (AFRL), Propulsion Directorate, Wright-Patterson Air Force Base, Ohio is conducting ongoing research into propulsive efficiency in supersonic ramjet (scramjet) technology. One current focus of this research is the usefulness of flameholding cavities implemented in the supersonic hydrocarbon-fueled combustion chamber. Because good mixing and proper cavity-core interaction lead to more efficient combustion, methods of optimizing fuel/air mixing both within and upstream the cavity are investigated. In a cooperative effort with the Air Force Institute of Technology (AFIT), AFRL provided a supersonic wind tunnel outfitted with an existing cavity design. A circular injection port was placed upstream of the cavity, and a series of three pylons (medium, tall, wide geometries) were in turn fitted just upstream of the port to improve mixing and penetration of the fuel into the core airflow. The main goals of this experiment were to characterize the mixing ability of injected fuel with the core flow as it propagated downstream of the pylon and to analyze the effects, if any, of this mixing strategy on cavity flow and overall efficiency compared to a no pylon case. The experiment was a non-reacting mixing study. Measurements were obtained from pressure transducers, Planar Laser-Induced Fluorescence (PLIF), and Mie scattering visualization. Of the three pylon geometries tested, the wide pylon provided the best combination of fuel penetration into the freestream (135% increase) and mixing potential. The taller pylon provided more penetration but incurred a large loss penalty. All pylons lifted the fuel from the injector to prevent flashback, and all pylons demonstrated equivalent or better mixing potential than the flat reference at various tunnel conditions.

15. SUBJECT TERMS
Pylon injection, Cavity flameholder, Scramjet combustion

16. SECURITY CLASSIFICATION OF:			17. LIMITATION OF ABSTRACT	18. NUMBER OF PAGES	19a. NAME OF RESPONSIBLE PERSON
a. REPORT	b. ABSTRACT	c. THIS PAGE			Dr. Paul I. King (ENY)
U	U	U	UU	233	19b. TELEPHONE NUMBER (Include area code) (937) 255-3636, ext 4628 (paul.king@afit.edu)